The Evolution of Gas Kinematics in Star-Forming Field and Cluster Galaxies Since $z \sim 1$

Helen Louise Johnson

A thesis presented in accordance with the regulations for admittance to the degree of Doctor of Philosophy

Centre for Extragalactic Astronomy
Department of Physics
University of Durham
United Kingdom

August 2017

The Evolution of Gas Kinematics in Star-Forming Field and Cluster Galaxies Since $z \sim 1$

Helen Louise Johnson

Abstract

A fundamental pursuit of astronomy is to understand how galaxies form and evolve. What drives the decline in the cosmic star formation rate density? Why are high redshift galaxies clumpy and turbulent? How can we explain the emergence of the Hubble sequence? To answer these questions we must unravel a complex interplay of different processes, including gas accretion, star formation, feedback, and environmental effects. Studying the gas kinematics of galaxies can provide valuable insight. In this thesis we use integral field spectroscopy to probe the evolution of star-forming field and cluster galaxies over the past 8 billion years.

We first present a multi-wavelength analysis of 27 dusty starburst galaxies in a massive cluster at $z \sim 0.4$. It is thought that starbursts represent an intermediate phase in the transition from spirals to S0s in dense environments. We combine Hα kinematics with far-infrared imaging and millimetre spectroscopy, and find that most galaxies are rotationally supported, with high angular momentum and large cold gas reservoirs. It appears that the starbursts have only recently been accreted to the cluster. To complete the transition to S0s, they must undergo a dynamical heating of the disk, increase in concentration, and reduce their angular momentum by $\sim 40\%$. We conclude that the most likely way to achieve this is via multiple tidal interactions with other cluster members.

We next study the velocity dispersion properties of 472 galaxies observed as part of the KMOS Redshift One Spectroscopic Survey (KROSS). Most galaxies at this epoch are rotationally supported, but dynamically hot and highly turbulent. In order to make robust kinematic measurements, we model the effects of beam smearing using a series of mock KMOS data cubes. We then combine KROSS with data from the SAMI survey ($z \sim 0.05$) and an intermediate redshift MUSE sample ($z \sim 0.5$), and find that while there is a weak trend between velocity dispersion and stellar mass, at fixed mass there is a strong increase

in velocity dispersion with redshift. At all redshifts, galaxies appear to follow the same weak trend of increasing velocity dispersion with star formation rate. We also test the predictions of two analytic models which suggest that turbulence in the ISM is driven by gravitational instabilities or stellar feedback. However we find that further observations are required to rule-out either model.

Finally, to understand the role of galaxy kinematics in "crystallising" the Hubble sequence, we study the *HST* images of 231 KROSS galaxies. We quantify differences in morphology using the asymmetry parameter. This metric correlates very well with our visual interpretation of "clumpiness", however there are no strong trends as a function of galaxy kinematics. On average, the velocity dispersion of clumps is consistent with the underlying disk, and there is no evidence to suggest that these star-forming regions are preferentially located towards the outskirts of the galaxy. We propose that adaptive optics assisted IFU observations would provide further insight, allowing us to test clump evolution theories and to study the radial distribution of angular momentum.

Dedicated to Grandma

Your star will always shine brightly

Declaration

The work described in this thesis was undertaken between October 2013 and August 2017 while the author was a research student under the supervision of Dr Mark Swinbank in the Department of Physics at the University of Durham. No part of this thesis has been submitted for any other degree at the University of Durham or any other University.
A section of this work has appeared in the following peer-reviewed paper:

- *Chapter 2:* Johnson, H. L.; Harrison, C. M.; Swinbank, A. M.; Bower, R. G.; Smail, Ian; Koyama, Y.; Geach, J. E.; 2016, MNRAS, 460, 1059: **The spatially resolved dynamics of dusty starburst galaxies in a $z \sim 0.4$ cluster: beginning the transition from spirals to S0s**

Further sections of this work have recently been accepted for publication in MNRAS:

- *Chapter 3 and Chapter 4:* Johnson, H. L.; Harrison, C. M.; Swinbank, A. M.; Tiley, A. L.; Stott, J. P.; Bower, R. G.; Smail, Ian; Bunker, A. J.; Sobral, D.; Turner, O. J.; Best, P.; Bureau, M.; Cirasuolo, M.; Jarvis, M. J.; Magdis, G.; Sharples, R. M.; Bland-Hawthorn, J.; Catinella, B.; Cortese, L.; Croom, S. M.; Federrath, C.; Glazebrook, K.; Sweet, S. M.; Bryant, J. J.; Goodwin, M.; Konstantopoulos, I. S.; Lawrence, J. S.; Medling, A. M.; Owers, M. S.; Richards, S.; arXiv:1707.02302 **The KMOS Redshift One Spectroscopic Survey (KROSS): the origin of disk turbulence in $z \sim 0.9$ star-forming galaxies**

The author carried out the work in this thesis with the following exceptions: (1) data reduction and analysis of the IRAM data and *Herschel* images in Chapter 2 was carried out by Mark Swinbank; (2) reduction of the KROSS data in Chapters 3 – 5 was performed by Chris Harrison and John Stott; (3) kinematic properties, star formation rates and stellar masses of the KROSS sample were derived by Chris Harrison and John Stott; (4) data reduction and analysis of the SAMI data in Chapter 4 was carried out by Alfie Tiley. All text was written by the author. All figures in Chapters 2 – 5 were produced by the author.

In addition to the work presented in this thesis, the author has also either worked on, or been involved in, the following work during the period of their PhD:

- Stott, John P.; Swinbank, A. M.; *Johnson, Helen L.*; Tiley, Alfie; Magdis, Georgios; Bower, Richard; Bunker, Andrew J.; Bureau, Martin; Harrison, Chris M.; Jarvis, Matt J.; Sharples, Ray; Smail, Ian; Sobral, David; Best, Philip; Cirasuolo, Michele; 2016, MNRAS, 457, 1888: **The KMOS Redshift One Spectroscopic Survey (KROSS): dynamical properties, gas and dark matter fractions of typical $z \sim 1$ star-forming galaxies**

- Tiley, Alfred L.; Stott, John P.; Swinbank, A. M.; Bureau, Martin; Harrison, Chris M.; Bower, Richard; *Johnson, Helen L.*; Bunker, Andrew J.; Jarvis, Matt J.; Magdis, Georgios; Sharples, Ray; Smail, Ian; Sobral, David; Best, Philip; 2016, MNRAS, 460, 103: **The KMOS Redshift One Spectroscopic Survey (KROSS): the Tully-Fisher relation at $z \sim 1$**

- Harrison, C. M.; *Johnson, H. L.*; Swinbank, A. M.; Stott, J. P.; Bower, R. G.; Smail, Ian; Tiley, A. L.; Bunker, A. J.; Cirasuolo, M.; Sobral, D.; Sharples, R. M.; Best, P.; Bureau, M.; Jarvis, M. J.; Magdis, G., 2017, MNRAS, 467, 1985: **The KMOS Redshift One Spectroscopic Survey (KROSS): rotational velocities and angular momentum of $z \approx 0.9$ galaxies**

- Swinbank, A. M.; Harrison, C. M.; Trayford, J.; Schaller, M.; Smail, Ian; Schaye, J.; Theuns, T.; Smit, R.; Alexander, D. M.; Bacon, R.; Bower, R. G.; Contini, T.; Crain, R. A.; de Breuck, C.; Decarli, R.; Epinat, B.; Fumagalli, M.; Furlong, M.; Galametz, A.; *Johnson, H. L.*; Lagos, C.; Richard, J.; Vernet, J.; Sharples, R. M.; Sobral, D.; Stott, J. P., 2017, MNRAS, 467, 3140: **Angular momentum evolution of galaxies over the past 10 Gyr: a MUSE and KMOS dynamical survey of 400 star-forming galaxies from $z = 0.3$ to 1.7**

- Thomson, A. P.; Simpson, J. M.; Smail, Ian; Swinbank, A. M.; Best, P. N.; Sobral, D.; Geach, J. E.; Ibar, E.; *Johnson, H. L.*, 2017, ApJ, 838, 119: **Evolution of Dust-obscured Star Formation and Gas to $z = 2.2$ from HiZELS**

- Turner, O. J.; Cirasuolo, M.; Harrison, C. M.; McLure, R. J.; Dunlop, J. S.; Swinbank, A. M.; *Johnson, H. L.*; Sobral, D.; Matthee, J.; Sharples, R. M., 2017, MNRAS, 471, 1280: **The KMOS Deep Survey (KDS) I: dynamical measurements of typical star-forming galaxies at $z \simeq 3.5$**

Acknowledgements

Firstly, thank you to my wonderful family – Mum, Dad, Mark and Grandad – for inspiring me, believing in me, and supporting me in everything I do. Ever since I was a little girl, gazing up at the stars in our back garden, you've encouraged me to dream big. I could never have done this without you! I would also like to thank my teachers over the years, particularly Keith Caulkin, for making Physics so much fun and for helping me to take my first steps on this crazy journey.

During my PhD I've been lucky to work with a fantastic team of people. Thank you to my supervisor Mark Swinbank for his guidance, encouragement, patience, and boundless enthusiasm. Special thanks also to Chris Harrison, Ian Smail, Richard Bower, John Stott, Alfie Tiley, Renske Smit, Dave Alexander, Alastair Edge and John Lucey for their wisdom, help and advice. John, Mark and Renske – thank you for the brilliant observing trips!

Thanks to the friends and officemates who have made my Durham experience such a special one. In particular my "batcave family" – Andrew, Paddy and Tim – thank you for being such incredible housemates. I'll be forever weirder because of you and I'm so grateful for all of our adventures. It's impossible to name everyone else here, but in particular I'd like to mention Greg, Steph, Sownak, Saavi, Charles, Tamsyn, Stuart, Andrew G, Matthieu, James T, Oliver, Alice, Flora, Steve, Will, and An. Thanks for all the coffee chat, pub trips, outreach fun, house parties, politics, and for being there when things got tough. I also don't know what I'd do without Amy, Franzi and Nadine. You're an inspiration, thank you for everything.

I feel lucky to have taken part in so many wonderful outreach events during my PhD. Thank you to Pete Edwards and Lorraine Coghill for such exciting opportunities, and for sharing your knowledge and enthusiasm with us. You've made my time in Durham so much more fun! Finally, thanks to Lindsay Borrero, Alan Lotts, Lydia Heck and Sabine Schindler, whose help has been invaluable.

"The cosmos is all that is or was or ever will be.
Our feeblest contemplations of the cosmos stir us – there is a tingling in the spine, a catch in the voice, a faint sensation, as if a distant memory, of falling from a height.
We know we are approaching the greatest of mysteries."

– Carl Sagan

Contents

List of Tables

List of Figures

CHAPTER 1

Introduction

> *"We find them smaller and fainter, in constantly increasing numbers, and we know that we are reaching into space, farther and farther, until, with the faintest nebulae that can be detected with the greatest telescopes, we arrive at the frontier of the known Universe."*
>
> – Edwin P. Hubble

1.1 Island Universes

The word galaxy derives from the Greek term γαλαξιας – "galaxias" or "the milky one" – used to describe the appearance of the Milky Way as a cloudy band of light across the night sky. As early as the 5th century BC, Greek philosophers proposed that the Milky Way was a concentration of distant stars, however it wasn't until 400 years ago that we knew this to be true. It was Galileo Galilei, with his early telescope, who discovered a multitude of stars "so numerous as almost to surpass belief" (Galilei 1610).

As telescopes became more powerful, astronomers began to catalogue other such hazy, extended, "nebulous objects" (Messier 1781; Herschel 1786). Thomas Wright of Durham speculated these may be galaxies outside of our own (Wright 1750), so-called "Island Universes" (Kant 1755), but this was disputed by others who thought that these nebulae were simply unresolved stellar systems within the Milky Way. Even at the beginning of the 20th century, a consensus had not yet been reached. This culminated in the "Great Debate" of 1921, with Haber Curtis and Harlow Shapley vigorously opposing each other's views about the scale of the Universe (Shapley & Curtis 1921).

Edwin Hubble finally settled the debate through observations of Cepheid variables made using the 100-inch Hooker telescope at Mount Wilson (Hubble 1925). By exploiting

the tight luminosity-period relation of these stars, he was able to infer distances to several nebulae. His observations placed these mysterious objects firmly outside of the Milky Way, meaning they must be galaxies in their own right. In the same decade, Hubble and his collaborators established a "relation between distance and radial velocity among extragalactic nebulae" (Hubble 1929; Hubble & Humason 1931; 1934), evidence that the Universe is expanding.

These two discoveries revolutionised how we view our place in the Universe, and laid the foundations for modern extragalactic astronomy. Our galaxy is not unique in its existence but is one of many. Observations using the *Hubble Space Telescope* (*HST*) now suggest there may be somewhere close to 100 billion. This opens the door to a myriad of questions: How do galaxies form and evolve? How do they differ from each other and how can we classify them? How typical is our own Milky Way?

1.2 The Hubble Sequence

Hubble also pioneered the classification of galaxies, sorting those he observed according to their morphology (Hubble 1926). This classification system – known as the Hubble Sequence or Hubble "tuning fork" – is shown in Fig. 1.1. Galaxies are separated into ellipticals, which are spheroidal and diffuse, and spirals, which are disk-like with bright spiral arms. Elliptical galaxies are futher grouped according to their axis ratio, from E0 (spherical) to E7 (flattened). Spirals are divided into two parallel sequences of barred and unbarred galaxies, and then grouped based on the prominence of the central bulge and appearance of the spiral arms, from Sa (arms tightly wound and a large, bright bulge) to Sc (arms loosely wound and a faint bulge). Lenticular (S0) galaxies are an intermediate morphological class, which appear disk-like but have ill-defined spiral arms.

Hubble's work was highly influential, and his classification system, later refined and expanded by de Vaucouleurs (1959; 1963), is still in use today. A common misconception is that Hubble intended the "tuning fork" to represent an evolutionary sequence, with a transition from "early-type" ellipticals and lenticulars to "late-type" spiral galaxies. In fact it was only ever intended as a sequence of morphological complexity, and these terms have their origins in the spectral classification of stars (see Baldry 2008). Although they

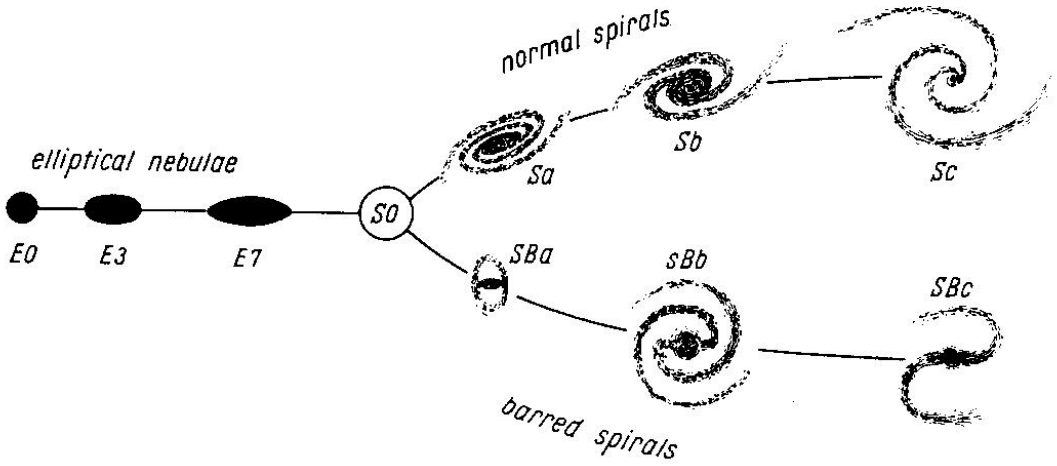

Figure 1.1: Hubble "tuning fork" diagram as published in Hubble & Rosseland (1936). Galaxies are classified morphologically according to their ellipticity, the existence and appearance of spiral arms, and the prominence of the central bulge.

have no temporal meaning, the terms "early-type" and "late-type" are still commonly used to refer to two these classes of galaxies.

Our understanding of galaxy populations has since moved far beyond the Hubble Sequence. We know that late-type galaxies are rich in the cold gas necessary for star formation. These systems therefore host many young, high-mass (OB type) stars which result in a characteristic blue colour. The disk is traced by the rotation of gas and stars, and this rotational velocity is correlated with the total luminosity (hence stellar mass) of the galaxy (Tully & Fisher 1977). The central bulge component is spheroidal, and primarily consists of older stars.

By contrast, early-type galaxies host little to no star formation. High mass stars evolve relatively quickly, leaving the stellar main sequence in 10s of Myr. What remains are the low mass, cooler stars with redder colours. Early-types are therefore characterised by older stellar populations and have a "red and dead" appearance. These galaxies are dominated by the random motions of gas and stars (though they also exhibit varying degrees of rotation, e.g. Emsellem et al. 2007; 2011). The range in orbital velocities of the stars, the velocity dispersion, is related to the total luminosity of the galaxy (Faber & Jackson 1976), while an even tighter relation (the Fundamental Plane) exists between velocity dispersion, surface brightness, and size (Djorgovski & Davis 1987).

These differences between galaxies are perhaps most evident in colour-magnitude space. Plotting optical colour against broad-band magnitude (or stellar mass) reveals two

relatively well-defined, distinct populations (Fig. 1.2; e.g. Strateva et al. 2001; Baldry et al. 2004; 2006). More massive galaxies tend to be early-type and redder, forming a tight "red sequence", while lower mass galaxies are generally late-type and bluer. The latter exhibit a wider distribution of colours for a fixed stellar mass, and so this region is referred to as the "blue cloud".

The challenge for theories of galaxy formation and evolution is to explain not only the existence of the Hubble sequence, but how these morphological types relate to each other and their complex interdependencies. In the following sections we describe our current understanding of galaxy formation, and the physical processes which shape the evolution of star-forming galaxies.

1.3 Galaxy Formation

The light we detect from galaxies comes from their stars and gas, however it is now widely accepted that these components constitute only a small fraction of the total mass. Most mass in galaxies, and indeed the wider Universe, is made up of weakly interacting, non-baryonic dark matter (e.g. Spergel et al. 2007; Planck Collaboration et al. 2014; 2016). Dark matter dominates the gravitational interactions of the Universe, acting as a "cosmic scaffolding" around which all other structure is formed.

Current theories of structure formation suggest that there were tiny fluctuations in the dark matter density distribution of the early Universe. These instabilities collapse under gravity to form virialised dark matter "haloes", which grow through accretion of new material. As gas in the dark matter halo cools and flows inwards, it eventually reaches a sufficiently high density that its self-gravity dominates over that of the dark matter. The gas is then able to collapse and fragment, forming stars and galaxies. Dark matter haloes typically have a small amount of angular momentum, introduced by tidal torques (see Schäfer 2009 for review). If this angular momentum is conserved during cooling, the gas will spin up and settle into a rotationally supported disk (as observed for late-type galaxies).

Over time, small haloes coalesce and merge to form larger structures (e.g. Peebles 1982; Blumenthal et al. 1984; Davis et al. 1985) in a process known as "hierarchical

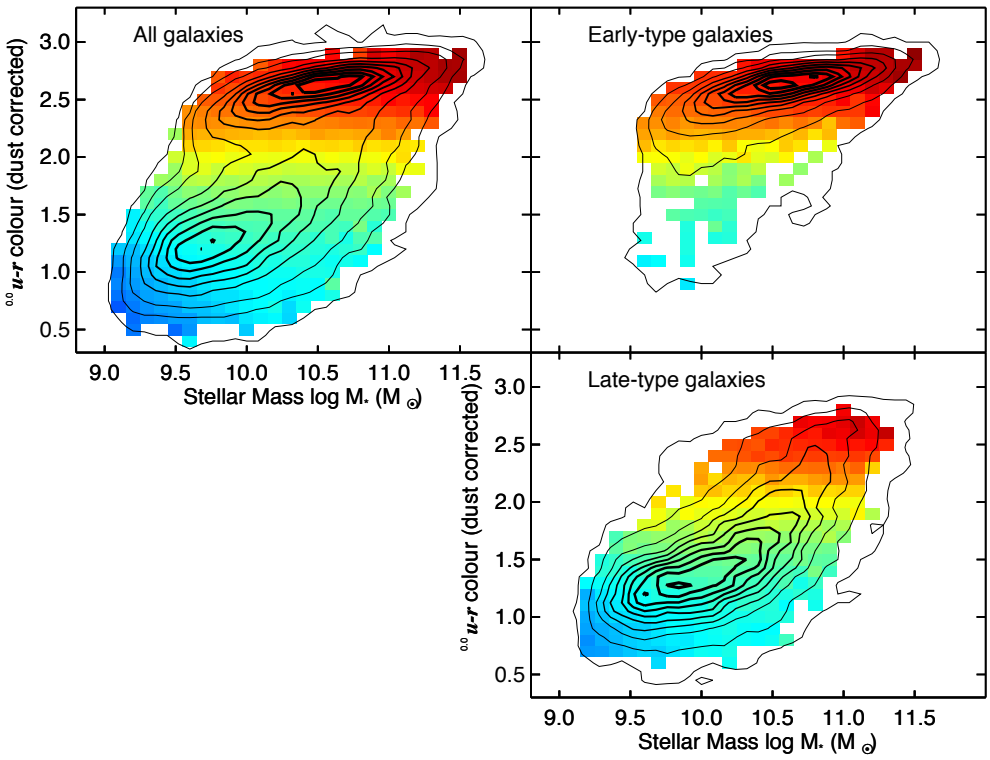

Figure 1.2: Dust-corrected $u-r$ band colour versus stellar mass for a mass-limited sample of local galaxies ($0.02 < z < 0.05$; Schawinski et al. 2014). The sample is based on observations from the Sloan Digital Sky Survey (SDSS), Data Release 7. The distribution of galaxies in this colour-mass plane is bimodal, separating into a "red sequence" (predominantly early-type galaxies) and "blue cloud" (predominantly late-types). Each region of the plot is coloured by the mean specific star formation rate (sSFR = SFR/$M_\star$), with bluer colours representing higher values.

assembly". As a result, in the local Universe a significant fraction of galaxies reside in groups and clusters ($\sim 50\%$; e.g. Bower & Balogh 2004). Within these regions, the number density of galaxies is tens to a few hundred times higher than average. In §1.5 we discuss how these differences in environment may influence how galaxies evolve.

1.4 Drivers of Galaxy Evolution

Following their formation, galaxies experience several internal and external processes which shape their evolution. A complex interplay of different factors determines how a galaxy looks (its morphology), how the gas and stars inside move (its kinematics), and how efficiently it forms stars. At the most basic level, these properties are governed by the inflow and outflow of gas, and the redistribution of angular momentum. In this section we discuss four key mechanisms – cold accretion, stellar feedback, AGN feedback, and mergers – and their implications.

1.4.1 Gas Accretion

The most important aspect of star formation is the raw material, cold gas (see §1.6.3). Recent numerical simulations suggest gas from the intergalactic medium (IGM) may flow continuously along clumpy, filamentary streams, through the galaxy halo and directly on to the disk (e.g. Kereš et al. 2005; Dekel et al. 2009; Ceverino et al. 2010). This process would supply large amounts of pristine gas (average metallicities of $Z \sim 0.001$ – $0.01\,Z_{\odot}$; e.g. van de Voort & Schaye 2012) to the galaxy, without significant disruption to the kinematics. So-called "cold mode" accretion ($T_{\rm gas} \sim 10^4 - 10^5$ K) is likely to be very efficient at early times, and has been invoked to explain the high star formation rates observed at high redshift (§1.6.4; e.g. Genzel et al. 2008; Cresci et al. 2009).

As the dark matter halo grows larger, more of the infalling material is expected to be shock heated at the virial radius ($T_{\rm gas} \sim 10^6 - 10^7$ K). Instead of being delivered directly onto the disk, the gas forms a hot halo which later settles via radiative cooling (e.g. Rees & Ostriker 1977; White & Rees 1978; White & Frenk 1991). This "hot mode" accretion is thought to dominate above halo masses of $M_{\rm h} \sim (2-3) \times 10^{11}\,{\rm M}_{\odot}$, and hence becomes increasingly important at low redshift ($z \leq 1$; e.g. Dekel & Birnboim 2006; Ocvirk et al.

2008; Kereš et al. 2009b). In general, cold accretion is the main driver of galaxy formation, in the sense that most of the baryons that make it into galaxies are accreted via this mode. However, the hot mode can contribute $\geq 10\%$ for halo masses of $M_{\rm h} \geq 10^{11}\,{\rm M}_{\odot}$ (e.g. van de Voort et al. 2011).

1.4.2 Feedback

In cosmological simulations without feedback, the gas in dark matter haloes rapidly cools and condenses to form stars. This leads to galaxies with higher star formation rates and more stellar mass than observations suggest is correct (the "overcooling problem"; e.g. Katz et al. 1996; Balogh et al. 2001; Kereš et al. 2009a; Schaye et al. 2010). In reality, only $\sim 5-10\%$ of baryons in the Universe are in the form of cold gas and stars (e.g. Bell et al. 2003; Fukugita & Peebles 2004; McGaugh et al. 2010). Fig. 1.3 shows the stellar-to-halo mass ratio as a function of halo mass, for three runs of a simulation (Somerville et al. 2008) and for a semi-empirical relationship (Moster et al. 2013). Without feedback, the baryon to stars conversion efficiency in the model is much higher than observed, at all halo masses (see also Conroy & Wechsler 2009; Behroozi et al. 2013). This implies that some physical process is required to either prevent the gas from cooling, or to eject it from the galaxy completely. Below we describe two ways that this can be achieved.

1.4.2.1 Stellar Feedback

Stars inject energy and momentum into the interstellar medium (ISM) in the form of stellar winds, radiation pressure, photoionization and supernovae (e.g. Larson 1974; Dekel & Silk 1986; Bower et al. 2012; Dale et al. 2014). In cosmological simulations, supernova feedback is usually invoked to regulate the star formation in low-mass haloes and distribute metals through the ISM/IGM (e.g. Oppenheimer & Davé 2006; Dubois & Teyssier 2008; Putman et al. 2012). There are two main mechanisms considered: kinetic feedback and thermal feedback. In kinetic feedback models, the supernovae impart momentum to the surrounding gas, directly ejecting it from disk (e.g. Springel & Hernquist 2003; Vogelsberger et al. 2014). In thermal feedback models, exploding supernovae simply heat the gas, and "blast waves" are generated due to an increased gas pressure (e.g. Dalla Vecchia & Schaye 2012; Schaye et al. 2015). If star formation is particularly vig-

orous, gas can be removed in dramatic, galactic scale outflows (e.g. Shapley et al. 2003; Swinbank et al. 2009; Genzel et al. 2011; Newman et al. 2012; Bradshaw et al. 2013). Observations suggest that these outflows are common and the rate of mass loss can often exceed the star formation rate of the galaxy (e.g. Veilleux et al. 2005). Energy from winds and supernovae may also drive turbulence in the ISM (see Mac Low & Klessen 2004 for review), something we discuss further in Chapter 4.

1.4.2.2 AGN Feedback

Supermassive black holes ($M_{\rm BH} \approx 10^5 - 10^{10}\,{\rm M}_\odot$) are found at the centre of massive galaxies (e.g. Kormendy & Richstone 1995; Magorrian et al. 1998; Ferrarese & Merritt 2000; Gebhardt et al. 2000). As matter is accreted by these black holes, they release vast amounts of energy and become visible as active galactic nuclei (AGN). It is typically assumed that $\sim 10\%$ of the rest-mass energy of the accreted material is liberated (i.e. $\epsilon \approx 0.1$), but efficiencies of between $\epsilon = 0.05 - 0.42$ can be achieved depending on the spin of the black hole (e.g. Kerr 1963; Shapiro & Teukolsky 1983; Merloni et al. 2004). This energy can be predominantly radiative (emission of energetic photons) or mechanical (energetic particles). AGN feedback is typically invoked to explain the inefficiency of star formation in high mass galaxies (e.g. Fabian 2012; Kormendy & Ho 2013; Heckman & Best 2014; Harrison 2017). Radiative AGN can suppress star formation via turbulence, shocks and heating of the ISM, or the removal of gas in galactic outflows (e.g. Veilleux et al. 2005; Alexander & Hickox 2012; King & Pounds 2015). Mechanically-dominated AGN can heat the gas via powerful radio jets, and prevent it from cooling to form stars (e.g. Cattaneo et al. 2009; McNamara & Nulsen 2012; Simpson et al. 2013).

1.4.3 Mergers

In a theory of hierarchical structure formation, mergers play an important role in the assembly of galaxies and dark matter haloes. The nature of the merger remnant is highly dependent on the mass ratio of the progenitor galaxies (e.g. Barnes & Hernquist 1996; Naab & Burkert 2003; Cox et al. 2006). If the masses of the two galaxies are very unequal (a minor merger), then the final system will tend to resemble the most massive progenitor. If both are of similar mass (a major merger), then the remnant will bear little resemblance

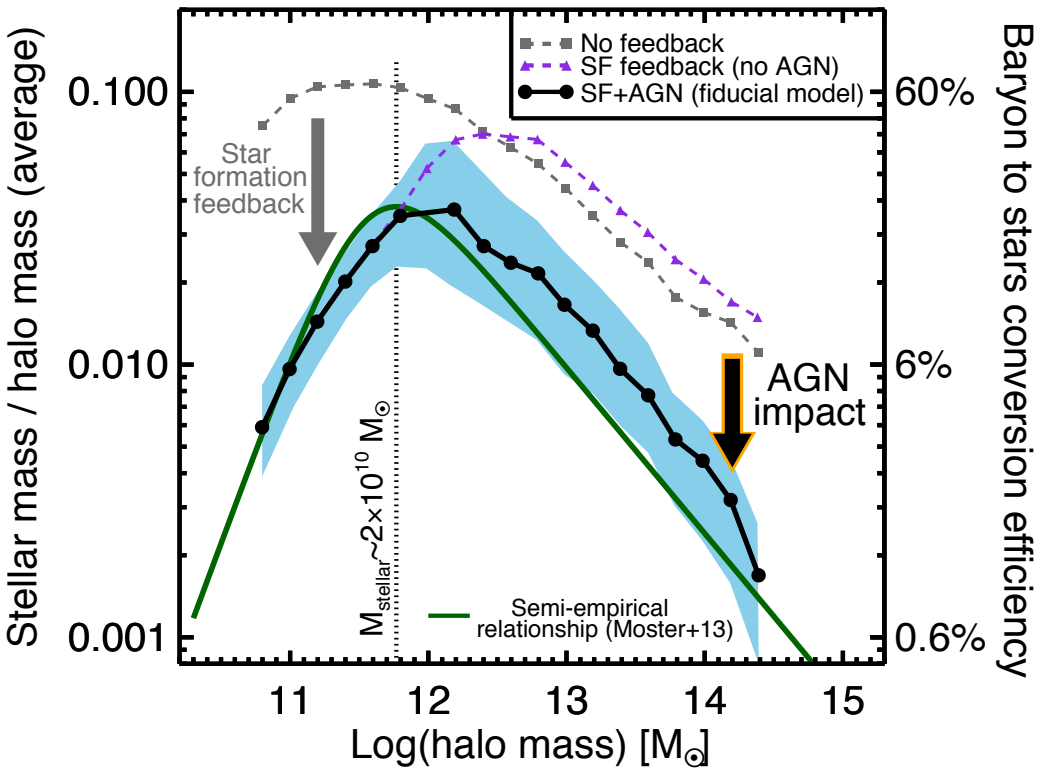

Figure 1.3: Figure from Harrison (2017) which shows the ratio between stellar mass and halo mass as a function of halo mass, for three runs of a cosmological simulation (Somerville et al. 2008) and the semi-empirical relationship of Moster et al. (2013). The blue shaded region shows the 16th to 84th percentile range of the fiducial model of the simulation (AGN + stellar feedback). Stellar feedback and AGN feedback act to reduce the star formation efficiency in low and high mass haloes, respectively.

to either, and any disk will be destroyed. Simulations suggest that ellipticals are likely the remnants of two (or more) disk galaxies (e.g. Farouki & Shapiro 1982; Hernquist 1992).

The outcome will also depend on the gas fraction of the progenitors. If the merger is gas-rich, gravitational torques can remove angular momentum from the gas and drive it inwards. This dense gas concentration at the centre of the remnant can trigger a nuclear starburst and/or AGN activity (e.g. Mihos & Hernquist 1996; Di Matteo et al. 2005; Hopkins et al. 2006; Hayward et al. 2014; Sparre & Springel 2016).

1.5 Influence of Environment

Strong trends exist between morphology and environment. Rich clusters are dominated by ellipticals and S0s, while in low density environments (the field) spiral galaxies are most abundant (e.g. Dressler 1980; Bower et al. 1992; Kodama et al. 2004; Bamford et al. 2009; van der Wel et al. 2010). This effect was first quantified by Dressler (1980), who established the "morphology-density" relation shown in Fig. 1.4.

Subsequent studies revealed that in higher redshift clusters, the fraction of S0s is lower and the fraction of spirals proportionately higher (e.g. Butcher & Oemler 1978; Dressler et al. 1997; Poggianti et al. 2009). This suggests a transformation between the two populations. Indeed, cluster spirals are redder (e.g. Hudson et al. 2010; Cantale et al. 2016), have lower star formation rates (e.g. Gómez et al. 2003; Wolf et al. 2009), and are gas poor (e.g. Cortese et al. 2011; Boselli et al. 2014a) compared to their counterparts in the field. A number of different mechanisms have been proposed for this evolution (see Boselli & Gavazzi 2006 for review). We summarise four of the most important below.

1.5.1 Galaxy Harassment

In high density environments, the relative velocities of galaxies are typically too large to lead to mergers ($v_{\rm gal} \sim 10^3$ kms^{-1}; Bialas et al. 2015). However, Moore et al. (1996; 1998) suggest that repeated, high-speed galaxy-galaxy encounters (so-called "galaxy harassment") can cause substantial mass loss from the disks of late-type (Sc, Sd) spiral galaxies. These interactions can dynamically heat the remaining disk, increasing the velocity dispersion and decreasing the angular momentum (see also Mastropietro et al. 2005;

Smith et al. 2010; 2015). Gas may also be driven inwards, feeding star formation in the central regions of the galaxy (e.g. Fujita 1998).

1.5.2 Galaxy-Cluster Tidal Interactions

Tidal interactions between galaxies and the cluster potential can compress molecular gas in the interstellar medium, triggering additional star formation (e.g. Byrd & Valtonen 1990; Henriksen & Byrd 1996; Fujita 1998). If the interaction is particularly efficient, gas in the disk is funnelled inward to fuel a nuclear starburst episode. The structure of the galaxy may also change, through the formation of a bar or bulge, and increased thickness of the disk (e.g. Valluri 1993).

1.5.3 Ram Pressure Stripping

Clusters are permeated by a hot, dense, X-ray emitting gas known as the intracluster medium (ICM). As a galaxy passes through the ICM, it experiences a drag force which can strip its cold gas component (e.g. Gunn & Gott 1972; Abadi et al. 1999; Quilis et al. 2000). This ram pressure stripping effect is often invoked to explain the HI deficiency of cluster spirals, and "tails" of gas streaming away from infalling galaxies have been directly observed (e.g. Merluzzi et al. 2013; Fumagalli et al. 2014; Boselli et al. 2016). Removal of this gas reservoir will eventually shut off star formation (although there may be a temporary enhancement, e.g. Bekki & Couch 2003). Numerical simulations suggest that as much as $\sim 80\%$ of the gas mass can be stripped within a single pass of the cluster core (Abadi et al. 1999).

1.5.4 Strangulation

Galaxies are surrounded by a halo of hot gas, which cools and condenses to fuel star formation in the disk (e.g. White & Rees 1978; White & Frenk 1991). In dense environments, this material can be removed through tidal interactions and ram pressure stripping. This leads to a slow decrease in star formation rate as the galaxy depletes its remaining supply of cold gas (e.g. Larson et al. 1980; Bekki et al. 2002; McCarthy et al. 2008). Observations suggest that this "strangulation" (starvation) may begin to take effect at large

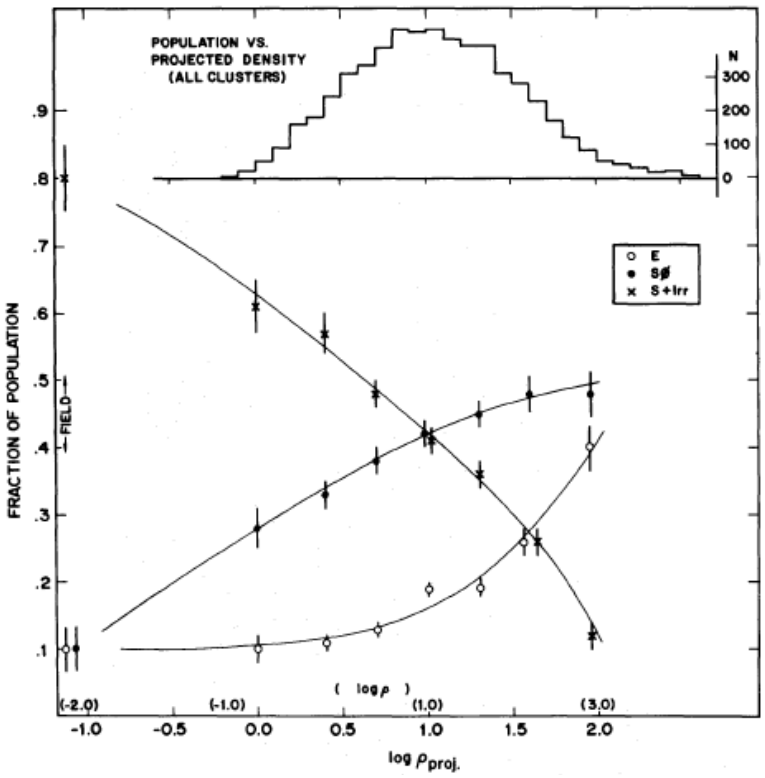

Figure 1.4: The morphology-density relation of Dressler (1980). The observed fraction of elliptical, S0 and spiral or irregular galaxies (in 55 rich clusters) as a function of the log of projected density, in galaxies Mpc^{-2}. With increasing density, there is a smooth increase in the fraction of early-type galaxies, and a decrease in the fraction of late-types.

cluster-centric radii (e.g. Balogh et al. 2000; Treu et al. 2003).

1.6 Star Formation

The ultimate goal is to understand how the physical processes introduced in §1.4 and §1.5 come together to shape the evolution of galaxies over many Gyr. One of the most fundamental properties of a galaxy is its star formation rate (SFR). Star formation is inherently complex; the typical mass and density of gas in a galaxy-sized halo are $\sim 10^{11}\,M_\odot$ and $\sim 10^{-24}\,g\,cm^{-3}$ respectively, but for a star are $\sim 1\,M_\odot$ and $\sim 1\,g\,cm^{-3}$. We must therefore understand the physical processes acting over a wide range of scales. Local late-type galaxies typically host large cold gas resevoirs, but most of this material ($\sim 70\%$ e.g. Catinella et al. 2010; Saintonge et al. 2011; Boselli et al. 2014b) is in the form of atomic hydrogen ($100-1000\,K$, $10^{-25}-10^{-23}\,g\,cm^{-3}$). For star formation, the gas must further cool and collapse to form dense molecular clouds ($\sim 10\,K$, $10^{-21}-10^{-19}\,g\,cm^{-3}$). Overdensities within an individual cloud then cause it to fragment, forming smaller clouds, and eventually stars. The fine details of this process are beyond the scope of this thesis, but have been discussed in a number of excellent reviews (e.g. Elmegreen & Scalo 2004; Mac Low & Klessen 2004; McKee & Ostriker 2007; Kennicutt & Evans 2012; Krumholz 2015). Our aim in this section is simply to consider star formation on a global scale: how it occurs, how we can measure it, and how it relates to other galaxy properties.

1.6.1 Disk Instability

Star formation on large scales proceeds by gravitational instabilities. According to the Jeans criterion, a uniform density gas cloud will collapse to form stars if its self-gravity can overcome the internal gas pressure (Jeans 1902). However, in a disk galaxy, pressure is not the only restoring force. Differential rotation adds an extra degree of stability to the gas. If a region is too large, it will be torn apart by shear faster than the gravitational free-fall time. For a thin gas disk, this can be expressed as the Toomre Q parameter (Toomre 1964; Wang & Silk 1994)

$$Q_g = \frac{\sigma_g \kappa}{\pi G \Sigma_g}, \tag{1.6.1}$$

where σ_g is the gas velocity dispersion, Σ_g is the gas surface density, and κ is the epicyclic frequency, defined as

$$\kappa = \frac{v}{r}\sqrt{2\left(1+\frac{r}{v}\frac{dv}{dr}\right)} \approx \sqrt{2}\frac{v}{r}, \tag{1.6.2}$$

where v is the rotation velocity and r is the disk radius. If $Q_g > 1$ then the rotation and internal pressure forces are sufficient to support the disk, hence it is stable. If $Q_g < 1$ then gravity can overcome this support, and the disk will collapse and fragment into cold gas clouds, resulting in widespread star formation (e.g. Kennicutt 1989; van der Hulst et al. 1993; Martin & Kennicutt 2001).

Observations suggest that gas-rich disks are typically driven to a state of marginal stability ($Q_g \sim 1$). One possible explanation is that if $Q_g < 1$ then star formation reduces Σ_g (by consuming gas) and increases σ_g (via stellar winds and supernovae), which in turn increases Q_g (e.g. Cacciato et al. 2012; Hopkins et al. 2012). Another possibility is that turbulence is driven by mass transport through the disk. Numerical simulations have shown that gravity alone may be able to regulate Q (e.g. Goldbaum et al. 2015; 2016).

1.6.2 Star Formation Tracers

The star formation rate of a galaxy can be determined by several different methods. In this section we discuss three commonly used tracers: nebular emission lines (e.g. Hα), ultraviolet (UV) continuum, and infrared (IR) continuum emission. We refer the reader to the review papers by Kennicutt (1998a) and Kennicutt & Evans (2012) for further details.

1.6.2.1 Ultraviolet Continuum

The most direct measure of star formation is rest-frame ultraviolet emission. Continuum UV traces the photospheric emission of young stars ($\sim$ 10-200 Myr). The optimal wavelength range is 1250-2500$\AA$, which for local galaxies requires space-based observations (e.g. *GALEX*; Morrissey et al. 2005), however at high redshift these wavelengths are easily accessible. The main disadvantage is that UV emission is highly attenuated by dust. Typical extinction corrections are 1-3 magnitudes, though can be even larger.

1.6.2.2 Nebular Emission Lines

Young, hot (O and B type) stars ionise the hydrogen gas in which they are embedded, creating what is known as a HII region. As the atoms recombine, electrons cascade down the energy levels, releasing emission at a range of characteristic wavelengths. Amongst the most common are the 3→2 transition, which gives rise to the Hα emission line (6562.8Å), and the 4→2 transition, which gives rise to Hβ (4861.3Å)[1]. Since OB stars are short-lived, this emission is indicative of recent star formation ($\sim$ 6-8 Myr). Hα is one of the brightest features in the spectrum of a star-forming galaxy and is therefore frequently used as a star formation rate indicator.

Another prominent spectral feature associated with star formation is the [OII] doublet (3726.0Å and 3728.8Å). Forbidden lines (denoted by square brackets) such as [OII], [OIII] and [NII] occur when an electron decays from a metastable state. Ordinarily, the timescale for spontaneous decay is $\sim 10^{-8}$ s, but for a metastable state this can be several seconds. In high-density environments, the electron will decay via collisional de-excitation before a forbidden transition can take place. However in low-density HII regions, spontaneous decay becomes more likely. Although the intensities of forbidden lines are sensitive to the ionisation and metallicity of the gas, [OII] can be empirically calibrated as a star formation rate tracer using Hα.

1.6.2.3 Infrared Continuum

A significant fraction of stellar light is reprocessed by dust. Interstellar dust consists of polyaromatic hydrocarbons (PAHs), silicates and graphites, which are formed in the atmospheres of cool stars and released by stellar winds and supernovae. Emission at wavelengths similar to the dust grain size ($\sim 0.001 - 1\,\mu$m) is scattered and absorbed most effectively. As a result, the UV radiation from stars is absorbed and re-emitted in the mid/far-infrared, at wavelengths of $\sim 5 - 1000\,\mu$m. This emission is commonly used as a star formation tracer, particularly in highly obscured systems (e.g. submm galaxies). Composite methods can also be used, combining dust-obscured and dust-unobscured emission for a more complete picture (e.g. UV+IR, Hα+IR; see Burgarella et al. 2005;

[1] Hβ is a poor SFR diagnostic because it is often weak and suffers from stellar absorption

Kennicutt et al. 2009; Treyer et al. 2010; Hao et al. 2011).

1.6.3 Cold Gas

As discussed in §1.6.1, for star formation to proceed the gas must first cool and fragment to form dense clouds. This relationship between star formation rate and gas density was first explored by Schmidt (1959), who concluded that "the rate of star formation varies with a power n of the density of interstellar gas". Kennicutt (1998b) later established a correlation between star formation rate density $\Sigma_{\rm SFR}$ and gas surface density $\Sigma_{\rm gas}$, for a large sample of local galaxies, as so:

$$\left(\frac{\Sigma_{\rm SFR}}{\rm M_\odot yr^{-1} kpc^{-2}}\right) = A \left(\frac{\Sigma_{\rm gas}}{\rm M_\odot pc^{-2}}\right)^N, \tag{1.6.3}$$

where $N = 1.4 \pm 0.15$. This relation, known as the Kennicutt-Schmidt law, appears to hold over at least four orders of magnitude in gas density. Fig. 1.5 demonstrates this trend using measurements of a more recent sample (Kennicutt & Evans 2012).

Subsequent studies have largely focussed on high-redshift galaxies (e.g. Daddi et al. 2010; Genzel et al. 2010; Tacconi et al. 2013), and how the atomic and molecular gas densities (i.e. $\Sigma_{\rm HI}$ and $\Sigma_{\rm H_2}$) individually relate to the star formation rate density (see Krumholz 2015 for review). Spatially resolved measurements of local galaxies reveal that on $0.5-1$ kpc scales there is an exceptionally tight correlation between molecular gas and star formation (e.g. Bolatto et al. 2011; Leroy et al. 2013). At high surface densities, the ISM is mostly H_2 and there is a roughly constant depletion time. However, below $\Sigma_{\rm gas} \sim 10\,{\rm M_\odot pc^{-2}}$ the HI component dominates, star formation rates drop, and there is significantly more scatter between $\Sigma_{\rm gas}$ and $\Sigma_{\rm SFR}$ (e.g. Bigiel et al. 2008; 2010).

It is crucial to understand how the gas properties of galaxies vary with stellar mass, redshift and environment. HI gas can be directly observed via the 21cm spectral line[2], but the H_2 molecule lacks a permanent dipole and hence its emission is very weak at low temperatures. The most commonly used proxy for H_2 is ^{12}CO (hereafter CO; Young & Scoville 1991; Solomon & Vanden Bout 2005; Carilli & Walter 2013). This is the second

[2]Emission when the Hydrogen electron flips from a parallel to anti-parallel spin state

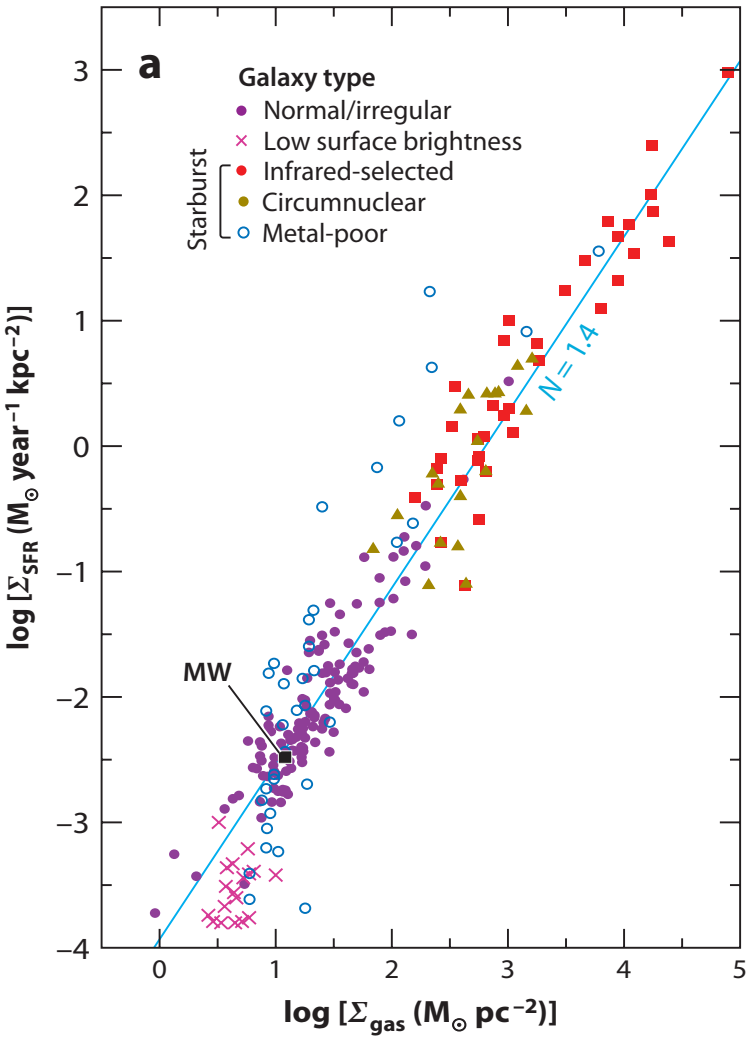

Figure 1.5: Relationship between the disk-averaged surface densities of star formation (as measured using Hα, Paα or IR emission) and gas (atomic and molecular), for different galaxy types. This figure is from Kennicutt & Evans (2012), adapted from the original version in Gao & Solomon (2004). For most galaxies, there is a remarkably tight relation between $\log(\Sigma_{\rm SFR})$ and $\log(\Sigma_{\rm gas})$. The pale blue line shows the Kennicutt-Schmidt relation with $N = 1.4$. For consistency, the same CO to H_2 conversion factor was used to derive all gas surface density estimates.

most abundant molecule in the ISM and has strong rotational emission lines at millimetre wavelengths. The CO(1→0) and CO(2→1) transitions are used to trace the bulk of cold gas in galaxies, while higher transitions correspond to warmer, denser regions. The main issue regarding the interpretation of CO observations is how the CO luminosity relates to H_2 mass. It has been suggested that the CO-H_2 conversion factor, X_{CO}, may be lower in starbursts and higher in metal-poor galaxies (see Bolatto et al. 2013 for review).

1.6.4 Redshift Evolution

One of the most important indicators of galaxy evolution is the cosmic star formation rate density, ρ_{SFR}. This measures how many stars (in units of stellar mass) per unit volume the Universe was forming at a particular epoch. Our current understanding is that the star formation rate density increases as $(1+z)^4$ out to at least $z \sim 1$ (e.g. Lilly et al. 1996; Madau et al. 1996; Karim et al. 2011; Burgarella et al. 2013; Sobral et al. 2013a; see Fig. 1.6) and then begins to flatten. Determining the exact redshift at which the star formation rate density peaked is challenging, since no single tracer is suitable for all epochs. However our best estimate is currently $z \sim 2$, when the Universe was approximately one-third of its present age. It was during this crucial time ($1 < z < 3$) that today's massive galaxies formed most of their stars (e.g. Marchesini et al. 2009; Muzzin et al. 2013; Madau & Dickinson 2014).

At a given epoch, most star-forming galaxies follow a tight relationship between stellar mass and star formation rate. This is commonly referred to as the galaxy "main sequence" (e.g. Noeske et al. 2007; Elbaz et al. 2011; Whitaker et al. 2012; Speagle et al. 2014; Schreiber et al. 2015). Observations have shown that the normalisation of this trend evolves with redshift, such that higher redshift galaxies have higher specific star formation rates (sSFR; the ratio between star formation rate and stellar mass). This increased activity is likely due to high molecular gas fractions (e.g. Daddi et al. 2010; Tacconi et al. 2010; 2013; Saintonge et al. 2013; Genzel et al. 2015).

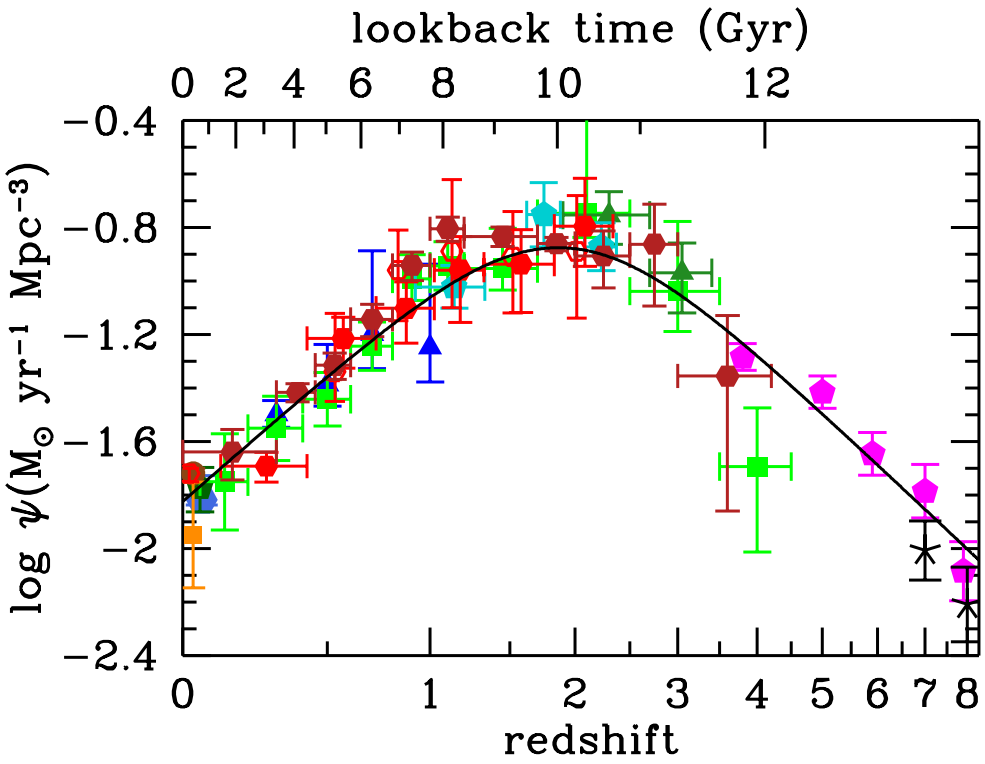

Figure 1.6: This figure from Madau & Dickinson (2014) shows the star formation history of the Universe, as traced by UV (blue, green and magenta data points) and infrared (red and orange data points) measurements from a number of different surveys. The cosmic star formation rate density peaks between $1 < z < 3$. All UV and IR luminosities were converted to instantaneous star formation rate densities using the factors $\kappa_{UV} = 1.15 \times 10^{-28}$ and $\kappa_{IR} = 4.5 \times 10^{-44}$, respectively, for a Salpeter IMF. The solid curve is a best-fit to all data points.

1.7 Galaxy Kinematics

The kinematics of gas and stars are another important probe of galaxy formation and evolution. Using high resolution spectroscopic observations we can study galaxy rotation and angular momentum, measure turbulence in the ISM, and search for evidence of outflows, mergers and tidal interactions. In this section we introduce an important observational technique used for much of our analysis in this thesis – integral field spectroscopy.

1.7.1 Integral Field Spectroscopy

For many decades after Slipher (1914) first discovered the rotation of "distant nebulae", the primary method of studying galaxy kinematics was to use long slit spectroscopy. Light from the galaxy is passed through a narrow slit and then dispersed, creating a spectrum at each point along that axis. However this technique has two key disadvantages: a) light outside of the slit is lost, and b) spatial information perpendicular to the slit is lost. The most interesting direction along which to place the slit is usually the major axis of the galaxy, however this can be difficult to identify, particularly when the angular size is small or the morphology is complex (e.g. at high redshift). An alternative is to make repeated observations of the same source, eventually achieving complete spatial coverage in two dimensions. This is incredibly time consuming.

Using integral field spectroscopy (IFS) a continuous spatial area can be observed. This information is packaged as a "data cube", which consists of two spatial dimensions and a wavelength dimension. Fig. 1.7 demonstrates how this data can be used to obtain images at different wavelength slices and a spectrum at each spatial pixel. In galaxies, integral field spectroscopy can be applied to study stellar and gas kinematics, the spatial distribution of star formation, and the spatial variation of emission line ratios (which reflect the metallicity and ionisation of the gas).

The most important element of an IFS instrument is the integral field unit (IFU; or several if the instrument is "multiplexing"), which samples the light into distinct spatial components. Fig. 1.8 illustrates three of the most common IFU setups:

- *Lenslet array*: A microlens array splits the image into small points of light, which are then dispersed by the spectrograph. The system is tilted to avoid overlap be-

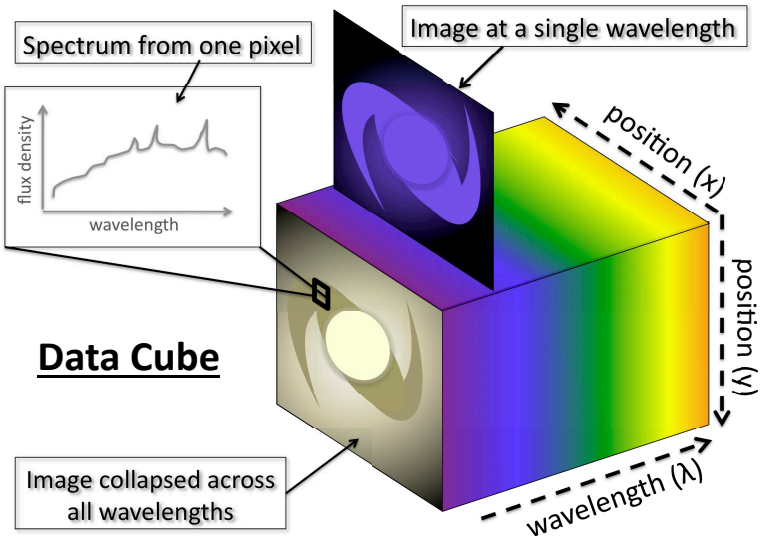

Figure 1.7: Schematic diagram of a data cube, originally from Harrison (2014). A data cube consists of information in three dimensions: two spatial dimensions (x,y) and a wavelength dimension (λ). Each spatial pixel is associated with a spectrum. The cube can be collapsed over a range in wavelengths (e.g. centered around an emission line) to obtain a two-dimensional image.

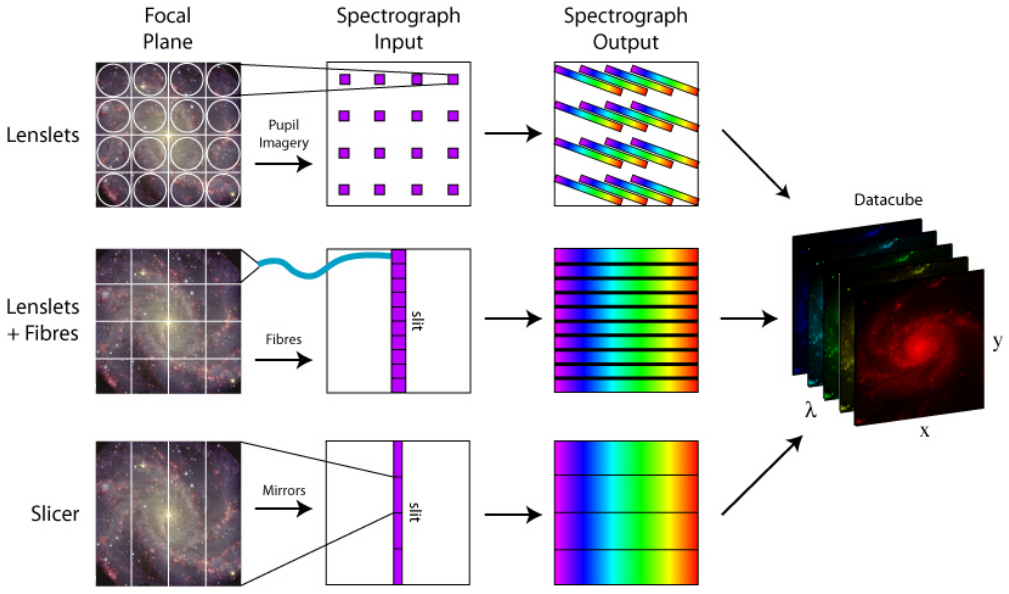

Figure 1.8: Diagram of integral field spectroscopy techniques, taken from Westmoquette (2007). IFUs can sample the light from the focal plane in a number of different ways (lenslets, lenslets plus fibres and an image-slicer are shown here). The light is then dispersed by a spectrograph, and reformatted into a data cube (Fig. 1.7).

tween the individual spectra.

- *Lenslet plus fibres*: A lenslet array focusses the light into a bundle of optical fibres, which reformat the image into a pseudo-slit. From the slit, light is directed to the spectrograph. Spectra are obtained without wavelength offsets.

- *Image-slicer*: The input image is formed on a mirror segmented into thin slices. These slices are reformatted into a pseudo-slit (using a second set of mirrors) and then dispersed by the spectrograph. Since this system uses only mirrors, it is achromatic and can be cooled to cryogenic temperatures. This makes image-slicers particularly suitable for infrared observations.

In this thesis we present observations made using the FLAMES (Chapter 2) and KMOS (Chapters 4 and 5) instruments on the ESO Very Large Telescope (VLT). FLAMES consists of 15 deployable IFUs with a lenslets plus fibres setup, while KMOS has 24 image-slicer IFUs which feed into three spectrographs. We will discuss each instrument in further detail in the relevant chapters.

1.7.2 High Redshift Galaxies

Integral field spectroscopy has revolutionised our understanding of the high redshift Universe. The rest-frame UV/optical morphologies of early star-forming galaxies are clumpy and irregular (e.g. Elmegreen et al. 2009; Förster Schreiber et al. 2011; Livermore et al. 2012), with the Hubble sequence only beginning to take form at $z \sim 1.5$ (e.g. Conselice et al. 2011; Buitrago et al. 2013; Mortlock et al. 2013). However, kinematic studies have revealed that despite photometric irregularity, many galaxies exhibit smooth and ordered rotation (e.g. Förster Schreiber et al. 2009; Epinat et al. 2012; Wisnioski et al. 2015; Stott et al. 2016; Harrison et al. 2017). The key difference between these galaxies and local disks is that the ISM is much more turbulent at high redshift, with average velocity dispersions a factor of two larger (e.g. Genzel et al. 2008; Lehnert et al. 2009; Newman et al. 2013; Turner et al. 2017).

The focus of recent surveys such as KROSS (Chapters 4 and 5; Stott et al. 2016; Harrison et al. 2017), KMOS^{3D} (Wisnioski et al. 2015) and KDS (Turner et al. 2017), is now

to build large and representative samples at high redshift. We can use integral field spectroscopy to analyse the kinematics, star formation and gas properties of these galaxies, and begin to untangle the physical processes responsible for their evolution. Large-scale IFU surveys at $z \sim 0$ such as SAMI (Croom et al. 2012) and CALIFA (Sánchez et al. 2012) will provide excellent local comparison samples.

1.8 Thesis Overview

The aim of this thesis is to probe physical processes which shape the evolution of star-forming galaxies, both secular and environmental, using integral field spectroscopy.

- In *Chapter 2* we study the kinematics, molecular gas content and far-infrared properties of 27 dusty starburst galaxies in a massive cluster at $z \sim 0.4$. As discussed in §1.5, star-forming galaxies accreted into a cluster environment are expected to undergo a transition from spirals to S0s. It is thought that starbursts represent an intermediate phase of this transition, and so studying their properties may help us to better understand the physical mechanisms at play. This work has been published as a first-author paper, Johnson et al. (2016).

- Seeing-limited IFU observations suffer from a phenomenon known as "beam smearing". As observations are convolved with the seeing PSF, information from each spatial pixel is combined with that of neighbouring regions. Since we expect our analysis in Chapter 4 to be particularly sensitive to these effects, in *Chapter 3* we create a series of mock KMOS observations to model the impact of beam smearing on measurements of galaxy rotation velocity and velocity dispersion. This allows us to understand the biases introduced and derive a series of correction factors.

- In *Chapter 4* we analyse the velocity dispersion properties of 472 star-forming galaxies observed as part of the KMOS Redshift One Spectroscopic Survey (KROSS). The cosmic star formation rate density peaks in the range $z \sim 1-3$, and so establishing the properties of galaxies at this redshift is key to constraining models of galaxy formation and evolution. One of the most important unanswered questions is why the velocity dispersions of high redshift galaxies are so much larger than those of

local galaxies (§1.7). We test the predictions of two analytic models which suggest that turbulence driven by either gravitational instabilities or stellar feedback. This work has recently been accepted for publication in MNRAS (Johnson et al. 2017; arXiv:1707.02302).

- In *Chapter 5* we investigate the relationship between the kinematic properties of KROSS galaxies and their optical morphology. To explore the idea that an increase in angular momentum and disk stability (Toomre Q) is what drives the morphological evolution from clumpy, irregular galaxies at high redshift, to thin disks at low redshift, we study the *HST* images of 231 KROSS galaxies.

- Finally, in *Chapter 6* we summarise our main results and consider the future direction of this work. We discuss a number of ongoing and future projects, and identify several key questions still to be addressed.

CHAPTER 2

The Spatially Resolved Dynamics of Dusty Starburst Galaxies in a $z \sim 0.4$ Cluster: Beginning the Transition from Spirals to S0s

Preamble

In this chapter we study the Hα kinematics, molecular gas content and far-infrared properties of dusty starburst galaxies in the intermediate redshift cluster, Cl 0024+17. The majority of this work has been published as a first author paper (Johnson et al. 2016). We include several additional figures (Fig. 2.4, 2.5, 2.8 and 2.11) to supplement the published material and to highlight certain aspects of the analysis.

Abstract

To investigate what drives the reversal of the morphology–density relation at intermediate/high redshift, we present a multi-wavelength analysis of 27 dusty starburst galaxies in the massive cluster Cl 0024+17 at $z = 0.4$. We combine Hα dynamical maps from the VLT / FLAMES multi-IFU system with far-infrared imaging from *Herschel* / SPIRE and millimetre spectroscopy from IRAM / NOEMA, in order to measure the dynamics, star formation rates and gas masses of this sample. Most galaxies appear to be rotationally supported, with a median ratio of rotational support to line-of-sight velocity dispersion of $v/\sigma_0 \sim 5 \pm 2$ and specific angular momentum of $\lambda_R = 0.83 \pm 0.06$, comparable to field spirals of a similar mass at this redshift. The star formation rates of $3 - 26\,M_\odot\,yr^{-1}$ and average CO-derived gas mass of $\sim 1 \times 10^{10}\,M_\odot$ suggest gas depletion timescales of ~ 1 Gyr (~ 0.25 of the cluster crossing time). We derive characteristic dust temperatures (mean $T_d = 26 \pm 1$ K) consistent with local galaxies of similar far-infrared luminosity, suggesting

that the low density gas is yet to be stripped. Taken together, these results suggest that the starbursts have only recently accreted from the field, with star formation rates likely enhanced due to the effects of ram pressure. In order to make the transition to cluster S0s these galaxies must lose $\sim 40\%$ of their specific angular momentum. We suggest this must occur ≥ 1 Gyr later, after the molecular gas has been depleted and/or stripped, via multiple tidal interactions with other cluster members.

2.1 Introduction

Rich clusters present a unique laboratory for studying the interaction between galaxies and their local environment. It has long been established that strong trends exist between the morphology, gas content and star formation of cluster galaxies, and the density of the neighbourhood in which they reside. The populations of rich clusters at $z = 0$ are dominated by passive, gas-poor ellipticals and S0s, with star formation all but extinguished in central regions (the morphology density relation e.g. Dressler 1980; Bower et al. 1992; Lewis et al. 2002; Kodama et al. 2004; Bamford et al. 2009). However, observations of clusters at intermediate redshift show a striking increase in the fraction of blue star-forming galaxies in cluster cores, from almost zero in the present day to $\sim 20\%$ by $z \sim 0.4$ (e.g. Butcher & Oemler 1978). This evolution is accompanied by another key evolutionary change: a sharp decline in the proportion of S0 galaxies (Dressler et al. 1997; Poggianti et al. 2009). Studies of emission line and luminous infrared-selected galaxies out to $z \sim 1.5$ have confirmed that star-forming galaxies in fact make up the majority of the population in high redshift clusters (Tran et al. 2010; Smail et al. 2014). This increase in the number of star-forming galaxies and decrease of cluster S0s with increasing redshift, implies that the two populations are linked in an evolutionary scenario.

An important realisation was that a large fraction of quiescent cluster members have suffered starburst activity in the recent past. Spectroscopic surveys have identified a significant population of k+a or "post-starburst" galaxies which appear to be more prevalent with increasing redshift (e.g. Couch & Sharples 1987; Poggianti et al. 1999; Pracy et al. 2005; Tran et al. 2007; Swinbank et al. 2007; De Lucia et al. 2009; Rodríguez Del Pino et al. 2014). Their spectra show strong Balmer absorption lines associated with the recent

formation of massive A-type stars (≤ 1 Gyr ago), but a lack of emission lines suggesting the burst was rapidly quenched (e.g. Poggianti et al. 1999; Poggianti & Wu 2000). However, difficulties arise when attempting to link these galaxies to the formation of S0s. Insufficient numbers of strong starbursts are detected in the optical to explain the post-starburst phase, and the luminosities of S0s are in fact substantially brighter than the proposed progenitor spirals (Poggianti et al. 1999; Kodama et al. 2004; Burstein et al. 2005; Sandage 2005). These problems could both be solved if a considerable fraction of starburst activity is heavily obscured. Indeed, deep mid-infrared observations of intermediate redshift clusters with *Spitzer* and *Herschel* have revealed an abundance of dusty star-forming galaxies that are missing from optical studies (e.g. Coia et al. 2005; Geach et al. 2006; 2009; Elbaz et al. 2007; Marcillac et al. 2007; Koyama et al. 2008; Oemler et al. 2009; Kocevski et al. 2011; Alberts et al. 2014). In an era in which clusters were still accreting much of their mass, there not only appears to be a significant population of star-forming galaxies, but also many with their star formation temporarily enhanced in this dense environment.

In a model where spirals transition to S0s, the star formation of infalling galaxies must be rapidly quenched, their gas disks stripped, and the dynamics transformed from rotationally supported disks (high angular momentum) to dispersion dominated spheroids (low angular momentum). Several authors also suggest that the bulge luminosity and bulge to disk ratio of S0s is too large for them to have evolved from spirals by disk fading alone (Dressler 1980; Simien & de Vaucouleurs 1986; Kodama & Smail 2001; Christlein & Zabludoff 2004; Cortesi et al. 2013), and spectral decomposition of local lenticulars has revealed that bulges have younger and more metal-rich stellar populations than their adjacent disk (Johnston et al. 2014). It may be that a final, circumnuclear starburst is required to achieve the transition between infalling spirals and passive S0s. The observational challenge is to identify the processes which may drive this transformation.

Several potential mechanisms have been invoked to explain galaxy transformations in local clusters: interactions with the intra-cluster medium (ICM) such as ram pressure stripping, strangulation and thermal evaporation (Kenney et al. 2004; McCarthy et al. 2008; Merluzzi et al. 2013; Fumagalli et al. 2014; Peng et al. 2015), and tidal interactions, harassment, minor mergers or halo stripping (Mastropietro et al. 2005; Bekki 2009;

Smith et al. 2010; Eliche-Moral et al. 2012; Bialas et al. 2015). The challenge is now to understand the relative contribution of each process, and how the timescales they operate on vary with cluster mass and size (hence redshift), as well as the stellar, halo and gas mass of the infalling galaxy (e.g. Boselli & Gavazzi 2006; 2014). Significant progress has already been made, particularly through the work of large surveys such as CLASH-VLT (Postman et al. 2012), LoCuSS (Haines et al. 2009), WINGS (Cava et al. 2009) and EDisCS (White et al. 2005).

It is important to study cluster galaxies over a range in redshift to thoroughly explore the mechanisms described above, and to understand what drives the reversal of the morphology–density relation. For example, due to the increased gas fractions of galaxies at high redshift (e.g. Tacconi et al. 2010; Geach et al. 2011), the initial compression of the ISM may be more likely to enhance the star formation (Quilis et al. 2000; Hopkins et al. 2006; Bekki 2014; Sales et al. 2015). Due to the lower mass of typical clusters (compared to those at $z \sim 0$), the lower ram pressure from the intra-cluster medium may result in starbursts being more intense and long-lived. Tidal forces from increased galaxy-galaxy interaction rates in rapidly assembling clusters may also destablise the gas disks, causing a burst of star formation, and a morphological and dynamical transformation.

Identifying cluster starbursts and measuring their dynamics, star formation rates and molecular gas properties appears to be key to unravelling the complexities of galaxy evolution in clusters. The short lifetime of the starburst activity provides a snapshot of galaxies which may be undergoing a transition, allowing us to search for potential triggers. For example, asymmetric gas disks may provide evidence for ram pressure stripping (Bekki 2014), high dust temperatures (compared to galaxies in the field) may imply that the cold gas/dust has been stripped (e.g. Rawle et al. 2012), whilst galaxy-galaxy interactions (mergers) may result in complex kinematic signatures (Mihos & Bothun 1998; Colina et al. 2005) depending on the interaction stage and nature of the system (Bellocchi et al. 2013; Hung et al. 2016). Complementing the dynamics with observations of molecular gas allows us to infer how long the starburst can be maintained.

In this work we present a multi-wavelength study of 27 spectroscopically confirmed, 24 μm-bright galaxies in Cl 0024+17. We study the optical morphologies and dynamics of the galaxies using *HST* and VLT / FLAMES multi-IFU observations respectively, infer

star formation rates from far-infrared observations with *Herschel* / SPIRE, and estimate molecular gas masses using IRAM/NOEMA observations of the ^{12}CO(1→0) emission. As an original "Butcher & Oemler" cluster, Cl 0024+17 has a significant population of blue, star-forming galaxies and is one of the best studied clusters at intermediate redshift ($z = 0.395$), with a virial mass of $M_{\rm vir} = (1.2 \pm 0.2) \times 10^{15}\,{\rm M}_{\odot} h^{-1}$ (Umetsu et al. 2010), and X-ray luminosity of $L_{\rm X} \sim 2.9 \times 10^{44}\,{\rm erg\,s^{-1}}$ (Zhang et al. 2005). With an abundance of star-forming galaxies and multi-wavelength ancillary data, Cl 0024 provides a useful pilot study for investigating the properties of dusty starbursts in galaxy clusters.

The structure of this chapter is as follows. In §2.2 we describe the target selection, observations and data reduction. In §2.3 we describe the galaxy integrated properties: star formation rates, stellar and gas masses, and dust temperatures. In §2.4 we study the internal properties of the galaxies, using IFU observations to spatially resolve the star formation, rotation velocity, and velocity dispersion. We then explore the properties of these dusty starbursts in the context of their environment, comparing to field spirals and local lenticulars, and searching for trends as a function of cluster radius. We consider which mechanisms may have already acted on these galaxies, and discuss what remains to be achieved to complete the transition to S0s. Finally §4.6 summarises our main results. Throughout we assume a ΛCDM cosmology with parameters $\Omega_m = 0.3$, $\Omega_\Lambda = 0.7$ and $H_0 = 70\,{\rm km\,s^{-1}\,Mpc^{-1}}$. The average seeing for our IFU observations, 0.5 arcsec, corresponds to a physical scale of 2.6 kpc at $z \sim 0.4$. All magnitudes are quoted on the AB system.

2.2 Target Selection, Observations & Data Reduction

2.2.1 Cl 0024+17

Cl 0024+17 is a well studied cluster with extensive archival multi-wavelength imaging and spectroscopy, and its large population of blue star-forming galaxies makes it an ideal environment for exploring the properties of cluster starbursts. In optical wavelengths Cl 0024 appears fairly unremarkable, with a well concentrated mass profile and relatively little sub-structure (Fig. 2.1), but it is thought this disguises a rather eventful dynamical history. Spectroscopic observations reveal two distinct components in the line of

sight: a dominant cluster component which has a velocity dispersion of $\sim 1000\,\mathrm{km\,s^{-1}}$, and a foreground group offset by $\Delta v \sim 3000\,\mathrm{km\,s^{-1}}$ which has a velocity dispersion of $\sim 500\,\mathrm{km\,s^{-1}}$ (Fig. 2.2). The group appears to have undergone a high speed collision with the cluster around ~ 3 Gyr ago (Czoske et al. 2001; 2002).

Czoske et al. (2002) explored the proposed cluster–group collision via numerical simulations of dark matter haloes, concluding that this scenario could explain a well documented discrepancy between mass estimates derived from lensing (e.g. Comerford et al. 2006; Hoekstra 2007; Zitrin et al. 2009; Umetsu et al. 2010), velocity dispersion (Diaferio et al. 2005) and X-ray studies (Soucail et al. 2000; Ota et al. 2004; Zhang et al. 2005). Cl 0024 has a lower X-ray flux and lower central velocity dispersion than expected for a virialised system, and this leads to some interesting implications. Processes such as galaxy harassment are usually most effective in the outskirts of clusters, or within groups as a method of "pre-processing", since the lower relative velocity of galaxies leads to longer interaction times. However Moran et al. (2007) suggest that for Cl 0024, harassment may be effective down to surprisingly small radii, with ram pressure stripping weak until ~ 300 kpc from the core. Passive spirals appear to be relatively long-lived (1–2 Gyr; Treu et al. 2003) with galaxies experiencing a slower transition due to tidal interactions. In this respect Cl 0024 makes a useful analog to higher redshift clusters which are still in the process of assembling.

2.2.2 Target Selection

To identify a sample of dust-obscured cluster starbursts suitable for VLT / FLAMES IFU observations, we exploit the *Spitzer* / MIPS 24 μm imaging from Geach et al. (2006) and select mid-infrared bright sources with flux densities of $S_{24\mu\mathrm{m}} = 0.15$–$1$ mJy which have also been spectroscopically confirmed as cluster members (Moran et al. 2005). Converting the median 24 μm flux of $S_{24\mu\mathrm{m}} = 0.33 \pm 0.03$ mJy to a total infrared luminosity (assuming the Chary & Elbaz 2001 library of template SEDs), we find a star formation rate of $\sim 10\,\mathrm{M_\odot yr^{-1}}$ (Kennicutt 1998a). This is approximately double the rate for a "main sequence" galaxy of mass $\log(\mathrm{M_\star/M_\odot}) = 10.5$ at the same redshift (Speagle et al. 2014; see also 2.3.2). Roughly two-thirds of the sample are known Hα or [OII] emitters, as identified from Suprime-Cam narrowband Hα imaging and DEIMOS spectroscopy (Kodama

et al. 2004; Moran et al. 2005). We also include two Hα emitters of unknown 24 μm flux (IDs 9 and 10) which we used to fill vacant IFUs. We find no further distinction between these two galaxies and the rest of the sample, suggesting they are cluster starbursts which are simply not as dust-obscured.

As shown by Fig. 2.1 & 2.2, our final starburst sample of 28 galaxies is well dispersed throughout the cluster, with projected cluster-centric radii of $R = 0.2 - 3.9$ Mpc. 20 of 28 galaxies lie within the cluster virial radius of $R_{\rm vir} = 1.7$ Mpc (Treu et al. 2003). Seven of our targets are associated with the foreground group, which will allow us to assess the effect of an accelerated environment on the galaxy properties.

In Fig. 2.2 we show the $(B-R)$ colour for all galaxies within the redshift range $0.36 \leq z \leq 0.42$ (equivalent to $\Delta v \sim 9000\,{\rm km\,s^{-1}}$). No colour cut was made in selecting our IFU sample, and as can be seen from this figure, the MIPS 24 μm detections and our IFU targets tend to lie either in the blue cloud or between the blue cloud and the cluster red sequence (which can be identified between $(B-R) \sim 2.5 - 3.2$). Some starbursts likely show redder colours due to the influence of dust on a population of intrinsically blue and star-forming galaxies.

In our analysis we also exploit archival observations of Cl 0024+17 which were taken with *HST* / WFPC2 as a 39-point sparse mosaic (Treu et al. 2003). The images were taken with the F814W filter (corresponding to rest-frame 580 nm) and cover approximately one-third of our sample (Fig. 2.9). We find a high incidence of disks with a range of bulge to disk ratios, and none of the galaxies appear to be undergoing a major merger. We note that there is no obvious trend in morphology with projected cluster-centric radius or association with the cluster or foreground group.

2.2.3 FLAMES IFU Observations

Observations of 28 starbursts were made using the FLAMES multi-object IFU system on the VLT between 13th December 2012 and 29th November 2013 as part of ESO runs 089.A-0983 and 092.A-0135. FLAMES employs 15 IFUs across a patrol field of 25 arcmin diameter (Fig. 2.1). Each of the deployable integral field units consists of a near rectangular array of 20 microlenses (with pixel scale 0.52×0.52 arcsec), resulting in a total aperture of $\sim 3 \times 2$ arcsec. All of the observations were taken in dark time and

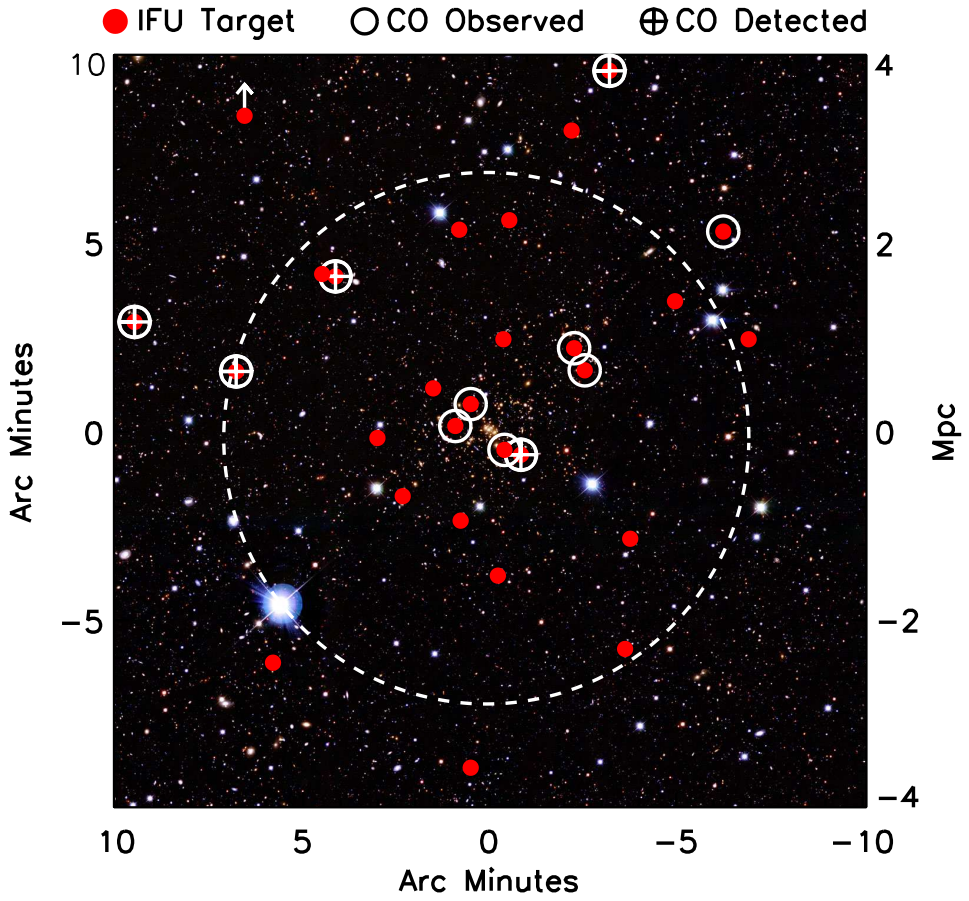

Figure 2.1: SUBARU SuprimeCam *BVI*-colour image of Cl 0024+17, centred on α: 00:26:36.0 δ: +17:08:36 (J2000). The dashed line represents the virial radius of the cluster, $R_{\rm vir} = 1.7$ Mpc. We highlight the 28 spectroscopically confirmed dusty starbursts which were observed using the FLAMES multi object IFU system. Our targets have projected cluster-centric radii of 0.2 – 3.9 Mpc. We circle galaxies also observed using IRAM PdBI, with crosses to indicate $>5\sigma$ ^{12}CO(1→0) detections. It appears that galaxies further from the cluster centre are perhaps more likely to be detected in CO (also see Fig. 2.2).

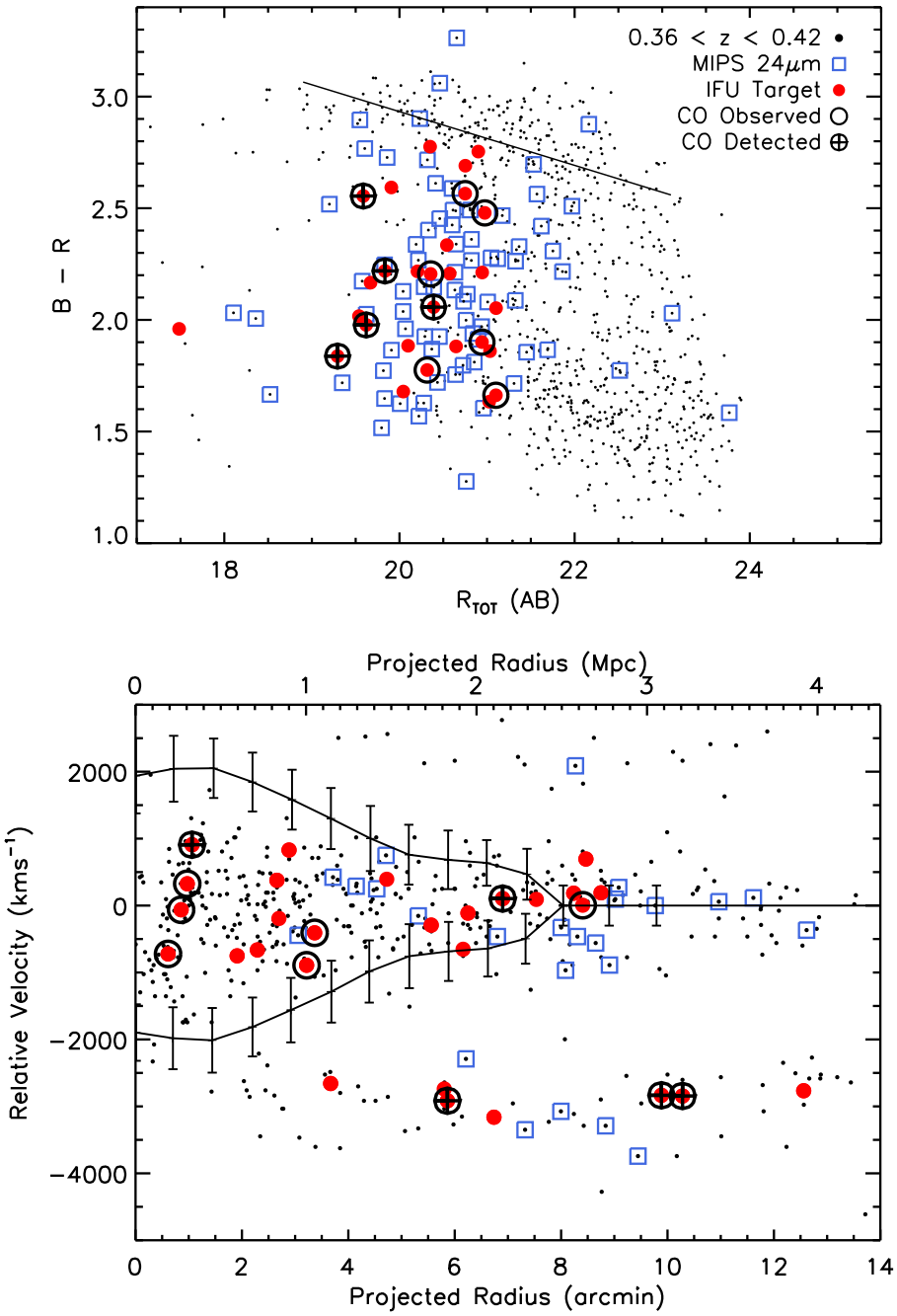

Figure 2.2: Properties of our starburst sample. *Top:* Colour-magnitude relation for galaxies within a 9 arcmin radius of the Cl 0024+17 cluster centre and within $\Delta z < 0.03$ of the cluster redshift. We identify the cluster red sequence (solid line). Many targets in our sample lie between the red sequence and blue cloud – a consequence of dust-obscured star formation in blue, star-forming galaxies. *Bottom:* Line of sight velocity with respect to the cluster centre, versus projected cluster-centric radius. Solid lines show the caustics which illustrate the escape velocity of the cluster (Diaferio et al. 2005). The structure at $\Delta v \sim -3000\,\mathrm{km\,s^{-1}}$ may be a group which has previously passed through the centre of the cluster (Czoske et al. 2002). Seven of our cluster starbursts lie within this foreground structure.

excellent seeing (<0.5 arcsec). We used the GIRAFFE spectrograph with the LR 881.7 filter to cover the Hα emission line in all of our targets, which at $z\sim0.39$ is redshifted to $\sim$9100Å. At this wavelength the spectral resolution is $R=\lambda/\Delta\lambda\sim9000$ (as measured from skylines), and we correct for this instrumental dispersion in all of our observations. Each observing block was split into two 1.2 ks observations, with sub-pixel dithers to improve the effective spatial sampling. The total on-source integration time per target was between three and four hours.

To reduce the data we used the standard ESOREX pipeline, which extracts the fibres from each IFU, flatfields and wavelength calibrates to form a set of preliminary datacubes. We reduced each observation individually, before sky subtracting and flux calibrating the spectra. For sky spectra we masked emission lines and continuum from the IFUs and then calculated an average sky spectrum which was then removed from all targets.

To create a mosaic for each galaxy we apply the sub-pixel offsets from our dither patterns, which were verified using the centroided continuum emission from the three brightest galaxies in the sample. This resulted in an effective pixel scale of 0.17 arcsec. In combining the data cubes we used a 3σ clipped average. The final spectra, integrated over each IFU, are shown in Fig. 2.3. In Fig. 2.9 we provide a *HST* (where available; Treu et al. 2003) or Subaru (Kodama et al. 2004) thumbnail for each galaxy. All but one of the targets were detected (and spatially resolved), leaving us with a final sample of 27 cluster starbursts. We note that the undetected target was the galaxy with the weakest Hα emission in the parent catalog. We exclude this source from the rest of the analysis.

To create the two-dimensional Hα emission, velocity, and velocity dispersion maps, we first measure the systemic redshift by fitting the Hα and [NII]$\lambda\lambda$6548, 6583 emission lines in the collapsed spectra. We then repeat this procedure on a pixel-by-pixel basis using a χ^2 minimisation procedure, inverse weighting the fit using a sky spectrum to account for increased noise at the positions of OH sky lines. We fit the Hα and [NII] doublet emission lines simultaneously, allowing the centroid, intensity and width of the Gaussian profile to vary. The full width half maximum (FWHM) of the Hα and [NII] lines are coupled and the intensity ratio of the [NII] λ6548 / λ6583 was fixed at 3.06 (Osterbrock & Ferland 2006). We require a signal-to-noise ratio greater than five to record a detection in a given pixel. During the fitting, we convolve the line profile with the instrumental

dispersion. As such, all measurements are corrected for the instrumental resolution. Since the pixels are smaller than the seeing PSF, the errors on the pixel-by-pixel fitting are not independent. This is something we take into account when modelling the velocity fields in §2.4.1 (each disk model is convolved with the PSF before fitting to the data).

In Fig. 2.9 we show the resolved Hα emission, dynamics and line-of-sight velocity dispersion maps of all galaxies. Although we observe a range of Hα morphologies, the majority of the sample appear to have regular (disk-like) velocity fields with velocity dispersions which peak towards the dynamical centre. It is interesting to note that in the galaxy integrated one-dimensional spectra (Fig. 2.3), more than half show emission lines profiles that are double-peaked. This is also indicative of disk-like dynamics, with either increased dust obscuration towards central regions, or ring-like emission. We will return to a more detailed discussion of the dynamics in §2.4.

2.2.4 Plateau de Bure Observations

To assess the evolutionary state of the cluster starbursts, we sought to obtain cold gas masses for a subset. This allows us to compare the gas properties of dusty starbursts to field galaxies of a similar mass at the same redshift. We used the IRAM PdBI and its NOEMA upgrade to target the ^{12}CO($1 \rightarrow 0$) transition in 11 galaxies, five of which were previously presented in Geach et al. (2009; 2011). These inital targets were predominantly in the outskirts of Cl 0024+17, with cluster-centric radii of $1.8-3.3$ Mpc, and so to complement these data we selected a further six galaxies which lie closer to the cluster core (Fig. 2.1). Observations took place in June 2014 as part of programme S14BT. Both sets of observations analysed here used the compact "D" configuration, with six or seven antennae. We targeted the ^{12}CO($1 \rightarrow 0$) 115.27 GHz rotational transition, which at $z = 0.395$ is redshifted into the 3 mm band with $\nu_{\rm obs} = 82.63$ GHz. The central frequency of the 3 mm receiver was set to coincide with the CO($1 \rightarrow 0$) line at the spectroscopic redshift. For further details on the setup of the first set of observations, see Geach et al. (2011).

For the most recent sample, since one frequency setup was sufficient to cover all targets we required only one phase calibrator, switching between three pointings. The correlator was set up with 2.5 MHz spacing (2×64 channels, 320 MHz bandwidth), to

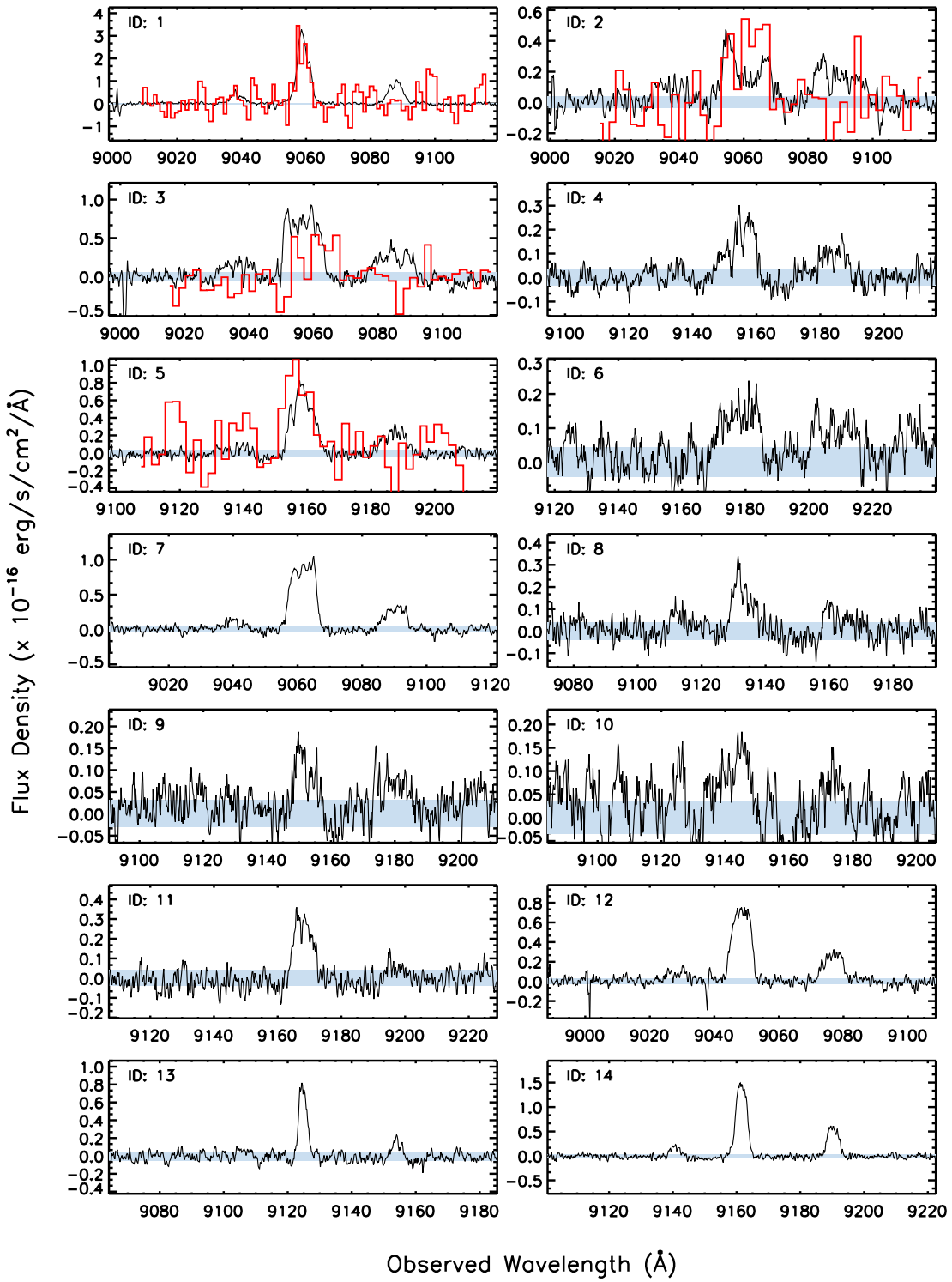

Figure 2.3: Integrated spectra around redshifted Hα and [NII] (6548,6583) emission lines. Parameters such as redshifts and [NII]/Hα ratios are listed in Table 2.1. Many galaxies show split emission line profiles, indicative of high velocity rotation and possibly strong obscuration towards the dynamical centre. We suspect the dynamics of galaxy IDs 23 and 24 may be affected by an AGN. For IDs 1, 2, 3, 5 and 16 we overlay the CO spectra in red, and find that the velocity centroid and line width are well matched to the Hα emission. Shaded regions show the $\pm 1\sigma$ noise, measured at wavelengths away from the Hα and any residual sky emission.

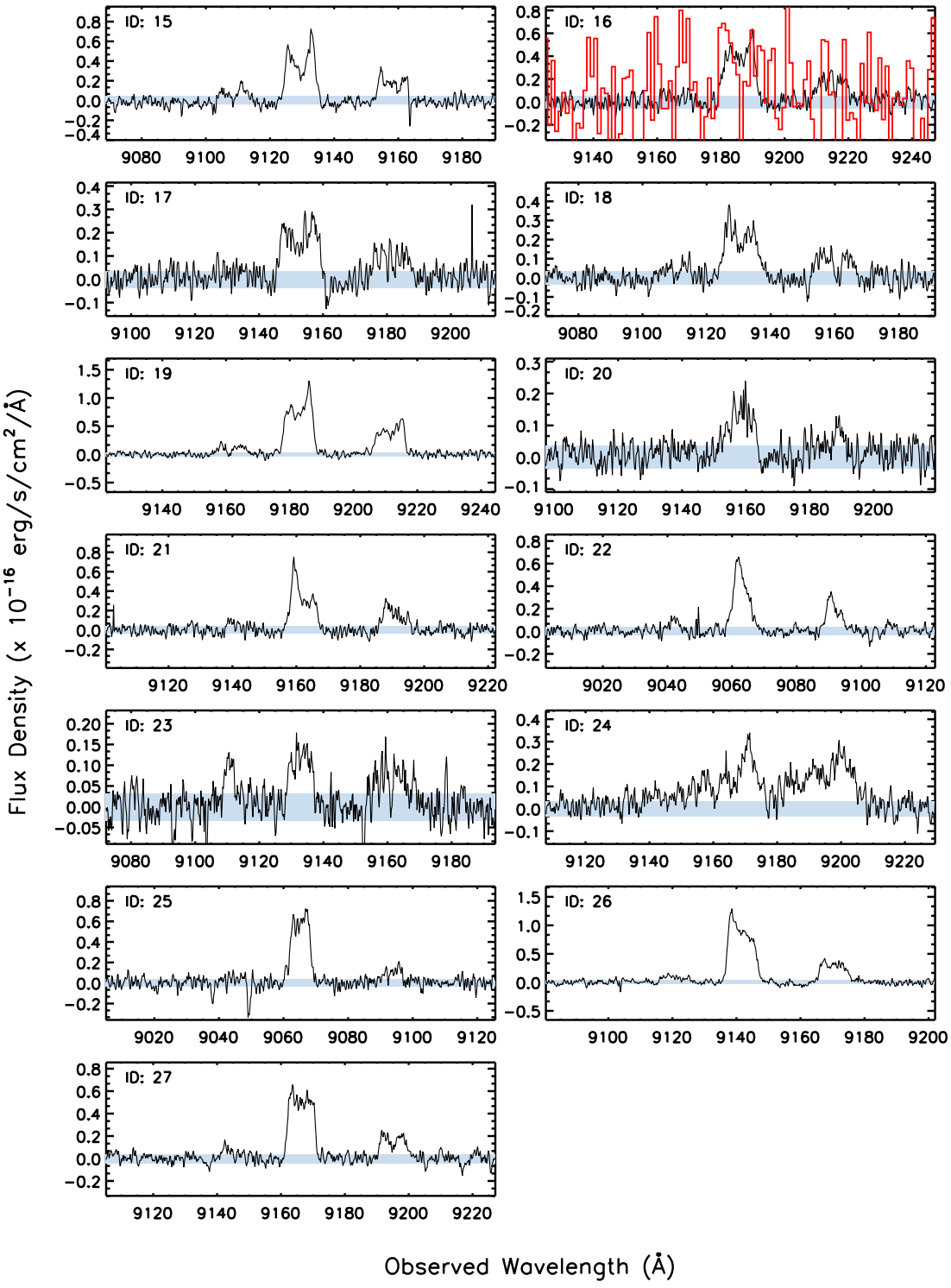

Figure 2.3: *continued*

accommodate any potential offset from the systemic redshift or a broad emission line profile. To increase observing efficiency, we chose pointings where two cluster starbursts had sufficiently small on-sky separations that they lay within a single primary beam. Exposure times were 4.15 hr per source pair. The data was calibrated, mapped and analysed using the software GILDAS (Guilloteau & Lucas 2000).

Combining our six new observations with those from Geach et al. (2011), we detect the CO($1 \rightarrow 0$) transition in five of eleven targets. We require 5σ for a detection, with upper limits on $L'_{\rm CO}$ for non-detections based on the rms noise and median line width of the sample. One dimensional spectra are shown in Fig. 2.3. For the five detections we find line fluxes in the range $f_{\rm CO(1-0)} = (255-788)\,{\rm mJy\,km\,s^{-1}}$ and an average line width of $\sigma_{\rm CO} = 140 \pm 25\,{\rm km\,s^{-1}}$. To estimate the average flux of the sample we stack the CO spectra from all 11 galaxies. We find $f_{\rm CO(1-0)} = 309 \pm 30\,{\rm mJy\,km\,s^{-1}}$, and derive the same flux independent of whether we take an average, a median, or a noise weighted sum. Despite only one new detection, stacking the data allows us to place important constraints on the gas properties of these starbursts. We will return to this in §2.3.

2.3 Analysis & Discussion: Galaxy Integrated Properties

Before discussing the dynamics, dust temperatures and molecular gas properties of our cluster starburst sample, we first derive their stellar masses and star formation rates using the multi-wavelength imaging available for the cluster. This allows the various properties (current and final stellar mass, dynamical state, gas depletion timescale) to be set in context with the field and cluster population at the same redshift.

2.3.1 Stellar Masses

We begin by deriving absolute K-band magnitudes and stellar masses for the galaxies in our sample, using eight-band photometry from the optical to mid-infrared. The $BVRI$-band fluxes were taken from Canada-France-Hawaii Telescope CFHT12k imaging (Czoske et al. 2002; Treu et al. 2003). The J- and K-band photometry was extracted from observations made with the WIRC camera on the Palomar Hale 200 inch telescope (Kneib et al. 2003; Smith et al. 2005). In the mid-infrared, we perform aperture photometry using

archival *Spitzer* IRAC imaging in the 3.6 and 4.5 μm bands. We estimate the magnitude within a 2.5 arcsec aperture and then apply aperture corrections based on the PSF.

To fit the spectral energy distributions (SEDs) of each galaxy and hence infer star formation histories and stellar masses, we employ the HYPERZ fitting code (Bolzonella et al. 2000). Model SEDs are characterised by their star formation history and parameterised by age, reddening and redshift. Using spectral templates derived from the Bruzual & Charlot (2003) evolutionary code we consider six star formation histories: a single burst (B), constant star formation (Im), and exponential decays of timescales 3, 5, 15 and 30 Gyr (Sa,b,c,d respectively). We use the Calzetti et al. (2000) reddening law and, given the obscured nature of these cluster starbursts, allow $A_V = 0.0 - 2.5$ magnitudes in steps of $A_V = 0.1$. We find an average extinction across the sample of $A_V = 1.2 \pm 0.4$ magnitudes. For each galaxy we fix the redshift of the synthetic templates to match the spectroscopic redshift of the Hα emission.

We next integrate the best-fit star formation history to calculate the stellar mass of each galaxy, accounting for mass loss from remnants using the STARBURST99 synthesis models (Leitherer et al. 2011). Given the dusty nature of these galaxies, we note that there are degeneracies between age and reddening which results in considerable uncertainty in the stellar mass-to-light ratios. This issue is likely to be compounded by complex star formation histories. To overcome some of these difficulties, we derive the rest-frame K-band mass-to-light ratio on a galaxy-by-galaxy basis, and then reapply the average value to the entire sample. The average mass-to-light ratio is $\langle \Upsilon_\star \rangle = M_\odot / L_\odot^{\rm K} = 0.35$, and using this technique we find galaxies in our sample to have stellar masses in the range of $M_\star = (1\text{–}10) \times 10^{10}\,{\rm M}_\odot$, with a median of $M_\star = (2.8 \pm 0.3) \times 10^{10}\,{\rm M}_\odot$. These are the values we use in the rest of our analysis. Absolute K-band magnitudes and stellar masses (using the median $\Upsilon_\star$) are provided in Table 2.2.

In Fig. 2.4 we plot the stellar mass derived from HYPERZ (i.e. before fixing the mass-to-light ratio) against dynamical mass. Dynamical masses were derived assuming a simple Keplarian relation: $M_{\rm dyn} = 2.2\, r_{1/2} v_{2.2}^2 / {\rm G sin}^2 i$, where $r_{1/2}$ is the half-light radius, $v_{2.2}$ is the galaxy rotation velocity at $2.2\, r_{1/2}$ (see §2.4 for analysis of the Hα dynamics) and i is the inclination. Each point is coloured to represent the age of the best-fit SED template. In general, older templates are associated with larger stellar masses, however there is much

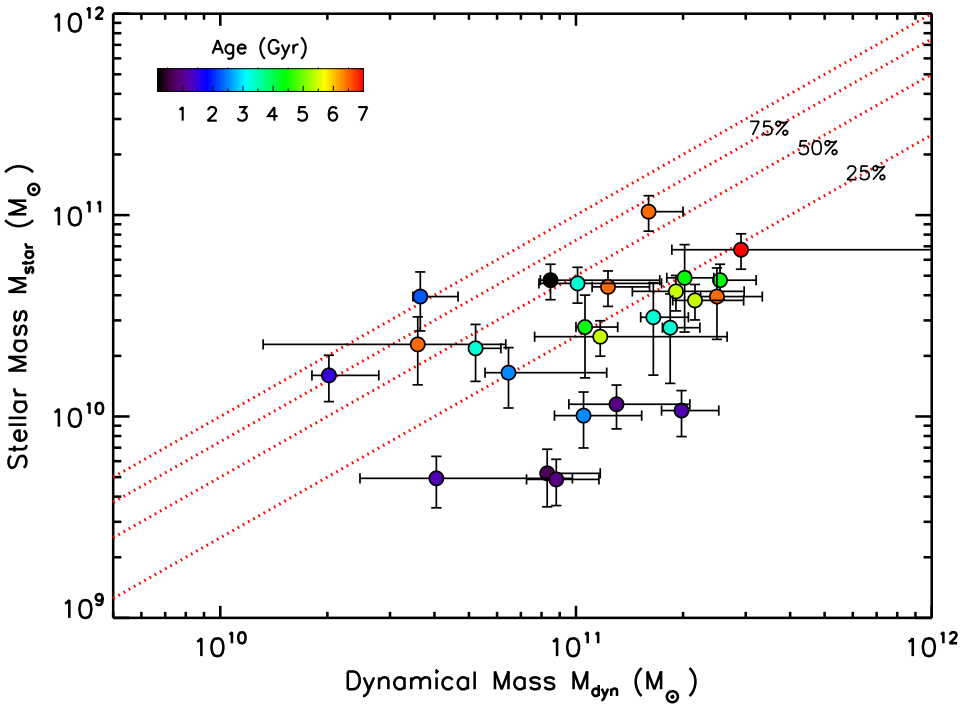

Figure 2.4: Stellar mass derived from the HYPERZ SED fitting code, versus dynamical mass. Dashed lines represent regions of $M_\star/M_{\rm dyn} = 0.25$, 0.5, 0.75 and 1.0. We consider spectral templates of six different star formation histories (single burst to 30 Gyr exponential decay), parametrised by age and dust extinction ($A_V = 0.0 - 2.5$ magnitudes). For dynamical masses we use the galaxy rotation curves to extract a velocity at $2.2\,r_{1/2}$ (see §2.4) and assume a simple Keplarian relation. Points are coloured by the age of the corresponding best-fit spectral template. Galaxies fit with older templates tend toward larger stellar masses, however as well as intrinsic variations we attribute much of the scatter to degeneracies between template age and dust reddening. We therefore derive the average mass-to-light ratio and apply this single value to the whole sample (Fig. 2.5).

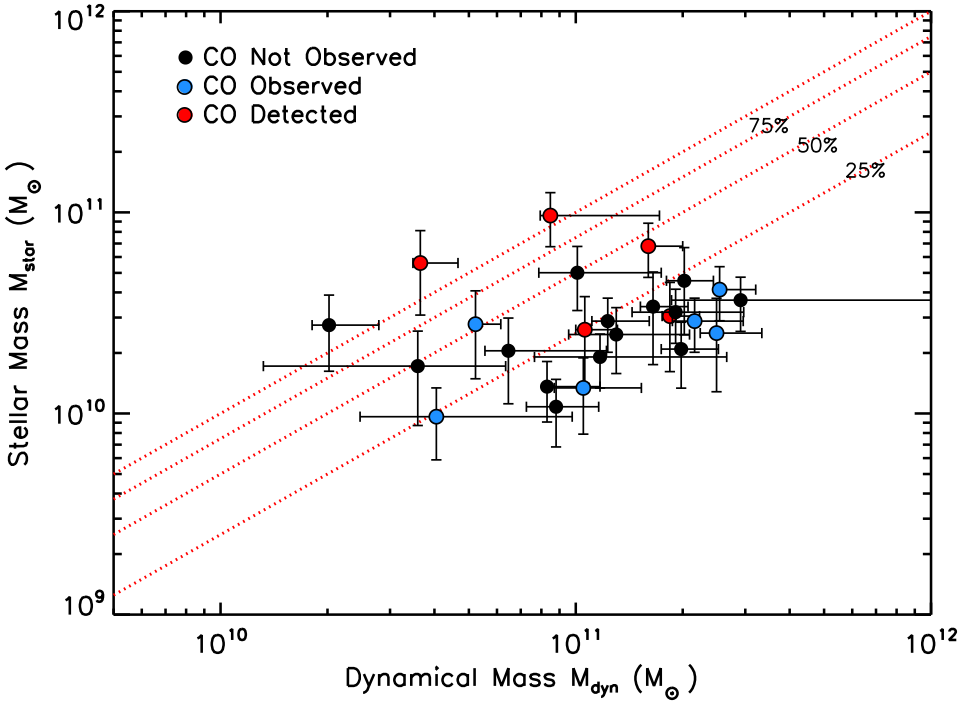

Figure 2.5: Stellar mass, applying the same K-band mass-to-light ratio to all galaxies, versus dynamical mass. Dashed lines represent regions of $M_\star/M_{\rm dyn} = 0.25$, 0.5, 0.75 and 1.0. Given the degeneracies between age and dust reddening, the mass-to-light ratios derived for individual galaxies in our "dusty starburst" sample are highly uncertain. We therefore adopt the median value of $M_\odot/L_\odot^{\rm K} = 0.35$, which reduces the scatter compared to Fig. 2.4. Blue and red points represent galaxies for which we targeted the CO($1 \rightarrow 0$) transition using IRAM (see §2.3.4). Successful detections (red points) tend to be for galaxies with larger stellar masses.

scatter due to the degeneracies between older and more dust reddened SEDs. In Fig. 2.5 we show how the distribution of stellar masses changes when a constant mass-to-light ratio is applied. The range of stellar masses is reduced, with fewer low mass galaxies ($M_\star < 10^{10}\,\mathrm{M}_\odot$). We note that successful CO($1 \rightarrow 0$) detections tend to be for galaxies with larger stellar masses (galaxies brighter in the K-band).

To compare the stellar masses of our sample to those of field galaxies at the same redshift, we refer to Muzzin et al. (2013) who study the stellar mass function of galaxies in the COSMOS / UltraVISTA survey. They derive a characteristic mass of $\mathrm{M}_* = (5.8 \pm 0.5) \times 10^{10}\,\mathrm{M}_\odot$ at $z \sim 0.4$. This suggests that, on average, the galaxies in our cluster starburst sample have slightly lower stellar masses than the "typical" field galaxy at this redshift.

2.3.2 Star Formation Rates

To estimate the star formation rates of our sample we adopt two approaches, using the (dust corrected) Hα fluxes and using the *Herschel* far-infrared imaging. We detect strong Hα emission in the integrated spectra of all but one of our 28 IFU targets (which we have consequently dropped from the sample), with luminosities in the range $L_{\mathrm{H}\alpha} \sim 10^{40.6-41.8}\,\mathrm{erg\,s^{-1}}$ (see Fig. 2.9 and Table 2.1). We also make clear detections of the neighbouring [NII]λ6583 line, with ratios of $-0.69 < \log([\mathrm{NII}]/\mathrm{H}\alpha) < 0.04$ and a median of -0.4 ± 0.02. Since two galaxies exhibit $\log([\mathrm{NII}]/\mathrm{H}\alpha) > 0$, we discuss the possibility of AGN contamination in §2.4. We note that while the Hα star formation rates of AGN may be unreliable, the far-infrared results are less likely to suffer contamination.

To estimate the star formation rate from the integrated Hα luminosity, we apply the calibration of Kennicutt (1998a) for a Chabrier IMF ($\mathrm{SFR}\,\mathrm{M}_\odot\,\mathrm{yr}^{-1} = 4.6 \times 10^{-42}\,\mathrm{L}_{\mathrm{H}\alpha}\,\mathrm{erg\,s^{-1}}$). To correct for dust extinction we use use the attenuation, A_V, returned by HYPERZ and adopt the dual reddenning law of Wuyts et al. (2013), which assumes that the nebular emission is more attenuated than the stellar continuum (since young, ionising stars will typically reside in dustier regions). Therefore applying dust corrections of an average $A_{\mathrm{gas}} = 1.8 \pm 0.5$ magnitudes, we estimate Hα star formation rates of $\mathrm{SFR}_{\mathrm{H}\alpha} = 0.3 - 16\,\mathrm{M}_\odot\,\mathrm{yr}^{-1}$.

To compare far-infrared star formation rates to those derived from Hα emission, we

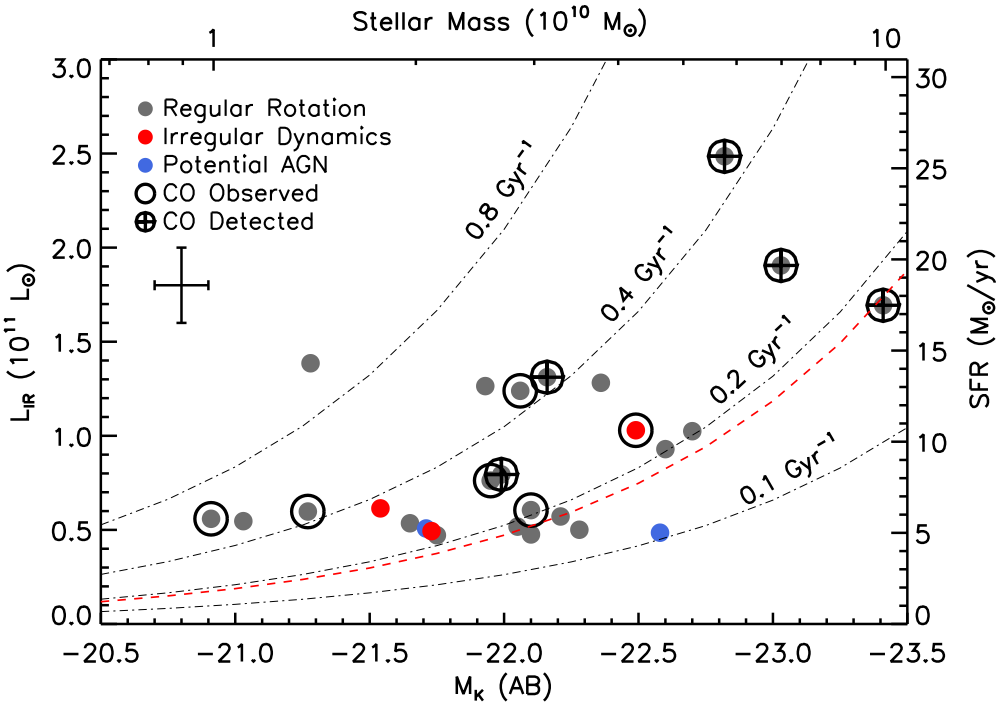

Figure 2.6: Infrared luminosity against K band absolute magnitude, with additional axes to demonstrate how this relates to star formation rate and stellar mass. We use the median mass to light ratio for our sample of $M_\odot/L^{\rm K}_\odot = 0.35$ (see §2.3.1). Dashed lines indicate a constant specific star formation rate (sSFR), with a red line used to illustrate the sSFR of the so-called main-sequence at $z = 0.4$. We highlight galaxies observed using PdBI / NOEMA, and find that detected galaxies tend to be of higher mass and brighter $L_{\rm IR}$. Red points are used to represent galaxies with dynamics which deviate from a rotating disk model, and blue points for galaxies which may have an AGN affect the dynamics (these classifications are assigned in §2.4). We find no relationship between $L_{\rm IR}$, $M_{\rm K}$ and Hα dynamics.

next exploit the *Herschel* PACS / SPIRE imaging of Cl 0024+17. For PACS, deblended catalogs are available for the cluster core (Lutz et al. 2011), which cover five of the galaxies in our sample. To derive 250, 350 and 500 μm flux densities, we use SPIRE imaging from the HerMES legacy programme (Oliver et al. 2012). We first align the astrometry of the images by stacking at the 24 μm positions, applying sub-arcsec shifts in ΔRA and ΔDec, and then deblend following the procedure of Swinbank et al. (2014), using the *Spitzer* 24 μm sources as priors. From our sample of 27 cluster starbursts, 20 are detected above 11 mJy at 250 μm. The median 250, 350 and 500 μm fluxes for the detections in each band are 20 ± 3, 11 ± 2 and 9 ± 3 mJy, respectively.

To derive far-infrared luminosities we fit the far-infrared flux densities at the spectroscopic redshift, using templates from the Chary & Elbaz (2001), Draine et al. (2007) and Rieke et al. (2009) SED libraries. These are empirical templates derived from star formation dominated local (U)LIRGs, with temperatures of between 15 – 90 K (as measured from the peak of the black-body fit). At the cluster redshift PAH and silicate features lie bluewards of the 24 μm band, so we include all photometry between 24 μm and 500 μm. Integrating the best fit SEDs we then derive bolometric luminosities of $L_{\rm IR} = (0.47 - 2.47) \times 10^{11}\,{\rm L}_{\odot}$, corresponding to star formation rates of ${\rm SFR}_{\rm IR} = 3 - 26\,{\rm M}_{\odot}{\rm yr}^{-1}$. Far-infrared luminosities and star formation rates are provided in Table 2.2.

For galaxies with many upper limits on their far-infrared fluxes, we take the Hα star formation rate and multiply this by the average ${\rm SFR}_{\rm IR}/{\rm SFR}_{\rm H\alpha}$ ratio, to estimate ${\rm SFR}_{\rm IR}$. On average, the star formation rate derived from the far-infrared is a factor 2.2 ± 0.4 larger than that derived from the Hα, even after applying a dust correction to the Hα luminosity. This is equivalent to an additional $A_{\rm gas} = 0.9 \pm 0.2$ (or $A_V = 1.3 \pm 0.2$). This offset may arise due to the differing structures between the dust and stars, particularly if the starbursts are centrally concentrated in an otherwise extended disk. Since the SED fitting provides a luminosity weighted result, the attentuation predicted from HYPERZ will be dominated by the extended disk and so systematically low. In the remainder of our analysis we will use the star formation rate estimates derived from the far-infrared fluxes.

In Fig. 2.6 we plot infrared luminosity versus absolute K-band magnitude for the galaxies in our sample, also converting these values to star formation rate and stellar mass, respectively. We derive specific star formation rates (sSFR) in the range (0.1 –

0.9) $M_{\odot}Gyr^{-1}$ with a median of $sSFR = 0.27 \pm 0.03\,Gyr^{-1}$. Our cluster galaxies (excluding one AGN candidate, see §2.4) lie on or above the so-called galaxy "main sequence" at $z \sim 0.4$ (Elbaz et al. 2007; Noeske et al. 2007; Karim et al. 2011). On average the galaxies are offset from the main sequence by a factor of 1.8 ± 0.2 at a fixed stellar mass, hence we adopt the term "starburst". In §2.4 we assign each galaxy a dynamical classification – rotationally supported or irregular – based on their velocity map and line of sight dispersion map. In Fig. 2.6 we split the sample by these classifications and do not see any strong trends between the star formation rate and the dynamical state of the galaxy.

2.3.3 Characteristic Dust Temperatures

The far-infrared observations also contain information regarding the characteristic dust temperature, $T_{\rm d}$. Recently, observations of local clusters have revealed a population of "warm dust" galaxies, with $T_{\rm d} \sim 50\,K$ and LIRG-like luminosities (Rawle et al. 2012). These galaxies may represent an early stage in the transition from spiral to S0. As cluster spirals move through the dense ICM, ram pressure stripping acts to remove loosely-bound gas (e.g. Fabello et al. 2012; Gavazzi et al. 2013; Boselli et al. 2014a; Jaffé et al. 2015) and dust (e.g. Cortese et al. 2010; Sivanandam et al. 2014). If material is preferentially stripped from the outskirts of the galaxy, where the dust is typically cooler (e.g. Bendo et al. 2010; Galametz et al. 2012; Hinz et al. 2012), this may result in a higher characteristic dust temperature. In order to test whether the cluster starbursts in our sample are more or less evolved than the Bullet Cluster galaxies of Rawle et al. (2012), we plot far-infrared luminosity versus dust temperature in Fig. 2.7. For consistency with other comparision samples we employ a modified black-body curve of the form $S_{\nu} \propto \nu^{\beta} B_{\nu}(T_{\rm d})$ to derive the dust temperatures, with an emissivity index of $\beta = 1.8$. We only include galaxies with detections in three or more bands, which constitutes approximately a third of the sample. This cut means that a reliable estimate of $T_{\rm d}$ can be derived.

On the plot, we include the relationship for local LIRGs / ULIRGs (which is derived from a sample of 60 μm selected galaxies at $z \sim 0$; Chapman et al. 2003; Chapin et al. 2009) and SPIRE-selected $z < 1$ (U)LIRGs (Symeonidis et al. 2013), both of which follow a power-law relation between $L_{\rm IR} \sim 10^{10}$–$10^{13}\,L_{\odot}$. We also plot similar measurements of high-z submillimeter-selected cluster starburst galaxies in XCS J2215.9-1738 ($z = 1.4$),

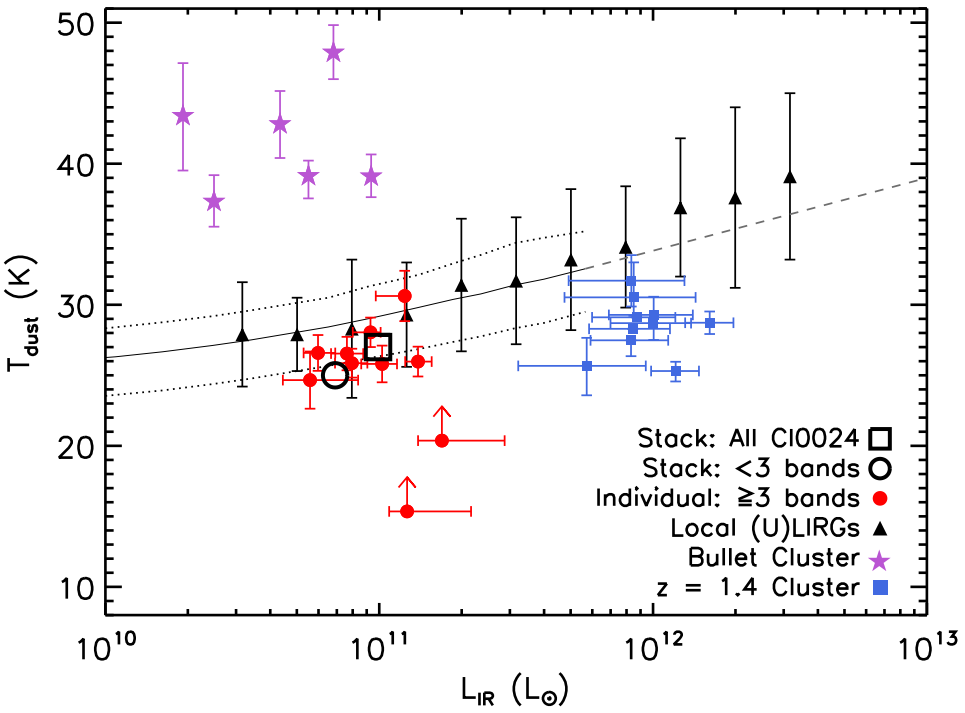

Figure 2.7: Characteristic dust temperature versus far-infrared luminosity for our cluster starburst sample, compared to the relation established for local starburst galaxies (black triangles show $z < 1$ (U)LIRGs; Symeonidis et al. 2013). Galaxies with detections in three or more infrared bands are shown in red points. We also show stacks of all 27 galaxies (open square) and those with fewer than three detections (open circle). We do not observe a significant offset from the local relation, in either direction. For comparison we plot the "hot" Bullet Cluster starbursts of Rawle et al. (2012) which may have been stripped of their low density gas, and starbursts from a cluster at $z = 1.4$ (which are consistent with high-redshift field galaxies; Ma et al. 2015).

which show systematically colder dust temperatures at fixed luminosity compared to the local relation (Ma et al. 2015). This is likely to be a result of the more extended gas resevoirs compared to $z = 0$ galaxies of the same luminosity.

For our sample of cluster starbursts we derive a median dust temperature of $T_{\rm d} = 26 \pm 1$ K and far-infrared luminosity $L_{\rm IR} = (9.1 \pm 0.9) \times 10^{10}\, L_{\odot}$. These dust temperatures are consistent with those measured for low-redshift field galaxies of similar far-infrared luminosity, and indeed we do not find any starburst galaxies with dust temperatures exceeding 31 K. However, we note that in this analysis we have only included the galaxies with detections in three (or more) bands, and for two of these galaxies we place lower limits on $T_{\rm d}$ since we do not resolve the peak of the emission. To infer the average dust temperature of the remaining sample we stack the PACS and SPIRE images in four different ways: all 27 galaxies, galaxies detected in ≤ 1 band, in ≤ 2 bands and in < 3 bands. The characteristic dust temperatures of these subsets are all within 2 K of each other (25 – 27 K), suggesting that the galaxies with well defined blackbody fits are representative of the full of the sample. We plot the temperatures of the full sample stack and the < 3 bands stack on Fig. 2.7 for comparison.

Finally, we note that although we only selected a small subsample for IFU follow-up, the 24 μm MIPS parent sample comprises 60 galaxies in total, approximately one third of which lie in the foreground group. To search for differences between the group and cluster starbursts, we stacked the PACS and SPIRE imaging of the 24 μm-detected galaxies in both subsets, but in each case the SPIRE colours and characteristic dust profiles are consistent, with $T_{\rm d,cluster} = 23 \pm 2$ K and $T_{\rm d,group} = 23 \pm 3$ K respectively.

Thus, it appears that the characteristic dust temperatures of cluster starbursts are consistent with a luminosity matched sample of field galaxies. In this respect, our sample appear to be less evolved than the "hot" starbursts seen in some local clusters (Rawle et al. 2012), perhaps indicating that they have been accreted more recently, and have not yet had their low density gas stripped by the ICM.

2.3.4 Molecular Gas Masses

To determine how the molecular gas content of these galaxies compares to similar mass field galaxies, and to calculate their likely final stellar mass if all available gas is converted

to stars, we use the ^{12}CO($1 \rightarrow 0$) emission. We overlay the CO spectra on top of the Hα in Fig. 2.3, and find that the velocity centroid and line widths are well matched. The two sets of spectra have an average velocity offset of $50 \pm 10\,\mathrm{km\,s^{-1}}$, and an average ratio between the Hα and CO line widths of 0.9 ± 0.2. This suggests that the CO traces the same dynamics as the Hα emission, hence the ionised gas and molecular gas components are similarly distributed throughout the disk.

Fitting each of these CO spectra with a single Gaussian profile, we find line luminosities of $L'_{\rm CO} = (2.2-6.8) \times 10^9\,\mathrm{K\,km\,s^{-1}\,pc^2}$ for the five detected galaxies (Solomon & Vanden Bout 2005), and upper limits of $L'_{\rm CO} = (3.9-4.9) \times 10^9\,\mathrm{K\,km\,s^{-1}\,pc^2}$ for the rest of the sample (see Table 2.2). To convert to the molecular gas mass we use $M(\mathrm{H_2 + He}) = \alpha L'_{\rm CO}$. The far-infrared luminosities of our targets are much larger than what is typical of local star-forming galaxies such as the Milky Way (Gao & Solomon 2004), however as discussed in Geach et al. (2011) the choice of $\alpha = 4.6$ may be the most appropriate given the late-type morphologies of the sample, and that the average $L_{\rm IR}/L'_{\rm CO}$ ratio we measure ($L_{\rm IR}/L'_{\rm CO} = 25 \pm 5$) is comparable to local spirals. Using this calibration we estimate molecular gas masses of $M_{\rm gas} = (1.0-3.0) \times 10^{10}\,\mathrm{M_\odot}$ which equates to gas fractions of $f_{\rm gas} = M_{\rm gas}/(M_{\rm gas} + M_\star) = 0.11-0.39$. As discussed in §2.2.4 we also stacked all 11 CO spectra to better characterise the sample as a whole. Using this stack we find a median line luminosity $L'_{\rm CO} = (2.7 \pm 0.3) \times 10^9\,\mathrm{K\,km\,s^{-1}\,pc^2}$, which translates to a gas mass of $M_{\rm gas} = (1.2 \pm 0.2) \times 10^{10}\,\mathrm{M_\odot}$ (towards the lower end of our detections). We will use this as a representative gas mass for our sample in all of the analysis below.

Our CO sample have an average star formation rate of $(13 \pm 1)\,\mathrm{M_\odot\,yr^{-1}}$ (compared to $\sim 10\,\mathrm{M_\odot\,yr^{-1}}$ for the wider sample) and so we estimate a gas depletion timescale of $\sim$1 Gyr, which is approximately ~ 0.25 of the cluster crossing time. This may explain the non-detections of the CO in the (projected) cluster core. We predict final stellar masses for our sample with an average of $\sim 4 \times 10^{10}\,\mathrm{M_\odot}$. From a sample of local cluster S0s ($0.04 < z < 0.07$; WINGs survey) Vulcani et al. (2011) find a characteristic stellar mass of $\mathrm{M_*} = 2.2 \times 10^{11}\,\mathrm{M_\odot}$. This implies that our cluster starbursts are destined to be sub-$\mathrm{M_*}$ members of the S0 population, unless they can achieve further growth through (for example) minor mergers. It may be that the most massive S0s are already in place at this redshift, or that their progenitors are passive spiral galaxies that have already completed

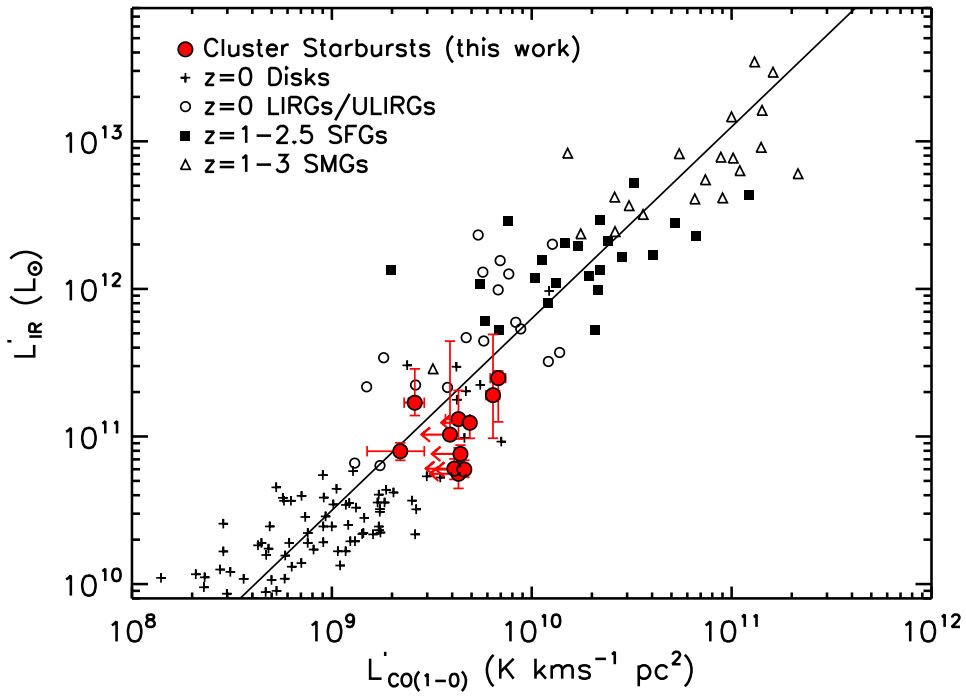

Figure 2.8: Far-infrared and CO luminosities of our sample, in comparison to other star-forming galaxies across cosmic time. Ivison et al. (2013) showed that the $L_{\rm IR} - L'_{\rm CO}$ properties of local disks, LIRGs and ULIRGs (Genzel et al. 2010), $z = 1-2.5$ BzK galaxies (also Genzel et al. 2010) and $z = 1-3$ SMGs may be described by a single relation. Although we have sufficient data to place only 11 galaxies in this context, our cluster starbursts are also consistent with this trend.

their starburst phase.

As shown in Fig. 2.2, our CO sample includes galaxies with a range of cluster-centric radii, which inhabit both the cluster and group component. While all three galaxies observed in the subgroup are detected in CO, only two of eight galaxies are detected in the larger structure. This could be an environmental trend. However, we also caution that the galaxies which we detect also tend to be more far-infrared luminous, and given the correlation between $L_{\rm IR}$ and $L'_{\rm CO}$, this may simply mean that the CO emission is easier to detect. Of course we cannot rule out the possibility that the same sources are brighter in the far-infrared due to some evolutionary effect. Considering our limited sample size it is difficult to draw definitive conclusions with respect to the gas content as a function of cluster radius, but this motivates a more detailed future study with a larger sample.

To compare the gas masses of these starbursts to galaxies on the star-forming "main-sequence" at this redshift, we use the scaling relations of Genzel et al. (2015). These relations predict that a star-forming galaxy at $z \sim 0.4$ with a similar stellar mass will have a gas-to-stellar ratio of $\log(M_{\rm gas}/M_\star) \sim -0.9$. This implies an average gas mass of $\rm M_{gas} \sim 4-8 \times 10^9\,M_\odot$. The molecular gas masses of our sample therefore appear to be slightly higher (a factor of ~ 2) than those of "typical" galaxies of similar stellar mass at this redshift. In Fig. 2.8 we demonstrate that the far-infrared and CO luminosities of our sample are consistent with the $L_{\rm IR} - L'_{\rm CO}$ relation fit to low- and high-redshift star-forming galaxies (including LIRGs, ULIRGs and SMGs) in Ivison et al. (2013).

Finally, we compare the gas properties of our cluster starbursts to starbursts in the field population, using a sample of ULIRGs ($L_{\rm IR} > 10^{12}\,\rm L_\odot$) at $0.2 < z < 1$ taken from Combes et al. (2013). This comparison sample have star formation rates $\sim 10\times$ higher than our cluster starbursts, but by mass matching their sample to the median stellar mass of our galaxy sample, we derive an average gas mass of $M_{\rm gas} = (1.2 \pm 0.5) \times 10^{10}\,\rm M_\odot$. This is consistent with the molecular gas masses derived for our cluster starburst sample.

On the basis of our CO observations it appears that these cluster starburst galaxies are richer in molecular gas than typical star-forming galaxies at a similar redshift. We derive molecular gas masses which are more closely matched to those of starbursts (ULIRGs) in the field with similar infrared luminosities. This could suggest a scenario in which the gas of infalling galaxies is compressed upon their encounter with the ICM, converting

available HI into H_2 and triggering a burst of star formation. These galaxies may have been typical star-forming galaxies upon accretion to the cluster, yet have their molecular gas fraction enhanced through this process. We will return to these results in the final section.

2.4 Analysis & Discussion: Ionised Gas Dynamics

2.4.1 Disk Fitting

Now that we have established the integrated properties of our sample, we next investigate the spatially resolved properties as measured from the Hα emission. The galaxies in our sample appear to resemble the field population in terms of their stellar masses and characteristic dust temperatures (although possibly with higher molecular gas masses), and so our aim in this section is to assess how evolved these galaxies appear in terms of their gas dynamics. We will search for evidence of the mechanisms which may eventually quench the star formation in these galaxies and transform their kinematics from regular, disk-like rotation to pressure-supported S0s.

In Fig. 2.9 we show the two-dimensional maps of Hα emission, velocity, and line of sight velocity dispersion for all 27 detected galaxies. In each instance there is a clear velocity gradient with peak-to-peak differences in the range $\Delta v = 100 - 500\,\mathrm{km\,s^{-1}}$. We note two galaxies (ID 23 and ID 24) exhibit very high [NII]/Hα ratios (i.e. $\log[\mathrm{NII}]/\mathrm{H}\alpha \gtrsim 0$); indicating the presence of an AGN (e.g. Kewley et al. 2013). Additionally, these sources show irregular velocity dispersion profiles, with spatially offset broad emission ($\gtrsim 150\,\mathrm{km\,s^{-1}}$; Fig. 2.9), which may indicate that outflows are affecting the gas kinematics in these sources (e.g. Harrison et al. 2016). For these reasons, we omit these two galaxies from the dynamical analysis below, leaving a sample of 25.

We next assign a dynamical classification to each of the galaxies (Fig 2.6; Table 2.3). We classify 22 of 25 starbursts ($\sim 90\,\%$) as rotationally supported, since their velocity map is regular (with a characteristic "spider" pattern), their rotation curve smooth, and they possess a line of sight velocity dispersion map which peaks towards the dynamical centre (caused by beam smearing; Chapter 3). The optical morphologies of these galaxies also appear smooth (and in some cases disk-like), with no evidence of multiple centres,

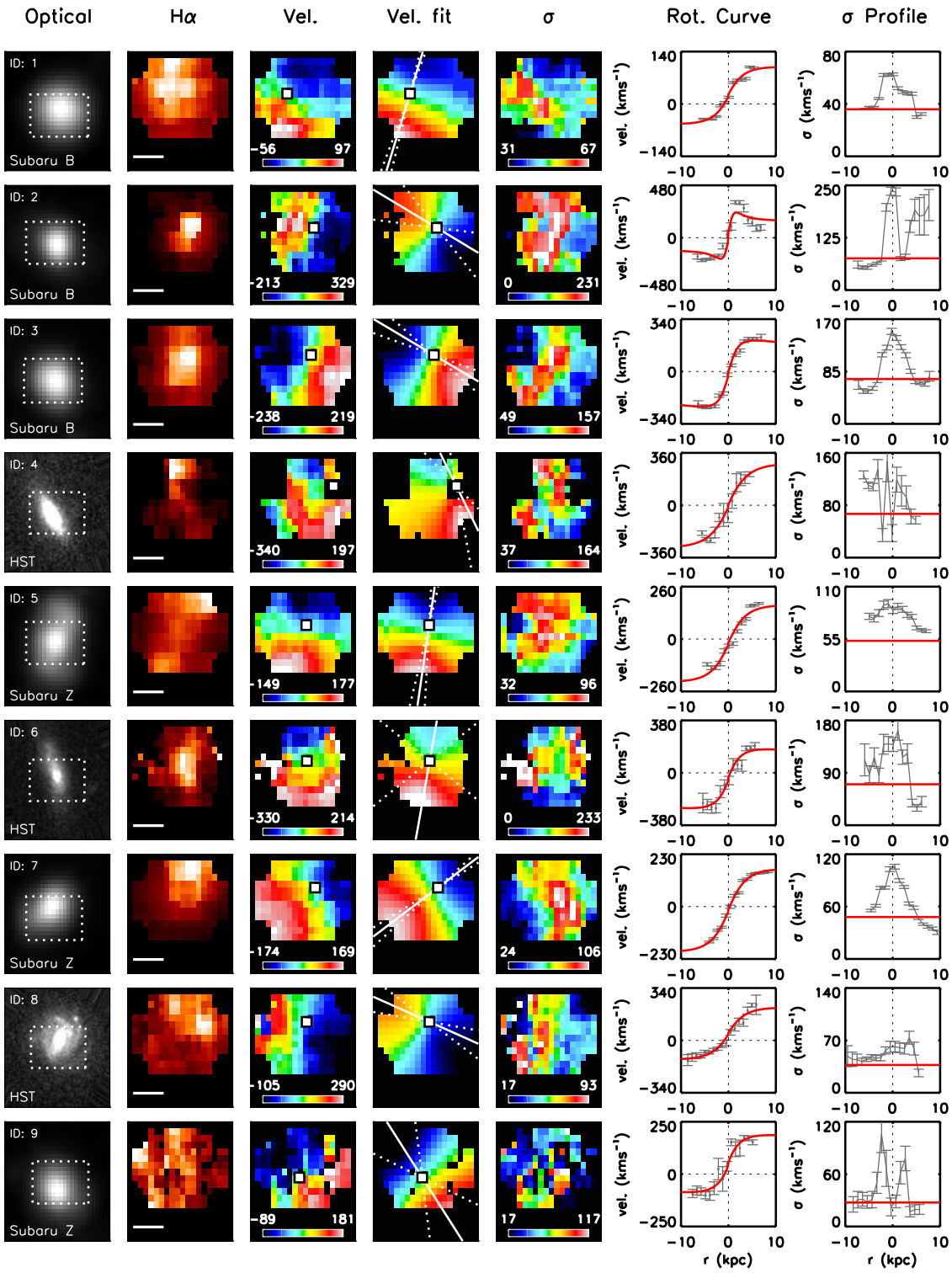

Figure 2.9: Broad-band image, Hα morphology and dynamical maps for all 27 galaxies in our cluster starburst sample. Left to right we show: Subaru or *HST* broad-band image (dashed lines illustrate the FLAMES field of view), Hα intensity map (with 5kpc scale bar), velocity field, best-fit model velocity field, dispersion map, and the rotation curve (red line is the model fit) and line of sight dispersion profile (red line is σ_0) extracted along the primary axis. The solid line on the velocity field shows the position angle, with dashed lines illustrating the 1σ uncertainty. Square points show the model dynamical centre.

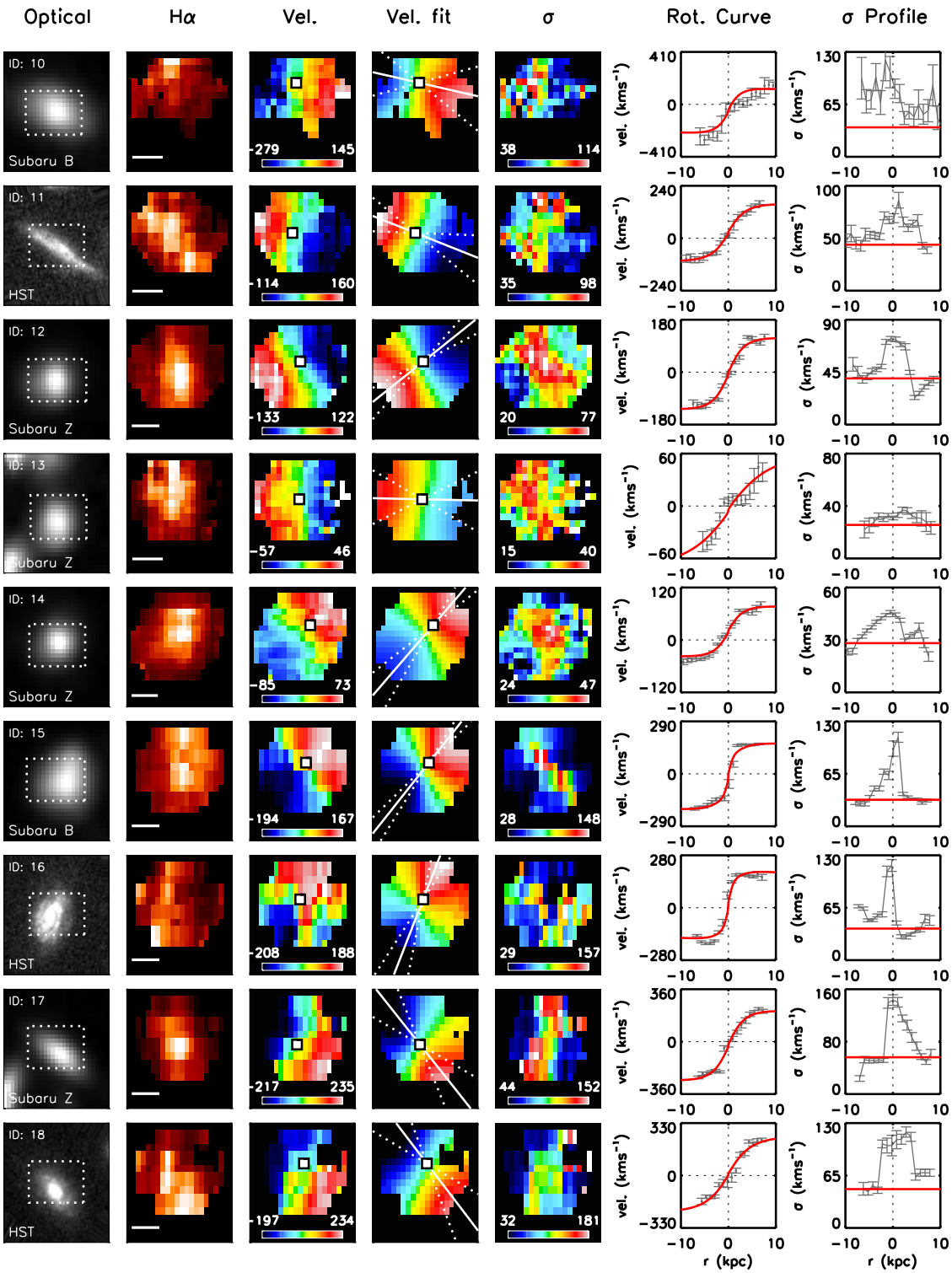

Figure 2.9: *continued*

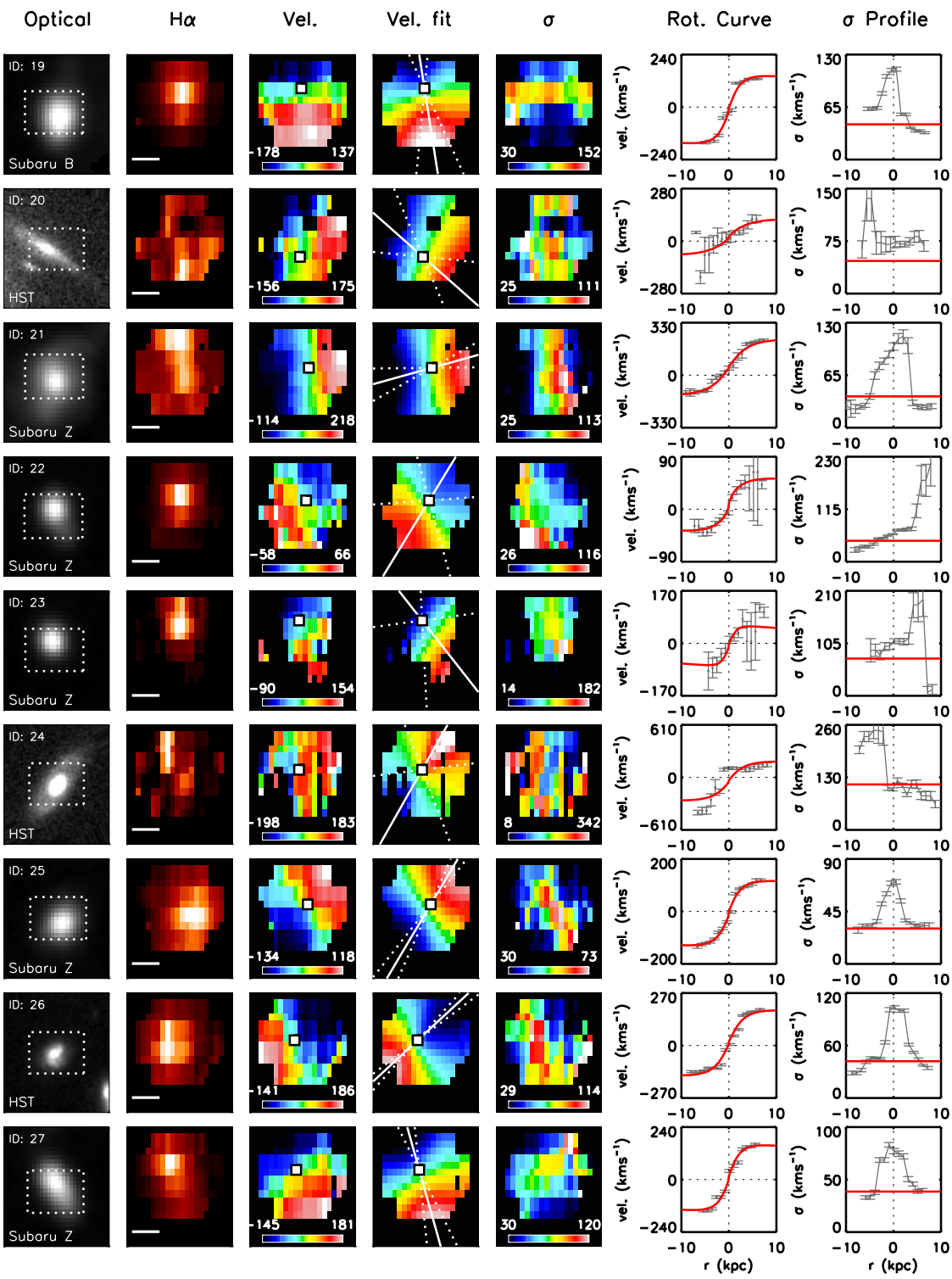

Figure 2.9: *continued*

tidal tails or merger activity. We class the remaining three galaxies as irregular, since they show complex dynamics in their two dimensional maps, rotation curves or dispersion profiles. This fraction of disks is consistent with field surveys at these redshifts, which have suggested that massive galaxies are the most well ordered at all redshifts up to $z \sim 1.5$ (e.g. Kassin et al. 2012; Wisnioski et al. 2015; Stott et al. 2016; but see also Puech et al. 2007). In Fig. 2.6 we demonstrated that the kinematics do not appear to be correlated with far-infrared luminosity or K band magnitude.

To provide a quantitative measure of the dynamics and derive their basic parameters (such as disk inclination, i and hence true rotational speed), we fit each each velocity field using a simple disk model with an arctan rotation curve (e.g. Courteau 1997). In total we fit for six different parameters: the dynamical centre (x_c, y_c), asymptotic velocity v_c, velocity at centre of rotation v_0, turnover radius r_t, position angle θ, and disk inclination i. Although all velocity fields show small discrepancies, the majority appear to be well fit by this simple model. We calculate the root-mean-square of the residuals in each velocity map and find a sample average of $< v_{\rm data} - v_{\rm model} > = 26 \pm 15\,{\rm km\,s^{-1}}$. Dynamical maps are shown for the full sample in Fig. 2.9. We note that the position angles returned by the model fit clearly pass through the regions of minimum and maximum rotation velocity. We also compare our inclination values to those derived from the *HST* and Subaru optical morphologies. Although there is some scatter, we find our conclusions in the following sections would be unchanged had we used inclinations derived directly from the images instead. Where the inclination of a particular galaxy is more uncertain, this is reflected in the larger errors assigned to dynamical parameters in Table 2.3.

Using the best-fit disk parameters, we extract one-dimensional rotation curves by collapsing the velocity field along the major kinematic axis. It is clear from these data that a number of the rotation curves flatten beyond $\sim$ 2kpc. To fully characterise this shape we fit the rotation curves with a model that includes a dark matter component. The velocity field can therefore be expressed as $v^2 = v_{\rm d}^2 + v_{\rm h}^2$, where the subscripts denote the stellar disk and dark matter halo respectively. For the stellar disk, we assume the stars follow an exponential surface density (Freeman 1970) which is characterised by a disk mass and radius, and for the dark matter we assume $v_{\rm h}^2(r) = GM_{\rm h}(< r)\,/\,r$, with a dark-matter density profile that is described by a core density and radius. Further details of the modelling

used are discussed in Swinbank et al. (2017). Although we do not attempt to infer the stellar/dark halo fractions (due to strong degeneracies), this parameterisation allows us to improve our measurement of total rotation speed at the disk radius. While in most cases we could extract this velocity directly from the raw data, a model is useful for when this is not possible. In the following analysis we use inclinations from the two-dimensional disk model and rotation velocities from this one-dimensional rotation curve fit.

As a representative rotation velocity we choose $v_{2.2}$, the velocity at 2.2 times the half-light radius, since this typically samples the rotation curve in a region where it is no longer rising steeply. Of our IFU sample, ten are covered by deep *HST* imaging and the remaining 17 have been imaged by Subaru (see Fig. 2.9). We use these images to establish the continuum half-light radius ($r_{1/2}$) by fitting a series of ellipses at the galaxy position angle. We deconvolve for the seeing, and use the model rotation curve to estimate the velocity at this radius. We give this rotation speed and the corresponding half-light radius in Table 2.3.

2.4.2 Turbulence and Rotational Support

To continue to address the question of which physical mechanism(s) drives the star formation in cluster starbursts, we next measure the turbulence in the ISM. By comparing to galaxies in the field with a mass and star formation rate matched sample, this will allow us to quantify the effect of environment on the stability of the disk. To calculate the intrinsic velocity dispersion, σ_0, we first correct for beam smearing effects using the two-dimensional velocity field. For each pixel we consider all neighbouring pixels within the PSF, and calculate the maximum velocity gradient across this element $\Delta v/\Delta R$. This contribution to the dispersion is then removed and we calculate the average velocity dispersion across the entire galaxy image (inverse weighting by the noise at each pixel). The final corrected velocity dispersions, σ_0, for each galaxy are given in Table 2.3 and their values also shown relative to the dispersion profiles in Fig. 2.9. It can be seen that these σ_0 values are comparable to the velocity dispersion in the outer regions of the disk, which is less affected by beam smearing.

We find our cluster starbursts to have a median velocity dispersion of $\sigma_0 = 50 \pm 15\,\mathrm{km\,s^{-1}}$. Dynamical studies between $0.2 < z < 1.0$ report values in the range

$\sigma_0 = 25-60\,\mathrm{km\,s^{-1}}$ (e.g. Kassin et al. 2012; Wisnioski et al. 2015; Stott et al. 2016), however it is difficult to make direct comparisons since estimates are highly sensitive to the properties of the sample and the method used (see Stott et al. 2016 and Chapters 3 and 4 for further discussion). To derive σ_0 in a consistent way and compare to the turbulence of field galaxies at similar redshift, we exploit the sample of Swinbank et al. (2017). This sample consists of ~ 500 [OII] emitters serendipitously identified in a series of commissioning and science verification observations using MUSE. There were 16 extragalactic fields observed, with the science targets largely "blank" fields or studies of high redshift ($z > 4$) galaxies and quasars. We match the redshift, stellar mass and star formation rate of this star-forming sample to our cluster starbursts and find a median of $\sigma_0 = 50 \pm 10\,\mathrm{km\,s^{-1}}$. This suggests that turbulence in the gas disks of our galaxies has not yet been enhanced by the various physical processes acting in this dense environment.

The ratio between inclination corrected rotation velocity and intrinsic velocity dispersion, v/σ_0, is often used as a measure of rotational support against turbulent pressure. We therefore calculate this parameter for each galaxy in order to compare their dynamics to the field population and cluster S0s, using the characteristic rotation velocities ($v_{2.2}$) calculated in §2.4.1. Across our sample we find inclination corrected values between $v_{2.2}/\sigma_0 = 2.8-8.2$, with a median of $v_{2.2}/\sigma_0 = 5 \pm 2$. Given that $v/\sigma_0 < 1$ is typically used as a cut-off for the classification of "dispersion dominated" galaxies, this further supports our conclusions that the majority of our sample are undisturbed, rotating disks.

In Fig. 2.10 we compare the rotation of the dusty starbursts to local S0s and spiral galaxies in low density environments at similar redshift. We plot the v/σ_0 values of 32 rotationally supported galaxies at $0.4 \leq z \leq 0.75$ (also observed using FLAMES). Puech et al. (2007) find a median $v/\sigma_0 = 3.8 \pm 2$, which is consistent with our sample. We also see that local S0s (Emsellem et al. 2011) typically have values of $v/\sigma_0 \leq 1$. The dynamics of infalling cluster galaxies must evolve significantly if a transformation is to take place between spirals and S0s.

The difference between the cluster starburst population and S0s is again evident in the lower panel of Fig. 2.11. We analyse the dynamics of local S0s (Emsellem et al. 2011), star-forming field galaxies (Swinbank et al. 2017) and our sample, within the context of the K-band Tully-Fisher relation. For a fixed K-band magnitude cluster starbursts appear

to rotate more rapidly than local S0s. Conversely, all three populations lie along the same $\sigma_{\rm tot} - M_K$ relation, where $\sigma_{\rm tot}$ is the linewidth of the galaxy integrated spectrum, tracing both rotational and turbulent motions. This confirms that it is the v/σ_0 ratio which is fundamentally different.

Finally, to search for trends in the dynamics as a function of cluster-centric radius, we divide the sample into galaxies within the (projected) cluster core, in the outskirts, and in the foreground group. However, we do not find any link between whether a galaxy resides in one of these regions and its dynamics (in terms of the observed dynamical state, σ_0 or $v_{2.2}/\sigma_0$). We show the median $v_{2.2}/\sigma_0$ of these two subsamples in Fig. 2.10. The kinematics also do not appear to be strongly correlated with galaxy mass or star formation rate (see Fig. 2.6). Although our results may be complicated by projection effects, it appears that the dynamics of the galaxies are not a strong function of location within the cluster. This implies that any dynamical transformation must take place over a longer period than the duration of the starburst (~ 1 Gyr), or once the starburst has been quenched.

2.4.3 Specific Angular Momentum

Although the ratio of $v\,/\,\sigma_0$ is a useful measure of the dynamical state of a galaxy, a better quantification is the spin, $\lambda_{\rm R}$, since this encodes how the rotational speed and line of sight velocity dispersion vary with radius. Dynamical studies of local galaxies have shown that early-type and late-type galaxies tend to (broadly speaking) have different spin values (Querejeta et al. 2015; Fogarty et al. 2015). Emsellem et al. (2011) define $\lambda_{\rm R}$, which is essentially a proxy for specific angular momentum, as:

$$\lambda_{\rm R} = \frac{\sum_{i=1}^{N} F_i R_i |V_i|}{\sum_{i=1}^{N} F_i R_i \sqrt{V_i^2 + \sigma_i^2}} \tag{2.4.1}$$

where F_i, V_i, σ_i, and R_i are the flux, velocity, velocity dispersion and radius of the ith pixel respectively. This spin parameter was initially used in the classification of early-type galaxies, with Cappellari et al. (2011) finding ellipticals and S0s could be split into two regimes – fast rotators and slow rotators – depending on their spin and ellipticity. However more recently the spin has been combined with the concentration of the stellar

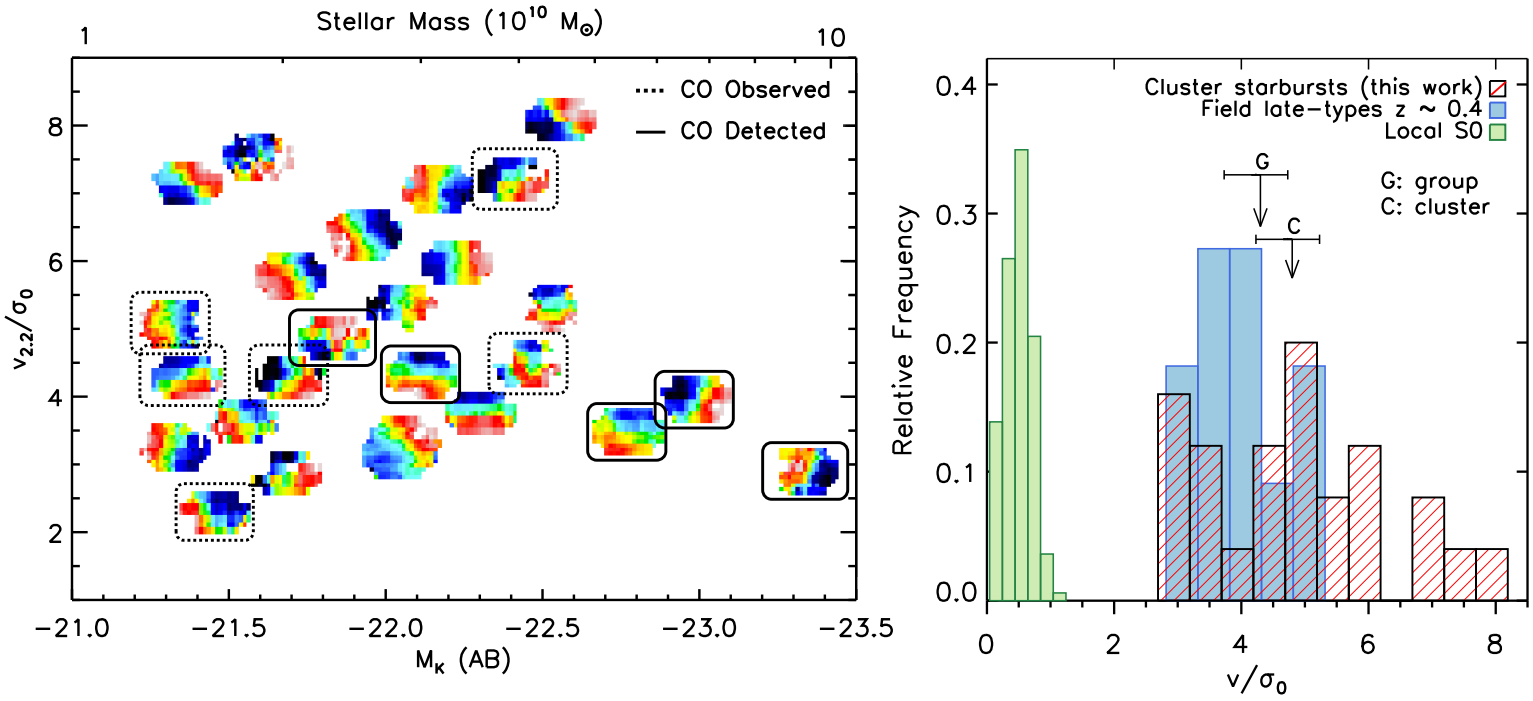

Figure 2.10: *Left*: Hα dynamics of the 25 galaxies as a function of rotational support ($v_{2.2}/\sigma_0$) and *K* band magnitude. We choose to define the characteristic rotation velocity at 2.2 × the half-light radius, as measured from *H*ST and Subaru continuum images. We convert M_K values to stellar masses, using the average mass-to-light ratio derived from the HYPERZ SED fitting (see §2.3.1). We circle galaxies for which we have observed the CO(1→0) transition, with solid lines corresponding to $> 5\,\sigma$ detections, and dashed lines elsewhere. Some velocity fields have been shifted a small distance from their original position for clarity, however these values are provided in Tables 2.2 and 2.3. The majority of galaxies resemble undisturbed, rotating disks, with no obvious trends between dynamics and galaxy mass or molecular gas content. *Right*: The rotational support of our galaxies compared to local S0s (Emsellem et al. 2011) and field spirals of a similar redshift (Puech et al. 2007). The fact that their v/σ_0 values are consistent with field spirals suggests that these galaxies have only recently been accreted. Their disks must be dynamically heated to decrease their v/σ_0 values to match S0s. The median v/σ_0 of the group does not appear to be significantly different to that of the "main" cluster ('G' arrow and 'C' arrow respectively).

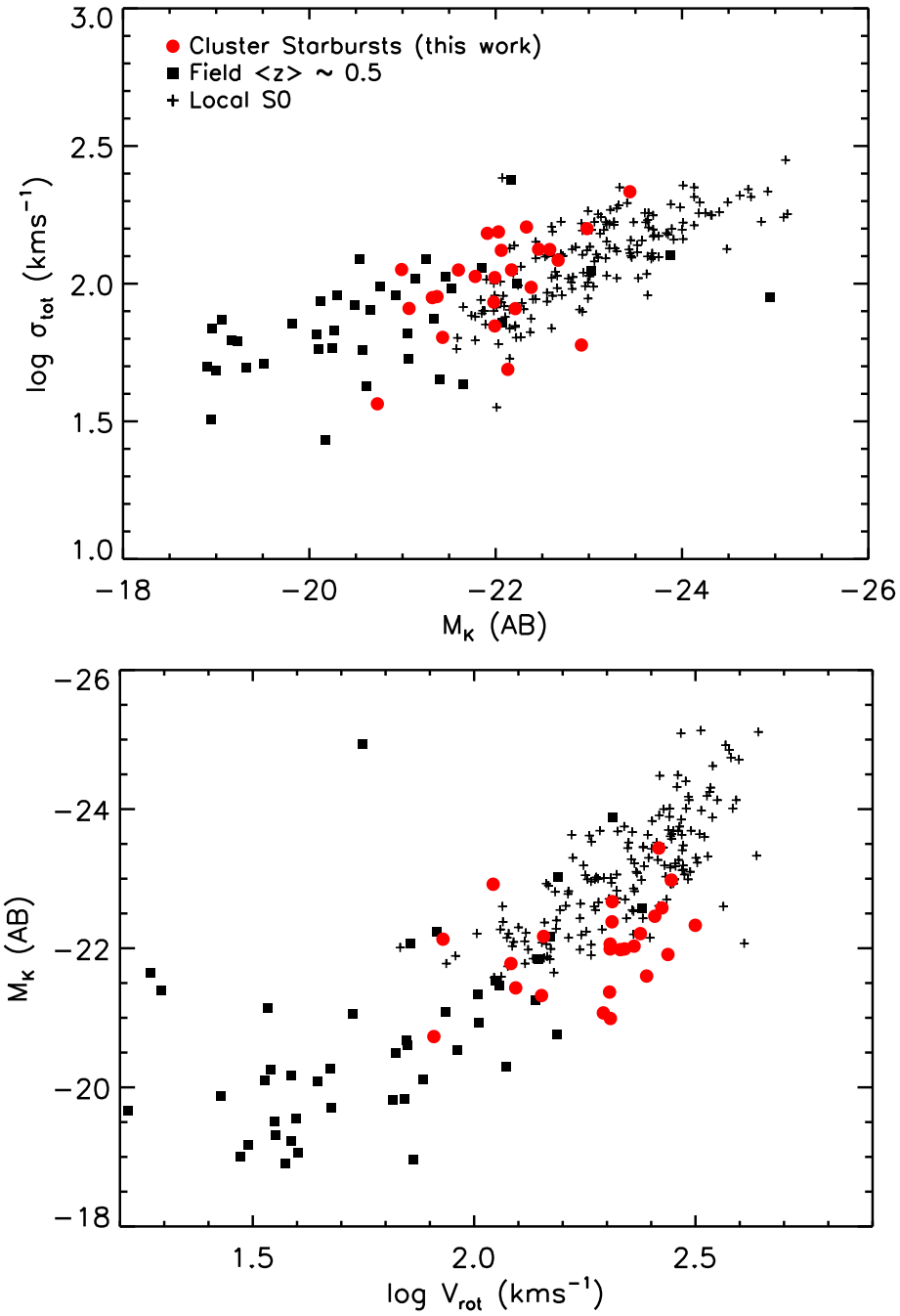

Figure 2.11: Dynamical properties in relation to local S0 galaxies (Emsellem et al. 2011) and [OII] emitters of a similar redshift (Swinbank et al. 2017). *Top*: Galaxy integrated linewidth (σ_{tot}) versus K-band absolute magnitude. σ_{tot} traces both the rotational and turbulent motions within a galaxy and so steadily increases with M_K for late-types and S0s alike. *Bottom*: K-band Tully-Fisher relation. For a given K-band magnitude, cluster starbursts in our sample are rotating more rapidly than local S0s. For starbursts to transition to S0s any increase in mass must be accompanied by a decrease in the ratio between the rotational velocity and velocity dispersion (i.e. v/σ_0).

light profile, as a diagnostic tool to test how galaxies might dynamically evolve from one type to another. Concentration, c, is defined as the ratio between the radii enclosing 90% and 50% of the Petrosian flux.

In Fig. 2.12 we compare the spin and concentration of our sample to the properties of spirals and S0s from the CALIFA survey ($z \sim 0$; Querejeta et al. 2015). For consistency with the comparison samples we evaluate λ_R for all pixels within the half-light radius and derive a median $\lambda_R = 0.83 \pm 0.06$ and concentration of $c = 2.1 \pm 0.3$ for the cluster galaxies. As Fig. 2.12 shows, the dynamics and concentration of our galaxies are consistent with field spirals, implying that the dynamics of our sample are still relatively unaffected by the cluster environment. If these galaxies are to eventually transition to S0s they clearly must undergo a process (or several) which not only dynamically heats the disk and reduces rotational support, but which also increases the bulge to disk ratio (and hence increases the concentration by a factor ~ 2).

Interactions with the dense ICM can effectively strip the gas disks of spirals and lead to a rapid truncation of star formation. It was recently suggested that ram pressure stripping may even cause a temporary enhancement of star formation in central regions (Bekki & Couch 2011; Bekki 2014). However, the same numerical simulations predict little effect on the dynamics of these galaxies due to interaction with the ICM. Conversely, tidal interactions are very efficient at disrupting the disk. Repeat galaxy-galaxy encounters can act to increase the velocity dispersion and decrease the spin, potentially channelling gas inwards to fuel episodes of bursty star formation. Indeed, Bekki (2014) predict that a high spin, low concentration late-type galaxy in a high mass group may be transformed via tidal interactions into a low spin, high concentration S0, over a period of 2 – 4 Gyr. We overlay this evolution in Fig. 2.12. Although the timescales likely increase in a cluster environment, such a mechanism would simultaneously achieve the two key changes required for a spiral to S0 transition. In this scenario, the concentration is increased gradually via multiple bursts of star formation in the central regions, and we may expect to find starbursts with a range of λ_R and c values. However, our cluster starburst sample are exclusively high-spin, low-concentration galaxies. We propose instead that the initial encounter with the ICM is responsible for triggering the starbursts observed in this cluster. Repeat galaxy-galaxy interactions may occur after the bursts have been quenched, to

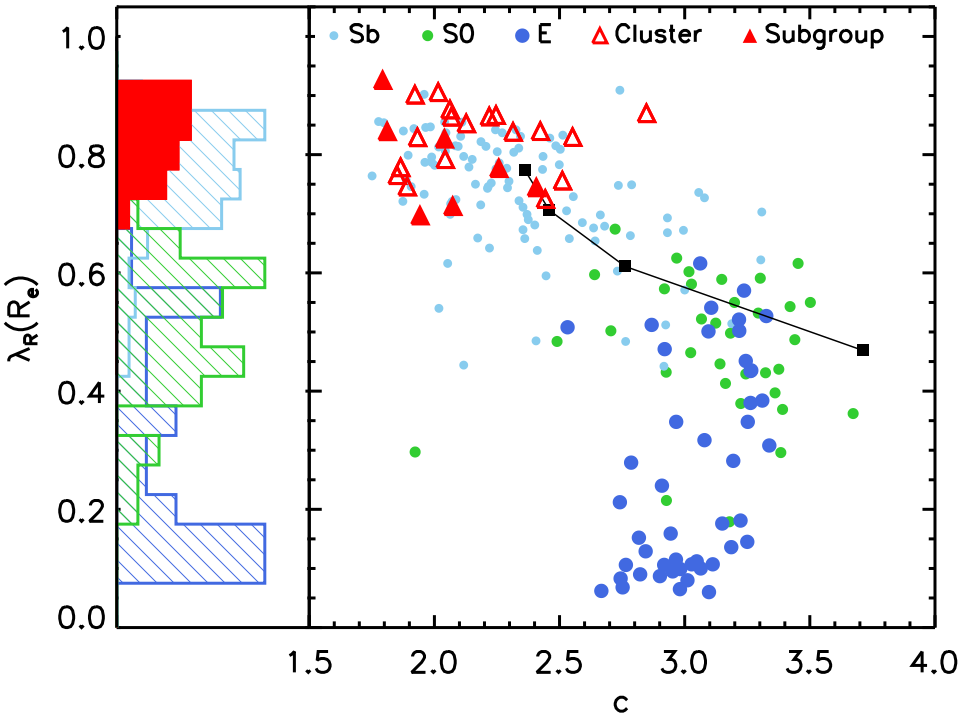

Figure 2.12: Galaxy spin, λ_R versus concentration, c for our starburst sample, as compared to galaxies of various morphological types from the CALIFA survey (Querejeta et al. 2015). We also overlay predictions from the numerical models of Bekki & Couch (2011) who simulate the impact of tidal interactions on a typical spiral galaxy in a dense environment. Squares along the tracks represent 0, 2.8, 4.2 and 5.6 Gyr since the beginning of this simulation. The high spin values of our galaxies suggest kinematics that are consistent with recently accreted field spirals. It seems that the mechanism which initiated the current burst of star formation has not had a dramatic effect on the disk dynamics. In order to make a transition between spirals and S0s these galaxies must lose angular momentum and increase their bulge to disk ratio (and therefore concentration).

eventually achieve the $\sim 40\%$ decrease in angular momentum.

2.4.4 The Beginning of the End?

Overall, the characteristic temperatures, gas masses and dynamics of these dusty starburst galaxies suggest that they have only recently been accreted from the field. The far-infrared star formation rates are on average twice that of a typical star-forming galaxy at this redshift, with our CO observations suggesting there is sufficient cold gas to sustain this activity for another ~ 1 Gyr. In fact we calculate molecular gas masses consistent with local ULIRGs. Dust temperatures in line with the local relation are further evidence that the gas disks have not yet been stripped by the intra-cluster medium.

The dynamics and morphologies of the cluster galaxies appear disk-like, with a high degree of rotational support (v/σ_0) and a high angular momentum (λ_R). There is no evidence to suggest that the current bursts of star formation were initiated by mergers or tidal interactions. Instead, it is possible that they were triggered by ram pressure, as an initial encounter with the ICM compresses the ISM of the infalling galaxies. This could also convert available HI into molecular H_2, and may explain why these galaxies are so rich in star-forming gas. Such a proccess is consistent with the small excess of starbursts seen inside the virial radii of some clusters (e.g. Hogg et al. 2006).

As we have seen in Fig. 2.12, in order for the cluster starbursts to transition from spirals to S0s they must increase their concentration (c) and decrease their angular momentum (λ_R). Multiple galaxy-galaxy interactions (harassment) seem a likely mechanism for the dynamical transformation, however the growth of the bulge does not appear to occur simultaneously. It is more likely that dynamical heating through tidal interactions occurs much later (≥ 1 Gyr), after the molecular gas has been depleted and/or stripped. Of course, it is also possible that these galaxies do *not* transition to S0s, but follow an alternative evolutionary path.

The current burst looks set to increase the mass of these galaxies by $\sim 1 \times 10^{10}\,M_\odot$, with final stellar masses consistent with sub-M_* S0s. However, how this starburst episode may affect the bulge to disk ratio remains to be seen. To determine how much of the star formation is confined to central regions of the galaxy requires high resolution millimetre/submillimetre observations, for example using ALMA.

2.5 Conclusions

At low redshift the effects of environment on the morphology, gas content and star formation of galaxies is a well established phenomenon. Yet we know relatively little about the mechanisms which drive these trends, and how they depend on the properties of both the cluster, and the infalling galaxies on which they act. It is vital to develop a greater understanding of these issues if we are to explain the reversal of the morphology–density relation at high redshift.

In this study we investigated the dynamics, star formation and gas properties of 27 cluster starbursts from Cl 0024+17 ($z \sim 0.4$), to learn more about the nature of these galaxies, and how dense environments at high redshift can promote star formation in some infalling galaxies. This problem is key to explaining the early and rapid formation of today's massive cluster galaxies. Our main findings are as follows:

- We use deblended *Herschel* PACS / SPIRE maps to derive bolometric luminosities of $L_{\rm IR} = (0.47 - 2.47) \times 10^{11}$ $L_{\odot}$ and star formation rates $\mathrm{SFR_{IR}} = 5 - 26\,M_{\odot}\mathrm{yr}^{-1}$. The enhanced activity of these galaxies places them above the star-forming "main-sequence" for this redshift and stellar mass (an average of $\sim 3 \times 10^{10}\,M_{\odot}$).

- From the far-infrared photometry, we derive characteristic dust temperatures of $T_{\rm d} = 26 \pm 1$ K, consistent with the local $L_{\rm IR}$-$T_{\rm d}$ relation for field galaxies. We do not find any evidence that the cold gas/dust has been stripped by the interaction of the galaxy ISM with the intra-cluster medium. If such an interaction occurs, then it must act on a much longer timescale, or occur after the initial burst.

- We search for the CO(1→0) emission from 11 galaxies in our sample. Of these targets, eight are within the cluster and three within the foreground group. Only two of eight galaxies are detected in the larger structure, while all three galaxies in the foreground group are detected at $> 5\sigma$. We find the average CO-derived gas mass of the sample (stacking detections and non-detections) to be $\sim 1 \times 10^{10}\,M_{\odot}$. A median star formation rate of $\sim 13\,M_{\odot}\,\mathrm{yr}^{-1}$ suggests gas depletion timescales of ~ 1 Gyr, which is ~ 0.25 of the cluster crossing time. Our galaxies appear to be richer in star-forming gas than typical field galaxies at the same redshift.

- We use FLAMES multi-IFU data to study the ionised gas dynamics of these cluster starbursts, as traced by Hα emission, and after excluding AGN we find the majority of the sample ($\sim 90\%$) have dynamics that appear to be consistent with undisturbed, uniformly rotating disks. To quantify the ratio between rotation and pressure support we calculate v/σ_0. The average for our sample is $v/\sigma_0 = 5 \pm 2$, in line with spirals of a similar redshift, further demonstrating that these galaxies have only recently accreted from the field.

- We also measure the spin, λ_R (a proxy for specific angular momentum) and concentration, c of the cluster starbursts. The relation between λ_R and c provides a useful means to follow the morphological and dynamical evolution of these galaxies. We derive a median spin and concentration of $\lambda_R = 0.83 \pm 0.06$ and $c = 2.1 \pm 0.3$, respectively. These values are consistent with typical field spirals. In order to evolve to S0s, these galaxies must double their concentration (through growth of the bulge) and decrease their angular momentum by a factor of ~ 1.5.

- Although limited by small numbers, galaxies in the group do not show evidence of an accelerated evolution. The only difference between the "main" cluster and group components is (potentially) in the molecular gas properties, where all three group members are detected in CO but only two of eight galaxies are detected in the larger structure.

It appears that these dusty, star-forming galaxies must have only recently been accreted to the cluster, with their dynamics, morphologies and molecular gas consistent with star-forming field galaxies. They show no evidence of having yet been significantly disrupted by the dense environment. We conclude that for these $z \sim 0.4$ cluster galaxies to make the transition to S0s they must undergo a dynamical heating of the disk, and an increase in concentration. While ICM-related processes such as ram pressure stripping will truncate the gas disk, the full transformation from spiral to S0 is unlikely to be achieved by this process alone. Of the various available mechanisms, galaxy-galaxy encounters within the cluster seem most probable. Since $\sim 90\%$ of our sample display disk-like dynamics, this must occur after the initial burst has been quenched, and without an associated starburst.

Table 2.1: Observed properties

ID	RA (J2000)	Dec (J2000)	$z_{H\alpha}$	S_{24} (μJy)	$f_{H\alpha}$ (10^{-16} erg s^{-1})	log([NII]/Hα)	B (AB)	R (AB)	Group
1	6.59050	17.3240	0.3804	950 ± 40	14.0 ± 0.2	-0.48 ± 0.01	21.63	19.80	y
2	6.81270	17.2131	0.3804	950 ± 50	4.2 ± 0.2	-0.11 ± 0.03	22.53	19.98	y
3	6.71870	17.2332	0.3800	830 ± 20	10.6 ± 0.3	-0.37 ± 0.02	22.31	20.10	y
4	6.53730	17.2530	0.3950	770 ± 30	2.2 ± 0.1	-0.28 ± 0.04	23.88	21.32	n
5	6.76520	17.1912	0.3955	706 ± 50	6.1 ± 0.1	-0.44 ± 0.02	22.42	20.45	n
6	6.60820	17.2976	0.3986	440 ± 20	1.5 ± 0.1	-0.24 ± 0.06	24.03	21.34	n
7	6.75580	17.3446	0.3808	350 ± 30	8.5 ± 0.2	-0.52 ± 0.01	22.16	20.48	y
8	6.66020	17.1254	0.3916	201 ± 5	1.50 ± 0.08	-0.38 ± 0.06	22.98	20.76	n
9	6.55990	17.2222	0.3944	< 150	0.83 ± 0.07	-0.29 ± 0.07	23.36	21.15	n
10	6.66080	17.2539	0.3935	< 150	0.72 ± 0.08	-0.22 ± 0.07	23.28	20.95	n
11	6.64020	17.2055	0.3970	350 ± 50	2.30 ± 0.08	-0.67 ± 0.06	23.57	21.71	n
12	6.58330	17.0687	0.3788	670 ± 40	5.27 ± 0.09	-0.42 ± 0.01	22.86	21.00	y
13	6.60210	17.1917	0.3904	290 ± 30	2.51 ± 0.06	-0.58 ± 0.05	23.09	21.43	n
14	6.65550	17.0162	0.3960	600 ± 30	6.44 ± 0.08	-0.39 ± 0.01	22.40	20.52	n
15	6.67300	17.1838	0.3911	311 ± 5	4.7 ± 0.2	-0.30 ± 0.04	22.26	20.10	n
16	6.63200	17.1545	0.3997	227 ± 4	5.1 ± 0.2	-0.35 ± 0.03	22.86	20.80	n
17	6.66270	17.1672	0.3947	214 ± 4	2.5 ± 0.1	-0.36 ± 0.05	23.91	21.42	n
18	6.63970	17.1566	0.3913	179 ± 4	3.1 ± 0.1	-0.30 ± 0.03	23.01	20.80	n
19	6.69910	17.1619	0.3993	307 ± 7	8.9 ± 0.2	-0.27 ± 0.02	22.13	20.17	n
20	6.52550	17.2054	0.3955	300 ± 50	1.33 ± 0.08	-0.44 ± 0.06	23.92	21.71	n
21	6.74790	17.0626	0.3960	280 ± 30	3.8 ± 0.1	-0.34 ± 0.03	22.53	20.51	n
22	6.63740	17.2581	0.3809	345 ± 30	3.05 ± 0.06	-0.36 ± 0.02	23.35	21.29	y
23	6.72500	17.2343	0.3916	300 ± 30	1.11 ± 0.07	-0.02 ± 0.04	23.79	21.03	n
24	6.58090	17.1174	0.3970	340 ± 30	3.1 ± 0.2	0.04 ± 0.03	23.46	20.69	n
25	6.64270	17.1011	0.3813	260 ± 30	4.5 ± 0.1	-0.69 ± 0.04	22.89	21.26	y
26	6.60710	17.2015	0.3929	340 ± 40	9.4 ± 0.2	-0.46 ± 0.03	22.30	20.53	n
27	6.65550	17.1768	0.3967	158 ± 5	5.2 ± 0.1	-0.49 ± 0.03	23.11	21.21	n

NOTES: The *B*- and *R*- band magnitudes were extracted at the same aperture, in order to derive the colours plotted in Fig. 2.2. In the final column we specify whether each galaxy is a member of the cluster (n) or the foreground group (y), as discussed in §2.2.1.

Table 2.2: Derived properties – galaxy integrated

ID	L_{IR} ($10^{11}\,L_\odot$)	SFR_{IR} ($M_\odot\,yr^{-1}$)	T_d (K)	M_K (AB)	$M_\star$ ($10^{10}\,M_\odot$)	L'_{CO} ($10^9\,K\,km\,s^{-1}\,pc^2$)	M_{gas} ($10^{10}\,M_\odot$)
1	2.5^{+2}_{-3}	26^{+3}_{-13}	29 ± 11	-22.8	5.6 ± 2.5	6.8 ± 0.6	3.1 ± 0.3
2	$0.5^{+0.9}_{-0.3}$ *	11^{+2}_{-2}	> 20	-23.4	9.6 ± 2.9	2.6 ± 0.3	1.2 ± 0.3
3	$1.4^{+1.5}_{-1.2}$	14^{+2}_{-1}	25 ± 12	-23.0	6.8 ± 2.0	6.4 ± 0.5	2.9 ± 0.2
4	1.3^{+2}_{-1}	13^{+9}_{-2}	> 18	-22.5	4.1 ± 1.2	< 3.9	< 1.8
5	$0.6^{+0.8}_{-0.4}$	6^{+3}_{-1}	> 23	-22.2	3.0 ± 1.4	4.3 ± 0.6	2.0 ± 0.3
6	$0.5^{+0.9}_{-0.3}$ *	10^{+2}_{-2}	31 ± 22	-22.4	3.7 ± 1.1	...	...
7	$0.9^{+1.0}_{-0.8}$	10^{+1}_{-2}	> 11	-21.8	2.1 ± 0.8	...	...
8	$0.8^{+0.9}_{-0.7}$	8^{+1}_{-1}	24 ± 2	-22.2	3.2 ± 1.0	...	...
9	$0.8^{+0.9}_{-0.7}$	8^{+1}_{-1}	> 11	-21.7	1.9 ± 0.6	...	...
10	$0.6^{+0.7}_{-0.5}$	6^{+1}_{-1}	> 11	-22.1	2.9 ± 0.9	...	...
11	1.6^{+3}_{-1}	17^{+13}_{-3}	25 ± 1	-21.3	1.4 ± 0.5	...	...
12	$1.0^{+1}_{-0.9}$	11^{+1}_{-2}	> 15	-21.9	2.5 ± 0.9	...	...
13	$0.5^{+1}_{-0.4}$ *	3^{+1}_{-1}	24 ± 2	-20.9	1.0 ± 0.4	< 4.3	< 2.0
14	$0.5^{+1}_{-0.4}$ *	17^{+3}_{-3}	> 11	-22.1	2.8 ± 1.1	...	...
15	$0.6^{+2}_{-0.4}$ *	9^{+2}_{-2}	28 ± 1	-22.6	4.6 ± 2.1	...	...
16	$0.5^{+1}_{-0.4}$ *	11^{+2}_{-2}	26 ± 1	-22.0	2.6 ± 1.2	2.2 ± 0.7	1.0 ± 0.3
17	$0.5^{+2}_{-0.1}$ *	12^{+2}_{-2}	26 ± 1	-22.0	2.5 ± 1.2	< 4.4	< 2.0
18	$0.5^{+0.9}_{-0.3}$ *	5^{+1}_{-1}	27 ± 2	-22.1	2.8 ± 0.9	< 4.1	< 1.9
19	1.2^{+1}_{-1}	13^{+1}_{-3}	26 ± 2	-22.7	5.0 ± 1.8	...	...
20	0.9^{+5}_{-1}	20^{+31}_{-9}	> 11	-21.7	2.1 ± 0.9	...	...
21	$0.6^{+0.7}_{-0.5}$	6^{+1}_{-1}	> 11	-22.3	3.4 ± 1.7	...	...
22	$1.0^{+4}_{-0.9}$	11^{+35}_{-1}	> 11	-21.5	1.7 ± 0.8	...	...
23	1.3^{+2}_{-1}	14^{+7}_{-4}	> 11	-21.7	2.0 ± 0.6	...	...
24	$1.3^{+2}_{-0.6}$	13^{+7}_{-6}	> 11	-22.6	4.5 ± 1.4	...	...
25	$0.5^{+0.5}_{-0.5}$ *	6^{+2}_{-2}	> 11	-21.0	1.1 ± 0.4	...	...
26	$0.6^{+0.6}_{-0.6}$	6^{+1}_{-2}	30 ± 2	-22.1	2.8 ± 1.3	< 4.9	< 2.3
27	$0.5^{+0.9}_{-0.4}$ *	8^{+2}_{-2}	27 ± 2	-21.3	1.3 ± 0.6	< 4.6	< 2.1

NOTES: L_{IR} is the bolometric luminosity of the best-fit template SED fit to *Herschel* far-infrared photometry. Star formation rates with an adjacent $*$ were derived by applying the average $SFR_{H\alpha}/SFR_{IR}$ correction factor, since these galaxies have detections in only ≤ 1 bands. The characteristic dust temperatures, T_d, come from a single-temperature blackbody fit, assuming an emissivity index of $\beta = 1.8$. Stellar mass estimates were calculated using a constant mass-to-light ratio of $M_\odot/L^K_\odot = 0.35$. L'_{CO} and M_{gas} are derived from a Gaussian fit to IRAM / NOEMA CO(1→0) spectra (see §2.3.4), for which we assume a CO to H_2 conversion factor of $\alpha = 4.6$.

Table 2.3: Derived properties – ionised gas dynamics

ID	σ_0 (km s^{-1})	$r_{1/2}$ (kpc)	$v_{2.2}$ (km s^{-1})	$v_{2.2}/\sigma_0$	λ_R	Class
1	36 ± 5	6.0 ± 0.4	120 ± 10	3.4 ± 0.5	0.71 ± 0.02	R
2	76 ± 8	6.2 ± 0.5	210 ± 40	2.8 ± 0.7	0.74 ± 0.01	R
3	72 ± 5	5.5 ± 0.4	270 ± 20	3.7 ± 0.5	0.77 ± 0.01	R
4	67 ± 5	8.5 ± 0.4	300 ± 20	4.4 ± 0.6	0.82 ± 0.01	I
5	53 ± 5	8.5 ± 0.5	230 ± 10	4.3 ± 0.5	0.82 ± 0.01	R
6	70 ± 9	9.6 ± 0.5	310 ± 20	4 ± 2	0.83 ± 0.01	R
7	48 ± 5	6.0 ± 0.5	280 ± 30	5.7 ± 0.9	0.83 ± 0.02	R
8	37 ± 5	5.8 ± 0.5	260 ± 50	7 ± 2	0.90 ± 0.02	R
9	28 ± 7	5.9 ± 0.4	210 ± 60	8 ± 2	0.85 ± 0.03	R
10	37 ± 7	9.5 ± 0.4	190 ± 20	5.3 ± 0.8	0.87 ± 0.01	R
11	44 ± 5	9.8 ± 0.5	140 ± 10	3.2 ± 0.5	0.83 ± 0.01	R
12	40 ± 5	5.0 ± 0.4	250 ± 50	6 ± 2	0.82 ± 0.07	R
13	26 ± 5	5.4 ± 0.6	130 ± 40	5 ± 2	0.72 ± 0.02	R
14	28 ± 5	6.9 ± 0.2	100 ± 10	3.4 ± 0.6	0.74 ± 0.03	R
15	33 ± 5	6.0 ± 0.4	300 ± 20	8 ± 1	0.90 ± 0.02	R
16	40 ± 4	5.7 ± 0.4	200 ± 10	5.0 ± 0.7	0.77 ± 0.04	R
17	57 ± 7	6.8 ± 0.8	290 ± 30	5.1 ± 0.8	0.86 ± 0.01	R
18	48 ± 5	6.0 ± 0.6	290 ± 30	6 ± 1	0.86 ± 0.05	R
19	44 ± 4	4.2 ± 0.3	220 ± 40	5 ± 1	0.79 ± 0.03	R
20	47 ± 6	8.8 ± 0.7	130 ± 30	2.8 ± 0.7	0.86 ± 0.01	I
21	40 ± 4	9.7 ± 0.4	230 ± 20	5.9 ± 0.8	0.76 ± 0.03	R
22	46 ± 5	5.2 ± 0.5	150 ± 20	3 ± 3	0.69 ± 0.02	I
23	75 ± 6	4.0 ± 0.4	90 ± 30	1.2 ± 0.4	0.47 ± 0.01	I
24	112 ± 7	8.0 ± 0.3	230 ± 20	2.0 ± 0.3	0.47 ± 0.03	I
25	30 ± 5	6.0 ± 0.4	220 ± 20	7 ± 1	0.92 ± 0.05	R
26	42 ± 4	3.7 ± 0.5	190 ± 10	4.5 ± 0.5	0.75 ± 0.06	R
27	38 ± 5	5.8 ± 0.4	200 ± 30	5.2 ± 0.8	0.86 ± 0.04	R

NOTES: To estimate the intrinsic velocity dispersion, σ_0, we correct the two-dimensional σ map for beam smearing and instrumental broadening, then take a pixel-by-pixel mean which is inverse weighted by the error. The rotational support, v/σ_0, is calculated using the value of the rotation curve at $2.2 \times r_{1/2}$ ($v_{2.2}$ and $r_{2.2}$ respectively), corrected for the inclination of the disk. The spin parameter, λ_R, is calculated using all pixels within the half-light radius (see §2.4.3). The final column describes the dynamical class we assign, taking into account the two-dimensional dynamical maps, optical morphology, rotation curve and line of sight velocity dispersion profile – 'R' if the galaxy resembles an undisturbed, rotating disk, and 'I' if the galaxy shows some sign of irregular kinematics or merger activity. We note that IDs 23 and 24 likely have an AGN which is disturbing the gas dynamics.

CHAPTER 3

The Impact of Beam Smearing on Measurements of Galaxy Rotation Velocity and Intrinsic Velocity Dispersion

Preamble

This work is adapted from the appendix of a forthcoming paper (Johnson et al. 2017, accepted for publication in MNRAS; arXiv:1707.02302). In Chapter 4 we study the Hα kinematics of a large sample of $z \sim 0.9$ star-forming galaxies, observed using the KMOS multi-object spectrograph. These observations are seeing-limited and hence suffer a phenomenon known as "beam smearing". Here we explore how our measurements of galaxy rotation velocity and velocity dispersion may be affected by this process, and we derive correction factors which can be applied.

3.1 Introduction

Integral field spectroscopy has allowed us to study the spatially resolved gas dynamics, star formation and ISM properties of distant galaxies in unprecendented detail. However as with any other technique it is not immune to systematics; in particular observations of galaxy dynamics can be biased as a result of ground-based seeing. In Chapter 4 we discuss the KMOS Redshift One Spectroscopic Survey (KROSS; Stott et al. 2016) – a study of 795 $z \sim 0.9$ star-forming galaxies using the multi-object spectrograph KMOS. Each of the 24 deployable IFUs on this instrument has a spatial sampling of 0.2 arcsec, however the observations are seeing-limited, and as such we must consider the impact of

the spatial PSF (the seeing) on our measurements.

As the observations are convolved with the PSF, information from each spatial pixel is combined with that of neighbouring regions – a phenomenon known as "beam smearing". Effects of this on the observed gas kinematics are two-fold. Firstly, the spectrum at each pixel is contaminated by components of slightly higher or lower velocities, acting to broaden spectral features and increase the observed velocity dispersion. Secondly, if the blueshifted components are brighter than the redshifted components (or vice versa) the intrinsic velocity of the pixel will be shifted slightly. Globally, this results in the rotation curve appearing flatter than it may be intrinsically.

Understanding the kinematics of our sample is central to achieving the key science goals of KROSS, e.g. investigating the origins of disk turbulence and studying angular momentum. It is therefore essential that we calibrate for the effects of beam smearing. In this chapter we investigate the systematic effects of beam smearing by creating a series of mock KMOS observations. This will allow us to constrain the biases introduced and derive an efficient method of correcting for them.

3.2 Methods

To explore the impact of beam smearing on our observations we create a catalogue of $\sim 10^5$ model galaxies, with properties to uniformly sample the KROSS parameter space. For each galaxy we create two sets of mock IFU observations. First, we model what the ionised gas dynamics would look like in the absence of atmospheric turbulence (i.e. KMOS sampling the intrinsic properties of the galaxy). Second, we generate the same dynamical maps for seeing-limited observations. Differences between these two datasets allow us to understand how beam smearing affects measurements of the rotation velocity (v_C) and intrinsic velocity dispersion (σ_0), and we can learn how to correct for it.

Using scaling relations between the observed and intrinsic dynamics is one of the simplest ways to account for beam smearing (see also Burkert et al. 2016). An alternative approach would be to fit each observed data cube with a disk model convolved with the seeing (e.g. Cresci et al. 2009; Epinat et al. 2010; Genzel et al. 2014; Turner et al. 2017). This would allow us to establish full, beam smearing corrected rotation curves and

dispersion profiles; however, it is also relatively time-consuming. Measuring a characteristic rotation velocity and velocity dispersion for each galaxy is (at this point) sufficient to achieve our science goals, so this is not something we choose to explore.

It is encouraging that even though our method is simpler, results from the two approaches do appear to be consistent. For example, Burkert et al. (2016) found that for a sample of $z \sim 0.8-2.6$ galaxies observed using KMOS and SINFONI, the rotation velocities derived from a disk fitting method and a scaling relation method agree to within 10%. Similarly, Turner et al. (2017) analysed a sample of $z \sim 3.5$ galaxies observed with KMOS. They made dynamical measurements by first using a disk model, then by using the correction factors derived in this chapter (Johnson et al. 2017). They found that v_C measurements were consistent to within 10% and σ_0 measurements to within 5%.

3.2.1 Intrinsic Properties of the Model Galaxies

In the local Universe, galaxy dynamics can be described by the contribution of a rotating disk of gas and stars plus a dark matter halo, with the velocities added in quadrature as $v^2 = v_h^2 + v_d^2$. To create model galaxies we apply the same principle, making some simple assumptions about each component, following Swinbank et al. (2017). Firstly, we assume that the baryonic surface density follows an exponential profile (Freeman 1970) characterised by a disk mass (M_d) and scale length (R_d):

$$\Sigma_d(r) = \frac{M_d}{2\pi R_d^2} e^{-r/R_d}. \tag{3.2.1}$$

The contribution of this disk to the circular velocity of the galaxy is

$$v_d^2(x) = \frac{1}{2}\frac{GM_d}{R_d}(3.2x)^2(I_0K_0 - I_1K_1), \tag{3.2.2}$$

where $x = R/R_d$ and I_n, K_n are the modified Bessel functions computed at $1.6\,x$. For the halo we assume $v_h^2 = GM_h(<r)/r$ with a dark matter density profile described by a core radius (r_c) and effective core density (ρ_{dm}):

$$\rho(r) = \frac{\rho_{dm} r_c^3}{(r + r_c)(r^2 + r_c^2)}, \tag{3.2.3}$$

(Persic & Salucci 1988; Burkert 1995; Salucci & Burkert 2000). This results in a velocity profile of the form

$$v_{\rm h}^2(r) = \frac{6.4 G \rho_{\rm dm} r_{\rm c}^3}{r} \left\{ \ln\left(1+\frac{r}{r_{\rm c}}\right) - \tan^{-1}\left(\frac{r}{r_{\rm c}}\right) + \frac{1}{2}\ln\left(1+\left(\frac{r}{r_{\rm c}}\right)^2\right)\right\}. \quad (3.2.4)$$

The dark matter fraction of a galaxy ($f_{\rm dm}$) greatly influences the shape of its rotation curve, hence it is important that the dark matter properties of our model galaxies closely match those of the KROSS sample. To satisfy this, we exploit results of the "Evolution and Assembly of GaLaxies and their Environments" cosmological simulation suite (EAGLE; Schaye et al. 2015; Crain et al. 2015). These are a set of hydrodynamical simulations, including sub-grid modelling of star formation, stellar feedback, and AGN feedback. The EAGLE simulations produce galaxies which closely match the observed Universe and so provide an ideal way to estimate $f_{\rm dm}$ for our $z \sim 0.9$ sample. Considering star-forming galaxies of a similar mass ($10^9 < M_{\rm d} < 10^{11}$) and redshift ($0.8 < z < 1.0$), we find a median and 1σ range of $f_{\rm dm} = 0.75 \pm 0.10$ within the central 10 kpc (Schaller et al. 2015). From this we can infer suitable values for $\rho_{\rm dm}$.

To complete our galaxy model, we assume that the intrinsic velocity dispersion of ionised gas (σ_0) is uniform across the disk and that the distribution of Hα (the emission line from which we measure the kinematics) is exponential. Following the results of Nelson et al. (2016) we assume that the Hα emission is more extended than the stellar continuum, with $R_{\rm H\alpha} \sim 1.1\, R_{\rm d}$. How we define the distribution of light is significant, since beam smearing effects are luminosity weighted. Star forming galaxies at $z \sim 1$ often appear irregular or "clumpy" in Hα emission and so in §3.5.2 we explore how this may impact our results.

From this simple prescription we create a series of intensity maps, velocity maps and velocity dispersion maps for model galaxies with similar properties to those in the KROSS sample. We vary the disk mass, disk scale length, inclination, dark matter fraction and intrinsic velocity dispersion as follows:

- $9.0 \leq \log(M_{\rm d}\ /\ {\rm M}_\odot) \leq 11.2$; steps of 0.15
- $0.5 \leq R_{\rm d} \leq 2.5$ kpc; steps of 0.25 kpc
- $20 \leq \theta \leq 70$ deg; steps of 5 degrees

- $0.65 \leq f_{\rm dm} \leq 0.85$; steps of 0.10
- $20 \leq \sigma_0 \leq 80\,{\rm km\,s^{-1}}$; steps of $10\,{\rm km\,s^{-1}}$

3.2.2 Mock IFU Observations

After defining the intrinsic properties of a given galaxy, we wish to understand how these same dynamics may appear under ground-based seeing conditions. To model this, we generate a mock observation of the galaxy, forming a KMOS data cube which we can then convolve with the seeing PSF. While the pixel scale of this cube is set to match that of our observations (a spatial resolution of 0.1 arcsec), we choose to retain a high *spectral* resolution ($R \sim 10{,}000$) and omit instrument noise. This allows us to attribute any difference between the model and "observed" data to beam smearing alone. The $x-y$ footprint of the array is initially also larger than the 2.8×2.8 arcsec size of the KMOS IFU, to allow for light outside of this region which may be introduced to the IFU pixels via beam smearing.

At each pixel we create a spectrum consisting of the Hα emission line and [NII] doublet, assuming that each line is described by a Gaussian profile with a linewidth set by the dispersion and a redshift set by the rotation velocity at that position. For simplicity, we adopt a fixed Hα/[NII] ratio and set the flux ratio of the [NII]$\lambda\lambda$6548, 6583 doublet to be 3.06 (Osterbrock & Ferland 2006). To simulate the effects of beam smearing we then convolve each wavelength slice with the spatial PSF. We model a range of atmospheric conditions, with $\mathrm{FWHM_{seeing}} = 0.5-0.9$ arcsec in increments of 0.1 arcsec, and assume a Gaussian PSF (the transfer functions of the atmosphere, telescope and instrument are all approximately Gaussian[1]). The median for our KROSS observations is 0.7 arcsec, with a standard deviation of 0.17 arcsec, so this range encompasses the data well. Finally, we extract a subsection of the array to match the size of the KMOS IFU. This is the "observed" data cube on which we perform our analysis.

To generate dynamical maps from the beam-smeared cube we fit the emission lines at each pixel using the same χ^2 minimisation method as for the KROSS data. We require that all lines are Gaussian profiles and share the same linewidth, with the relative positions

[1] https://www.eso.org/observing/etc/doc/helpkmos.html

of the lines and [NII] flux ratio fixed to their model values. These constraints leave the Hα and [NII] intensity, centroid and line width free to vary. Since our model does not include noise, spatial binning is not necessary, however we explore how this process may affect results in §3.5.1. Finally, we extract the rotation curve and one-dimensional dispersion profile of each galaxy. To do so we take the median value of pixels along a 0.7 arcsec pseudo-slit along the major kinematic axis.

3.2.3 Kinematic Measurements

In order to quantify the effects of beam smearing, we measure the kinematics in the same way as for the KROSS sample (Harrison et al. 2017 and Chapter 4). Each rotation curve is fit by an exponential disk model of the form

$$v(r)^2 = \frac{r^2 \pi G \mu_0}{R_{\rm d,fit}} (I_0 K_0 - I_1 K_1) + v_{\rm off}, \tag{3.2.5}$$

where r is the radial distance, μ_0 is the peak mass surface density, $R_{\rm d,fit}$ is the disk radius, $v_{\rm off}$ is the velocity at the kinematic centre, and $I_n K_n$ are Bessel functions evaulated at $\frac{1}{2}\, r/R_{\rm d,fit}$. We use this model to interpolate through the data and measure the velocity at a given radius. Other kinematic surveys define the characteristic rotation velocity in a number of different ways, depending on their goals. We therefore wish to understand how beam smearing may affect our results as a function of radius. Using the input value of $R_{\rm d}$ for each model we measure velocities at $2.2R_{\rm d}$ and $3.4R_{\rm d}$, two radii frequently used within the literature. The first of these coincides with the peak rotation velocity of an ideal exponential disk, while the second probes outer regions of the galaxy, where we expect the rotation curve to have flattened. We also measure the rotation velocity at the same radii convolved with the seeing, i.e. $2.2R_{\rm d,conv}$, $3.4R_{\rm d,conv}$.

To characterise the velocity dispersion we record the median of the one-dimensional dispersion profile for $R > 3.4R_{\rm d}$ and the median of all pixels within the map. Although our simulated galaxies are constructed such that it is possible to make both measurements, for 56% of KROSS galaxies it is only possible to make the latter (due to poor signal-to-noise). Hence it is important to understand both parameters. Since beam smearing is expected to be strongest towards the dynamical centre, the median dispersion will likely depend on the

maximum radii of detected pixels. We therefore measure the median velocity dispersion of pixels within both a $2R_{\rm d}$ and $3R_{\rm d}$ aperture, to see how this varies our results.

3.3 Results

3.3.1 Dynamical Maps

Before we perform a more rigorous analysis, quantifying the effects of beam smearing using the variables defined in §3.2.3, we already notice several trends in the dynamical maps. In Fig. 3.1 – 3.3 we show the dynamical maps, rotation curves and velocity dispersion profiles of 12 model galaxies, where input parameters are kept fixed except for mass (Fig. 3.1), inclination angle (Fig. 3.2) or seeing (Fig. 3.3). We compare the intrinsic kinematics to those recovered after the data cube has been convolved with the spatial PSF. While the extent of the beam smearing depends on the input parameters, the effects are broadly similar in each case. The observed velocity map appears smoother and the observed rotation curve (in black) is flatter than the intrinsic rotation curve (in red), particularly close to the dynamical centre. The beam smeared rotation curve also peaks at a lower maximum velocity. Finally, the observed dispersion map is no longer uniform, and we now see a characteristic rise in the region of the steepest velocity gradient.

Fig. 3.1 explores the relationship between disk mass and beam smearing, and we show four models which are identical apart from their mass. We increase the disk mass over the range $\log(M_{\rm d}\,/\,{\rm M}_{\odot}) = 9.9 - 10.8$ and find that the beam smearing effect becomes more apparent at each interval. As the disk mass increases the velocity gradient across the disk becomes larger, hence the components combined by the PSF have a greater velocity difference. The effect of this is that the peak of the observed velocity dispersion profile increases from $\sigma_{\rm out} \sim 70\,{\rm km\,s^{-1}}$ in the low mass galaxy, to $\sigma_{\rm out} \sim 160\,{\rm km\,s^{-1}}$ in the high mass example.

In Fig. 3.2 we use the same fiducial model as in Fig. 3.1, however this time fix the mass as $\log(M_{\rm d}\,/\,{\rm M}_{\odot}) = 10.2$ and vary the inclination from 30 to 60 degrees. This figure shows that the more inclined the disk, the greater the beam smearing effect. As the disk approaches edge-on the iso-velocity contours of the map are "pinched" together more closely, an effect similar to increasing the disk mass.

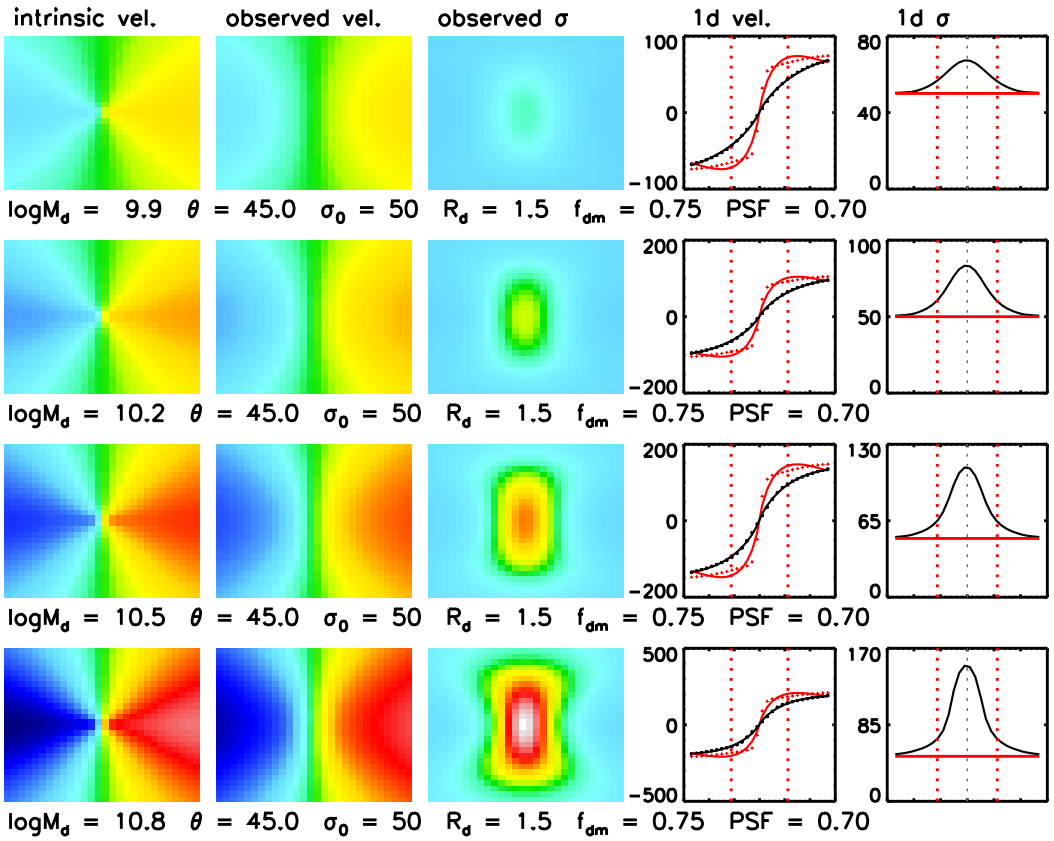

Figure 3.1: Dynamical maps for a subset of $\sim 10^5$ model galaxies created to explore the impacts of beam smearing. We investigate how closely we can recover the intrinsic rotation velocity and velocity dispersion of a galaxy as a function of disk mass. In successive rows we increase the mass of the model, while keeping all other input parameters fixed. An increase in mass results in a steeper velocity gradient across the disk. This leads to a stronger beam smearing effect, with a larger peak in the observed velocity dispersion. *Left to right*: intrinsic velocity map, observed velocity map, observed velocity dispersion map, and the rotation curve and line-of-sight dispersion profile extracted along the major kinematic axis before (solid red line) and after (black) convolution with the seeing. Dashed red lines show a radius of $3.4R_{\rm d}$. On each row we list the model input parameters where $M_{\rm d}$ is disk mass ($\mathrm{M}_\odot$), θ inclination (degrees), σ_0 intrinsic velocity dispersion ($\mathrm{km\,s^{-1}}$), $R_{\rm d}$ disk radius (kpc), $f_{\rm dm}$ dark matter fraction within 10 kpc, and PSF the FWHM of the seeing (arcsec). Each velocity map is scaled between -250 and $250\,\mathrm{km\,s^{-1}}$, and each dispersion map between 0 and $(\sigma_0{+}100)\,\mathrm{km\,s^{-1}}$.

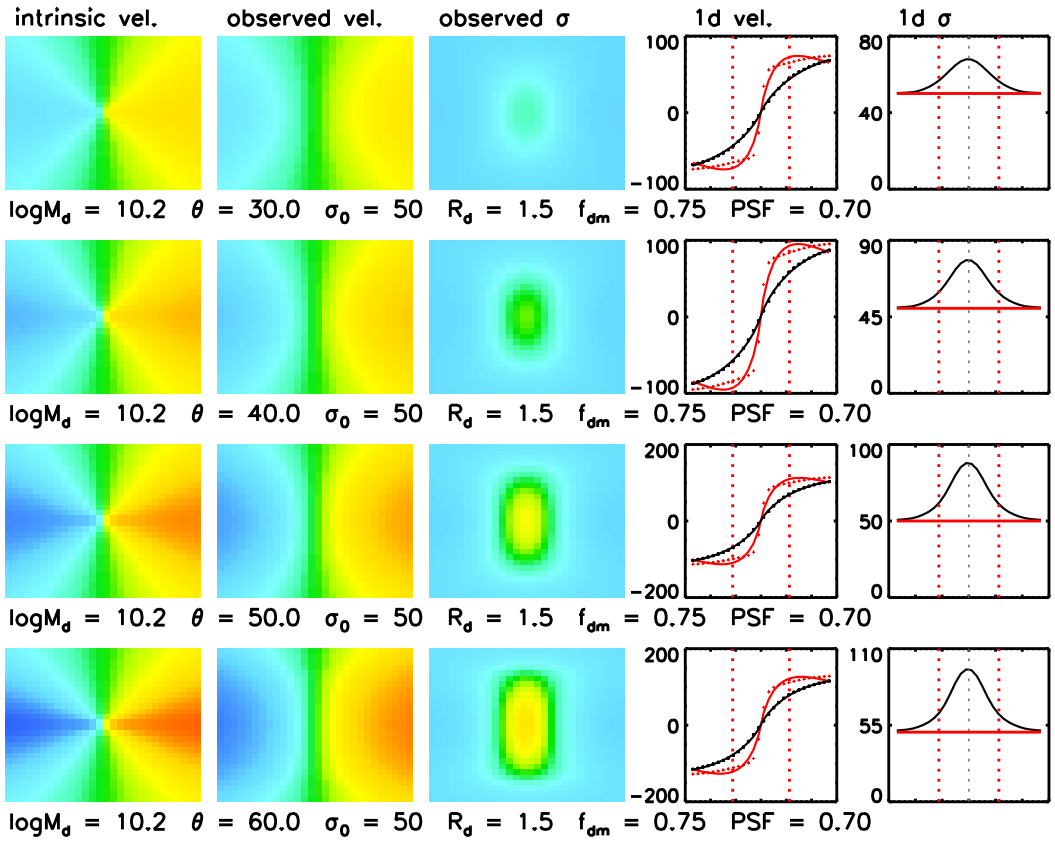

Figure 3.2: Example dynamical maps and velocity profiles with properties as described in Fig. 3.1. *Left to right*: intrinsic velocity map, observed velocity map, observed velocity dispersion map, rotation curve and line-of-sight dispersion profile. In successive rows we increase the inclination of the model while all other input parameters remain fixed. As the disk is tilted towards edge-on, the maximum velocity of the rotation curve increases and the contours of the velocity map are pushed closer together (with a characteristic "spider diagram" shape). A steeper velocity gradient results in a stronger beam smearing effect. The more highly inclined the disk, the larger the peak in the observed velocity dispersion profile.

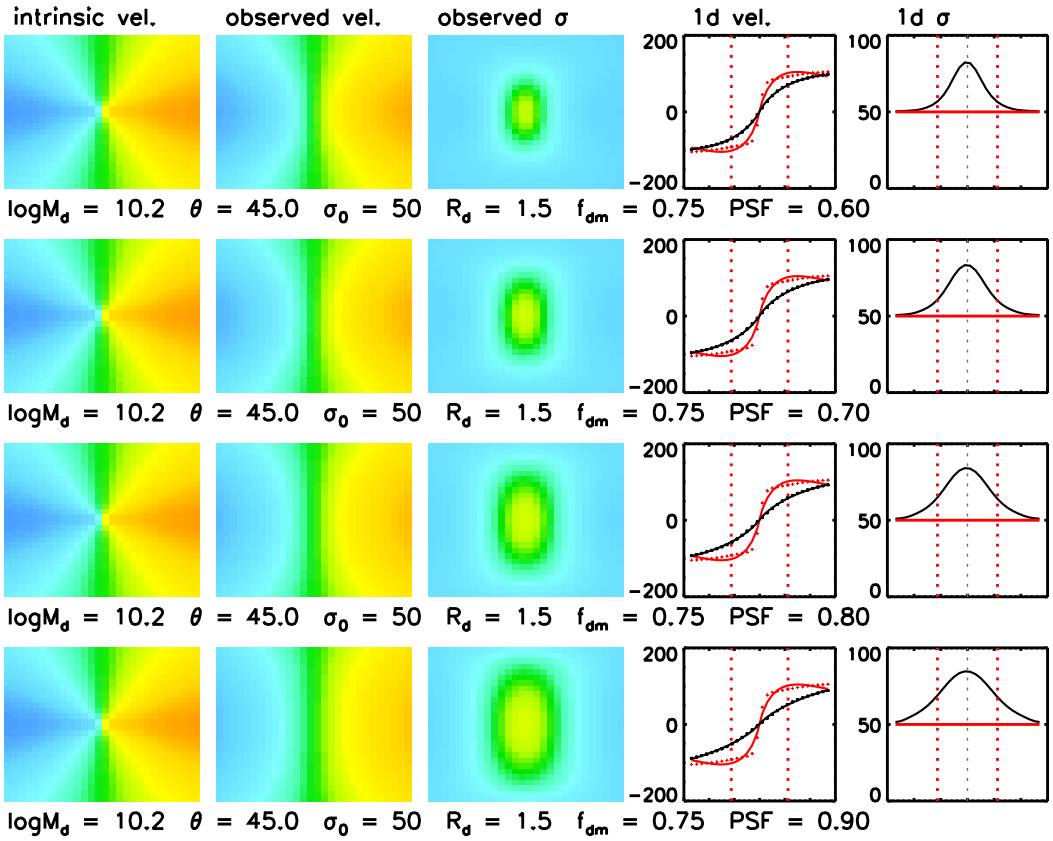

Figure 3.3: Dynamical maps and velocity profiles with properties as described in Fig. 3.1. *Left to right*: intrinsic velocity map, observed velocity map, observed velocity dispersion map, rotation curve and line-of-sight dispersion profile. In successive rows we increase the spatial PSF (the seeing) of the model while all other input parameters remain fixed. Poorer atmospheric conditions result in a stronger beam smearing effect. As the seeing is increased, the observed velocity gradient becomes shallower, structure in the velocity map is less visible and the peak in the observed velocity dispersion becomes broader. While at 0.6 arcsec the dispersion measured in the outskirts of the galaxy (beyond $3.4R_{\rm d}$, shown by the dashed red lines) is close to the intrinsic value, at 0.9 arcsec this is a significant overestimate.

Finally, Fig. 3.3 demonstrates the effect of broadening the spatial PSF. We increase the seeing from 0.6 arcsec to 0.9 arcsec and study the impact this has on the observed rotation velocity and velocity dispersion. As with an increase in disk mass or disk inclination, poorer atmospheric conditions result in a rotation curve which is shallower than it would be intrinsically. However, while the most noticeable effect of increasing the inclination or disk mass is to increase the peak of the dispersion profile, the same is not true of the seeing. An increase in the seeing instead acts to *broaden* the dispersion profile. At a seeing of 0.6 arcsec the intrinsic dispersion can be recovered at a radius of $\sim 3.4\,R_{\rm d}$, but for a seeing of 0.9 arcsec the required radius is approximately double.

3.3.2 Impact of Model Parameters

As discussed in §3.3.1, from visual inspection of the dynamical maps it is already possible to identify several trends between model input parameters and the impact of beam smearing. However we now wish to quantify these effects such that we can apply corrections to our kinematic measurements of KROSS galaxies.

Galaxies which are small in comparison to the PSF are more affected by beam smearing (Fig. 3.3), and the shape of the rotation curve and ability to recover σ_0 in the outskirts of the galaxy deteriorate rapidly as the seeing is increased. Since this is perhaps the strongest universal trend, we choose to study how our measurements of rotation velocity and velocity dispersion are affected as a function of $R_{\rm d}/R_{\rm PSF}$, where $R_{\rm PSF}$ is half of the FWHM of the spatial PSF. To assess the impact of other variables relative to this, we then bin the data in terms of disk mass (Fig. 3.4), inclination (Fig. 3.5), dark matter fraction (Fig. 3.6) and intrinsic dispersion (Fig. 3.7).

In each figure we demonstrate how four measurements are impacted by beam smearing: the rotation velocity ($v_{\rm out}$) at $3.4R_{\rm d}$, the rotation velocity at the same radius convolved with the seeing, the median of the velocity dispersion profile at radii greater than $3.4R_{\rm d}$ ($\sigma_{\rm out}$), and the median of the velocity dispersion map within a $3R_{\rm d}$ aperture ($\sigma_{\rm out,med}$). Measurements made at smaller radii result in the same trends but with a systematic offset. We will discuss this further in §3.4.1.

The tracks in Fig. 3.4 – 3.7 confirm many of our conclusions in §3.3.1. That is, for low values of $R_{\rm d}/R_{\rm PSF}$ (i.e. galaxies which are small compared to the spatial PSF), the rotation

velocity we recover is an underestimate of the intrinsic value. Nevertheless, as the model galaxy is increased in size (or the seeing is decreased) we approach $v_{out}/v_0 = 1$. When extracting measurements from the rotation curve at $3.4R_d$, a ratio of $R_d/R_{PSF} = 0.2$ results in an average underestimate of a factor of two. However, this effect is less significant when we measure at the same radius convolved with the seeing. Here the rotation velocity is only underestimated by $\sim 10\,\%$ at $R_d/R_{PSF} = 0.2$. In Fig. 3.1 – 3.3 we can see why this may be so; it is the innermost regions of the rotation curve which are most affected by beam smearing.

In the lower two panels of Fig. 3.4 – 3.7 we can see that beam smearing affects our ability to recover the intrinsic velocity dispersion even more strongly. The lower the R_d/R_{PSF} ratio, the more we overestimate the intrinsic velocity dispersion. However, measuring the velocity dispersion in the outskirts of the disk is a much better estimate than calculating the median of all pixels in the dynamical map. This is because the beam smearing effects are strongest in regions of steep velocity gradients (i.e. towards the dynamical centre of a uniformly rotating disk). Using the "outskirts" method we measure $\sigma_{out}/\sigma_0 = 1.0 - 1.5$, as opposed to $\sigma_{out,med}/\sigma_0 = 1.0 - 4.0$ for the "median" method.

Coloured tracks in these figures show the results for models with one particular input parameter fixed and all others allowed to vary. The shaded region shows the 1σ (16-84th percentile) range of all 10^5 models. In Fig. 3.4 we see that higher mass galaxies result in estimates of rotation velocity closer to the intrinsic value, since their rotation curve peaks more quickly, but the systematic offset in σ_0 is larger due to the steeper velocity gradient. The tracks of fixed disk mass cover the full 1σ range of the data, suggesting that mass is an important parameter.

As discussed in §3.3.1, galaxy models of a higher inclination are more susceptible to beam smearing (Fig. 3.5). However the difference between the track for inclinations below 30 degrees and the track for inclinations greater than 60 degrees is small, suggesting this effect is secondary to that caused by increasing the disk mass. The same is true for models of different dark matter fractions (Fig. 3.6). Nonetheless, it is interesting to note that galaxies with a higher dark matter fraction suffer more beam smearing. We suggest that this is because the dark matter fraction determines the degree of turn-over in the rotation curve, which in turn affects the velocity gradient across pixels in the outer regions

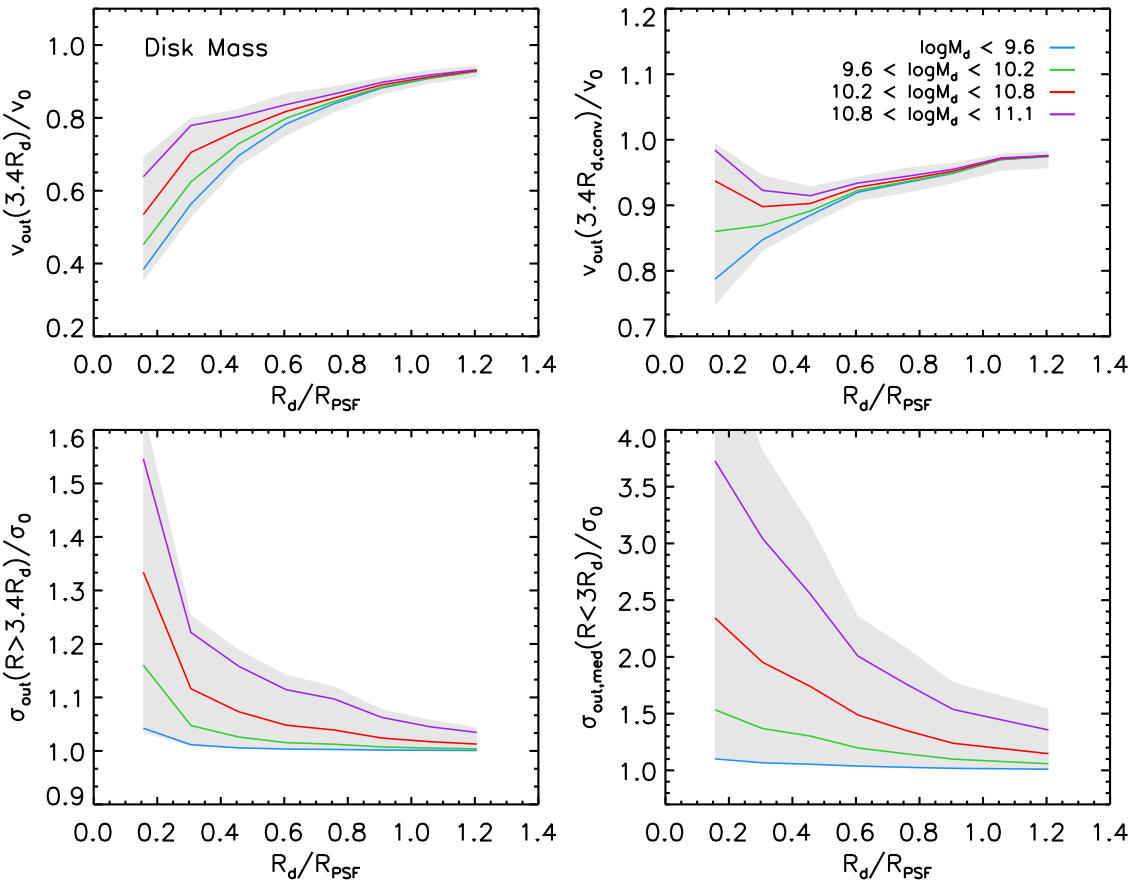

Figure 3.4: The impact of beam smearing on measurements of rotation velocity and velocity dispersion, as a function of disk mass. $R_\mathrm{d}/R_\mathrm{PSF}$ is the ratio between the disk radius and the half of the FWHM of the PSF, which determines which velocity components are combined by the seeing and thus the extent of the beam smearing. We split models into four mass bins and plot a running median for each (solid lines). Shaded regions represent the 1σ scatter of all models. The disk mass appears to account for most, if not all, of this variation. *Top Left:* Model velocity at $3.4R_\mathrm{d}$ as a fraction of the intrinsic value (v_0). The lower the $R_\mathrm{d}/R_\mathrm{PSF}$ and the lower the disk mass, the more we underestimate the intrinsic rotation velocity. *Top Right:* Velocity at the same radius convolved with the seeing. This is a better estimate of $v_0(3.4R_\mathrm{d})$, with at most a 20% difference. *Bottom Left:* Median of the velocity dispersion profile beyond $3.4R_\mathrm{d}$ as a fraction of the intrinsic value (σ_0). The lower the $R_\mathrm{d}/R_\mathrm{PSF}$ and larger the disk mass, the more we overestimate the dispersion, with up to a 50% difference. *Bottom Right:* The median dispersion within an aperture of $3R_\mathrm{d}$. This measurement is more susceptible to beam smearing, with overestimates of up to a factor of four.

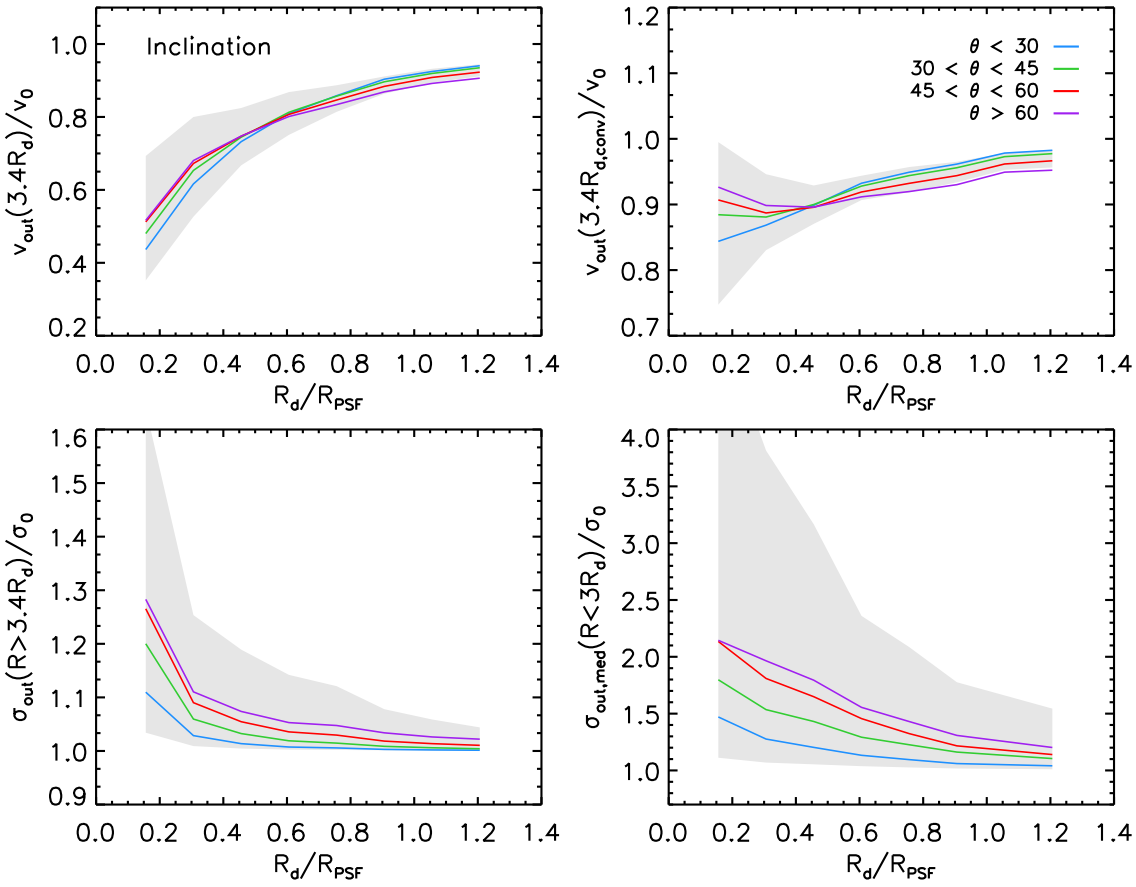

Figure 3.5: The impact of beam smearing on measurements of rotation velocity and velocity dispersion, as a function of disk inclination. *Top Left:* The lower the $R_{\rm d}/R_{\rm PSF}$, the more we underestimate the intrinsic rotation velocity (v_0). The extent of this difference is very similar for models of different inclinations (typically within 5%). *Top Right:* We extract the observed rotation velocity at the same radius convolved with the seeing. This results in a better estimate, but varying the disk inclination has very little impact. *Bottom Left:* The lower the $R_{\rm d}/R_{\rm PSF}$ and the more inclined the disk, the more we overestimate the intrinsic velocity dispersion. Differences between a low inclination model (< 30 degrees) and a high inclination model (> 60 degrees) are small ($\sim 10\%$) and cannot account for the full 1σ scatter of the data (shaded region). The trend between disk mass and beam smearing appears to be more dominant. *Bottom Right:* If we estimate the velocity dispersion from a median of the map, as opposed to the outskirts of the dispersion profile, we overestimate σ_0 by almost twice as much.

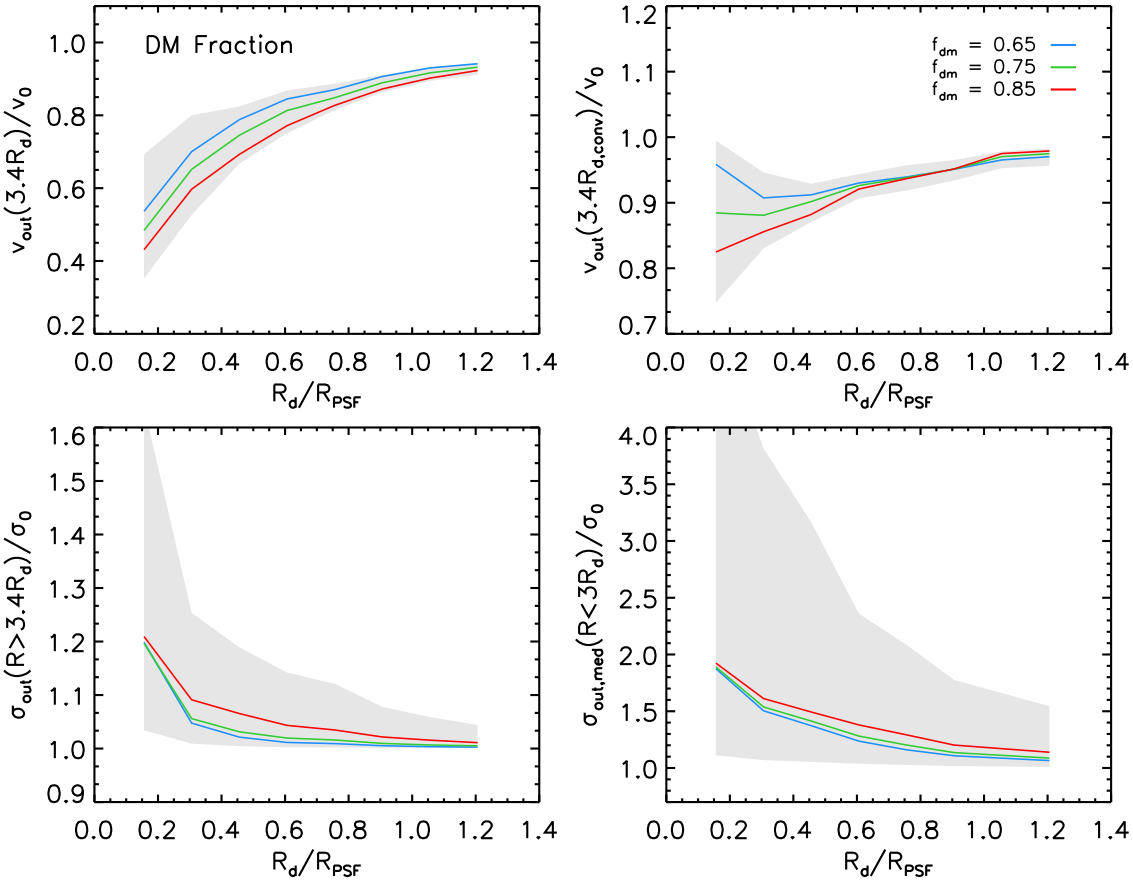

Figure 3.6: The impact of beam smearing on measurements of rotation velocity and velocity dispersion, as a function of the dark matter fraction within a radius of 10 kpc. *Top Left:* The lower the $R_{\rm d}/R_{\rm PSF}$ and the larger the dark matter fraction, the more we underestimate the intrinsic rotation velocity (v_0). There is approximately a 10% difference between $f_{\rm dm} = 0.65 - 0.85$. Adjusting the dark matter fraction changes the shape of the rotation curve in the outer regions (more or less of a "turn-over"), hence the velocity components merged by the seeing will be slightly different. *Top Right:* We extract the observed rotation velocity at the same radius convolved with the seeing. This results in a better estimate. For low $R_{\rm d}/R_{\rm PSF}$ the difference in $f_{\rm dm}$ models is 5-10%, but for $R_{\rm d}/R_{\rm PSF} > 0.6$ the models converge. *Bottom Left:* The lower the $R_{\rm d}/R_{\rm PSF}$, the more we overestimate the intrinsic velocity dispersion. The difference between models of $f_{\rm dm} = 0.65$ and models of $f_{\rm dm} = 0.85$ is extremely small (a few percent). *Bottom Right:* If we estimate the velocity dispersion from a median of the map, as opposed to the outskirts of the dispersion profile, we overestimate σ_0 by almost twice as much. Again, the dark matter fraction appears to have little impact on this aspect of beam smearing.

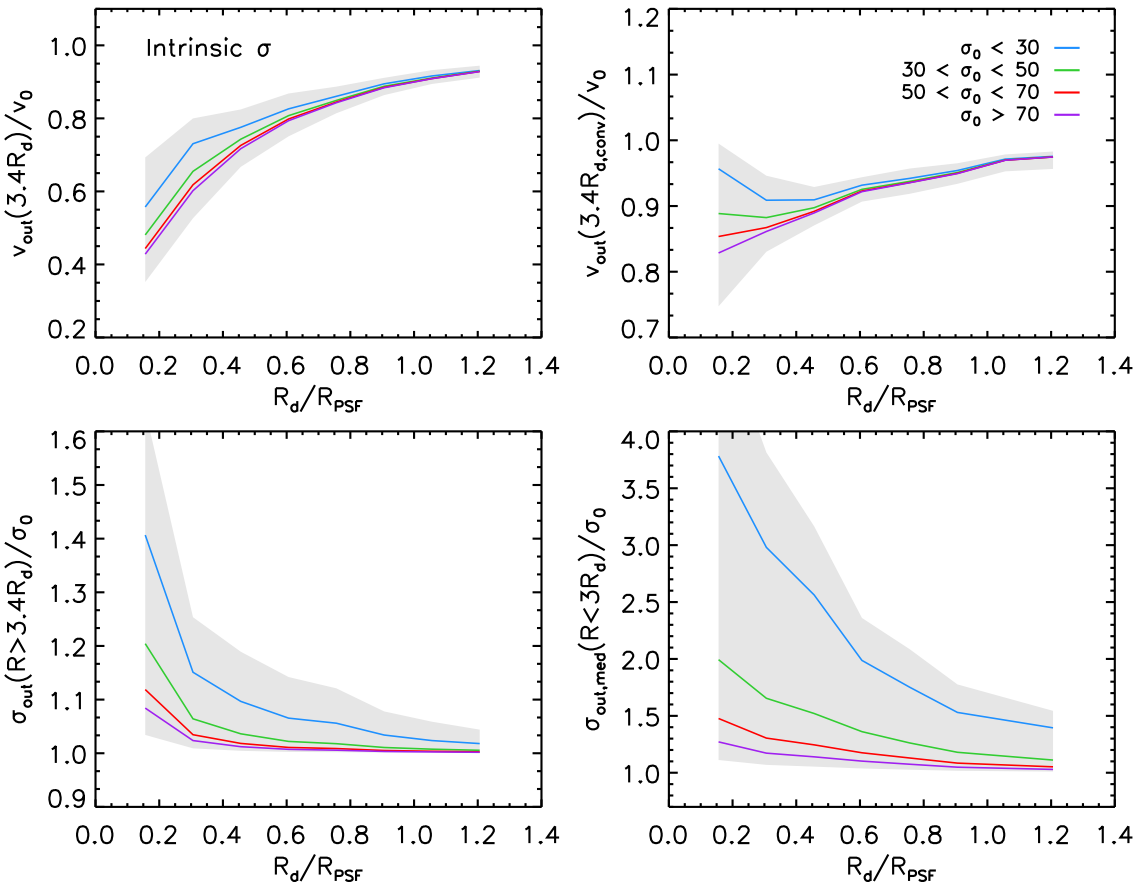

Figure 3.7: The impact of beam smearing on measurements of rotation velocity and velocity dispersion, as a function of input velocity dispersion. *Top Left:* The lower the R_d/R_{PSF} and the greater the input dispersion of the model, the more we underestimate the intrinsic rotation velocity (v_0). The difference between model galaxies of $\sigma_0 = 30\,km\,s^{-1}$ and $\sigma_0 = 70\,km\,s^{-1}$ is $\sim 10\%$ at low R_d/R_{PSF}, but the models converge as R_d/R_{PSF} increases. *Top Right:* We extract the observed rotation velocity at the same radius convolved with the seeing. This results in a better estimate. Again, results for the binned data converge beyond $R_d/R_{PSF} = 0.6$. *Bottom Left:* The lower the R_d/R_{PSF}, the more we overestimate the intrinsic velocity dispersion. The difference between model galaxies of $\sigma_0 = 30\,km\,s^{-1}$ and $\sigma_0 = 70\,km\,s^{-1}$ is as much as $\sim 30\%$. How well we can recover the intrinsic velocity dispersion appears to be strongly dependent on what its value was to begin with. *Bottom Right:* If we estimate the velocity dispersion from a median of the map, as opposed to the outskirts of the dispersion profile, it is more difficult to recover σ_0. For very low dispersions ($\sigma_0 < 30\,km\,s^{-1}$) the beam smearing effect is as strong as for very high mass galaxies ($10.8 < \log(M_d/M_\odot) < 11.1$), with σ_0 overestimated by a factor of four at low R_d/R_{PSF}.

of the galaxy.

Finally, we explore the impact of adjusting the intrinsic velocity dispersion of the model (Fig. 3.10). We find that the lower the input dispersion, the more successful we are in recovering the true rotation velocity. However the opposite is true of the velocity dispersion itself. For very low dispersions ($\sigma_0 < 30\,\mathrm{km\,s^{-1}}$) the beam smearing effect is as strong as for very high mass galaxies ($10.8 < \log(M_\mathrm{d}/\mathrm{M}_\odot) < 11.1$). This is because the ratio of $(\sigma_\mathrm{out} - \sigma_0)/\sigma_0$ is larger.

3.4 Beam Smearing Corrections

In §3.3.2 we found that adjusting the input parameters our model galaxies can lead to a stronger or weaker beam smearing effect. Now that we understand these systematics, we wish to derive a series of corrections which can be applied to our kinematic measurements of the KROSS sample. In this section we discuss how best this can be achieved.

3.4.1 Measurements of Rotation Velocity

In Fig. 3.4 – 3.7 (top left panel) we plot the relationship between v_out/v_0 and $R_\mathrm{d}/R_\mathrm{PSF}$. The systematic offset between the input and output rotation velocity is strongly correlated with how large the galaxy is compared to the seeing. Values range between $v_\mathrm{out}/v_0 = 0.5 - 0.9$. However if we make measurements at the same radii convolved with the seeing (top right panel) this relation is less steep, with a range of only $v_\mathrm{out}/v_0 = 0.85 - 0.95$. This is therefore the method we decide to use for the KROSS sample. We note that if we had instead measured the velocity at $2.2R_\mathrm{d}$ (a radius commonly used by other kinematic surveys) the results follow a similar trend, with a small ($\lesssim 5\%$) shift towards lower ratios of v_out/v_0.

While varying model parameters such as disk mass (Fig. 3.4) and inclination (Fig. 3.5) introduces scatter in v_out/v_0, at the median $R_\mathrm{d}/R_\mathrm{PSF}$ of the KROSS sample (~ 0.75) these effects are of the order of a few percent. Moreover, one of the most dominant influences on the ratio of v_out/v_0 is the dark matter fraction, f_dm, which we are unable to constrain from our observations. In order to correct the KROSS rotation velocities for beam smearing we therefore consolidate the information from our models into a single relation for each of

$v_{\rm out}(3.4R_{\rm d})$ and $v_{\rm out}(2.2R_{\rm d})$. We define each correction track as the median outcome of all models, with uncertainties to reflect the 1σ scatter. Data points are fit by an exponential of the form

$$1/\xi_v = v_{\rm out}/v_0 = 1 - Ae^{-B(R_{\rm d}/R_{\rm PSF})^C}, \tag{3.4.6}$$

where ξ_v is the velocity correction factor and A, B and C are constants defined in Table 3.1. An exponential profile was chosen since when a galaxy is very large compared to the seeing, we expect to recover the instrinsic rotation velocity (i.e. $v_{\rm out}/v_0 = 1$). The exact functional form was chosen by trial-and-error, trying to achieve a close fit to the data while minimising the number of free parameters. Final tracks for beam smearing corrections to the rotation velocity are presented in Fig. 3.8.

3.4.2 Measurements of Velocity Dispersion

The effects of beam smearing on measurements of the intrinsic velocity dispersion ($\sigma_{\rm out}$) are generally more significant than for the rotation velocity. In Fig. 3.4 – 3.7 (bottom left, bottom right) we see that for galaxies small in comparison to the spatial PSF (i.e. for low $R_{\rm d}/R_{\rm PSF}$) the dispersion in the outskirts of the disk can be a factor of ~ 1.5 higher than the intrinsic value. Estimates made using the median of the map may be as large as $\sigma_{\rm out}/\sigma_0 = 5$. However for larger galaxies (or a smaller spatial PSF) $\sigma_{\rm out}/\sigma_0$ appears to decrease exponentially.

Binning the data in Fig. 3.4 – 3.7 by disk mass, inclination, dark matter fraction and intrinsic dispersion reveal that the input parameters of the model have a significant impact on how we measure the velocity dispersion. At the median $R_{\rm d}/R_{\rm PSF}$ of our KROSS sample, the difference between high mass and low mass models (for measurements made in the outskirts of the dispersion profile) is $\Delta(\sigma_{\rm out}/\sigma_0) \sim 0.1$. The difference between high inclination and low inclination disks is $\Delta(\sigma_{\rm out}/\sigma_0) \sim 0.05$. Changes to $f_{\rm dm}$ or the input σ_0 itself have the least impact (unless σ_0 is very small i.e. $< 30\,{\rm km\,s^{-1}}$), with an average difference of only a few percent.

Given the strong variation seen in our models, it is clear that we cannot reduce the beam smearing correction to a single track for each of the dispersion measurements ("outer" and "median" methods). Instead, we choose to make corrections as a function of $v_{\rm out}(3.4R_{\rm d,conv})$, the rotation velocity measured at a radius of $3.4R_{\rm d}$ convolved with the

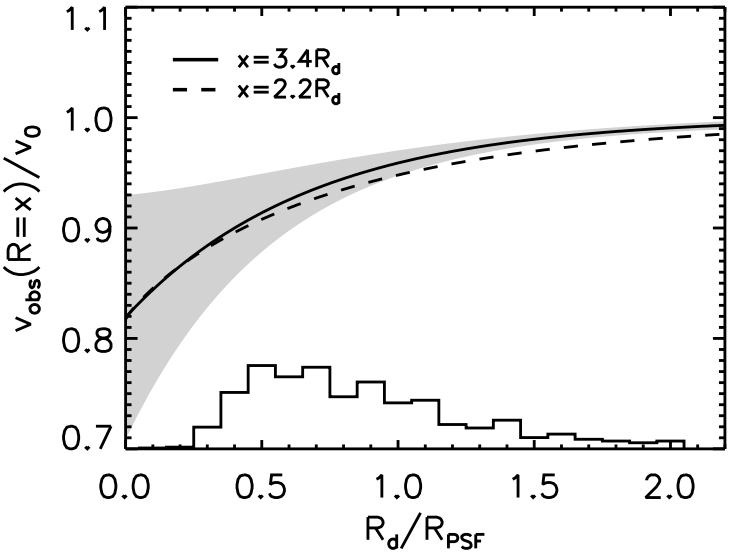

Figure 3.8: Beam smearing correction to be applied to measurements of rotation velocity at 3.4 and $2.2R_{\rm d}$ (solid and dashed lines, respectively) as a function of $R_{\rm d}/R_{\rm PSF}$. The shaded region represents the 1σ scatter of outcomes for $\sim 10^5$ mock galaxies (shown only for when measured at $3.4R_{\rm d}$). Tracks represent the median of these outcomes and are defined by Eq. 3.4.6 and the parameters listed in Table 3.1. The histogram along the x-axis represents the $R_{\rm d}/R_{\rm PSF}$ distribution of the KROSS sample.

seeing, before inclination corrections (hereafter $v_{\rm out}$). This combines the effects of both disk mass and inclination. For each method, we split the data into $50\,{\rm km\,s^{-1}}$ bins of $v_{\rm out}$ and calculate a series of running medians.

Models run with $\sigma_0 < 30\,{\rm km\,s^{-1}}$ exhibit as much beam smearing as high mass models, however we are obviously unable to make corrections as a function of σ_0 (it is what we are trying to measure!). To account for the effect the intrinsic dispersion has on the beam smearing, we instead resample the model data such that the distribution of *observed* velocity dispersions ($\sigma_{\rm out}$) matches that of KROSS, and we refit the correction tracks.

As discussed in §3.2.3, we measured the median velocity dispersion of each model within two apertures ($2R_{\rm d}$ and $3R_{\rm d}$) since the size of the galaxy compared to the IFU, or the surface brightness of the galaxy (hence signal-to-noise) will affect the number of available pixels. Fig. 3.9 compares these two sets of results. If the observed rotation velocity is small ($v_{\rm out} < 100\,{\rm km\,s^{-1}}$) corrections at the median $R_{\rm d}/R_{\rm PSF}$ of KROSS range between $\sigma_{\rm out,med}/\sigma_0 = 1.0-1.3$ and the difference between results for the two apertures is typically $\sigma_{\rm out,med}/\sigma_0 < 0.1$. If the rotation velocity exceeds this then corrections for the larger and smaller apertures are $\sigma_{\rm out,med}/\sigma_0 = 1.8$ and 2.2 respectively. However fewer

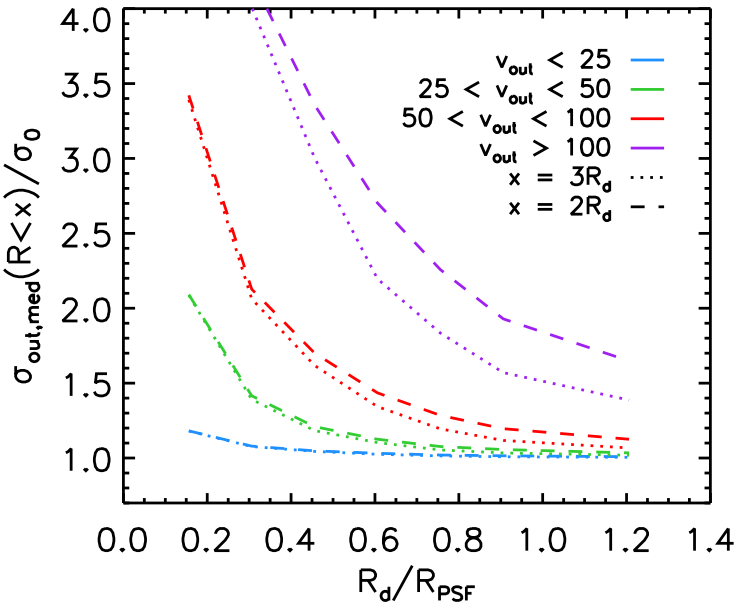

Figure 3.9: Factor by which the intrinsic velocity dispersion is overestimated when measuring the pixel-by-pixel median within a $3R_{\rm d}$ (dotted lines) or $2R_{\rm d}$ (dashed lines) aperture. If the observed rotation velocity of the galaxy is small then the two estimates are almost identical (within 10%). For higher velocities ($v_{\rm out} > 100\,{\rm km\,s^{-1}}$) corrections for the larger and smaller apertures at the median $R_{\rm d}/R_{\rm PSF}$ of KROSS are $\sigma_{\rm out,med}/\sigma_0 = 1.8$ and 2.2 respectively. However fewer than 25% of our sample have velocities this large. We therefore create final correction tracks (Fig. 3.10) based on the results for a $3R_{\rm d}$ aperture.

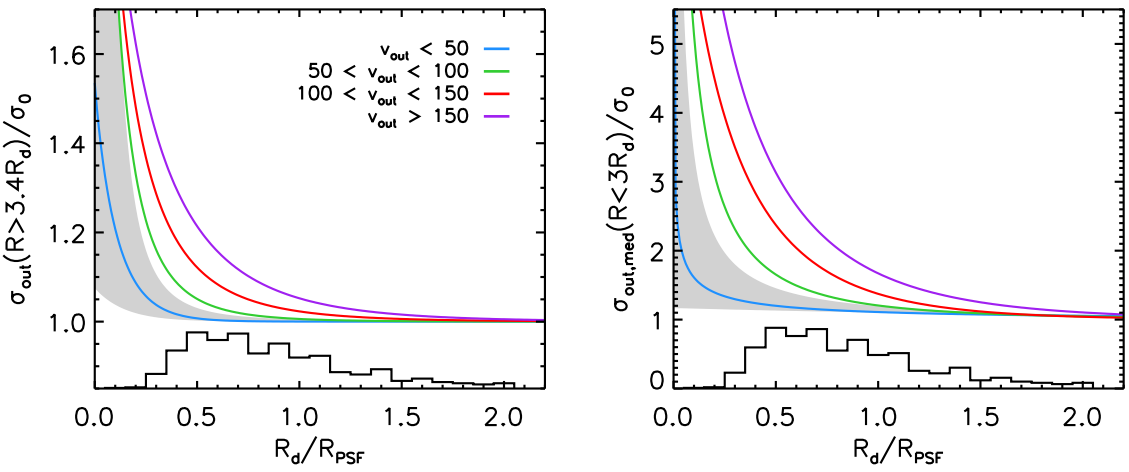

Figure 3.10: Beam smearing corrections for measurements of velocity dispersion, as a function of observed rotation velocity ($v_{\rm out}$). Tracks were derived by simulating observations of $\sim 10^5$ model galaxies with a uniform dispersion (σ_0) disk. We fit a running median to the results projected over all other input parameters. Each track is defined by Eq. 3.4.7 and parameters in Table 3.1. Shaded regions show the 1σ scatter of models in each velocity bin, and the histograms show the $R_{\rm d}/R_{\rm PSF}$ distribution of the KROSS sample. Note the different scales on the y-axes. *Left:* Velocity dispersion as measured in the outskirts ($R > 3.4R_{\rm d}$) of the 1d profile, as a fraction of the intrinsic dispersion. *Right:* Dispersion as measured from a median of all pixels within an aperture of $3R_{\rm d}$.

Table 3.1: Parametrisation of beam smearing correction tracks

Correction Track	$v_{\rm min}$ (km s^{-1})	$v_{\rm max}$ (km s^{-1})	A	B	C
Velocity ($3.4R_{\rm d}$)	-	-	0.18	1.48	1.00
Velocity ($2.2R_{\rm d}$)	-	-	0.18	1.26	0.88
Dispersion (outskirts)	0	50	0.53	8.22	0.94
	50	100	6.98	7.07	0.52
	100	150	3.27	4.96	0.59
	150	-	2.06	3.67	0.70
Dispersion (median)	0	50	11.50	4.65	0.20
	50	100	52.85	5.55	0.34
	100	150	8.74	3.15	0.77
	150	-	14.15	3.05	0.69

NOTES: Constants A, B, C for the beam smearing correction tracks in Fig. 3.8 and 3.10, as defined by Eq. 3.4.6 and 3.4.7. For the velocity dispersion, $v_{\rm min}$ and $v_{\rm max}$ are the minimum and maximum observed rotation velocities (uncorrected for inclination) that each track covers.

than 25% of our sample have velocities this large. We therefore combine the results into a single set of (velocity binned) tracks. We find that a function similar to Eq. 3.4.6 provides a good description of the data. Hence the correction $\sigma_{\rm out}$ to σ_0 as a function of $R_{\rm d}/R_{\rm PSF}$ is expressed as

$$1/\xi_\sigma = \sigma_{\rm out}/\sigma_0 = 1 + Ae^{-B(R_{\rm d}/R_{\rm PSF})^C}, \tag{3.4.7}$$

where the constants A, B and C are defined in Table 3.1. Final tracks for beam smearing corrections to the velocity dispersion are presented in Fig. 3.10.

3.5 Further Discussion

3.5.1 Adaptive Binning

To construct dynamical maps for each of the KROSS galaxies we employed an "adaptive binning" technique. In fitting the spectrum of each spatial pixel (§3.2.2) we required that the Hα emission line was detected with a signal-to-noise ratio of greater than five. If the line was too weak then we binned the spectra of neighbouring pixels, increasing the size of the region until either this criterion was met, or we reached an area of 0.7×0.7 arcsec (the typical seeing of our observations). To explore how this process may affect our

measurements of the kinematics, we analyse our model data a second time. When fitting the spectrum of each pixel we now include all data within a 0.5×0.5 arcsec region.

Fig. 3.11 shows that binning acts to magnify the effects of beam smearing, resulting in lower rotation velocities and greater velocity dispersions. In the instances where data has been binned, the rotation velocity is underestimated by an additional $\sim 5-10\%$ and the dispersion overestimated by an additional $2-3\%$ ($\sim 5\%$ for large $v_{\rm out}$). This is a rather exaggerated picture, since our models have been uniformly binned regardless of the surface brightness profile. In reality, outer regions are more likely to have been binned, and some galaxies may not have been binned at all. While this is an important effect to note we do not attempt to correct for it, since the details of the process are unique to each KROSS galaxy.

3.5.2 Hα Flux Distribution

For each model galaxy we have assumed that the stellar mass and light follow an exponential profile, and this was propagated through to the construction of model Hα intensity maps. However, observations suggest that the Hα morphology of $z \sim 1$ galaxies is often irregular, with the presence of $\sim$kpc scale star-forming "clumps" (e.g. Genzel et al. 2011; Wisnioski et al. 2012; Swinbank et al. 2012a; Livermore et al. 2012; 2015). These deviations from an exponential profile may affect the beam smearing, since within each pixel it will affect the relative contribution of each new velocity component introduced (i.e. beam smearing is luminosity weighted).

In Fig. 3.12 we compare the results of modelling galaxies with an exponential or a uniform Hα intensity profile. The presence of bright, star-forming clumps may act to flatten the Hα profile, so this is suitable test of how (in the most extreme case) this may affect the beam smearing. Measurements of velocity dispersion are less affected by beam smearing in the case of a uniform flux distribution, with a difference of $\sigma_{\rm out}/\sigma_0 \sim 0.1$ on average. Effects on the shape of the rotation curve are also less severe. Pixels in the outskirts of the galaxy are still contamined by light from central regions, however these regions are no longer as bright (relative to the outer regions) and therefore contribute less flux. Thus, pixels in the outskirts do not become as skewed towards lower velocities. In the right hand panel of Fig. 3.12 we see that the rotation velocity at $3.4R_{\rm d,conv}$ is now an

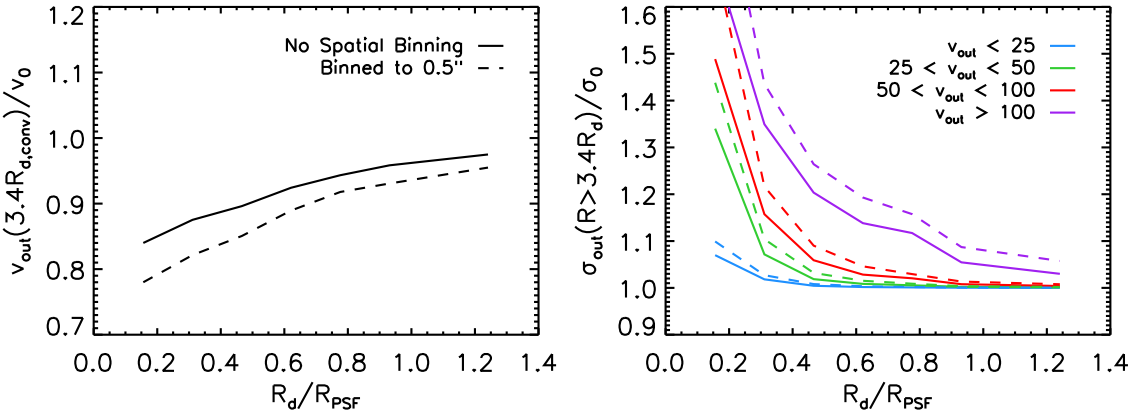

Figure 3.11: Effects of spatial binning on measurements of the rotation velocity and velocity dispersion. Results are generated from our mock observations when the spectrum of each pixel is fit individually (solid lines) and when the signal has been binned within a 0.5×0.5 arcsec region (dashed lines). In the instances where data has been binned, the rotation velocity (*left*) is underestimated by an additional $\sim 5-10\%$ and the dispersion (*right*) overestimated by an additional $2-3\%$ ($\sim 5\%$ for large $v_{\rm out}$).

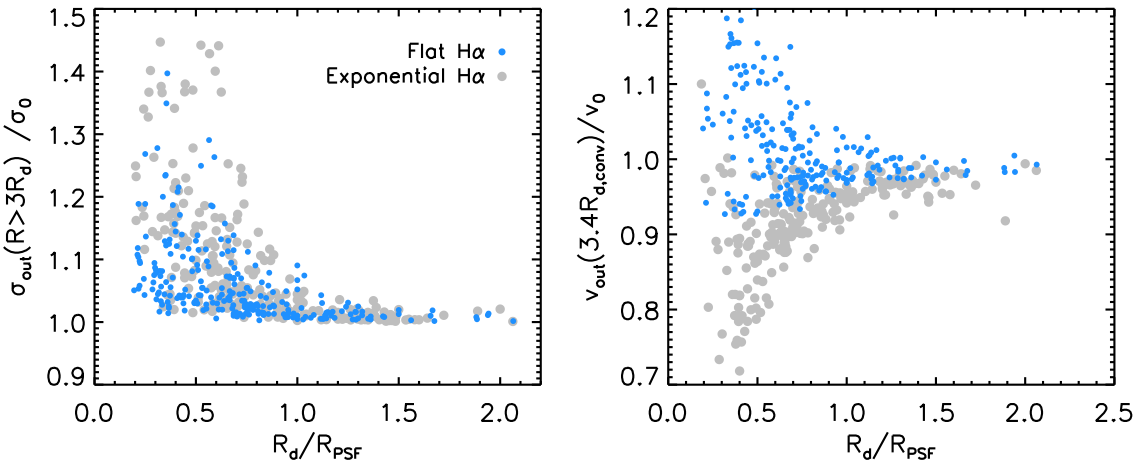

Figure 3.12: The impact of beam smearing on measurements of rotation velocity and velocity dispersion, as a function of surface brightness profile. These results are generated from mock observations when the Hα intensity follows an exponential profile (black points) or is uniform across the IFU (blue points). *Left:* For a "flat" Hα profile the effects of beam smearing on the velocity dispersion are weaker by $\sigma_{\rm out}/\sigma_0 \sim 0.1$ at low $R_{\rm d}/R_{\rm PSF}$. *Right:* Results for the two flux distributions diverge significantly for $R_{\rm d}/R_{\rm PSF} < 0.7$. When the Hα follows a uniform distribution the recovered rotation curve is close to the intrinsic, hence if there is a turnover within the data using the convolved radius may actually result in an overestimate of the velocity. We see that the rotation velocity may be overestimated by as much as 20%.

overestimate by as much as 20% at low R_d/R_{PSF}. However for $R_d/R_{PSF} > 0.7$ the required corrections are within a few percent of those for an exponential profile.

3.5.3 Structural Properties

Recent morphological studies suggest that most galaxies at $z \sim 1$ are best described by two components: a bulge and a disk (e.g. Buitrago et al. 2013; McLure et al. 2013; Bruce et al. 2014). However, for simplicity, we chose not to include a stellar bulge in our beam smearing models. To derive the kinematics of KROSS galaxies we use the Hα emission line, which traces recent star formation in the disk, so it is reasonable to expect that an evolved bulge, consisting of an older stellar population, would not have a significant impact on the shape of the dispersion profile (e.g. Davies et al. 2011). The main difference would be a deeper gravitational potential in the centre of the galaxy, and hence a steeper intrinsic rotation curve. This would lead to a stronger beam smearing effect in these regions. Nevertheless, since we measure the observed rotation velocity (v_{out}) and velocity dispersion (σ_{out}) in the outskirts of the galaxy, the changes to these parameters would likely be small ($< 5\%$).

It is common practice when analysing high-redshift IFU data to assume that the intrinsic gas velocity dispersion is uniform across the disk (as in e.g. Epinat et al. 2012; Genzel et al. 2014; Simons et al. 2016). However, Davies et al. (2011) explore the possibility that for a thick disk there may be an additional dispersion component such that $v/\sigma_0 = R/H$ where R is the radius and H is the scale height. The effect is to increase the intrinsic dispersion towards the centre of the galaxy. We wish to test the impact of this in future modelling. Again we would expect σ_{obs} to be biased high, but only by a small amount since we are measuring away from dynamical centre. It is interesting to note that the disk-fitting method tested in Davies et al. (2011) actually *underpredicts* the intrinsic dispersion, due to the degeneracy between dispersion and beam-smeared velocity gradient.

3.6 Summary

Accurately measuring the kinematic properties of high-redshift galaxies is challenging, but particularly so when observations are seeing-limited. Beam smearing blurs together

emission from spatially distinct regions of the galaxy, flattening the intrinsic velocity gradient and increasing the local dispersion. Correcting for these effects is therefore essential. In this chapter, we created a series of mock data cubes to model the impact of beam smearing on our kinematic measurements of KROSS galaxies. Comparing the input properties of each galaxy to those "observed", we derived correction factors – as shown by the tracks in Fig. 3.8 and 3.10. We apply these corrections to our measurements in Chapter 4. With the final measurements in hand, we next present a detailed investigation into the velocity dispersion (turbulence) properties of the KROSS sample.

CHAPTER 4

The KMOS Redshift One Spectroscopic Survey (KROSS): The Origin of Disk Turbulence in $z \approx 0.9$ Star-Forming Galaxies

Preamble

The work in this chapter has recently been accepted for publication in MNRAS as a first-author paper (Johnson et al. 2017; arXiv:1707.02302). We study the intrinsic velocity dispersions of a large sample of $z \sim 0.9$ star-forming galaxies, observed using the KMOS multi-object spectrograph. To mitigate the effects of beam smearing, we apply the corrections derived in Chapter 3 to our measurements.

Abstract

We analyse the velocity dispersion properties of 472 $z \sim 0.9$ star-forming galaxies observed as part of the KMOS Redshift One Spectroscopic Survey (KROSS). The majority of this sample are rotationally dominated ($83 \pm 5\%$ with $v_C/\sigma_0 > 1$) but also dynamically hot and highly turbulent. After correcting for beam smearing effects, the median intrinsic velocity dispersion for the final sample is $\sigma_0 = 43.2 \pm 0.8\,\mathrm{km\,s^{-1}}$ with a rotational velocity to dispersion ratio of $v_C/\sigma_0 = 2.6 \pm 0.1$. To explore the relationship between velocity dispersion, stellar mass, star formation rate and redshift we combine KROSS with data from the SAMI survey ($z \sim 0.05$) and an intermediate redshift MUSE sample ($z \sim 0.5$). While there is, at most, a weak trend between velocity dispersion and stellar mass, at fixed mass there is a strong increase with redshift. At all redshifts, galaxies appear to follow the same weak trend of increasing velocity dispersion with star formation rate. Our results

are consistent with an evolution of galaxy dynamics driven by disks that are more gas rich, and increasingly gravitationally unstable, as a function of increasing redshift. Finally, we test two analytic models that predict turbulence is driven by either gravitational instabilities or stellar feedback. Both provide an adequate description of the data, and further observations are required to rule out either model.

4.1 Introduction

The past decade has seen significant advancements in our understanding of the high-redshift Universe. The cosmic star formation rate density peaks in the redshift range $z \sim 1$–3 (e.g. Lilly et al. 1996; Karim et al. 2011; Burgarella et al. 2013; Sobral et al. 2013a), and so establishing the properties of galaxies at this epoch is key to constraining models of galaxy formation and evolution. It is at this crucial time that today's massive galaxies formed the bulk of their stars. The increased activity is thought to be driven (at least in part) by high molecular gas fractions (e.g. Daddi et al. 2010; Tacconi et al. 2010; 2013; Saintonge et al. 2013; Genzel et al. 2015), which may naturally explain the clumpy and irregular morphologies prevalent in *Hubble Space Telescope* (*HST*) images (e.g. Livermore et al. 2012; 2015).

The introduction of integral field spectroscopy (e.g. see Glazebrook 2013 for review) has been pivotal in allowing us to resolve the internal complexities of distant galaxies. Each spatial pixel of an integral field unit (IFU) is associated with a spectrum such that galaxy kinematics, star formation and metallicity can be mapped. Early studies often involved the in-depth analysis of small samples, since observations were time-consuming (e.g. Förster Schreiber et al. 2006; Law et al. 2009; Lemoine-Busserolle et al. 2010; Swinbank et al. 2012b). However second-generation instruments such as the K-band Multi Object Spectrograph (KMOS; Sharples et al. 2004; 2013), now allow for the simultaneous observation of multiple targets and as such we can construct large and well-selected samples in reasonable exposure times (e.g. Wisnioski et al. 2015; Stott et al. 2016).

A surprising discovery has been that while high-redshift samples are kinematically diverse, with a higher incidence of mergers than observed locally (e.g. Molina et al. 2017), many galaxies appear to be rotationally supported (e.g. Förster Schreiber et al.

2009; Epinat et al. 2012; Wisnioski et al. 2015; Stott et al. 2016; Harrison et al. 2017). Often, despite morphological irregularity, the dynamical maps of these galaxies reveal a smooth, continuous velocity gradient. Clumps visible in broad-band imaging appear to be giant star-forming complexes (e.g. Swinbank et al. 2012a; Genzel et al. 2011; Livermore et al. 2012; Wisnioski et al. 2012) which are embedded within the disk and share the same underlying dynamics.

The existence of settled disks supports the emerging consensus that a galaxy's star-formation history is not dominated by mergers but by an ongoing accretion of gas from the cosmic web (Dekel et al. 2009; Ceverino et al. 2010). Observations of a tight relation between stellar mass and star formation rate (the so-called galaxy "main sequence"; Noeske et al. 2007; Elbaz et al. 2011; Karim et al. 2011) are considered further evidence of this. A gradual decrease in the available gas supply would explain the evolution of this trend as a function of redshift, whereas stochastic, merger-driven bursts would introduce significantly more scatter (e.g. Rodighiero et al. 2011).

Kinematic surveys have revealed that while typical rotation velocities of high-redshift disks are similar to those seen locally, intrinsic velocity dispersions are much higher (e.g. Genzel et al. 2008; Lehnert et al. 2009; Gnerucci et al. 2011; Epinat et al. 2012; Newman et al. 2013; Wisnioski et al. 2015; Turner et al. 2017). These dispersions are supersonic and most likely represent turbulence within the interstellar medium (ISM). Measurements of velocity dispersion are consistently high, both for natural seeing observations and those which exploit adaptive optics (e.g. Law et al. 2009; Wisnioski et al. 2011) or gravitational lensing (e.g. Stark et al. 2008; Jones et al. 2010). While most high-redshift studies use emission lines such as Hα or [OII] to trace the ionised gas dynamics of galaxies, observations of spatially resolved CO emission have been made (e.g. Tacconi et al. 2010; 2013; Swinbank et al. 2011; Genzel et al. 2013). These studies suggest that the molecular gas is also turbulent – it is the entire disk which is dynamically hot, not just "flotsam" on the surface that has been stirred up by star formation.

Since turbulence in the ISM decays on timescales comparable to the disk crossing time, a source of energy is required to maintain the observed high velocity dispersions (e.g. Mac Low et al. 1998; Stone et al. 1998). Several potential mechanisms have been suggested, including star formation feedback (e.g. Lehnert et al. 2009; 2013; Le Tiran

et al. 2011), accretion via cosmological cold flows (Klessen & Hennebelle 2010), gravitational disk instabilities (e.g. Bournaud et al. 2010; 2014; Ceverino et al. 2010; Goldbaum et al. 2015), interactions between star-forming clumps (Dekel et al. 2009; Aumer et al. 2010), or some combination thereof. However there have been few observational tests of these theories.

Recent advancements in instrumentation such as multi-IFU systems (e.g. KMOS, SAMI; Sharples et al. 2013, Croom et al. 2012) and panoramic IFUs (e.g. MUSE; Bacon et al. 2010) allow for large, un-biased samples of galaxies to be subdivided into bins of redshift, star formation rate, stellar mass and morphology. In this work we investigate the velocity dispersion properties of high-redshift galaxies using data from the KMOS Redshift One Spectroscopic Survey (KROSS; Stott et al. 2016). This mass-selected sample consists of ~ 800 Hα-detected, typical star-forming galaxies at $z \sim 1$. We supplement these observations with data from SAMI ($z \sim 0.05$) and an intermediate redshift MUSE sample ($z \sim 0.5$).

We organise this chapter as follows. In §4.2 we describe the KROSS survey, sample selection and observations. In §4.3 we outline our analysis, the measurement of kinematic quantities and corrections applied for beam smearing. In §4.4 we present our results. We discuss how velocity dispersion relates to star formation rate and stellar mass, and explore how galaxy dynamics evolve as a function of redshift. In §4.5 we investigate which physical processes may drive turbulence in the ISM, using KROSS to test the predictions of analytic models. Finally in §4.6 we summarise our main conclusions. In this work, we adopt a $H_0 = 70\,\mathrm{km\,s^{-1}\,Mpc^{-1}}$, $\Omega_\mathrm{M} = 0.3$, $\Omega_\Lambda = 0.7$ cosmology. We assume a Chabrier IMF (Chabrier 2003), and quote all magnitudes as AB. Throughout, the errors associated with median values are estimated from a bootstrap re-sampling of the data.

4.2 Survey, Sample Selection & Data Reduction

KROSS is an ESO Guaranteed Time survey (PI: R. Sharples) designed to study the spatially resolved dynamics of typical $z \sim 1$ star-forming galaxies using KMOS. With 24 individual near-infrared IFUs, the high multiplexing capability of KMOS has allowed us to efficiently construct a statistically significant sample at this epoch. The programme is

now complete, with a total of 795 galaxies observed. Full details of the sample selection, observations and data reduction can be found in Stott et al. (2016) and Harrison et al. (2017), however in the following sub-sections we briefly summarise key aspects.

4.2.1 Sample Selection

The main aim of KROSS is to study the ionised gas kinematics of a large and representative sample of star-forming galaxies at $z \sim 1$. We use KMOS to target the Hα emission line, which combined with the adjacent [NII] doublet allows us to trace star formation, dynamics and chemical abundance gradients. Targets were selected such that Hα is redshifted into the *YJ* band and are located in the following extragalactic fields: (1) Cosmological Evolution Survey (COSMOS); (2) Extended *Chandra* Deep Field South (ECDFS); (3) SA22 and (4) UKIDSS Ultra-Deep Survey (UDS).

In addition to these redshift criteria we prioritised galaxies with an observed K-band magnitude of $K_{\rm AB} < 22.5$, which translates to a stellar mass of $\log(\mathrm{M}_\star/\mathrm{M}_\odot) \gtrsim 9.5$ at this redshift (see §4.2.2), and with colours of $r - z < 1.5$. For completeness, redder galaxies (more passive or potentially more dust obscured) were also included but were assigned a lower priority for observation. Our sample therefore favours star-forming and unobscured galaxies which may have strong line emission.

From the original sample of 795 galaxies, we follow Harrison et al. (2017) by removing 52 sources which were found to have unreliable photometry or to have suffered KMOS pointing errors. The remaining sample therefore consists of 743 galaxies between $z = 0.6 - 1.0$, with a median redshift of $z = 0.85^{+0.11}_{-0.04}$. Of these targets, 586 are detected in Hα. This is the sample we use for the dynamical analysis described in this work.

4.2.2 Stellar Masses

Since our targets were selected from a number of well-studied, deep extragalactic survey fields, a wealth of archival photometry data (from X-ray to radio) exists. We use imaging from the U-band through IRAC 4.5 μm to derive stellar masses and absolute magnitudes, as described in Stott et al. (2016). Briefly, we applied the SED fitting code HYPERZ (Bolzonella et al. 2000) to fit U-band through 4.5 μm photometry using spectral templates

derived from the Bruzual & Charlot (2003) evolutionary code. Although individual estimates of stellar mass can be made, in this work we follow Harrison et al. (2017) in applying a single mass-to-light ratio to ensure consistency across the four target fields. We convert rest-frame H-band absolute magnitudes using the median mass-to-light ratio returned by HYPERZ ($\Upsilon_H = 0.2$), as $M_\star = \Upsilon_H \times 10^{-0.4\times(M_H - 4.71)}$, resulting in a median stellar mass of $\log(\mathrm{M}_\star/\mathrm{M}_\odot) = 10.0 \pm 0.4$.

4.2.3 Star Formation Rates

We find a median Hα luminosity for the KROSS sample of $\log(L_{\mathrm{H}\alpha}/\mathrm{erg\,s^{-1}}) = 41.5 \pm 0.3$, which equates to $\sim 0.6 \times L^\star_{\mathrm{H}\alpha}$ at $z \sim 1$ (Sobral et al. 2015). To convert to star formation rates we adopt a simple approach and apply the Kennicutt (1998a) calibration (using a Chabrier IMF; Chabrier 2003), assuming a dust attenuation of $A_{\mathrm{H}\alpha} = 1.73$ (the median for the sample as returned by HYPERZ, converted from stellar to gas extinction using the relation from Wuyts et al. 2013). From this method, we derive a median star formation rate of $7.0 \pm 0.3\,\mathrm{M_\odot yr^{-1}}$ (see also Harrison et al. 2017).

In Fig. 4.1 we plot Hα luminosity versus estimated stellar mass for the 586 galaxies detected in Hα. We overlay the star-forming "main sequence" (as described by Speagle et al. 2014) at the median redshift of KROSS and find the properties of our sample to be consistent with this trend. Approximately 95% of galaxies have star formation rates within a factor of five of the median for their mass. We therefore conclude that our sample appears to be representative of typical star-forming galaxies at this redshift.

4.2.4 Observations and Data Reduction

Observations for KROSS were taken using KMOS, a near-infrared integral field spectrograph on ESO/VLT. The instrument consists of 24 individual IFUs deployable within a 7.2 arcmin diameter patrol field. Each covers a 2.8×2.8 arcsec field of view with a uniform spatial sampling of 0.2 arcsec. All targets were observed with the YJ-band filter which covers a wavelength range of $1.03 - 1.34\,\mu$m, thus allowing us to measure the rest-frame optical properties of our sample. The spectral resolution in this band ranges between $R \sim 3000 - 4000$.

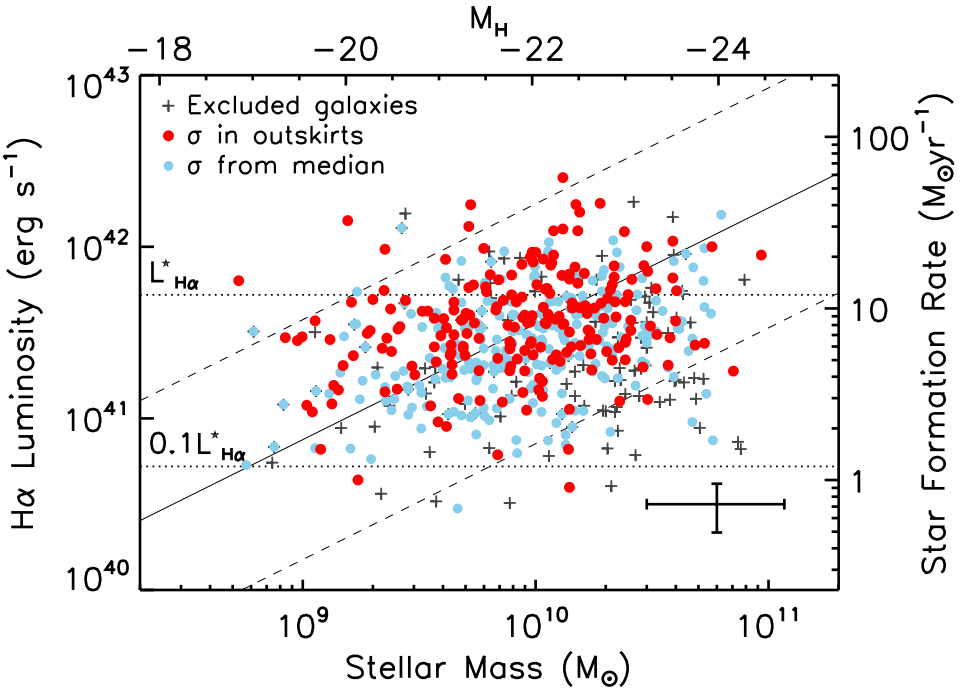

Figure 4.1: Observed Hα luminosity against stellar mass (scaled from M_H, top axis, assuming a constant mass-to-light ratio) for all 586 Hα–detected KROSS galaxies. Targets cut from the final kinematic sample (potential AGN or mergers, unresolved or low data quality sources; see §4.3.7) are marked by crosses. We differentiate between galaxies for which the dispersion is measured in the outskirts of the disk, and those where it comes from the median of all available pixels (see §4.3.5). We find a median star formation rate of $7\,\mathrm{M}_\odot\,\mathrm{yr}^{-1}$ and a median stellar mass of $10^{10}\,\mathrm{M}_\odot$, in line with the star forming "main sequence" at $z = 0.85$ (Speagle et al. 2014; solid line, with dashed lines a factor of five above or below). Dotted lines show $0.1\times$ and $1\times L_{\mathrm{H}\alpha}$ at this redshift (Sobral et al. 2015). A typical systematic error is shown in the bottom right.

Data was taken primarily between October 2013 and October 2015 using guaranteed time, but was supplemented with some science verification observations (Sobral et al. 2013b; Stott et al. 2014). Median seeing in the J-band was 0.7 arcsec, with 92% of observations made during conditions of < 1 arcsec, and throughout the analysis we account for the seeing conditions of individual observations. In Chapter 3 we presented a detailed investigation into the impact of the seeing on our kinematic measurements (so-called "beam smearing"). Observations were made in an ABAABAAB nod-to-sky sequence, where A represents time on target and B time on sky. Total on-source integration time was an average of 9 ks per galaxy.

Initial data reduction was performed using the standard ESOREX/SPARK pipeline which dark subtracts, flat-fields and wavelength calibrates individual science frames, and applies an additional illumination calibration. Each AB pair was reduced individually, with the temporally closest sky frame subtracted from each object frame. Further sky subtraction was then performed using residual sky spectra extracted from a series of dedicated sky IFUs (one for each of the three KMOS detectors). Finally, we combined all observations of the same galaxy using a 3σ clipped average and re-sampled the data onto a pixel scale of 0.1 arcsec. This forms the final datacube which we used to extract the Hα and continuum images, velocity maps and line of sight velocity dispersion maps discussed in the following sections.

4.3 Analysis

In this work we explore the velocity dispersion properties of the KROSS sample, investigating which processes may drive the high levels of disk turbulence typically observed in galaxies at this redshift. We first require measurements of galaxy size, inclination, position angle, rotation velocity and velocity dispersion. Harrison et al. (2017) discussed how high resolution broad-band imaging can be combined with KMOS data in order to make robust measurements of kinematic and morphological properties. In the following section we summarise this analysis. A catalogue of raw and derived properties for all 586 Hα detected targets is available online (see §4.7). With the release of Johnson et al. (2017) on the arXiv, this catalogue has been updated to include measurements and derived quantities

relating to the velocity dispersion, as shown in Table 4.1.

4.3.1 Broad-band Imaging

We used the highest quality broad-band imaging available to measure the half-light radius ($R_{1/2}$), inclination (θ) and position angle (PA_{im}) of each galaxy. For 46% of our sample there is archival *HST* imaging. All of our targets in ECDFS and COSMOS, and a subset of those in UDS, have been observed with *HST* in the H, I or z'-band. For all other targets we use K-band ground-based imaging taken with the United Kingdom Infrared Telescope as part of the UKIDSS survey (Lawrence et al. 2007). These images have a typical PSF of FWHM = 0.65 arcsec in UDS and 0.85 arcsec in SA22.

In Harrison et al. (2017) we discuss the implications of using imaging of different rest-frame wavelengths and spatial resolutions, and perform a series of tests to determine any systematics introduced. We find that the half-light radii measured from I-band *HST* images are $\sim 10\%$ larger than those measured from H-band images (consistent with the results of van der Wel et al. 2014). A small correction is therefore applied. We also degrade the H-band *HST* images to assess whether the poorer spatial resolution of ground-based images introduces any bias. On average, position angle measurements are unaffected by this convolution, but there is a 10 and 20% scatter introduced at the UDS PSF and SA22 PSF, respectively. Inclination measurements are also consistent on average, but with 15 and 20% scatter. Half-light radii are slightly larger; however an introduced scatter of 25 and 35% is what dominates. We incorporate these 1σ scatters into our uncertainties for measurements of $R_{1/2}$, θ and PA_{im} made using ground-based imaging.

4.3.2 Sizes, Inclinations and Position Angles

We first fit each image as a two dimensional Gaussian profile in order to determine a morphological position angle and best-fit axis ratio (b/a). We deconvolve for the PSF of the image and convert this axis ratio to an inclination angle as

$$\cos^2\theta_{im} = \frac{(b/a)^2 - q_0^2}{1 - q_0^2}, \tag{4.3.1}$$

where q_0 is the intrinsic axial ratio of an edge-on galaxy. This parameter could have a wide range of values ($\approx 0.1-0.65$; see Law et al. 2012), however we adopt the ratio for a thick disk, $q_0 = 0.2$. Adjusting q_0 would not have a significant impact on our results. For 7% of galaxies we are unable to estimate $\theta_{\rm im}$ due to poor resolution imaging. We therefore assume the median axis ratio of the *HST* observed sources and assign these a "quality 2" flag (see §4.3.7).

To estimate the half-light radius we measure the flux of each broad-band image within a series of increasingly large elliptical apertures. For each ellipse we use the continuum centre, and the position angle and axis ratio derived above. We define $R_{1/2}$ as the radius of the ellipse which contains half the total flux, deconvolved for the PSF of the image.

For 14% of the sample we are unable to measure the half-light radius from the image, but instead infer an estimate using the turn-over radius of the rotation curve ($R_{\rm d}$; see §4.3.4). We calibrate these radii using sources for which both $R_{1/2}$ and $R_{\rm d}$ can be measured, and again assign a "quality 2" flag. For an additional 6% of sources neither of these methods were suitable and we therefore place a conservative upper-limit on $R_{1/2}$ of $1.8 \times \sigma_{\rm PSF}$. We assign these a "quality 3" flag.

4.3.3 Emission Line Fitting

A detailed description of how we extract two dimensional maps of Hα flux, velocity and velocity dispersion from the IFU data can be found in Stott et al. (2016). However, we include a brief summary here. In each spatial pixel we fit the Hα and [NII] 6548,6583 emission lines via a χ^2 minimisation procedure, weighting against the positions of bright OH skylines (Rousselot et al. 2000). Each emission line is modelled as a single Gaussian component within a linear local continuum. We fit the Hα and [NII] emission simultaneously, allowing the centroid, intensity and width of the Gaussian profile to vary. The FWHM of the lines are coupled and the flux ratio of the [NII] doublet fixed to be 3.06 (Osterbrock & Ferland 2006). During the fitting, we convolve the line profile with the instrumental dispersion, as measured from the widths of nearby skylines. As such, our dispersion measurements are corrected for the instrumental resolution.

If the detection in a given pixel does not exceed a signal-to-noise of five then we bin the data into successively larger regions, stopping either when this criteria is met or an area

of 0.7×0.7 arcsec (the typical seeing of our observations) is reached. Using this method, 552 (94%) of the Hα detected sample are spatially resolved. We classify all unresolved sources as having a "quality 4" flag. Since the typical seeing of our observations is larger than the pixel size, pixel-by-pixel errors are not independent. This is something we try to account for by modelling the effects of beam smearing (see §4.3.6). In Fig. 4.2 we show example Hα intensity, velocity and velocity dispersion maps for eight KROSS galaxies.

4.3.4 Rotation Velocities

In order to measure a rotation velocity we must first establish the position of the major kinematic axis (PA_{vel}). We rotate the Hα velocity field around the continuum centre in one degree increments and extract a velocity profile each time. We find the profile with the largest velocity gradient and identify this position angle as PA_{vel}. To extract a rotation curve along this axis, we calculate the median velocity at positions along a 0.7 arcsec "slit" through the continuum centre. Example rotation curves are included in Fig. 4.2, where the error bar associated with each point represents all variation within the "slit".

To minimise the impact of noise on our measurements, we fit each rotation curve as an exponential disk (Freeman 1970) of the form:

$$v(r)^2 = \frac{r^2 \pi G \mu_0}{R_{\rm d}} (I_0 K_0 - I_1 K_1) + v_{\rm off}, \tag{4.3.2}$$

where r is the radial distance, μ_0 is the peak mass surface density, $R_{\rm d}$ is the disk radius and $I_n K_n$ are the Bessel functions evaluated at $0.5r/R_{\rm d}$. The final parameter, $v_{\rm off}$, is the velocity measured at the centre of the galaxy and we apply this offset to the rotation curve before making measurements. We model each galaxy in this way with the intention of interpolating the data to obtain a more robust measurement. However, for 13% of galaxies we must extrapolate (> 0.4 arcsec; ~ 3 kpc) beyond the data to evaluate the rotation velocity at the desired radius.

We measure the rotation velocities of our sample at two radii frequently used within the literature, $1.3R_{1/2}$ and $2R_{1/2}$ ($\approx 2.2R_{\rm d}$ and $3.4R_{\rm d}$ for an exponential disk). The first of these coincides with the peak rotation velocity of an ideal exponential disk, while the second probes outer regions of the galaxy, where we expect the rotation curve to have

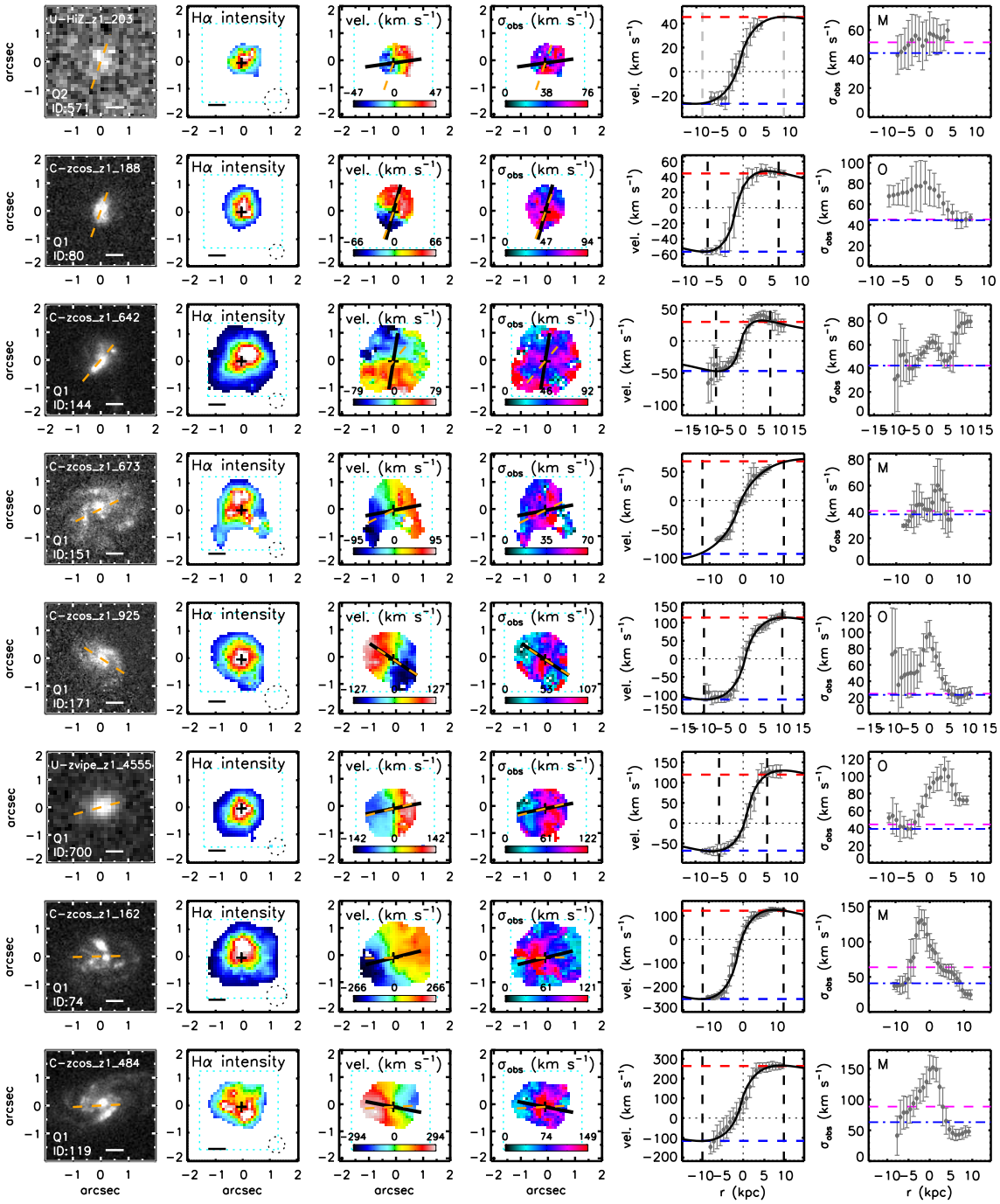

Figure 4.2: Example data for eight galaxies in the KROSS sample, arranged by increasing stellar mass from top to bottom. *Left to right:* (1) Broad-band image with orange dashed line to represent PA_{im}. We also display the quality flag (see §4.3.7) and a 5 kpc scale bar. (2) Hα intensity map with cross to mark the continuum centre and dashed circle to represent the seeing FWHM. (3) Hα velocity map with dashed orange line to represent PA_{im} and solid black line to represent PA_{vel}. (4) Observed Hα velocity dispersion map with lines as in panel 3. (5) Rotation curve extracted along a 0.7 arcsec wide "slit" of PA_{vel}. The solid curve describes a model which we use to find the rotation velocity at $\pm 3.4\,R_d$ (dashed vertical lines). To estimate $v_{C,obs}$ we take the average of these two values (horizontal dashed lines). (6) Observed velocity dispersion profile extracted along PA_{vel}, with dashed line to represent $\sigma_{0,obs}$ as measured in the outskirts of the disk (O) or from the median of all pixels (M). The dot-dashed line shows this same value corrected for beam smearing (σ_0). In general, as the stellar mass of the galaxy increases, we see a larger peak in the dispersion profile due to beam smearing.

flattened. We refer to these measurements as $v_{2.2}$ and v_C, respectively. For each galaxy we convolve $R_{1/2}$ with the PSF of the KMOS observation[1] and extract velocities from the model rotation curve. At a given radius, our final measurement is half the difference between velocities on the blue and red side of the rotation curve. We account for beam smearing using the correction factors derived in Chapter 3. Finally, we correct for the inclination of the galaxy, as measured in §4.3.2.

A small subset of our sample (11%) are unresolved in the KMOS data ("quality 4") or the broad-band imaging ("quality 3"). As such we are unable to extract rotation velocities for these galaxies from a rotation curve. Instead we make estimates using the linewidth of the galaxy integrated spectrum, and calibrate our results using galaxies for which both methods are available. From a sample of 586 Hα detected galaxies, 433 are flagged as "quality 1", 88 are "quality 2", 31 are "quality 3" and 34 are "quality 4".

4.3.5 Velocity Dispersions

Throughout our analysis, we assume that the intrinsic velocity dispersion is uniform across the disk (as in e.g. Epinat et al. 2012; Genzel et al. 2014; Simons et al. 2016). Most galaxies at $z \sim 1$ are best described by two components, a bulge and a disk (e.g. Buitrago et al. 2013; McLure et al. 2013; Bruce et al. 2014). However, we would not expect a stellar bulge to have a significant impact on the gas dispersion profile, as traced by Hα (see §3.5.3 for discussion). In the same way as we extract a rotation curve from the velocity map, we also extract a profile along the major kinematic axis of the velocity dispersion map. We use this profile to measure the observed dispersion, $\sigma_{0,\mathrm{obs}}$, by taking the median of values at either end of the kinematic axis $|R| > 2R_{1/2}$ ($3.4\,R_\mathrm{d}$ for an exponential disk) and adopting whichever value is smallest (see Fig. 4.2). We assume the uncertainty on this measurement is the scatter of values included in the median. Evaluating $\sigma_{0,\mathrm{obs}}$ at radii far from the dynamical centre reduces any bias introduced by beam smearing (Chapter 3; §4.3.6), and measurements here should be close to the intrinsic dispersion.

While this is our preferred method, 56% of the resolved sample (307 galaxies) have insufficient signal-to-noise in the outer regions of the galaxy ($\pm\,2R_{1/2}$) to be able to mea-

[1] i.e. $R^2_{1/2,\mathrm{conv}} = R^2_{1/2} + \mathrm{FWHM}^2_{\mathrm{PSF}}$

sure the dispersion in this way. Instead we measure the median of all available pixels within the dispersion map. Once we apply the relevant beam smearing corrections derived in Chapter 3, we find that the $\sigma_{0,obs}$ values from each method are in good agreement. In cases where we can follow either approach the results are (on average) consistent to within 4%, with $\approx 50\%$ scatter around this offset. We therefore assign an uncertainty of 50% to measurements made using this second method. We do not estimate σ_0 for unresolved galaxies.

4.3.6 Beam Smearing Corrections

Since our KMOS observations are seeing-limited, we must consider the impact of the spatial PSF (the seeing) on our kinematic measurements. As IFU observations are convolved with the PSF, information from each spatial pixel is combined with that of neighbouring regions – a phenomenon known as "beam smearing" (see e.g. Epinat et al. 2010; Davies et al. 2011; Burkert et al. 2016). This acts to increase the observed velocity dispersion (particularly towards the dynamical centre) and to flatten the observed rotation curve, thereby reducing the observed velocity. In order to calibrate for these effects, we create a series of mock KMOS observations and derive correction factors which can be applied to the kinematic measurements. Our method for this correction is similar to that adopted by other authors (e.g. Burkert et al. 2016; Turner et al. 2017) and we derive similar results. Full details of this investigation were presented in Chapter 3, however the following is a brief summary.

To begin this process we create a sample of $\sim 10^5$ model disk galaxies, with stellar masses and radii representative of the KROSS sample. We assume an exponential light profile and model the galaxy dynamics as the sum of a stellar disk plus a dark matter halo. An appropriate range of dark matter fractions is determined using results of the cosmological simulation suite "Evolution and Assembly of GaLaxies and their Environments" (EAGLE; Crain et al. 2015; Schaye et al. 2015; Schaller et al. 2015). For simplicity, the intrinsic velocity dispersion (σ_0) is assumed to be uniform across the disk. From these properties we can predict the intensity, linewidth and velocity of the Hα emission at each position. We use this information to create an "intrinsic" KMOS data cube for each galaxy.

To simulate the effects of beam smearing we convolve each wavelength slice of the cube with a given spatial PSF. We model a range of seeing conditions to match our KMOS observations. This forms the "observed" data cube from which we extract dynamical maps (in the same way as for the observations) and measure $v_{C,obs}$, $v_{2.2,obs}$ and $\sigma_{0,obs}$. Differences between the input values of the model and these "observed" values then form the basis of our beam smearing corrections. The amplitude of the beam smearing is most sensitive to the size of the galaxy relative to the PSF. These corrections are best parameterised as a function of R_d/R_{PSF}, where R_{PSF} is half of the FWHM of the seeing PSF.

Fig. 3.8 in the previous chapter shows the ratio of the observed and intrinsic rotation velocity as a function of R_d/R_{PSF}. As expected, the larger the spatial PSF is compared to the disk, the more we underestimate the intrinsic velocity. Averaging over all stellar masses and inclinations, we find a median correction to v_C of $\xi_v = 1.07 \pm 0.03$, with a range of $\xi_v = 1.0 - 1.17$. Applying this correction acts to increase the median rotation velocity measurement by $4\,\mathrm{km\,s^{-1}}$.

Similarly, the smaller the value R_d/R_{PSF} the more we overestimate the intrinsic velocity dispersion. However, the impact of beam smearing on measurements of σ_0 also depends strongly on the velocity gradient across the disk (which is a function of both dynamical mass and inclination angle). In Fig. 3.10 we split corrections into four separate tracks as a function of $v_{C,obs}$. The majority of galaxies in our sample (67%) have observed rotation velocities of $v_{C,obs} \leq 100\,\mathrm{km\,s^{-1}}$, so most corrections are made using the green and blue tracks of Fig. 3.10. The required adjustments are therefore relatively small. When using the velocity dispersions extracted from outer regions of the disk, we apply a median beam smearing correction of $\xi_\sigma = 0.97^{+0.02}_{-0.06}$. If a value is extracted from the median of the map, we apply a median factor of $\xi_\sigma = 0.8^{+0.1}_{-0.3}$. Applying these beam smearing corrections to KROSS data reduces the median velocity dispersion measurement by $9\,\mathrm{km\,s^{-1}}$.

4.3.7 Definition of the Final Sample

In §4.2 we presented a mass- and colour-selected sample of 743 KROSS galaxies, 586 of which are detected in Hα. In Fig. 4.1 we show that this forms a representative sample of

star-forming galaxies at this redshift ($z \approx 0.85$), in the context of the $M_\star$ – SFR "main sequence". With kinematic and morphological properties of these galaxies now established (e.g. Fig.4.2), we make a number of additional cuts to the sample.

Firstly, as in Harrison et al. (2017) we exclude 20 galaxies with line ratios of [NII]/H$\alpha > 0.8$ and/or a broad-line component to the Hα emission of $\geq 1000\,\mathrm{km\,s^{-1}}$. These sources may have a significant AGN component or kinematics which are influenced by shocks (e.g. Kewley et al. 2013; Harrison et al. 2016). We also remove 30 sources which have multiple components in their broad-band imaging and/or IFU data. In doing so we hope to remove any potential major mergers. Finally, we exclude "quality 4" and "quality 3" sources which are unresolved or without a half-light radius measurement, respectively. This leaves a final sample of 472 galaxies.

The various cuts applied have little impact on the global properties of the sample. Fig. 4.1 shows that after the removal of 114 galaxies (highlighted as grey crosses), the sample is still uniformly scattered about the star-forming "main sequence". Overall, 400 (85%) of the final sample satisfy the high priority selection criteria of $r - z < 1.5$ and $K_{\mathrm{AB}} < 22.5$ (see §4.2.1 and Harrison et al. 2017), compared to 83% of all Hα-detected KROSS galaxies.

Of the final sample, 18% (84 galaxies) are classified as "quality 2", owing to a fixed inclination angle or half-light radius measured from the rotation curve. For 49% of the sample (231 galaxies) we are able to measure the velocity dispersion (σ_0) using data in the outer regions of the galaxy. For the remaining 51% of cases (241 galaxies) we must measure the median of all IFU pixels and correct this value appropriately. As discussed in §4.3.5 these two methods are consistent, however we attribute larger uncertainities to measurements made using the latter approach.

4.4 Results

In the previous section we summarised the morphological and kinematic analysis of 586 Hα detected galaxies in the KROSS sample. After the removal of 114 sources which have either uncertain kinematic measurements, or show signs of a significant AGN component or merger event, we construct a final sample of 472 clean, well-resolved galaxies.

In the following subsections we present a detailed discussion of the velocity dispersion properties of this sample.

4.4.1 Velocity Dispersions

We measure a median intrinsic velocity dispersion of $\sigma_0 = 43.2 \pm 0.8\,\mathrm{km\,s^{-1}}$ and a 16–84th percentile range of $27-61\,\mathrm{km\,s^{-1}}$. This median dispersion is lower than the 59 ± 2 $\mathrm{km\,s^{-1}}$ previously reported for KROSS in Stott et al. (2016) due to a more rigorous beam smearing analysis, different measurement techniques, and further refinement of the kinematic sample (see §4.3 and Harrison et al. 2017). As discussed in §4.3.5, we measure the dispersion of each galaxy using one of two different methods. For approximately half of the sample we measure σ_0 in outer regions of the disk ($|R| > 2R_{1/2}$) while for the remaining galaxies we calculate the median of all pixels. Galaxies in the "median" sample tend to be larger than those in the "outskirts" sample (median half-light radii of 3.5 ± 0.1 kpc and 2.07 ± 0.08 kpc, respectively) and also more passive (median star formation rates of $6.2 \pm 0.3\,\mathrm{M_\odot yr^{-1}}$ and $8.2 \pm 0.4\,\mathrm{M_\odot yr^{-1}}$). This results in a lower surface brightness, which makes it more difficult to resolve kinematics in the outskirts of the galaxy. The velocity dispersions of this subset are also slightly higher, with a median of $\sigma_0 = 45 \pm 1\,\mathrm{km\,s^{-1}}$ as opposed to $41 \pm 1\,\mathrm{km\,s^{-1}}$ for the "outskirts" sample.

In Fig. 4.3 we explore the relationship between stellar mass and velocity dispersion. We may expect these quantities to be related, since dispersions are important in measuring the dynamical support of galaxies, regardless of morphological type. For example, several authors have noted that the $S_{0.5}$ parameter [$S_{0.5} = (0.5\,v^2 + \sigma^2)^{1/2}$] correlates more strongly with stellar mass than rotational velocity alone (e.g. Kassin et al. 2007; Vergani et al. 2012; Cortese et al. 2014). Fig. 4.3 shows that before we account for beam smearing, the average velocity dispersion increases significantly with stellar mass. We measure a median σ_{obs} of $48 \pm 2\,\mathrm{km\,s^{-1}}$ in the lowest mass bin compared to $64 \pm 5\,\mathrm{km\,s^{-1}}$ in the highest. However as discussed in §4.3.6 (and extensively in Chapter 3), a more massive galaxy is typically associated with a steeper velocity gradient across the disk (e.g. Catinella et al. 2006) and hence stronger beam smearing. After we apply corrections as a function of $R_{\mathrm{d}}/R_{\mathrm{PSF}}$ and $v_{\mathrm{C,obs}}$ (Fig. 3.10) we no longer observe this trend and instead find the median σ_0 to be consistent across the four mass bins, with values between

$42 \pm 2\,\mathrm{km\,s^{-1}}$ and $45 \pm 3\,\mathrm{km\,s^{-1}}$. If we consider only dispersion measurements made in the outskirts of the disk, values are almost identical – lower by a factor of 0.98 ± 0.03. Our results suggest that σ_0 is independent of stellar mass between $\log(M_\star/\mathrm{M}_\odot) = 9.4 - 10.4$.

4.4.2 Rotational Support

To quantify the balance between rotational support and turbulence of the gas, we calculate the ratio between rotation velocity and velocity dispersion, v_C/σ_0, for each of the KROSS galaxies. We find a median value of $v_C/\sigma_0 = 2.6 \pm 0.1$ and a 16–84th percentile range of $0.9 - 5$. We can use this ratio between rotation velocity and intrinsic dispersion to achieve a crude separation of "dispersion dominated" and "rotationally dominated" galaxies. Following e.g. Genzel et al. (2006) we adopt $v_C/\sigma_0 = 1$ as a boundary between the two. By this definition we find a rotationally dominated fraction of $83 \pm 5\%$, which suggests that the majority of star-forming galaxies at this redshift are already settled disks. The KROSS sample used for this work is slightly different to that presented in Harrison et al. (2017), for example we include only "quality 1" or "quality 2" sources. However, our results are consistent, suggesting that this does not introduce a bias. Harrison et al. (2017) find a median value of $v_C/\sigma_0 = 2.4 \pm 0.1$ and a rotationally dominated fraction of $81 \pm 5\%$. Despite a more detailed treatment of the beam smearing effects, our results are also consistent with the initial KROSS values derived in Stott et al. (2016).

In Fig. 4.4 we study how rotational support relates to stellar mass. Observations suggest that galaxies evolve hierarchically from disordered, dynamically hot systems to regularly rotating disks, with the most massive galaxies settling first (kinematic downsizing; e.g. Kassin et al. 2012; van der Wel et al. 2014; Simons et al. 2016; 2017). At a given redshift it is expected that high mass galaxies are more stable to disruptions due to gas accretion, winds or minor mergers (e.g. Tacconi et al. 2013; Genzel et al. 2014). As such, we expect the most massive galaxies to exhibit the largest v_C/σ_0 values. Fig. 4.4 demonstrates that this is indeed true for the KROSS sample, with median v_C/σ_0 values of 1.3 ± 0.1 and 4.3 ± 0.3 in the lowest and highest mass bins, respectively, and "dispersion dominated" systems more prevalent at low stellar mass. Since we observe no correlation between velocity dispersion and stellar mass, this increase must be a result of higher mass galaxies rotating more quickly. If $\mathrm{M}_\star \propto v_C^2$ then we would expect v_C to increase by a factor

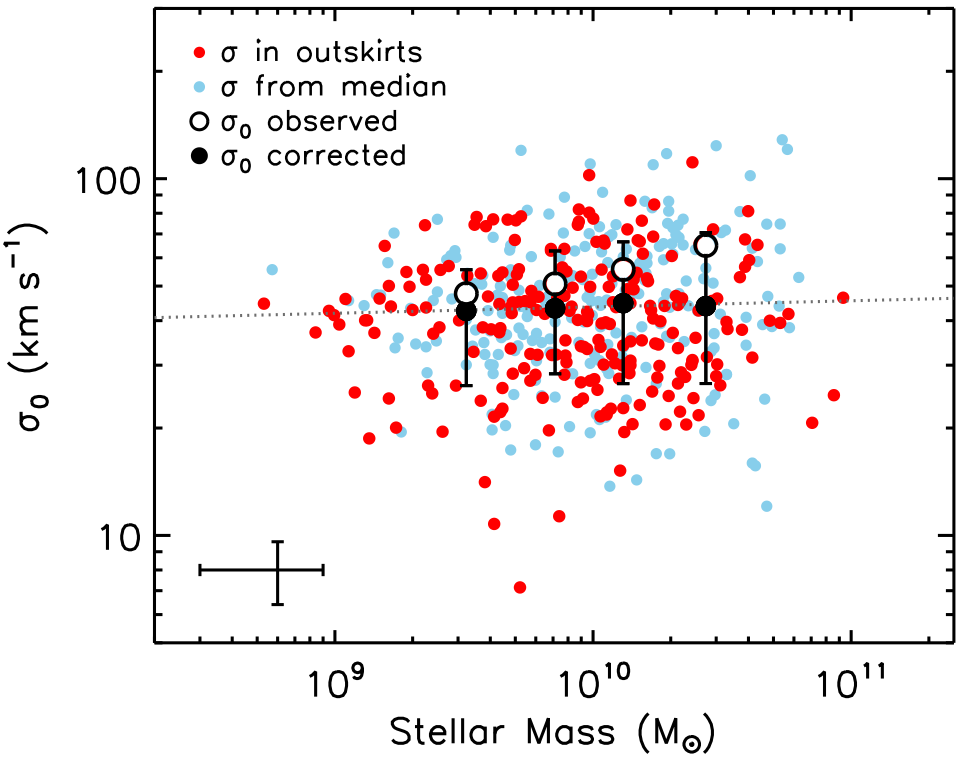

Figure 4.3: Beam smearing corrected velocity dispersion against stellar mass, with points coloured by the technique used to measure σ_0. Large black symbols show the median dispersion (and standard deviation) in bins of stellar mass. If we consider only measurements made in the outskirts of the disk, these average values are almost identical – a factor of 0.98 ± 0.03 lower. Large open symbols show the median in each bin prior to the correction being applied. The large black points show that once we have accounted for the effects of beam smearing (see §4.3.6) we find σ_0 to be independent of stellar mass. The dotted line is a fit to this trend.

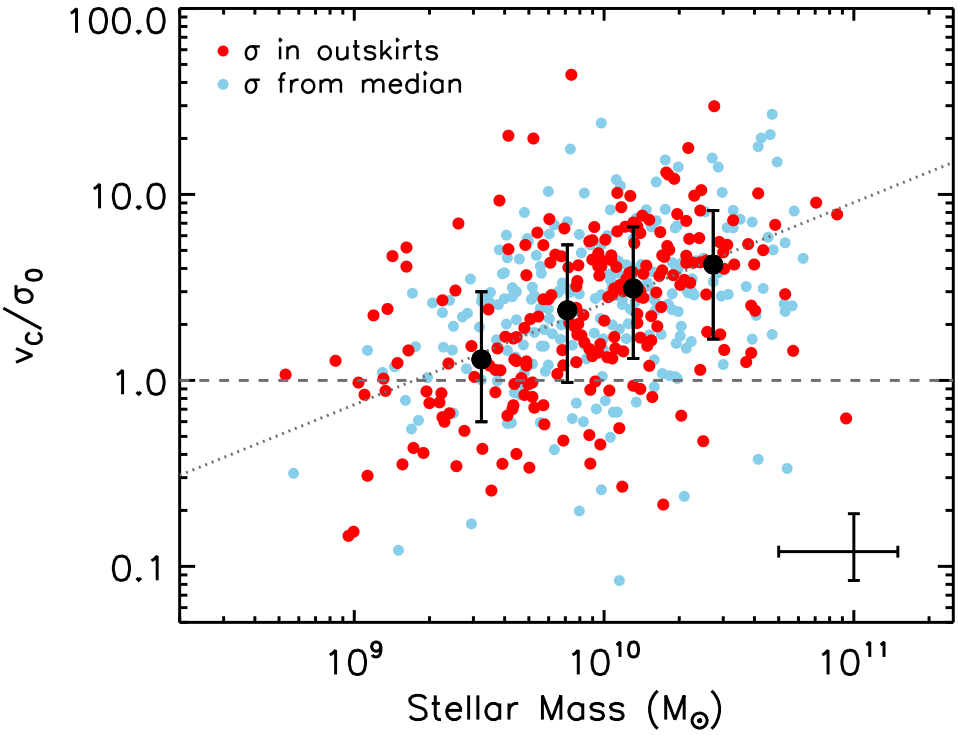

Figure 4.4: Ratio between inclination corrected rotational velocity (v_C) and intrinsic velocity dispersion (σ_0) against stellar mass. Fig. 4.3 shows that the average σ_0 is roughly the same in each mass bin, however due to larger rotational velocities we see an increase in v_C/σ_0 with increased stellar mass. We fit a trend to the median values in bins of increasing stellar mass (large black points) and plot this as a dotted line. The dashed line acts as a crude boundary between "dispersion dominated" (below) and "rotationally dominated" galaxies (above, $\sim 80\%$ of our sample). More massive galaxies appear to be more rotationally supported.

of ~ 3.2 over the mass range $\log(M_\star/\mathrm{M}_\odot) = 9.4 - 10.4$. This is consistent with our results in Fig. 4.4.

4.4.3 Trends Between Velocity Dispersion and Stellar Mass, Star Formation Rate and Redshift

To analyse the kinematics of KROSS galaxies in an evolutionary context, and to further explore how dispersion relates to other galaxy properties, we introduce comparison samples. In the "IFU era" there are a multitude of kinematic surveys to choose from, however it is often difficult to make comparisons since the techniques used, particularly for beam smearing corrections, can vary a great deal. In this subsection we therefore consider only two additional samples, for which we can measure (and correct) σ_0 in a consistent way. In §4.4.4 we will study the average properties of a further five comparison samples.

4.4.3.1 SAMI sample

Our first comparison sample consists of 824 galaxies from the Sydney-AAO Multi-object Integral field (SAMI; Croom et al. 2012) Galaxy Survey. The goal of this survey is to provide a complete census of the spatially resolved properties of local galaxies ($0.004 < z < 0.095$; Bryant et al. 2015; Owers et al. 2017). SAMI is a front-end fibre feed system for the AAOmega spectrograph (Sharp et al. 2006). It uses a series of "hexabundles" (Bland-Hawthorn et al. 2011; Bryant et al. 2014), each comprised of 61 optical fibres and covering a ~ 14.7 arcsec field of view, to observe the stellar and gas kinematics of up to 12 galaxies simultaneously. Reduced SAMI datacubes have a 0.5 arcsec spatial sampling. A detailed description of the data reduction technique is presented in Sharp et al. (2015). The data used for this analysis was kindly provided by the SAMI team ahead of its public release (Green et al. in prep), however an early data release is presented in Allen et al. (2015).

In order to compare SAMI data to KROSS we first make a series of cuts to the sample. In particular, the SAMI survey contains a number of early-type and elliptical galaxies with high Sérsic indicies, high stellar masses and low star formation rates (hence very low specific star formation rates), which are not representative of the KROSS sample

selection, that is to select typical star-forming galaxies for that epoch. We therefore remove galaxies from the SAMI sample with masses greater than $M_\star = 8\times10^{10}\,\mathrm{M}_\odot$ and a Sérsic index of $n > 2$ (since the derived σ_0 measurements for these galaxies are likely to be measuring different physical processes). We also remove sources which are unresolved at the SAMI resolution or have kinematic uncertainities greater than 30%. This leaves a total of 274 galaxies with a median redshift $z \sim 0.04$ and median stellar mass $\log(M_\star/\mathrm{M}_\odot) = 9.34 \pm 0.07$.

In Fig. 4.5 we plot star formation rate versus stellar mass for this sample. Stellar masses were estimated from $g-i$ colours and i-band magnitudes following Taylor et al. (2011), as described in Bryant et al. (2015). Star formation rates were estimated using Hα fluxes corrected for dust attenuation. Most SAMI galaxies are representative of the star-forming "main sequence" at $z = 0$ (Peng et al. 2010), and hence at fixed stellar mass, star formation rates are 30 – 50 times lower than for KROSS galaxies.

To measure rotation velocities and dispersions, we exploit the gas velocity maps, which use 11 strong optical emission lines including Hα and [OII]. From these maps we make measurements using the same methods as for the KROSS sample (for an independent study of SAMI velocity dispersions see Zhou et al. 2017). However, since the angular sizes of galaxies at this redshift are much larger, the field of view of SAMI often does not extend to $3.4R_\mathrm{d}$. Instead, we use a radius of $2R_\mathrm{d}$ and correct the derived quantities appropriately based on our modelling in Chapter 3.

4.4.3.2 MUSE sample

For a second comparison we exploit the sample of Swinbank et al. (2017), who study the kinematics of 553 [OII] emitters serendipitously detected in a series of commissioning and science verification observations using MUSE (Multi-Unit Spectroscopic Explorer; Bacon et al. 2010), a panoramic IFU with 1×1 arcmin field of view and 0.2 arcsec spatial sampling. Science targets were largely extragalactic "blank" fields or high-redshift galaxies and quasars. Due to the nature of the sample, sources span a wide range of redshifts, with $0.28 < z < 1.49$. To provide an intermediate between the redshifts of KROSS and SAMI, we restrict this sample to galaxies between $0.3 < z < 0.7$. In Swinbank et al. (2017) sources were classified as rotationally supported, merging, interacting or compact,

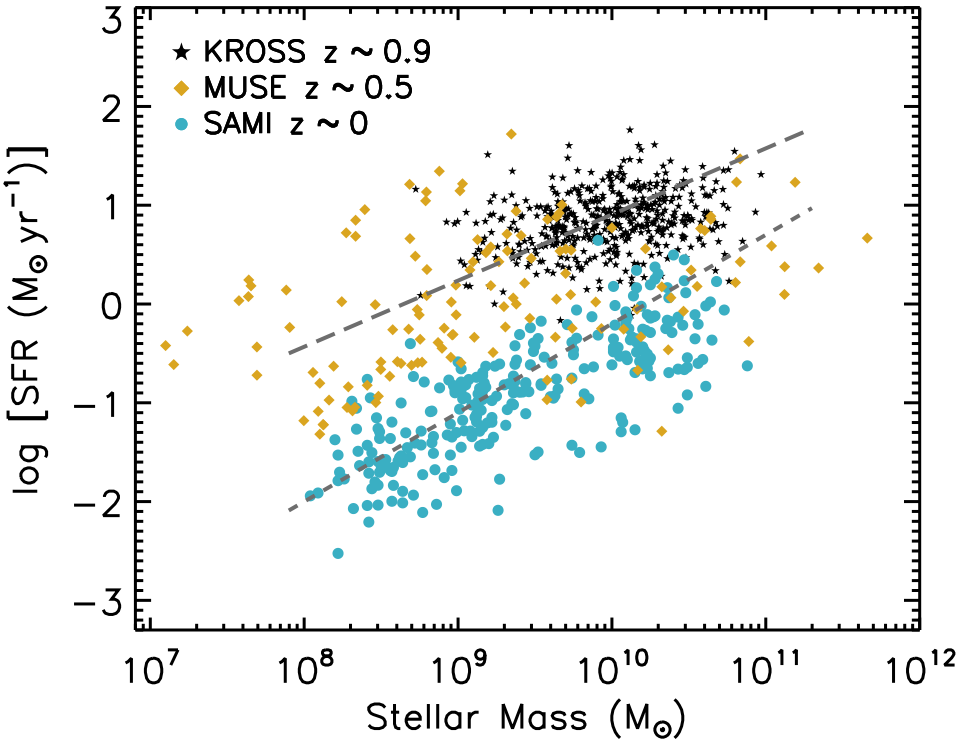

Figure 4.5: Star formation rate versus stellar mass for the KROSS galaxies studied in this work (as in Fig. 4.1), and the MUSE and SAMI comparison samples discussed in §4.4.3. We overlay the star-forming "main sequence" at $z = 0$ (Peng et al. 2010) and $z = 0.85$ (Speagle et al. 2014), which illustrate that the KROSS and SAMI samples are representative of typical star-forming galaxies at their respective redshifts. The MUSE sample are [OII] emitters serendipitously detected within observations of other targets, hence these galaxies have a wide range of masses and star formation rates.

based on their dynamics and optical morphologies. We choose to exclude major mergers and compact (unresolved) galaxies from our analysis, and also those which have poorly defined masses or optical radii. With the implementation of these cuts our comparison sample consists of 133 galaxies with a median redshift of $z \sim 0.5$ and median stellar mass $\log(M_\star/\mathrm{M}_\odot) = 9.1 \pm 0.1$. Stellar masses were derived from M_H magnitudes, using the same method as for KROSS, and the star formation rates calculated using dust-corrected [OII] fluxes. Fig. 4.5 shows that since the selection is based only on [OII] flux, galaxies are scattered within the $M_\star$ – SFR plane and it is more difficult than for SAMI and KROSS to identify a "main sequence", however star formation rates are generally between those of the $z \sim 0$ and $z \sim 0.9$ samples.

Swinbank et al. (2017) extract rotation velocities at radii of $3R_\mathrm{d}$ and we apply the beam smearing corrections derived in §4.3.6 to these values. Velocity dispersions are calculated by first applying a pixel-by-pixel $\Delta v/\Delta R$ correction to the map (i.e. subtracting the average shear across the pixel in quadrature), and then finding the median of all pixels outside of the seeing PSF. This beam smearing method is similar to that for KROSS and so no additional corrections are applied in our comparison.

4.4.3.3 Dispersion Properties

In Fig. 4.6 we explore the relationship between velocity dispersion and stellar mass, star formation rate and specific star formation rate. At a given redshift, there appears to be at most only a weak trend between stellar mass and velocity dispersion. This is consistent with the results of other high redshift kinematic studies (e.g. Wisnioski et al. 2015; Simons et al. 2017; Turner et al. 2017). We observe a larger trend of increasing dispersion with stellar mass for the SAMI sample than for KROSS (where any change is not significantly detected) and MUSE, however this is still only a $12 \pm 5\,\mathrm{km\,s^{-1}}$ change associated with a factor ~ 100 increase in stellar mass. What is more apparent is an increase in σ_0 with redshift. In the lower left panel of Fig. 4.6 we show that for a fixed stellar mass the average velocity dispersions of KROSS and MUSE galaxies are $\sim$50 % higher than for the SAMI sample at $z \sim 0$.

In Fig. 4.6 we also investigate how dispersion is affected by global star formation rate. While there is little overlap between the datasets, the three samples combined indicate

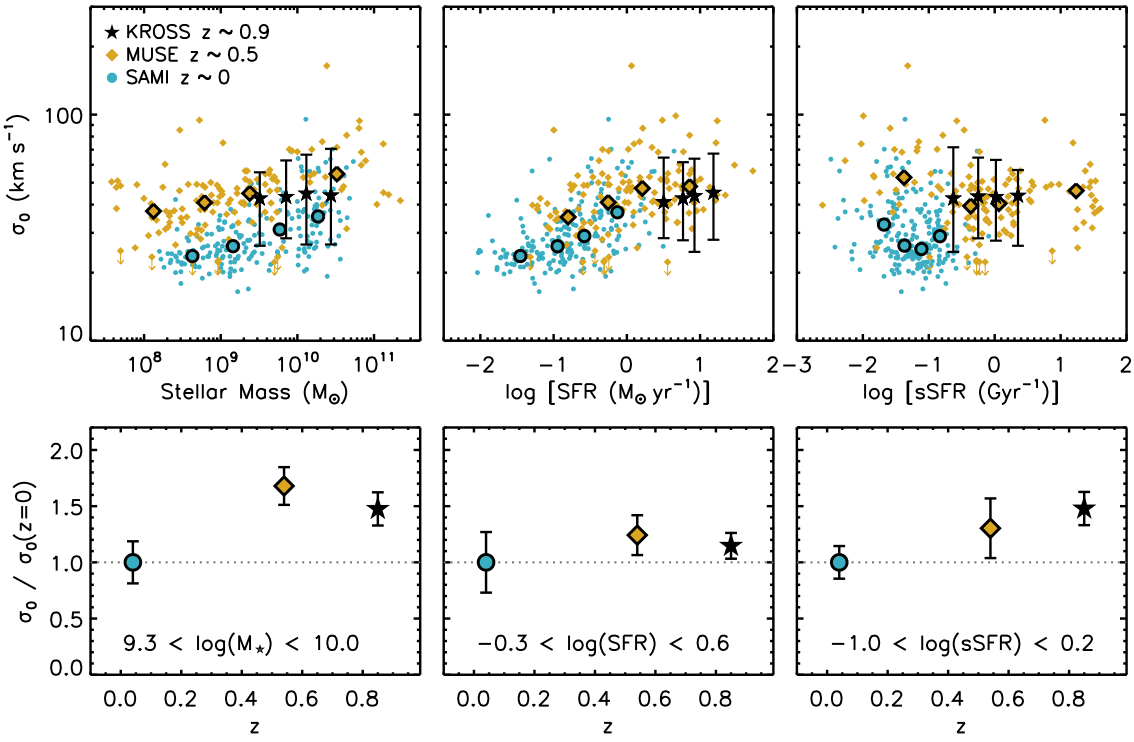

Figure 4.6: *Top:* Trends between velocity dispersion (σ_0) and a selection of non-kinematic properties, for KROSS galaxies (this study) and the two comparison samples outlined in §4.4.3. For the SAMI and MUSE samples we plot properties of individual galaxies and overlay medians within a series of x-axis bins (each containing 25% of the sample). For clarity, for KROSS galaxies we show only the median values, with error bars to represent the 1σ scatter. *Top Left:* Velocity dispersion versus stellar mass. At any given redshift there is no strong correlation between dispersion and stellar mass, however higher redshift galaxies appear to have larger dispersions. *Top Middle:* Velocity dispersion versus star formation rate. While there is little overlap in star formation rate between the three samples, we observe a weak trend of increasing dispersion with increasing star formation rate. *Top Right:* Velocity dispersion versus specific star formation rate. For individual samples we see no significant trend between dispersion and specific star formation rate, but again there appears to be an increase with redshift. *Bottom:* Velocity dispersion versus redshift, relative to the SAMI sample. We calculate the median dispersion of each sample over the same range in (left to right) $M_\star$, SFR or sSFR, and plot these values as a function of redshift. For fixed stellar mass or fixed sSFR we see a weak trend of increasing dispersion with redshift. For fixed SFR the values are consistent within the uncertainties.

a weak trend of increasing dispersion with increasing star formation rate. Although we observe only a $20-25\,\mathrm{km\,s^{-1}}$ change (a factor of ~ 2 increase) in σ_0 across three orders of magnitude in star formation rate, this result is consistent with a number of previous studies (e.g. Lehnert et al. 2009; 2013; Green et al. 2010; 2014; Le Tiran et al. 2011; Moiseev et al. 2015). Typically a weak trend is observed below $10\,\mathrm{M_\odot yr^{-1}}$ and it is only above this threshold that there is a strong increase in velocity dispersion with star formation rate. Few KROSS galaxies fit this criteria. Several authors have interpreted the relationship between star formation and dispersion as evidence of feedback driven turbulence, however Krumholz & Burkhart (2016) argue that turbulence driven by disk instability would manifest in a similar way. In §4.5 we investigate whether it is possible to distinguish between these two different scenarios using our dataset.

One way to normalise for differences in star formation rate and mass between samples is to plot the specific star formation rate (sSFR; SFR/$M_\star$). In the top right panel of Fig. 4.6 we plot velocity dispersion against sSFR, and find that for all three samples σ_0 is remarkably constant. There is a variation of less than $5\,\mathrm{km\,s^{-1}}$ across an order of magnitude in sSFR for KROSS and SAMI, and of less than $10\,\mathrm{km\,s^{-1}}$ across three orders of magnitude for the MUSE sample. In the panel below this we study the relationship between velocity dispersion and redshift, calculating the median of each sample for a fixed range in sSFR. It is difficult to make a robust comparison since the SAMI galaxies tend to have a much lower specific star formation rate, however there appears to be a systematic increase in dispersion with redshift. We see an increase of $\sim 50\%$ between $z \sim 0$ and $z \sim 0.9$.

4.4.4 Dynamics in the Context of Galaxy Evolution

Kinematic studies at high-redshift suggest that star-forming galaxies at early times were dynamically "hot", with velocity dispersions much larger than those observed for disks in the local Universe. In this section we examine how the KROSS galaxies fit within a wider evolutionary context, comparing their dynamics to those of the SAMI and MUSE samples discussed in §4.4.3 and five additional comparison samples between $0 < z < 2.5$. For this comparison we include data from the GHASP (Epinat et al. 2010; $\log(M_\star^{\mathrm{avg}}/\mathrm{M_\odot}) = 10.6$), KMOS$^{3\mathrm{D}}$ (Wisnioski et al. 2015; $\log(M_\star^{\mathrm{avg}}/\mathrm{M_\odot}) = 10.7$ and 10.9 for the $z \sim 1$ and 2 samples respectively), MASSIV (Epinat et al. 2012; $\log(M_\star^{\mathrm{avg}}/\mathrm{M_\odot}) = 10.5$), SIGMA (Simons

et al. 2016; $\log(M_\star^{\rm avg}/{\rm M}_\odot) = 10.0$) and SINS (Cresci et al. 2009; Newman et al. 2013; $\log(M_\star^{\rm avg}/{\rm M}_\odot) = 10.6$) surveys. These are all large samples ($\gtrsim 50$ galaxies) of "typical" star-forming galaxies, with star formation rates representative of the main sequence at a particular redshift. Beam smearing of the intrinsic velocity dispersion has been accounted for in each sample, either through disk modelling or post-measurement corrections. With the exception of GHASP (Fabry-Pérot) and SIGMA (MOSFIRE multi-object spectrograph), these are IFU-based studies.

In calculating average dispersion and v_C/σ_0 values, we note that different authors adopt different approaches. For example Wisnioski et al. (2015) consider only "disky" galaxies within the KMOS^{3D} sample, selected based on five criteria including $v_C/\sigma_0 > 1$, a smooth gradient within the velocity map ("spider diagram"; van der Kruit & Allen 1978), and a dispersion which peaks at the position of the steepest velocity gradient. However it is difficult to isolate a similar subset for each of the samples discussed here. For example, Epinat et al. (2010) have shown that up to 30% of rotators may be misclassified if a velocity dispersion central peak is required. Low spatial resolution may also lead kinematically irregular galaxies to be misidentified as rotators (e.g. Leethochawalit et al. 2016).

In the left panel of Fig. 4.7 we plot the median, mean and distribution of velocity dispersion measurements for each of the eight samples, as a function of redshift. As has been noted before, there is a gradual increase in the average velocity dispersion from $\sim 25\,{\rm km\,s^{-1}}$ at $z = 0$ to $\sim 50\,{\rm km\,s^{-1}}$ at $z = 2$. At $z \sim 1$ Wisnioski et al. (2015) report an average of $\sigma_0 = 25 \pm 5\,{\rm km\,s^{-1}}$ for the KMOS^{3D} sample, whereas for KROSS we measure a median of $\sigma_0 = 43.2 \pm 0.8\,{\rm km\,s^{-1}}$. We attribute this difference to the samples used to calculate the median. We restrict the KROSS, SAMI and MUSE samples to "rotationally dominated" galaxies, to be consistent with their sample, and plot the medians as open symbols. For KROSS we find a reduced median of $\sigma_0 = 36 \pm 2\,{\rm km\,s^{-1}}$, which is in better agreement.

There has been much discussion as to which physical processes drive the observed evolution of velocity dispersion with redshift. We explore the theoretical arguments in §4.5. However in this subsection we follow the analysis of Wisnioski et al. (2015), interpreting the results of Fig. 4.7 in the context of a rotating disk with a gas fraction and specific star formation rate that evolve as a function of redshift. In this simple model the

gas fraction of the disk is defined as in Tacconi et al. (2013):

$$f_{\rm gas} = \frac{1}{1+(t_{\rm dep}{\rm sSFR})^{-1}}, \tag{4.4.3}$$

where the depletion time evolves as $t_{\rm dep}({\rm Gyr}) = 1.5 \times (1+z)^{\alpha}$. From molecular gas observations of $z = 1-3$ galaxies, Tacconi et al. (2013) measure $\alpha = -0.7$ to -1.0, however the analytic models of Davé et al. (2012) predict $\alpha = -1.5$. Here $\alpha = -1.0$ is adopted as a compromise. The cosmic specific star formation rate is assumed to follow the evolution described in Whitaker et al. (2014), where

$${\rm sSFR}(M_\star, z) = 10^{A(M_\star)}(1+z)^{B(M_\star)}. \tag{4.4.4}$$

This sSFR relation was derived to fit UV+IR star formation rates of $\sim$39,000 galaxies in the redshift range $0.5 < z < 2.5$ (3D-*HST* survey; Momcheva et al. 2016). Finally, the Toomre disk stability criterion for a gas disk ($Q_{\rm g}$; Toomre 1964) can be rewritten in terms of $f_{\rm gas}$ (see Glazebrook 2013) as

$$\frac{v_{\rm C}}{\sigma_0} = \frac{a}{f_{\rm gas}(z, M_\star) Q_{\rm g}} \tag{4.4.5}$$

where $a = \sqrt{2}$ for a disk of constant rotational velocity. In the left panel of Fig. 4.7 we overplot the relationship between velocity dispersion and redshift derived for a range of stellar masses. Following the approach of Turner et al. 2017, the value of $Q_{\rm g} v_{\rm C}$ is set such that the $\log(M_\star/{\rm M}_\odot) = 10.0$ track is normalised to fit the median dispersion of the KROSS sample. For a marginally stable thin gas disk ($Q_{\rm g} = 1$), this requires a model rotation velocity of $v_{\rm C} = 150\,{\rm km\,s^{-1}}$. By comparison, we measure a median velocity for the KROSS sample of $v_{\rm C} = 118 \pm 4\,{\rm km\,s^{-1}}$. We note that the data in Fig. 4.7 do not demand a model of this exact form, particularly given the large 1σ scatter associated with some of the samples. However, these simple (observationally motivated) scaling relations do appear to provide a reasonable description of the data.

While these tracks provide useful guidance, we would typically expect the average rotation velocity, and not just the gas fraction, to vary as a function of mass. To eliminate this dependency, in the right panel of Fig. 4.7 we show how $v_{\rm C}/\sigma_0$ is expected to evolve

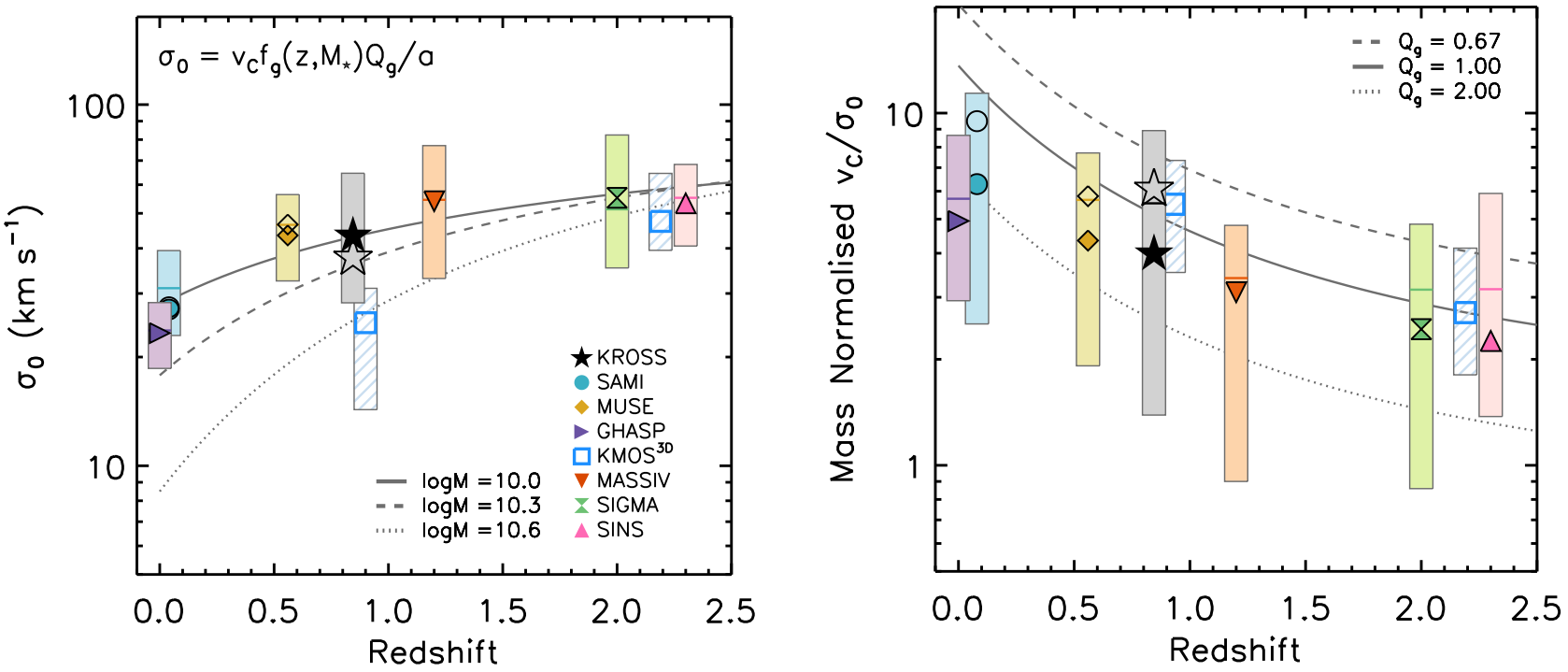

Figure 4.7: Velocity dispersion and (mass normalised) ratio between rotational velocity and velocity dispersion as a function of redshift. Alongside our results for KROSS we include the SAMI and MUSE samples described in §4.4.3 and five samples from the literature, chosen such that our measurements and beam smearing corrections are comparable. Filled symbols represent the median, horizontal lines the mean, and vertical bars the 16-84th percentile range. Open symbols for KMOS^{3D} represent the median of "rotationally dominated" galaxies only, and shaded bars represent the central 50% of the distribution. We plot open symbols for the KROSS, SAMI and MUSE samples for comparison, showing the median of galaxies with $v_C/\sigma_0 > 2$. *Left:* Intrinsic velocity dispersion as a function of redshift, with a simple Toomre disk instability model (Eq. 4.4.3–4.4.5) plotted for $\log(M_\star) = 10.0 - 10.6$. The value of $Q_g v_C$ is set such that the $\log(M_\star/M_\odot) = 10.0$ track is normalised to fit the median dispersion of the KROSS sample. The model appears to provide a good description of the data. *Right:* v_C/σ_0 as a function of redshift, with a simple disk model overlaid for $Q = 0.67 - 2$. Values have been normalised to a stellar mass of $\log(M_\star) = 10.5$. The data is broadly consistent with the model, and we observe a decrease in v_C/σ_0 with redshift. For KMOS^{3D} data was only available for "rotationally dominated" galaxies. If we consider the same subsample of KROSS our results are similar.

for a galaxy of stellar mass $\log(M_\star/\mathrm{M}_\odot) = 10.5$ and Toomre parameter of $Q_\mathrm{g} = 0.67$, 1 or 2. These are the critical values for a thick gas disk, thin gas disk and stellar-plus-gas disk, respectively (see e.g. Kim & Ostriker 2007). We then plot the median, mean and distribution of v_C/σ_0 values for the eight samples, normalising each to the stellar mass of the models. These correction factors range between $0.7-3.0$ with a median of 1.1 ± 0.2, with the largest applied to the SAMI sample (median $\log(M_\star/\mathrm{M}_\odot) = 9.3$).

The data follow the general trend described by the model, with a decrease from $v_\mathrm{C}/\sigma_0 \sim 6$ at $z = 0$ to $v_\mathrm{C}/\sigma_0 \sim 2$ at $z = 2$. This general trend is consistent with the results of Turner et al. (2017)[2]. The model predicts that this is due to higher gas fractions in galaxies at early times. Again we highlight the effect of restricting the KROSS, SAMI and MUSE samples to "rotationally dominated" galaxies, with open symbols. For KROSS, the median *mass-weighted* v_C/σ_0 increases from 3.9 ± 0.2 to 6.1 ± 0.2. This result is consistent with KMOS$^{3\mathrm{D}}$ at $z \sim 1$, who find $v_\mathrm{C}/\sigma_0 = 5.5$ (Wisnioski et al. 2015).

The right panel of Fig. 4.7 appears to suggest a weak trend between Toomre Q_g and redshift. We caution that Q_g is a galaxy averaged value, sensitive to systematics, and is therefore only a crude measure of disk stability. However to explore this potential trend, in Fig. 4.8 we plot the "best fit" Toomre parameter required to fit the observed median v_C/σ_0 for each of the samples, given their respective redshifts and stellar masses. To calculate error bars we propagate the typical uncertainties associated with measurements of the dynamics and stellar mass. Within the framework of this model, we find that lower redshift samples are associated with higher average values of Q_g.

This increase in Q_g is consistent with recent numerical simulations (Danovich et al. 2015; Lagos et al. 2017) and observational studies (Obreschkow et al. 2015; Burkert et al. 2016; Harrison et al. 2017; Swinbank et al. 2017) which suggest that the specific angular momentum of galaxy disks (j_s) increases with time. An increase in angular momentum would act to increase the global Q parameter, stabilising disks against fragmentation. Obreschkow et al. (2015) and Swinbank et al. (2017) suggest this is likely what drives the morphological transition between clumpy, irregular disks at high redshift, and the bulge-dominated galaxies with thin spiral disks we see today. Obreschkow et al. (2015) propose

[2]We note that for the GHASP sample, Turner et al. (2017) use the results from Epinat et al. (2008), whereas we use the results presented in Epinat et al. (2010).

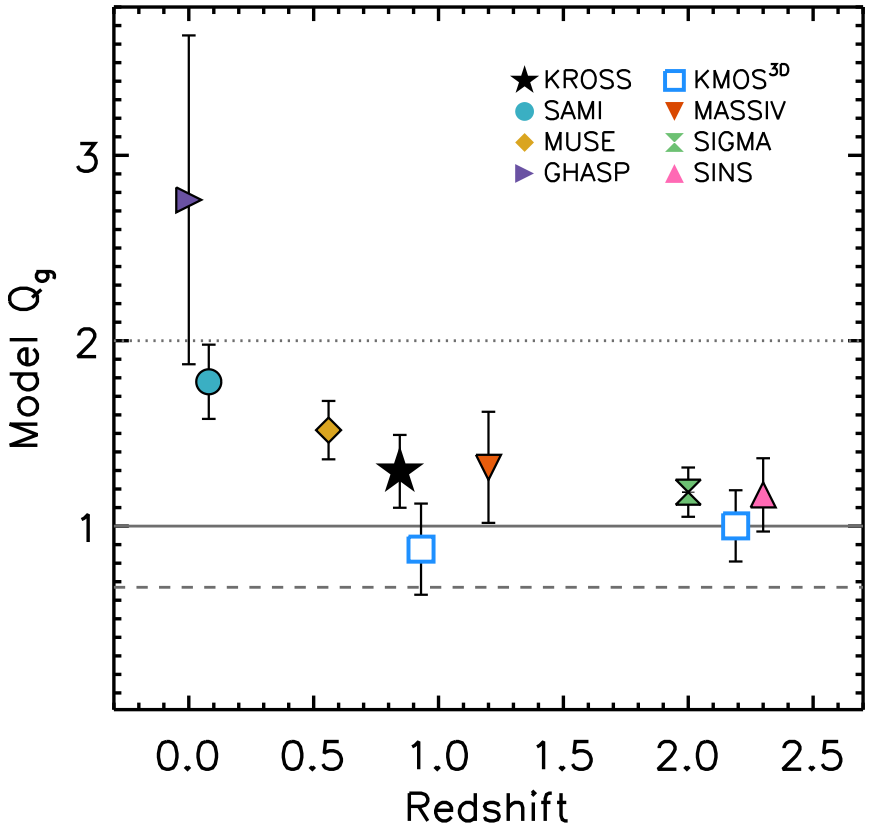

Figure 4.8: Inferred Toomre Q versus redshift for KROSS and comparison samples. Assuming a simple disk instability model (see §4.4.4 and Eq. 4.4.3–4.4.5), we calculate the Toomre Q parameter required to fit the average v_C/σ_0 observed for KROSS and various comparison samples, given their respective redshifts and stellar masses. Error bars reflect typical uncertainties associated with measurements of the stellar mass and dynamics. The lines overplotted at $Q_g = 0.67$, 1 and 2 represent the critical values for a thick gas disk, thin gas disk and stellar-plus-gas disk, respectively. We find that higher redshift samples are best fit by lower values of Q, which would suggest that these galaxies are more unstable disks.

that $Q \propto (1 - f_g) j_s \sigma_0$. Hence if the gas fraction decreases by a factor of four between $z \sim 2$ and $z \sim 0$ (e.g. Tacconi et al. 2010; Saintonge et al. 2013; Genzel et al. 2015), and the dispersion by a factor of two (Fig. 4.7), then a factor of ~ 2.6 increase in specific angular momentum would achieve the increase in disk stability suggested by Fig. 4.8.

The "toy model" described in this section is a useful tool, allowing us to interpret the evolution of galaxy dynamics in terms of gas fraction and disk instability. However it provides little information about the physical mechanisms involved. For a deeper understanding we must combine our observations with theoretical predictions.

4.5 The Origin of Disk Turbulence: Star Formation Feedback versus Gravitational Instability

Although the simple framework in §4.4.4 provides an adequate description of the data, other – more detailed – physical models have been proposed to explain the origin of these high turbulent motions. Turbulence in the interstellar medium (ISM) decays strongly within the disk crossing time (~ 15 Myr; Mac Low et al. 1998; Mac Low 1999; Stone et al. 1998), so a source of energy is clearly required to maintain disorder in the system. What this might be is the subject of active discussion, however a large and well-selected sample such as KROSS may be able to provide useful constraints. In this section we consider whether our data can be used to distinguish between two potential disk turbulence mechanisms.

One model is that the high level of turbulence is driven by stellar feedback. Supernovae and winds inject energy into the ISM, and several authors have identified a correlation between velocity dispersion and star formation rate, either on global or spatially resolved scales (e.g. Lehnert et al. 2009; 2013; Green et al. 2010; 2014; Le Tiran et al. 2011; but see Genzel et al. 2011). However simulations including only stellar feedback struggle to reproduce these large observed dispersions (Joung et al. 2009; Shetty & Ostriker 2012; Kim et al. 2013; 2014) without high rates of momentum injection (e.g. Hopkins et al. 2011; 2014).

An alternative framework is a clumpy, gas-rich disk fed by rapid accretion from the intergalactic medium (IGM). While accretion of material *onto* the disk appears in itself

insufficient to drive large velocity dispersions (e.g. Elmegreen & Burkert 2010; Hopkins et al. 2013, though see Klessen & Hennebelle 2010), simulations suggest that gravitational instabilities may induce high levels of turbulence (e.g. Aumer et al. 2010; Bournaud et al. 2010; 2014; Ceverino et al. 2010; Goldbaum et al. 2015; 2016) which can be sustained by the accretion of mass *through* the disk. As mass is transported inwards, the dispersion, and hence Q, is increased. Decay of this turbulence then acts to reduce Q, and eventually the disk saturates at a state of marginal stability. Several authors have considered whether gravitational interactions between clumps (formed via fragmentation of the disk) may also help to generate turbulence (Dekel et al. 2009; Aumer et al. 2010).

Krumholz & Burkhart (2016) noted that while the origins of disk turbulence have been explored in detail from a theoretical point of view, there had previously been few direct observational tests. To address this, the authors formulated two simple models – describing gravity-driven turbulence and feedback-driven turbulence – which could be used to make observational predictions. We outline each of these below.

4.5.1 Gravity-Driven Model

For a model in which turbulence is driven by gravitational instabilities in the gas, Krumholz & Burkhart (2016) adopt expressions for gas surface density (Σ) and velocity dispersion (σ) derived for the "steady state configuration" described in Krumholz & Dekel (2010). Within this framework the gas surface density depends on the total Toomre Q parameter (as opposed to that of the gas or stars alone; i.e. $Q_{\rm g}$ or $Q_{\star}$), since the turbulence is driven by a global instability of the disk. The Wang & Silk (1994) approximation is adopted such that $Q^{-1} = Q_{\rm g}^{-1} + Q_{\star}^{-1}$ and

$$Q \approx \frac{a v_{\rm C} \sigma f_{\rm g}}{\pi G r \Sigma}, \tag{4.5.6}$$

with $a = \sqrt{2}$. Here $v_{\rm C}$ is the rotational velocity measured at a radius of r, σ is the velocity dispersion and Σ is the gas surface density. It is expected that the disk self-regulates at $Q \approx 1$. Star formation is then added to the model assuming a so-called "Toomre regime" (Krumholz et al. 2012), in which the "entire ISM is a single star-forming structure". This is a key distinction between this model and the feedback-driven model discussed below.

Together, these assumptions lead to a star formation rate which depends on the velocity dispersion as

$$SFR = \frac{16}{\pi}\sqrt{\frac{\phi_P}{3}}\left(\frac{\varepsilon_{ff} v_C^2}{G}\ln\frac{r_1}{r_0}\right) f_g^2 \sigma, \tag{4.5.7}$$

where ε_{ff} is the star formation rate per freefall time, f_g the gas fraction, ϕ_P a constant to account for the presence of stars, and $\ln(r_1/r_0)$ relates to the radial extent of the disk.

4.5.2 Feedback-Driven Model

One way for analytic models to achieve large velocity dispersions via stellar feedback is to assume that the star formation efficiency within giant molecular clouds (GMCs) is closely coupled to the Toomre parameter of the gas disk (Q_g). Activity on the scale of GMCs is driven by self-gravity of the gas clouds and hence feedback-driven models do not require a global $Q \approx 1$ provided $Q_g \approx 1$. The expression for the gas Toomre parameter is similar to Eq. 4.5.6,

$$Q_g \approx \frac{a v_C \sigma}{\pi G r \Sigma}. \tag{4.5.8}$$

In their model Krumholz & Burkhart (2016) adopt the star-forming relation of Faucher-Giguère et al. (2013), which balances the momentum per unit mass ($p_\star/m_\star$) injected by feedback against the gas surface density squared. This results in a relationship between star formation rate and velocity dispersion of

$$SFR = \frac{8\sqrt{2}\phi v_C^2}{\pi G Q_g \mathcal{F}}\left(\ln\frac{r_1}{r_0}\right)\left(\frac{p_\star}{m_\star}\right)^{-1}\sigma^2, \tag{4.5.9}$$

where ϕ and $\mathcal{F}$ are constants associated with various model uncertainties. There are two key differences between this and the gravity-driven model. Firstly, since stellar feedback depends on the amount of gas unstable to gravitational collapse, we assume $Q_g \approx 1$ and not $Q \approx 1$. As a consequence, Eq. 4.5.9 does not depend on f_g. Secondly, the star formation rate is more strongly dependent on the velocity dispersion than for a gravity-driven model. For turbulence to balance gravity in the ISM the star formation rate density must be proportional to the gas surface density squared. Since $\Sigma \propto \sigma$ for constant Q_g, we therefore obtain $\mathrm{SFR} \propto \sigma^2$, as opposed to $\mathrm{SFR} \propto \sigma$ for the gravity-driven model (Eq.4.5.7).

4.5.3 Comparison of Models to Observations

KROSS offers a large and representative sample of ~ 500 star-forming galaxies, with velocity dispersions measured and corrected for beam smearing in a consistent way. This is an ideal opportunity to test predictions of the aforementioned analytic models. Krumholz & Burkhart (2016) compared observational data to their models of feedback-driven and gravity-driven turbulence. However, while this data covers many orders of magnitude in star formation rate, it consists of samples of differing selection criteria, redshift and data quality.

4.5.3.1 Model Tracks

In Fig. 4.9 we plot velocity dispersion against star formation rate for KROSS and overlay the models of Krumholz & Burkhart (2016)[3]. In the top left panel we plot trends for a feedback-driven model, adopting the median rotation velocity of the sample ($\sim 120\,\mathrm{km\,s^{-1}}$) and Toomre $Q_\mathrm{g} = 0.5$, 1.0 and 2.5. These tracks show only a moderate increase in velocity dispersion with star formation rate, which is consistent with our data. For KROSS, galaxies in the lower quartile of star formation rate have a median dispersion of $42 \pm 2\,\mathrm{km\,s^{-1}}$ and those in the upper quartile a median of $45 \pm 2\,\mathrm{km\,s^{-1}}$. The dispersion predicted by the model is much more sensitive to rotation velocity than Q_g. The shaded region around the $Q_\mathrm{g} = 1.0$ track shows the effect of adjusting the rotation velocity of the model by $20\,\mathrm{km\,s^{-1}}$, with larger values of v_C corresponding to smaller values of σ_0. The 68th percentile range for our sample is $44 - 204\,\mathrm{km\,s^{-1}}$, so it is possible that datapoints are consistent with a narrow range of Q_g if this effect dominates the scatter.

In the top right panel of Fig. 4.9 we show trends for a gravity-driven model, with the same rotation velocity and gas fractions of $f_\mathrm{g} = 0.2$, 0.5 and 1.0. These models predict a sharp increase in velocity dispersion with star formation rate, however this is not something seen in the data – we measure $\sigma_0 \geq 100\,\mathrm{km\,s^{-1}}$ for only a handful of KROSS galaxies. The expected velocity dispersion is very sensitive to the input rotation velocity and gas fraction. Despite our data being predominately low dispersion, this model may still be valid if the galaxies have a wide range in these other properties.

[3]We adopt the same fiducial values of $\epsilon_\mathrm{ff} = 0.01$, $\phi_\mathrm{P} = 3$, $r_1 = 10$, $r_0 = 0.1$, $\phi = 1$, $\mathcal{F} = 2$ and $p_\star/m_\star = 3000$

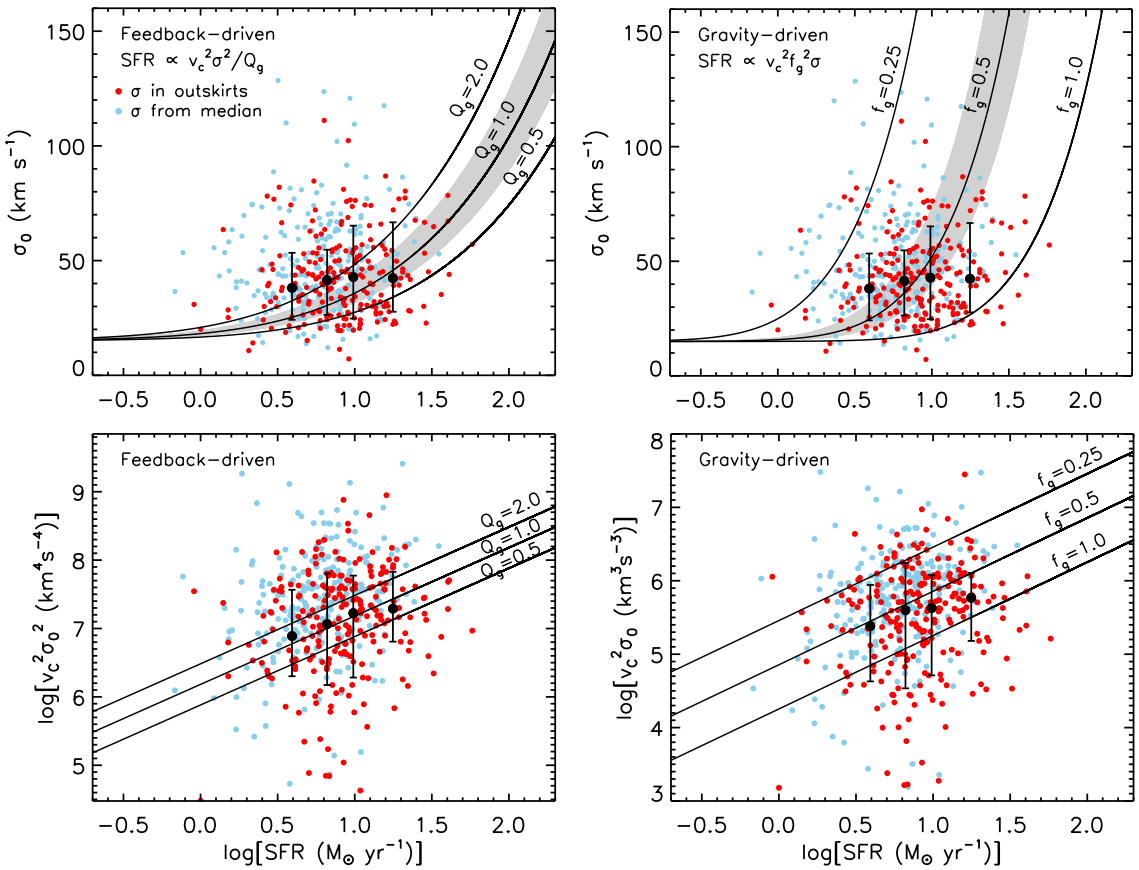

Figure 4.9: Properties of KROSS galaxies compared to predictions of the analytic models discussed in §4.5. Points are coloured by the technique used to measure the velocity dispersion, σ_0. Large black symbols show the median dispersion (and standard deviation) in bins of star formation rate. *Top Left:* Predictions of a model in which turbulence is driven by star formation feedback (see §4.5.2, Eq. 4.5.9) assuming the median rotation velocity of the sample ($v_C \approx 120\,\mathrm{km\,s^{-1}}$) and a gas Toomre parameter of $Q_g = 0.5$, 1.0, 2.0. The shaded region shows the impact of increasing/decreasing the rotation velocity by $20\,\mathrm{km\,s^{-1}}$; the 68th percentile range of our data is $v_C = 44-204\,\mathrm{km\,s^{-1}}$ so we would expect a large amount of scatter even if only one value of Q_g was valid. *Top Right:* Predictions of a model in which turbulence is driven by gravitational instabilities (see §4.5.1, Eq. 4.5.7), assuming the median v_C and gas fractions of $f_g = 0.25$, 0.5, 1.0. This model results in a much steeper increase in σ_0 as a function of star formation rate. We measure $\sigma_0 \geq 100\,\mathrm{km\,s^{-1}}$ for only a handful of KROSS galaxies, and do not observe a strong trend with star formation rate. However this model could still be valid if the galaxies have a wide range of rotation velocities and/or gas fractions. *Bottom:* To eliminate dependency on the rotation velocity, we also plot $\log(v_C^2\sigma_0^2)$ and $\log(v_C\sigma_0^2)$ as a function of star formation rate for the feedback- and gravity-driven model, respectively. Both models provide an adequate description of the data, however there is a large amount of residual scatter. This could be due to measurement uncertainties, an intrinsic variation of Q_g and f_g, or (most likely) a combination of these two factors.

To eliminate this dependency on rotation velocity, in the lower panels of Fig. 4.9 we plot $\log(v_C^2\sigma_0^2)$ and $\log(v_C\sigma_0^2)$ as a function of star formation rate for the feedback- and gravity-driven model, respectively. The median properties of the KROSS sample follow trends similar to those predicted by the models. Each provides an adequate description of the data, however there is a large amount of residual scatter. This could be due to measurement uncertainties, an intrinsic variation of Q_g and f_g, or a combination thereof.

We note that low dispersion galaxies ($\sigma_0 \leq 20\,\mathrm{kms}^{-1}$, scattered below the model trends) tend to be smaller compared to the seeing, and as such have larger beam smearing corrections (see §4.3.6). This sample has a median of $R_d/R_{PSF} = 0.35 \pm 0.08$, as opposed to $R_d/R_{PSF} = 0.61 \pm 0.02$ for all KROSS galaxies. In this situation it is more difficult to recover the intrinsic velocity dispersion. Galaxies that lie *above* the model trends tend to be those where the dispersion comes from the median of all available pixels. As discussed in §4.3.5, these measurements are associated with larger uncertainties.

4.5.3.2 Best-Fit Model Toomre Q and Gas Fractions

Directly comparing the observed velocity dispersions to those predicted by the analytical models is a poor test of gravity-driven versus feedback-driven turbulence. Offsets for the feedback-driven model tend to be smaller than for the gravity-driven model, since the latter has a much steeper relationship between star formation rate and velocity dispersion. An alternative approach is to calculate the Toomre parameter and gas fraction required for each galaxy to be fit by the models. These are properties which we can also estimate directly from the observations, independent of any turbulence model, with a few simple assumptions. By comparing these two sets of parameters, we can test which model provides a better fit to the data.

In Fig. 4.10 we compare the distribution of Toomre Q_g values inferred from the feedback-driven turbulence model (rearranging Eq. 4.5.9) to those estimated using Eq. 4.5.8. To estimate the gas surface density we calculate the star formation rate surface density and then invert the Kennicutt-Schmidt relation, $\Sigma_{SFR} = A\,\Sigma_{gas}^n$, where $A = 1.5 \times 10^{-4}\,\mathrm{M_\odot yr^{-1} pc^{-2}}$ and $n = 1.4$ (Kennicutt 1998b; for a Chabrier IMF). We find a median of $Q_{g,med} = 1.6 \pm 0.2$ for the model and $Q_{g,med} = 1.01 \pm 0.06$ for the empirically derived values (close to the $Q_g \sim 1$ expected for a marginally unstable disk). The model

distribution is noticeably broader, with a 68th percentile range of 7.0 as opposed to 2.1 for the empirically derived values.

In Fig. 4.10 we also compare gas fractions inferred from the gravity-driven turbulence model (rearranging Eq.4.5.7) to those calculated using the inverse Kennicutt-Schmidt relation. We estimate the gas mass within twice the half-light radius, and then express this as a fraction of the total baryonic mass $f_{\rm g} = M_{\rm g}/(M_{\rm g} + M_\star)$. We find a median of $f_{\rm g,med} = 0.52 \pm 0.02$ for the model and $f_{\rm g,med} = 0.45 \pm 0.01$ for the empirically derived values. In comparison, the relations described in §4.4.4 predict an average gas fraction of $f_{\rm g} = 0.41 \pm 0.02$. The model distribution is again the broadest, with a 68th percentile range of 0.95 compared to 0.44 for the observations, and this additional scatter results in unphysical values of $f_{\rm g} > 1$ for $\sim 25\%$ of galaxies.

Both models appear to be consistent with the data and, as such, we are unable to definitively rule out either turbulence mechanism. Firstly, the medians of the distributions for model and empirically derived quantities are very similar. For the gravity-driven model, increasing the star formation rate per freefall time from $\epsilon_{\rm ff} = 0.01$ to 0.013 in Eq. 4.5.7 would eliminate the offset completely (note Federrath 2013; 2015 suggest values between $\epsilon_{\rm ff} = 0.01$–0.02). For the feedback-driven model this could be achieved by adjusting $\mathcal{F} = 2$ to $\mathcal{F} = 3$ in Eq. 4.5.9. This dimensionless normalisation parameter ensures that the model fits observations of the relationship between gas surface density and star formation rate surface density (Fig. 4 of Faucher-Giguère et al. 2013). Such an increase would be inconsequential in this regard.

Secondly, although the distributions of the best-fit model parameters are much broader and include unphysical or implausible values (e.g. $f_{\rm g} > 1$ or $Q_{\rm g} > 100$), this is likely due to measurement uncertainties. Estimates of the Toomre $Q_{\rm g}$ parameter for the model have a stronger dependence on rotation velocity and velocity dispersion than the observational estimates. Similarly, best-fit model gas fractions depend on $v_{\rm C}$ and σ but the observational estimates do not. These dynamical parameters are the largest source of uncertainty and as such, fractional errors associated with model $Q_{\rm g}$ and $f_{\rm g}$ values are approximately twice as large as for the empirically derived values.

Direct observation of the molecular gas component would help to provide further constraints. If turbulence in the ISM is gravity-driven, we would expect the velocity dis-

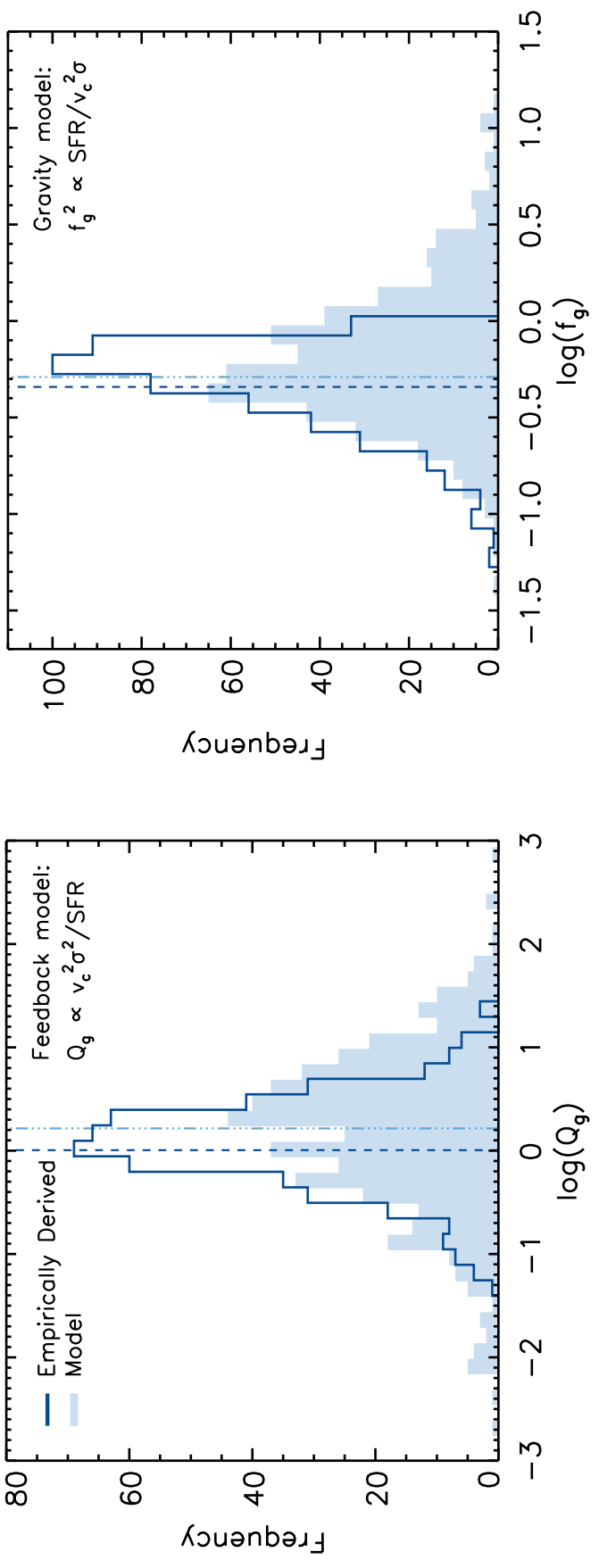

Figure 4.10: Toomre parameters and gas fractions required for the turbulence models in §4.5 to fit KROSS galaxies, compared to estimates of these properties made from observations. Dashed vertical lines show the median of each distribution. *Left:* Model (Eq. 4.5.9, filled histogram) versus empirically derived (outlined histogram) Toomre Q_g. The model distribution is broader and has a slightly larger median – $Q_{g,med} = 1.6 \pm 0.2$ as opposed to $Q_{g,med} = 1.01 \pm 0.06$. *Right:* Model (Eq. 4.5.7, filled histogram) versus empirically derived (outlined histogram) gas fractions. Model values have a similar median – $f_{g,med} = 0.52 \pm 0.02$ versus $f_{g,med} = 0.45 \pm 0.01$. In both panels the offset between distributions is small, and could be accounted for with a minor adjustment in model parameters. We are unable to definitively rule out either turbulence model. Uncertainties associated with the best-fit model parameters are approximately twice as large, which may explain why these distributions are broader.

persion to be strongly dependent on the gas fraction ($\sigma \propto 1/f_g^2$). However in a feedback-driven scenario, the two properties should not be related. Alternatively, both mechanisms may contribute. Krumholz et al. (2017) predict a transition from mostly gravity-driven turbulence at high redshift, to feedback-driven turbulence at low redshift. They argue that this evolution would explain why bulges form at high redshift and disks form at lower redshift. Galaxies at $z \sim 0.9$ (of a similar mass to the KROSS sample) would be expected to have a ratio between star formation-supported dispersion (σ_{SF}) and total gas velocity dispersion (σ_g) of $\sigma_{SF}/\sigma_g \sim 0.3-0.4$. In this context, it would be unsurprising that we are unable to rule out either model.

4.6 Conclusions

In this work we have analysed the velocity dispersion properties of 472 Hα-detected star-forming galaxies observed as part of KROSS (Stott et al. 2016; Harrison et al. 2017). KROSS is the largest near-infrared IFU survey of $z \sim 1$ galaxies to date, and consists of a mass- and colour-selected sample which is typical of the star-forming "main sequence" at this redshift. Our key results are as follows:

- Galaxies at this epoch are highly turbulent with large intrinsic velocity dispersions. We measure a median dispersion of $\sigma_0 = 43.2 \pm 0.8\,\mathrm{km\,s^{-1}}$ and rotational velocity to dispersion ratio of $v_C/\sigma_0 = 2.6 \pm 0.1$ for galaxies with stellar masses of $\log(M_\star/M_\odot) = 8.7-11.0$. Although dynamically hotter than their local counterparts, the majority of our sample are rotationally dominated ($83 \pm 5\,\%$). We observe a strong increase in v_C/σ_0 with increasing stellar mass: evidence of "kinematic downsizing".

- We combine KROSS with data from SAMI ($z \sim 0.05$; Croom et al. 2012) and an intermediate redshift MUSE survey ($z \sim 0.5$; Swinbank et al. 2017) to explore the relationship between intrinsic velocity dispersion, stellar mass and star formation rate. At a given redshift we see, at most, a $\sim 15\,\mathrm{km\,s^{-1}}$ increase in dispersion for a factor ~ 100 increase in stellar mass.

- All three samples (SAMI, MUSE and KROSS) are consistent with a weak increase

in velocity dispersion with increasing star formation rate. We see an increase of $20-25\,\mathrm{km\,s^{-1}}$ across three orders of magnitude in star formation rate. This trend appears to be independent of redshift.

- At a given redshift the average velocity dispersion is consistent across several orders of magnitude in specific star formation rate. Normalising for the effects of star formation rate and stellar mass, we see a $\sim 50\%$ increase in velocity dispersion between $z \sim 0$ and $z \sim 0.9$.

- To understand the dynamics of KROSS in a wider evolutionary context, we consider five additional samples between $0 < z < 2.5$. We find an increase in the average velocity dispersion with redshift, from $\sigma_0 \sim 25\,\mathrm{km\,s^{-1}}$ at $z = 0$ to $\sigma_0 \sim 50\,\mathrm{km\,s^{-1}}$ at $z = 2$. After normalising for the effects of stellar mass, we also find a decrease in the average v_C/σ_0 ratio for a $\log(M_\star/\mathrm{M}_\odot) = 10.5$ galaxy, from $v_C/\sigma_0 \sim 6$ at $z = 0$ to $v_C/\sigma_0 \sim 2$ at $z = 2$.

- We show that the observed evolution in galaxy dynamics can be reasonably well described by a simple "toy model", in which galaxies are asummed to be thin disks of constant rotational velocity with higher gas fractions at early times. To provide the best possible fit to the data, this model would require lower redshift samples to be associated with higher average values of Toomre Q_g (a more stable gas disk).

- Finally, we test the predictions of two different analytical models – one which assumes turbulence is driven by stellar feedback and another which assumes it is driven by gravitational instabilities. Each predicts a different relationship between star formation rate and velocity dispersion, with tracks parameterised by Toomre Q_g or gas fraction, respectively. We find that both models provide an adequate description of the data, with best-fit parameters close to what we derive independently from the observations, using a different set of assumptions. Direct measurement of the gas fraction, f_g, would help to provide further constraints.

4.7 KROSS Catalogue

With Harrison et al. (2017) we released a catalogue of all 586 Hα detected galaxies in the KROSS sample. This is available online at `http://astro.dur.ac.uk/KROSS`. With the release of Johnson et al. (2017) on the arXiv, we have updated this catalogue to include all velocity dispersion measurements and related quantities. Examples of this additional data are provided in Table 4.1.

Table 4.1: Intrinsic velocity dispersion and related quantities

Name	RA (J2000)	Dec (J2000)	z	$\sigma_{0,\mathrm{obs}}$ (km s^{-1})	σ_0 (km s^{-1})	Flag	R_d / R_PSF	Q_g
C-HiZ_z1_111	+49:55:07	00:08:27.2	0.8498	79 ± 40	53 ± 27	M	0.8 ± 0.2	$2.5^{+1.8}_{-1.6}$
C-HiZ_z1_112	+49:55:13	00:09:08.0	0.8539	33 ± 13	33 ± 13	O	0.4 ± 0.1	$0.1^{+0.1}_{-0.1}$
C-HiZ_z1_186	+50:08:04	00:09:05.5	0.8445	46 ± 3	45 ± 3	O	0.3 ± 0.1	$0.2^{+0.1}_{-0.1}$
C-HiZ_z1_195	+50:08:40	00:08:58.0	0.8454	22 ± 5	22 ± 5	O	0.5 ± 0.2	$0.5^{+0.3}_{-0.2}$
C-HiZ_z1_215	+50:11:50	00:09:08.7	0.8441	12 ± 3	11 ± 3	O	0.6 ± 0.2	$1.3^{+2.7}_{-0.9}$
C-HiZ_z1_224	+50:13:05	00:08:27.7	1.0137	46 ± 23	40 ± 20	M	0.7 ± 0.2	$0.9^{+0.7}_{-0.6}$
C-HiZ_z1_230	+50:13:39	00:09:02.1	0.8445	48 ± 3	46 ± 3	O	0.2 ± 0.1	$0.6^{+0.3}_{-0.3}$
C-HiZ_z1_231	+50:13:40	00:08:38.6	0.8377	58 ± 2	55 ± 2	O	0.3 ± 0.1	$0.1^{+0.1}_{-0.1}$
C-HiZ_z1_235	+50:14:02	00:08:30.2	0.8378	85 ± 42	37 ± 18	M	0.3 ± 0.1	$0.8^{+0.9}_{-0.6}$
C-HiZ_z1_245	+50:15:26	00:07:27.4	0.8334	66 ± 33	52 ± 26	M	1.0 ± 0.3	$1.7^{+1.2}_{-1.1}$
C-HiZ_z1_246	+50:15:33	00:09:17.8	0.8422	51 ± 26	32 ± 16	M	0.5 ± 0.1	$0.8^{+0.6}_{-0.6}$
C-HiZ_z1_251	+50:15:57	00:09:20.7	0.8544	57 ± 10	45 ± 8	O	0.2 ± 0.1	$0.9^{+0.6}_{-0.5}$
C-HiZ_z1_255	+50:16:17	00:09:19.6	0.8502	41 ± 21	34 ± 17	M	0.9 ± 0.3	$1.4^{+1.0}_{-0.9}$
C-HiZ_z1_257	+50:16:24	00:09:05.6	0.8501	73 ± 14	66 ± 13	O	0.3 ± 0.1	$0.9^{+0.6}_{-0.5}$
C-HiZ_z1_258	+50:16:25	00:07:31.8	0.8376	43 ± 21	38 ± 19	M	1.3 ± 0.4	$2.1^{+1.5}_{-1.4}$
C-HiZ_z1_263	+50:17:11	00:08:42.1	0.8370	41 ± 10	40 ± 10	O	0.3 ± 0.1	$0.3^{+0.2}_{-0.2}$
...	...	...	...	...	...	...	...	...

NOTES: A catalog of all 586 Hα detected galaxies in the KROSS sample is available online at `http://astro.dur.ac.uk/KROSS`. Columns $\sigma_{0,\mathrm{obs}}$ and σ_0 are the observed and beam smearing corrected velocity dipersions, respectively. Corrections were applied as a function of $R_\mathrm{d}/R_\mathrm{PSF}$ – the ratio between the disk radius (in arcsec) and half of the seeing FWHM (see §4.3.6). We flag whether the dispersion was measured in the outskirts of the disk (O), or from the median of all available pixels (M). We also provide the global Toomre Q_g parameter for each galaxy, which we derived by inverting the Kennicutt-Schmidt relation to estimate Σ_gas.

CHAPTER 5

The KMOS Redshift One Spectroscopic Survey (KROSS): The Relationship Between Galaxy Dynamics and Optical Morphology

Preamble

In Chapter 4 we introduced the KMOS Redshift One Spectroscopic Survey (KROSS; Stott et al. 2016). With 795 targets observed, this is a rich dataset with which to study the ionised gas kinematics of typical $z \sim 0.9$ star-forming galaxies (Tiley et al. 2016; Harrison et al. 2017). One aspect we have not yet explored in detail is how galaxy dynamics may relate to optical morphology. In this chapter we present a preliminary analysis, combining the dynamical measurements of Chapter 4 with deep *HST* imaging of 231 galaxies.

5.1 Introduction

The rest-frame UV/optical morphologies of many high redshift star-forming galaxies are disordered and irregular, dominated by luminous $\sim$kpc scale clumps (e.g. Elmegreen et al. 2009; Förster Schreiber et al. 2011; Guo et al. 2015; Shibuya et al. 2016). It is only at $z \sim 1.5$ that spirals and ellipticals outnumber peculiar galaxies (e.g. Conselice et al. 2011; Buitrago et al. 2013; Mortlock et al. 2013) and the Hubble sequence begins to take form. Understanding what drives this transition is essential for theories of galaxy formation and evolution.

A key theoretical expectation of ΛCDM is that the specific angular momentum of dark matter halos, and hence galaxy disks, increases over time. This is supported by a number

of recent hydrodynamical simulations (e.g. Danovich et al. 2015; Lagos et al. 2017) and observational studies (e.g. Obreschkow et al. 2015; Burkert et al. 2016; Harrison et al. 2017; Swinbank et al. 2017). A consensus is now beginning to emerge that this kinematic evolution is what drives such a dramatic morphological change. Obreschkow et al. (2015) propose a simple model in which the global instability of a disk is related to its specific angular momentum (j_s), stellar mass (M_s), velocity dispersion (σ_0) and gas fraction (f_g) as $Q \propto M_s^{-1}(1-f_g)j_s\sigma_0$. This suggests that while large amounts of cold gas are required to fuel the intense bursts of star formation at high redshift (e.g. Daddi et al. 2010; Tacconi et al. 2010; 2013), it is low angular momentum which acts to destabilise the disk and provide the trigger.

If angular momentum and Toomre Q increase together over time, this would explain important differences between low and high redshift galaxies. At $z \sim 0$, star-forming galaxies are settled into thin, rotationally supported disks of $Q \sim 2$ (Westfall et al. 2014). In these galaxies, star formation is a local process, and gravitational instabilities within spiral arms result in giant molecular clouds (GMCs) of typically $10^5 - 10^6\,M_\odot$ (e.g. Larson 1981; Elmegreen 1989). This is in sharp contrast to high redshift, where *global* instabilities cause the disk to fragment into giant star-forming clumps of $10^8 - 10^9\,M_\odot$ (e.g. Elmegreen et al. 2007; Guo et al. 2012). Galaxies subsequently self-regulate close to $Q \sim 1$ (e.g. Wisnioski et al. 2015; Swinbank et al. 2017, Chapter 4).

In recent years, significant progress has been made in understanding how the morphology of distant galaxies relates to their colours, masses, and star formation rates (e.g. see Conselice 2014 for review). Much work has also been done to establish the properties of star-forming clumps (e.g. Förster Schreiber et al. 2011; Genzel et al. 2011; Livermore et al. 2012; 2015; Swinbank et al. 2012a; Wuyts et al. 2012). Depending on the effectiveness of feedback prescriptions, numerical simulations disagree as to whether the clumps eventually migrate inwards, coalescing to form a bulge (e.g. Ceverino et al. 2010; Bournaud et al. 2014; Mandelker et al. 2017), or are quickly torn apart by tidal stripping and intense outflows (e.g. Hopkins et al. 2012; Zolotov et al. 2015; Oklopčić et al. 2017).

What is increasingly clear is that morphology and galaxy dynamics are closely linked. In Chapter 4 we introduced KROSS – a survey of 795 $z \sim 0.9$ star-forming galaxies observed using the KMOS spectrograph (Stott et al. 2016; Harrison et al. 2017). Approxi-

mately one-third of this sample have both spatially-resolved Hα kinematics and *Hubble Space Telescope* (*HST*) imaging. However we have not yet explored in any detail how the two relate. Our aim in this work is therefore to address this, exploring how optical morphology varies with the kinematic properties derived in Chapter 4.

5.2 Analysis

So far, we have primarily used the broad-band imaging of KROSS galaxies to aid our kinematic analysis (Harrison et al. 2017, Chapter 4). From optical *HST* observations and ground-based near infrared images, we measured the half-light radius ($R_{1/2}$), inclination (θ) and position angle (PA_{im}) of each galaxy. Applying these values to the Hα dynamical maps then allowed us to make estimates of rotation velocity (v_C) and intrinsic velocity dispersion (σ_0). However, there is the potential to learn much more from these images. In this chapter we explore the relationship between galaxy dynamics and optical morphology, using a subset of KROSS with the highest quality broad-band imaging.

Of 586 Hα-detected galaxies in our sample, 234 have *HST* imaging. These data come from four separate surveys: (1) CANDELS (Grogin et al. 2011; Koekemoer et al. 2011); (2) ACS COSMOS (Leauthaud et al. 2007); (3) GEMS (Rix et al. 2004) and (4) observations under *HST* proposal ID 9075 (Amanullah et al. 2010). Of these images, 36% are WFC3 H-band observations (FWHM ≈ 0.2 arcsec), 57% are ACS I-band and 7% are ACS z-band (each FWHM ≈ 0.1 arcsec). All but three galaxies are classified as "quality 1" (spatially resolved, with θ and $R_{1/2}$ measured directly from the imaging; see Harrison et al. 2017), and it is this sample that we take forward for further analysis. A complete set of 231 *HST* thumbnails is provided in Appendix A.

5.2.1 Visual Inspection

We begin our analysis with a simple visual assessment, ordering the thumbnails of galaxies as a function of their various dynamical properties. The first parameter we consider is the intrinsic velocity dispersion, σ_0, which we studied in detail in Chapter 4. This measures turbulence within the ISM, and as such, we may naïvely expect high dispersion galaxies to appear more disordered. In Fig. 5.1 we show a selection of *HST* images for KROSS galaxies of a similar stellar mass ($9.7 < \log(M_\star/M_\odot) < 10.1$), ranked by in-

creasing velocity dispersion. We observe a variety of morphologies at both high and low dispersion (with evidence of extended disks, spiral arms and clumps), however more compact galaxies appear to be associated with larger values of σ_0. One possibility is that these galaxies have unresolved rotation which, as a result of beam smearing (see Chapter 3), manifests as a higher dispersion (e.g. Newman et al. 2013). Another is that there is a single, bright region within a "clump cluster" galaxy that dominates the emission.

Compact star-forming galaxies may also be associated with quenching. Recent studies have suggested that a fraction of $z > 1$ star-forming galaxies undergo a process of "fast compaction", leading to the formation of massive, gas-rich bulges (e.g. Barro et al. 2013; 2014a; 2016; Dekel & Burkert 2014; Zolotov et al. 2015; Tadaki et al. 2017). This can be triggered by mergers or an internal redistribution of angular momentum. The latter is thought to be particularly effective in high-redshift disk galaxies (e.g. Immeli et al. 2004; Genzel et al. 2008; Bournaud et al. 2014), where viscous dissipation can drive gas and stars inwards, forming a dense central core in just a few 100Myr (Dekel et al. 2009). Due to their high central mass concentration, these "compacted" galaxies would likely have high (stellar and gas) velocity dispersions (e.g. Barro et al. 2014b; Nelson et al. 2014). Eventually, star formation would be quenched, as the bulge exhausts the remaining gas supply or stabilises it against further collapse.

We can also study how morphology relates to v_C/σ_0, the ratio between rotational velocity and velocity dispersion, and Toomre Q_g, which describes how unstable the gas is to gravitational collapse. As explained in §5.1, we expect high angular momentum, high Q galaxies to be settled into rotationally supported disks with fewer clumps. In order to control for trends with stellar mass or galaxy size, we first select an appropriate subsample. In Fig. 5.2 we show v_C/σ_0 (left panel) and Q_g (right panel) against disk radius for galaxies within a stellar mass bin of $9.7 < \log(M_\star/M_\odot) < 10.1$. For a fixed stellar mass and velocity dispersion, we expect the rotation velocity to vary as $v_C^2 \propto 1/r$ and disk stability as $Q \propto r$. We overplot these trends for guidance, normalised to fit the data. Larger galaxies indeed appear to have higher values of Q and slightly lower v_C/σ_0. To avoid these biases, we therefore select a subsample of galaxies within the shaded regions of Fig. 5.2, with radii of $1.5 < R_d < 2.4$ kpc.

In Fig. 5.3 we display the *HST* thumbnails for this subsample, ranked by an increasing

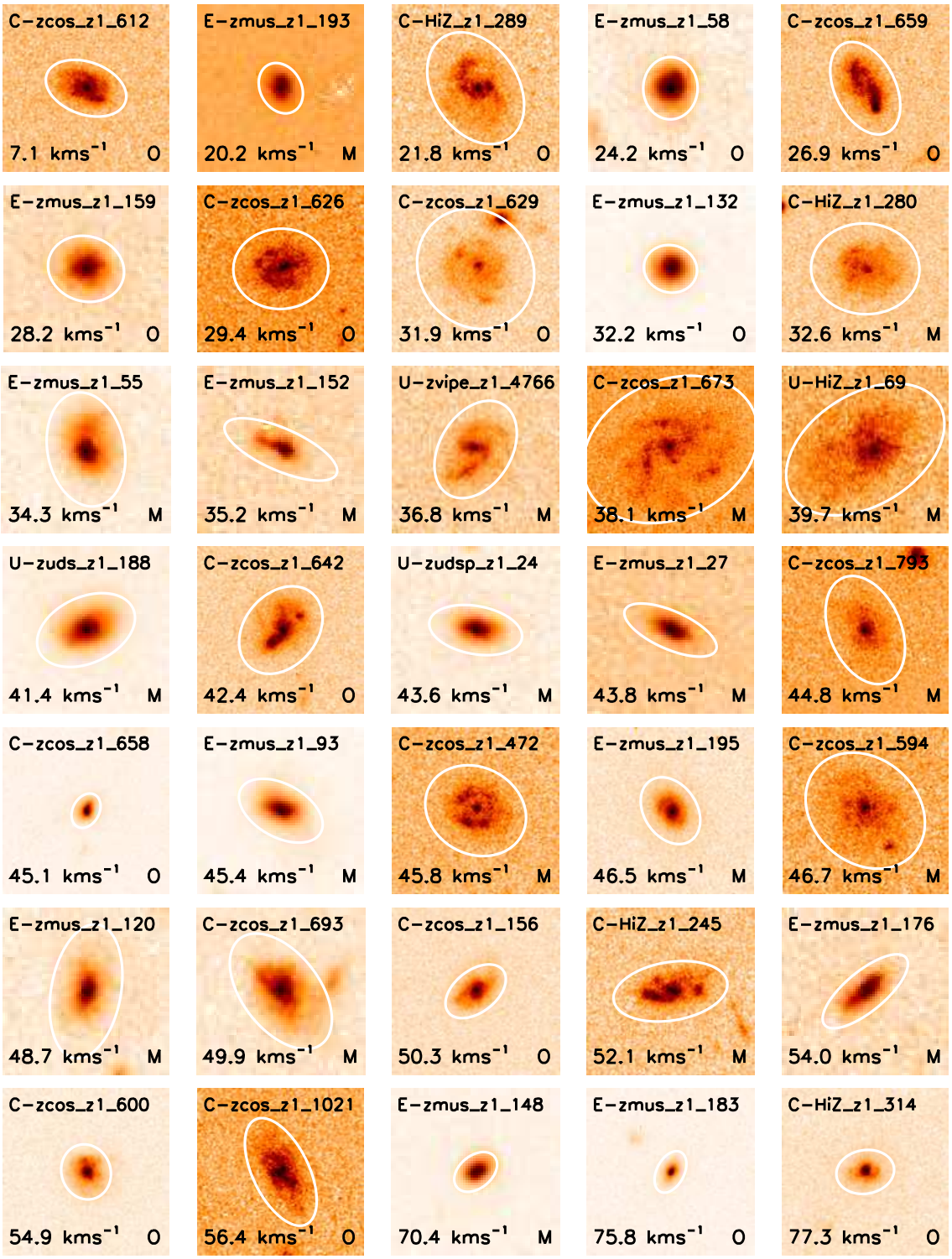

Figure 5.1: Broad-band *HST* images for KROSS galaxies of similar stellar mass ($9.7 < \log(M_\star/\mathrm{M}_\odot) < 10.1$), ranked by increasing velocity dispersion (σ_0, inset values). Each thumbnail covers an area of 4×4 arcsec and we overlay an ellipse at three times the half-light radius. We differentiate between dispersions measured in the outskirts of the disk ('O') and those calculated from the median of all available pixels ('M'). There is no clear trend between σ_0 and morphology, however galaxies with very high velocity dispersions appear to be slightly smaller.

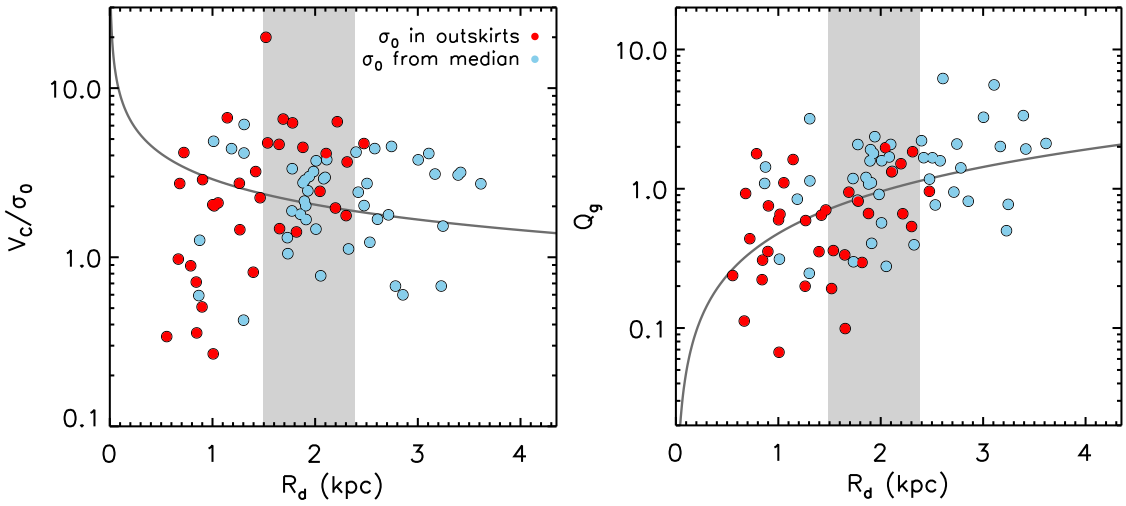

Figure 5.2: Rotational velocity to velocity dispersion ratio (v_C/σ_0, left panel) and Toomre parameter (Q_g, right panel) against disk radius (R_d) for KROSS galaxies within a stellar mass bin of $9.7 < \log(M_\star/M_\odot) < 10.1$. Again we differentiate between galaxies for which the dispersion is measured in the outskirts of the disk and those where it is calculated from the median of all available pixels. Solid black lines show trends expected for a simple disk model, normalised to fit the data. To explore the relationship between galaxy dynamics and optical morphology, we must control for these trends with disk radius. Therefore in Fig. 5.3 and Fig. 5.4 we consider only galaxies within the shaded grey regions.

ratio between rotational velocity and velocity dispersion. For a wide range of v_C/σ_0 values there are galaxies which resemble disks, with a prominent bulge and occassionally spiral features. There are also a number of more irregular, clump-dominated galaxies. We are unable to identify a clear trend between rotational support and galaxy morphology. In Fig. 5.4 we arrange the same subsample by increasing Toomre Q_g. There is perhaps an indication that galaxies which are more gravitationally stable are more "disk-like", however these differences are subtle. On this basis, we conclude that a more detailed analysis is required.

5.2.2 Quantifying Irregularities

Visual inspection of the *HST* thumbnails is a useful starting point, however in the absence of a strong trend between galaxy dynamics and morphology, a more sophisticated approach is necessary. As shown in Fig. 5.1,5.3 and 5.4, many of the galaxies in our sample are highly asymmetric or exhibit large, bright clumps. In the following section we attempt to quantify these irregularities.

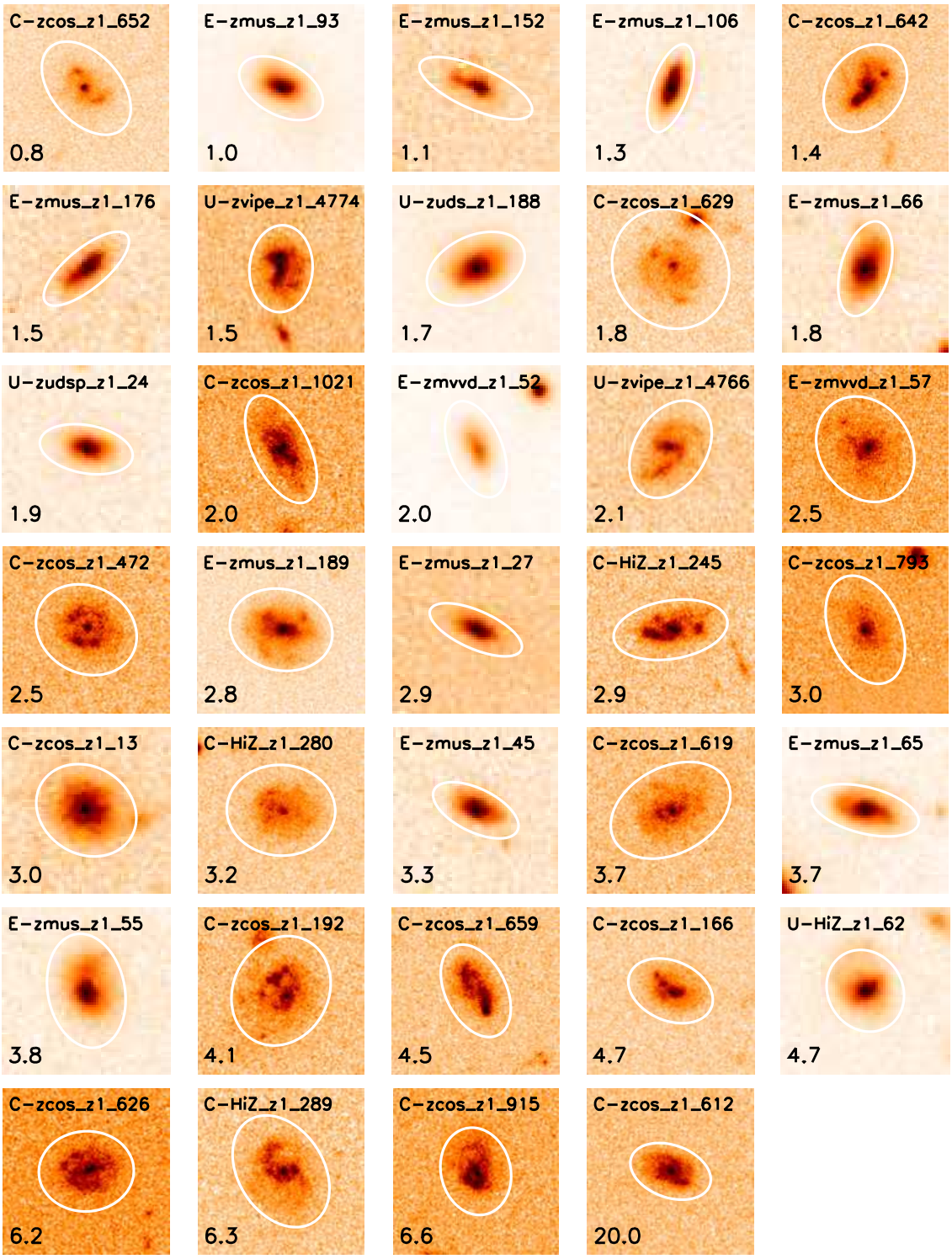

Figure 5.3: Broad-band *HST* images for KROSS galaxies of a similar stellar mass ($9.7 < \log(M_\star/\mathrm{M}_\odot) < 10.1$) and size ($1.5 < R_\mathrm{d} < 2.4\,\mathrm{kpc}$), ranked by an increasing ratio between rotational velocity and velocity dispersion (v_C/σ_0, inset values). Thumbnails cover 4×4 arcsec and we overlay an ellipse at three times the half-light radius. Galaxies across a wide range of v_C/σ_0 values exhibit extended disks and/or spiral features. There is no clear trend between v_C/σ_0 and how closely each galaxy resembles a settled, well-organised disk.

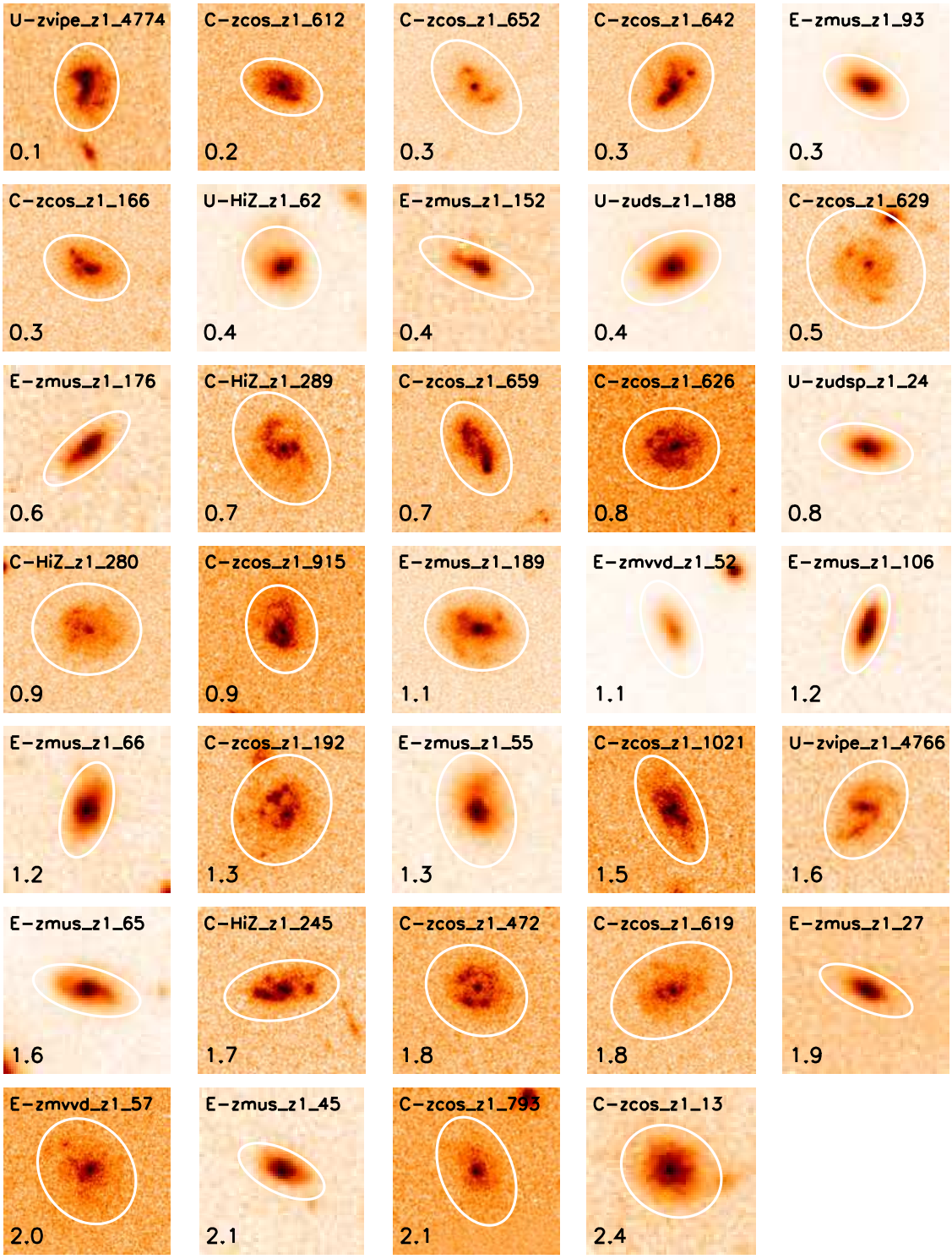

Figure 5.4: Broad-band *HST* images for KROSS galaxies of a similar stellar mass ($9.7 < \log(M_\star/\mathrm{M}_\odot) < 10.1$) and size ($1.5 < R_\mathrm{d} < 2.4\,\mathrm{kpc}$), ranked by increasing Toomre parameter (Q_g, inset values). Each thumbnail covers 4×4 arcsec and we overlay an ellipse at three times the half-light radius. Galaxies with larger Q_g values (i.e. which are more stable against gravitational collapse) appear to be more "disk like", and those with lower Q_g more clumpy, however this trend is very subtle.

One of the most popular non-parametric methods of measuring galaxy structure is the concentration, asymmetry, clumpiness (CAS) system (e.g. Conselice 2003). This technique is particularly useful since it does not require any knowledge of the underlying structure of the galaxy (unlike e.g. Sérsic fitting). It is also effective across a range of redshifts. Here we adopt a variation of the asymmetry test. This is designed to isolate the nonsymmetric components of an image, and estimate their contribution to the overall flux.

First, each thumbnail is masked for neighbouring galaxies and other artefacts, using the SExtractor (Bertin & Arnouts 1996) segmentation map. We then rotate this image through 180 degrees and subtract it from the unrotated original. The centre of rotation is not defined a priori but by an iterative process, applying sub-pixel shifts and recalculating the residuals until a minimum value is found. We limit this search to within 0.25 arcsec of the galaxy centre (defined by fitting a two dimensional Gaussian profile; see Chapter 4). To account for any strong residuals in the centre of the galaxy which may still remain, we mask a small region (an ellipse with semi-major axis of 0.25 arcsec) at the centre of the image. Examples of this process are shown in Fig. 5.5.

Finally, from the optimised residual map, we calculate the asymmetry parameter A within three times the half-light radius ($3R_{1/2}$). This is defined as the sum of the positive residuals within this area, minus background noise, divided by the total flux of the original image within the same region; or:

$$A = min\left(\frac{\Sigma|I_0 - I_{180}|}{\Sigma|I_0|}\right) - min\left(\frac{\Sigma|B_0 - B_{180}|}{\Sigma|B_0|}\right) \quad (5.2.1)$$

where I_0 is the original image, I_{180} the rotated, and B_0, B_{180} the same for a background region of equal area. Values derived for the 231 KROSS *HST* images have a 16th – 84th percentile range of $A = 0.06 - 0.30$ and a median of $A = 0.15 \pm 0.01$. This means that, on average, 15% of the image flux originates from nonsymmetric components. For comparison, Conselice (2003) analysed R-band images of 240 local galaxies and found an average of $A = 0.07 \pm 0.04$ for early type disks (Sa, Sb), 0.15 ± 0.06 for late type disks (Sc, Sd) and 0.32 ± 0.19 for ULIRGs.

To test how well this parameter correlates with our visual interpretation of the images,

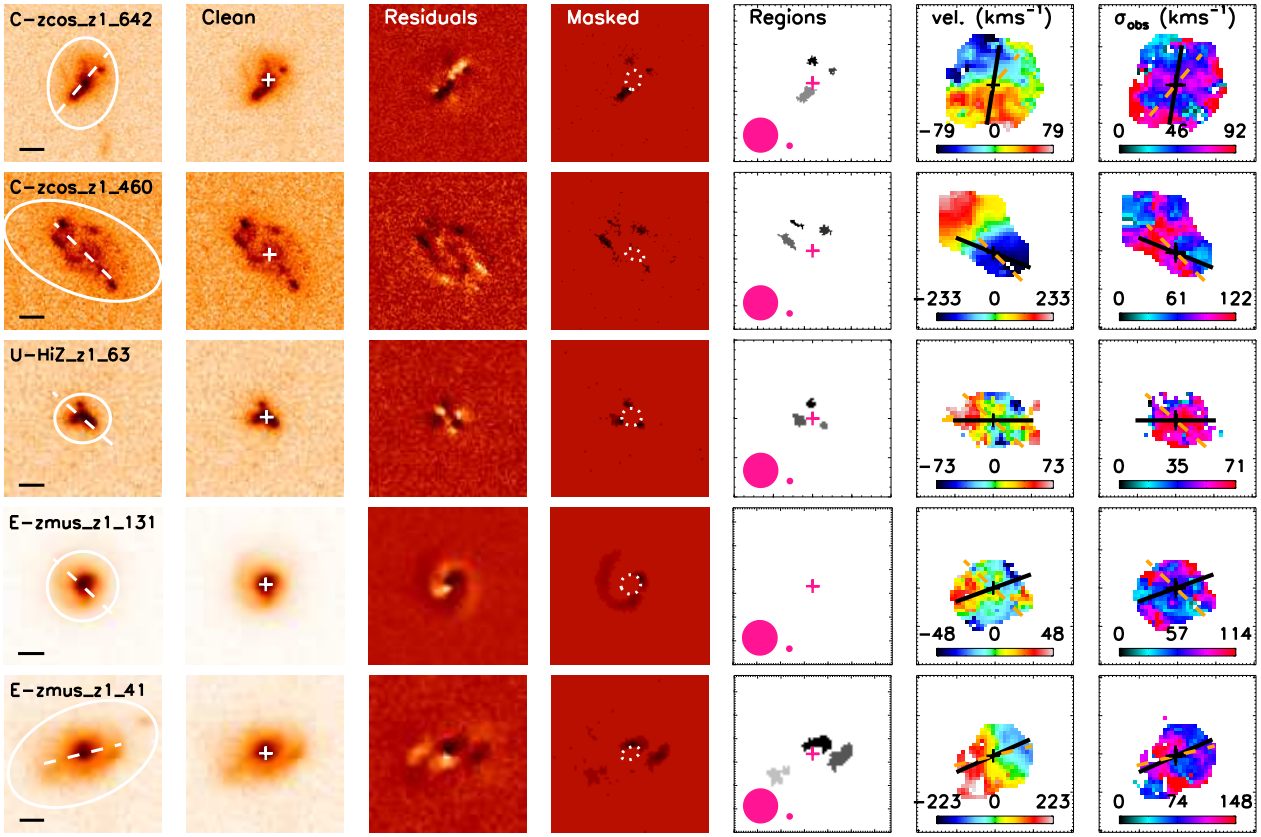

Figure 5.5: Example data for five randomly selected galaxies in the KROSS sample. All images are 4×4 arcsec and are centered in the same way. *Left to right:* (1) Broad-band *HST* image with dashed line to represent PA_{im} and an ellipse to show $3\,R_{1/2}$. We also display a 5 kpc scale bar. (2) Broad-band image with neighbouring galaxies and artefacts masked. We rotate this image by 180 degrees and subtract from the un-rotated version. A cross represents the centre of rotation, which was chosen to minimise residuals. (3) Residual *HST* image. (4) Residual image with a 3σ signal-to-noise cut applied. Pixels within the dashed region – an ellipse around the centre of rotation with a 0.25 arcsec semi-major axis – have also been masked. (5) Regions within the residual image which cover an area larger than the small pink circle, but smaller than the large pink circle. We make this cut to remove noisy pixels and any larger asymmetries such as spiral arms. The pink cross represents the dynamical centre of the galaxy. Each distinct "clump" region has been coloured differently. (6) Hα velocity map with dashed orange line to represent PA_{im} and solid black line to represent PA_{vel}. (7) Hα velocity dispersion map with lines as panel 6.

we assign each galaxy a visual classification from 1 to 5, which describes how clumpy and/or asymmetric it appears. The classifications are as follows: (1) no clumps, smooth light profile; (2) low surface brightness asymmetric components; (3) faint clumps within a disk; (4) bright clumps within a disk; (5) galaxy is dominated by clumps. In Fig. 5.6 we plot the median asymmetry parameter A (and bootstrap error) for galaxies of each visual classification. The two quantities are well correlated, suggesting that although the asymmetry test is more generalised than the "clumpiness" test (the S in CAS), it is still a useful a useful proxy for how clumpy a galaxy may appear.

In §5.2.1 we studied whether we could relate the global kinematic properties of galaxies to their morphology. From visual inspection alone it was difficult to identify any clear trends, however we are now able to quantify subtle differences between broad-band images. In Fig. 5.7 we show the ratio between rotational velocity and velocity dispersion, v_C/σ_0 (top panel), and Toomre Q_g (bottom panel), against disk radius, with points coloured by the asymmetry parameter, A. The most striking result is that larger galaxies tend to have higher residuals. Galaxies with $R_d > 2$ kpc have a median of $A = 0.19 \pm 0.01$, whereas those with $R_d < 2$ kpc have a median of $A = 0.10 \pm 0.01$. This is likely due to resolution effects. At $z \sim 1$ a disk radius of 2 kpc corresponds to ~ 0.25 arcsec, while the average seeing of our *HST* observations is 0.1 arcsec in the I and z-band, and 0.2 arcsec in the H-band (Harrison et al. 2017). It would therefore be very difficult to observe clumps and asymmetries within the most compact galaxies. For galaxies of a similar disk radius, however, we find no strong correlation between global disk instability (Q_g) or rotational support (v_C/σ_0) and asymmetry or "clumpiness".

5.2.3 Dynamical Properties of Clumps

As the examples in Fig. 5.5 show, rotating an image through 180 degrees and subtracting from the original, provides an effective method of identifying asymmetries. For many KROSS galaxies, these asymmetries appear to be star-forming clumps. Clumps are widely considered to be regions of intense star formation formed by gravitational instabilities within the gas disk (e.g. Elmegreen & Elmegreen 2005; Ceverino et al. 2010; Bournaud et al. 2014). As such, it is interesting to explore how the ionised gas dynamics in these regions (as traced by Hα emission) may differ from the rest of the galaxy.

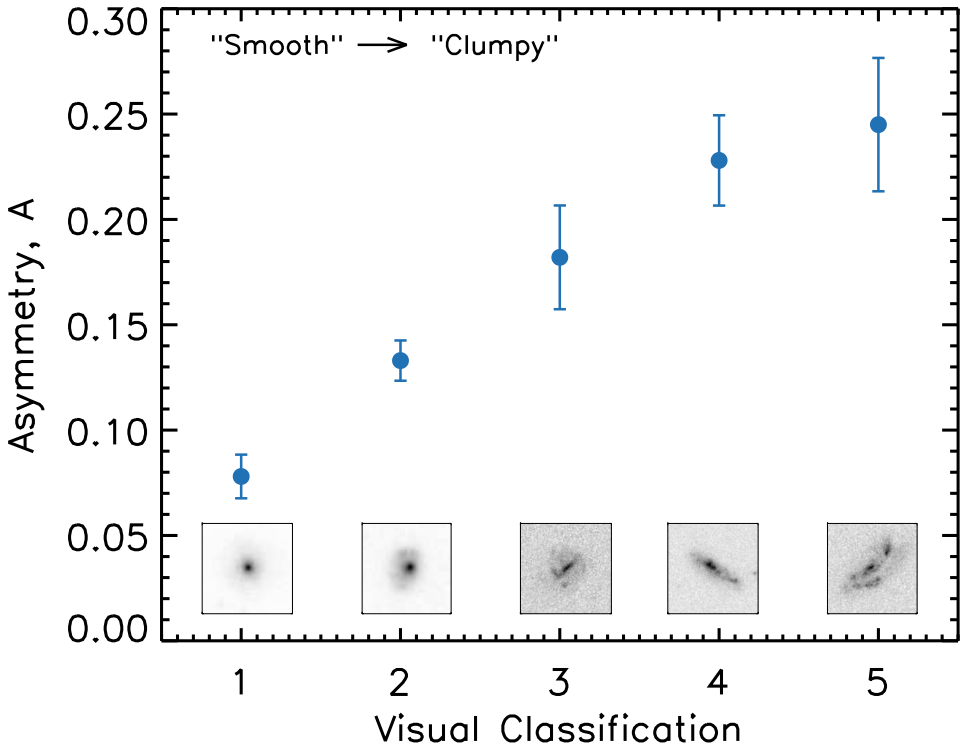

Figure 5.6: We visually inspect 231 *HST* thumbnails and classify each galaxy on a scale of 1 (smooth and featureless) through 5 (multiple bright clumps). We also rotate each thumbnail 180 degrees and subtract this image from the original (Fig. 5.5). The asymmetry parameter, A, is defined as the fraction of the flux within $3\,R_{1/2}$ that appears in this residual image. Here we plot the median value of A (and bootstrap error) for galaxies of each visual classification. The two quantities are well correlated, suggesting that the asymmetry parameter is a useful proxy for "clumpiness". Inset are thumbnails of example galaxies, one for each of the visual classifications.

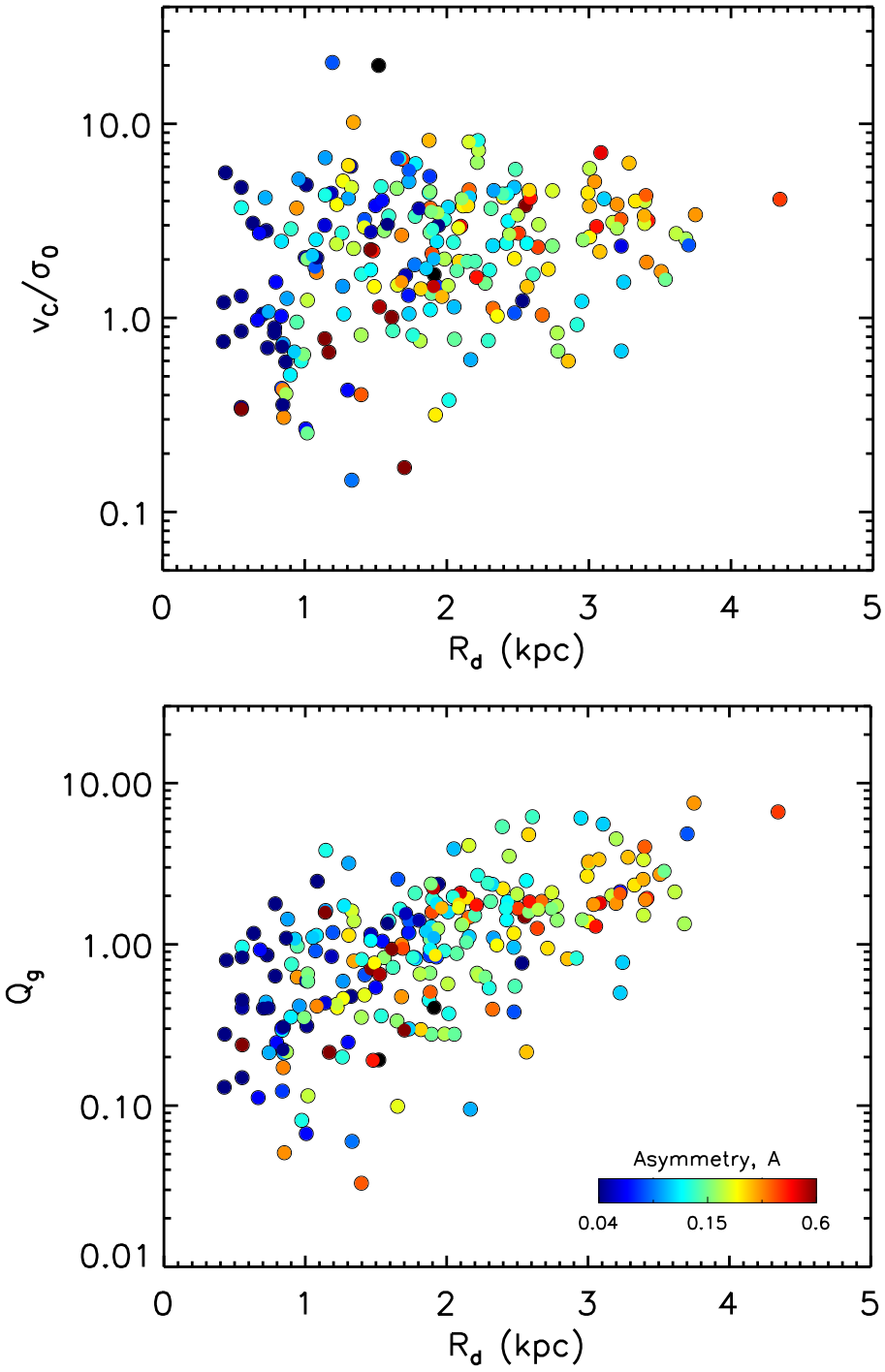

Figure 5.7: Ratio between rotational velocity and velocity dispersion (v_C/σ_0, top) and Toomre parameter (Q_g, bottom) versus disk radius R_d. Points are coloured by the asymmetry parameter, A, which measures the fraction of light within the *HST* image that contributes to nonsymmetric components, e.g. clumps. Galaxies with larger disk radii tend to have higher residuals. This may be because it is easier to resolve clumps within larger galaxies, or because the existence of clumps results in larger half-light radius measurements. At a fixed disk radius, there is no obvious trend between irregularities in the broad-band image and gravitational instability or rotational support.

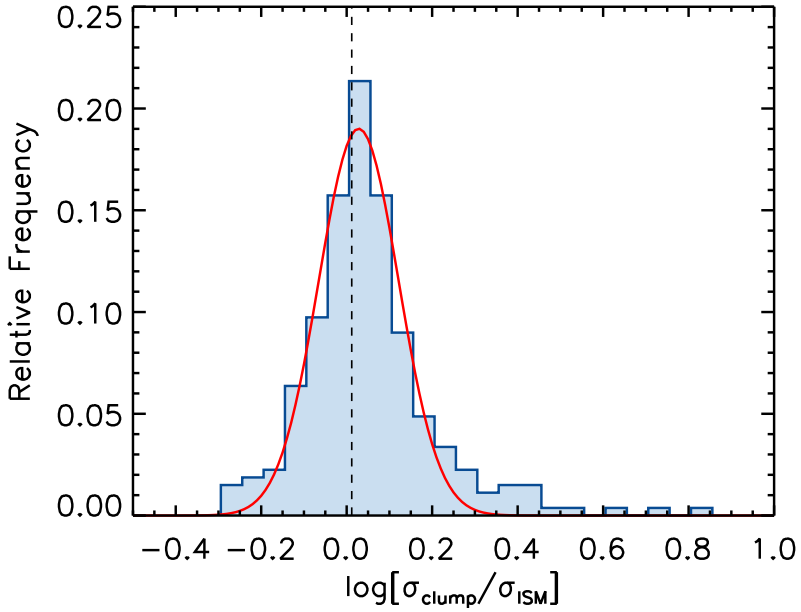

Figure 5.8: Histogram of the ratio between the velocity dispersion of each clump ($\sigma_{\rm clump}$) and the velocity dispersion of other regions in the galaxy at the same radius ($\sigma_{\rm ISM}$). We show a Gaussian fit to the distribution in red. To measure $\sigma_{\rm ISM}$ we calculate the median of all pixels within an annulus bound by the minumum and maximum (observed) radii of the clump. We find no evidence to suggest the velocity dispersion at the position of star-forming clumps is systematically higher or lower than elsewhere. The median of the distribution is $\sigma_{\rm clump}/\sigma_{\rm ISM} = 1.02 \pm 0.02$, shown as a dashed vertical line. However there is a "tail" of larger values and this skew results in a mean of $\sigma_{\rm clump}/\sigma_{\rm ISM} = 1.15 \pm 0.04$.

In order to isolate the regions and study their properties, we follow a simple three step process. Starting with the residual map, we first mask any negative pixels and those below a signal-to-noise of three. These cuts remove the inverse image of the galaxy and more diffuse, low surface brightness components. We next mask pixels within a small region at the centre of the image (an ellipse with semi-major axis of 0.25 arcsec), to remove residuals due to centering issues. Finally, we group connected pixels together into distinct regions, identifying each as a clump if the total area is between $0.15 < A_{\rm region} < 0.8$ arcsec^2. This is to remove noisy pixels and any larger asymmetries such as spiral arms. In Fig. 5.5 we show examples of the residual features identified by this process.

To begin our analysis, we first match each of the clumps in the *HST* image to a corresponding region in the KMOS velocity dispersion map. As discussed in Chapter 4, "beam smearing" artificially inflates the measured dispersion in each pixel, with regions close to the dynamical centre affected more. Since it is difficult to correct for this on a pixel-by-pixel basis, we instead calculate the ratio between this median value and the dispersion of

other pixels with similar radii, $\sigma_{\rm clump}/\sigma_{\rm ISM}$. To measure $\sigma_{\rm ISM}$ we calculate the median of all pixels within an annulus bound by the minimum and maximum (observed) radii of the clump. Fig. 5.8 shows the distribution of measured $\sigma_{\rm clump}/\sigma_{\rm ISM}$ values. On average, the velocity dispersion at the position of the clump is consistent with that of the underlying disk, with a median ratio of $\sigma_{\rm clump}/\sigma_{\rm ISM}$ 1.02 ± 0.02. However there is a "tail" of larger values and this skew results in a mean of $\sigma_{\rm clump}/\sigma_{\rm ISM} = 1.15 \pm 0.04$.

Since clumps form via gravitational instabilities, it is likely that they would be preferentially found towards low shear, outer regions of the galaxy. To test this theory, we again exploit the KMOS data. In Chapter 4 we described how we used the Hα velocity maps to derive a model rotation curve for each of the galaxies. At a given distance from the dynamical centre, $R_{\rm clump}$, we can use this model to estimate the local shear due to rotation, dv/dR. The *observed* radius at which the clump is located, R_{obs}, is straightforward to measure. However this distance will appear smaller or larger depending on the inclination of galaxy and the position of the clump relative to the major kinematic axis. We must therefore apply a correction as follows:

$$\begin{aligned} R^2_{obs} &= R^2_{x,obs} + R^2_{y,obs} \\ &= R^2_x + R^2_y cos^2\theta \\ &= R^2_x + R^2_y - R^2_y sin^2\theta \\ &= R^2_{\rm clump} - R^2_y sin^2\theta \\ &= R^2_{\rm clump} - \left(\frac{R_{obs} sin\phi}{cos\theta}\right)^2 sin^2\theta \end{aligned}$$

$$\therefore\ R^2_{\rm clump} = R^2_{obs}\left(1 + sin^2\phi tan^2\theta\right) \equiv R^2_{obs} + R^2_{y,obs} tan^2\theta \qquad (5.2.2)$$

where $R_{x,obs}$, $R_{y,obs}$ and ϕ are defined by Fig. 5.9, R_x, R_y are the equivalent intrinsic distances, and θ is the inclination of the disk. We then estimate the shear within a 1 kpc region of the rotation curve.

In Fig. 5.10 we plot rotational shear versus clump radius (normalised by $R_{\rm d}$) for all clumps identified within our sample. Due to the shape of the rotation curves, shear is highest towards the dynamical centre. To test whether clumps preferentially form in low shear regions, we also calculate dv/dR and R for a set of randomly selected pixels within

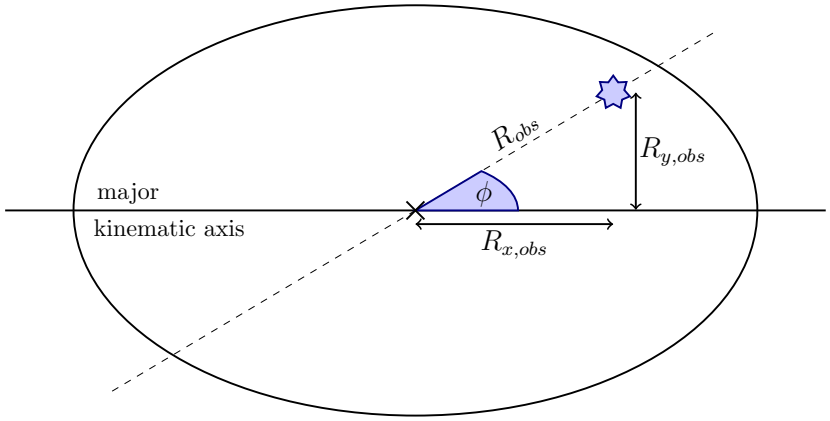

Figure 5.9: Schematic of an inclined disk galaxy with an embedded star-forming clump (blue star). The distance between this clump and the dynamical centre of the galaxy ($R_{\rm obs}$) will appear smaller or larger depending on the orientation of the observer (the disk inclination θ) and the position of the clump relative to the major kinematic axis (ϕ). We must therefore apply Eq. 5.2.2 in order to estimate the intrinsic radius.

each *HST* image. To do so we exclude the very central region of the galaxy, since we did not search for clumps here, and any pixels below a signal-to-noise ratio of three. Properties of these regions are shown in Fig. 5.10 as blue contours.

The clumps have a median distance from the dynamical centre of $R_{\rm clump} = 2.4 \pm 0.1\, R_{\rm d}$ and a median shear of $dv/dR = 7.1 \pm 0.8\,{\rm km\,s^{-1}\,kpc^{-1}}$, whereas for the randomly sampled population we measure $R = 5.07 \pm 0.03\, R_{\rm d}$ and $dv/dR = 1.02 \pm 0.03\,{\rm km\,s^{-1}\,kpc^{-1}}$. Hence the clumps are closer to the dynamical centre than would be expected if regions in the *HST* image were chosen at random. This may simply imply that clumps are easier to identify in the bright inner regions of the galaxy (where signal-to-noise is highest). However, if it is a genuine result then there are two potential explanations. One possibility is that the gas surface density is much higher towards the centre of the disk, acting to counteract the increased shear. Another is that the clumps do in fact form at large radii, but migrate inwards over time (as suggested by e.g. Dekel & Krumholz 2013; Mandelker et al. 2014).

This is something we could test through further observation. If the clumps are static and short lived, we would expect their properties to be similar to the surrounding ISM. These regions would appear much like "scaled up" versions of local GMCs. If they instead survive long enough to migrate inwards, their ages and metallicities would be more evolved (e.g. Förster Schreiber et al. 2011), and their scaling relation between luminosity and size different to that of local HII regions (e.g. Krumholz & Dekel 2010).

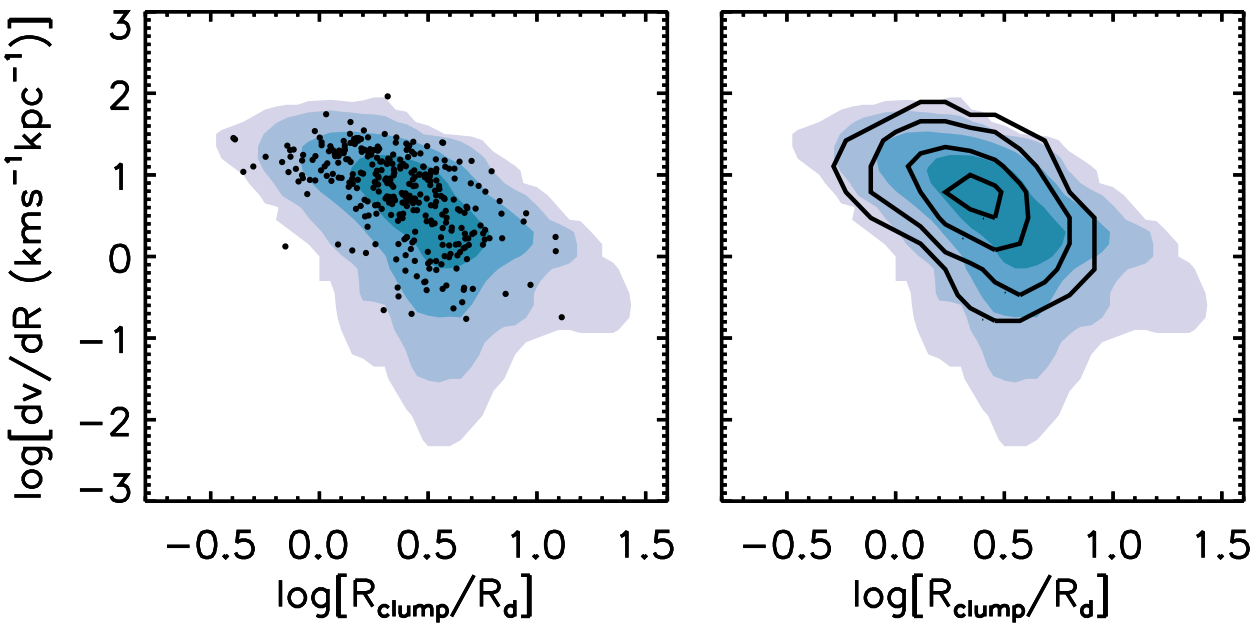

Figure 5.10: *Left:* Rotational shear (dv/dR) versus distance from the dynamical centre (normalised by the disk radius, $R_{\rm d}$) for all clumps identified (black points) and for a randomly selected sample of positions within each *HST* image (blue contours). $R_{\rm clump}$ radii are corrected for inclination effects using Eq. 5.2.2. We then use this corrected radius to estimate the shear across a 1 kpc region, using the model rotation curve. *Right:* As left, but with black contours used to better illustrate the distribution of the clumps. For each set of contours we use levels of 20, 50, 70 and 90% of the maximum density. The clumps have a median radius of $R_{\rm clump} = 2.4 \pm 0.1\, R_{\rm d}$ and a median shear of $dv/dR = 7.1 \pm 0.8\,{\rm km\,s^{-1}\,kpc^{-1}}$. This is closer to the dynamical centre than would be expected if regions in the *HST* image were chosen at random. The fact that we do not see an overdensity of clumps in outer regions of the galaxies, where the shear is lowest, may suggest that the gas density within these regions is insufficiently high, or that clumps migrate inwards over time.

5.3 Conclusions

In Chapter 4 we introduced the KROSS survey, a study of 795 typical $z \sim 0.9$ star-forming galaxies using KMOS. In this chapter we combined the spatially resolved Hα kinematics of KMOS with deep *HST* imaging for 231 of our sample, to investigate how galaxy dynamics may relate to optical morphology. Our main conclusions are as follows:

- The KROSS sample exhibit a wide range of morphologies, from disks with well-defined bulges and spiral arms, to highly asymmetric, clumpy galaxies. From a simple visual assessment, we found that high velocity dispersion (σ_0) galaxies are more frequently compact. On a similar basis, we found no strong trends between v_C/σ_0 or Toomre Q and morphology, for galaxies of a similar mass and size.

- To quantify irregularities, we calculated the asymmetry parameter, A, for each of the *HST* thumbnails. The sample have a median of $A = 0.15 \pm 0.01$ and a 16th – 84th percentile range of $A = 0.06 – 0.30$. We found that larger galaxies tend to have higher asymmetry values, however there are no strong trends as a function of galaxy kinematics.

- Finally, we isolated individual clumps within the images and crossmatched their positions with the KMOS data. On average, the velocity dispersion at the position of clumps is consistent with the underlying disk, with a median ratio of $\sigma_{\rm clump}/\sigma_{\rm ISM} = 1.02 \pm 0.02$. There is no evidence to suggest that clumps are preferentially located towards the outskirts of the galaxy.

To understand the role of galaxy kinematics in "crystallising" the Hubble sequence, we propose that high resolution, adaptive optics assisted IFU observations are required. Using KMOS we successfully mapped the large-scale (5 – 10 kpc) dynamics of hundreds of galaxies, however our observations are seeing-limited and suffer from beam smearing. High resolution data (1 – 5 kpc scales) would allow us to identify individual star-forming regions in Hα emission, and measure their properties (e.g. luminosities, sizes, velocity dispersions, metallicities) to test clump evolution theories. It would also enable us to study the radial distribution of angular momentum and test whether this relates to galaxy morphology (i.e. settling of the disk and the formation of a central bulge).

CHAPTER 6

Conclusions and Future Work

The aim of this thesis has been to explore the many physical processes, both secular and environmental, which together shape the evolution of star-forming galaxies. We have done so through the analysis of galaxy kinematics, combining KMOS and FLAMES IFU observations with far-infrared photometry, millimetre spectroscopy and *HST* imaging. In this final chapter we summarise our key results, and discuss a number of ongoing and future projects. We end by considering what the future holds for observational studies of galaxy evolution, and identifying the key questions still to be addressed.

6.1 Summary of the Presented Work

6.1.1 Dusty Starburst Galaxies in an Intermediate Redshift Cluster

Star-forming galaxies accreted into a cluster environment are expected to undergo a transition from spirals to S0s. To achieve this, infalling galaxies must have their gas disks stripped, star formation quenched, and dynamics transformed from rotationally supported disks to dispersion dominated spheroids. It is thought that starbursts represent an intermediate phase of this transition, and so studying their properties may help us to understand the physical mechanisms at play.

In Chapter 2 we presented a multi-wavelength analysis of 27 dusty starburst galaxies in the massive cluster Cl 0024+17 at $z = 0.4$. We combined Hα dynamical maps from the VLT/FLAMES multi-IFU system with far-infrared imaging using *Herschel*/SPIRE and millimetre spectroscopy from IRAM/NOEMA, to study the kinematics, star formation rates and gas masses of this sample. Most galaxies are rotationally supported, with a

median rotation velocity to velocity dispersion ratio of $v/\sigma_0 = 5 \pm 2$ and a specific angular momentum of $\lambda_R = 0.83 \pm 0.06$. These dynamics are consistent with field spirals of a similar mass and redshift. Star formation rates of $3 - 26\,M_\odot\,yr^{-1}$ and an average CO-derived gas mass of $\sim 1 \times 10^{10}\,M_\odot$ suggest gas depletion timescales of ~ 1 Gyr (~ 0.25 of the cluster crossing time). From the far-infrared photometry, we derived characteristic dust temperatures (mean $T_d = 26 \pm 1$ K) consistent with local galaxies of similar far-infrared luminosity, suggesting that the low density gas is yet to be stripped.

Together, our results suggest that these dusty, star-forming galaxies have only recently been introduced to the cluster. We conclude that for the galaxies to complete the transition from spirals to S0s, they must undergo a dynamical heating of the disk, increase in concentration, and reduce their specific angular momentum by $\sim 40\%$. The most likely way to achieve this is via multiple tidal interactions with other cluster members. While this was a useful pilot program, we now wish to extend our observations to starburst galaxies in a number of additional clusters, across a range of redshifts. We briefly discuss the first observations from this extended project in §6.2.1.

6.1.2 Modelling the Effects of Beam Smearing

Seeing-limited IFU observations suffer from a phenomenon known as "beam smearing". As observations are convolved with the seeing PSF, information from each spatial pixel is combined with that of neighbouring regions. This acts to artificially inflate measurements of the velocity dispersion (particularly towards the dynamical centre) and flatten the observed rotation curve. Since we anticipated that our analysis in Chapter 4 would be particularly sensitive to these effects, in Chapter 3 we created a series of mock KMOS observations to model the impact of beam smearing on our dynamical measurements. This allowed us to constrain the systematics and derive correction factors.

We found that the biases introduced by beam smearing are most effectively parameterised by the ratio between the disk radius and half of the seeing FWHM (R_d/R_{PSF}). The smaller a galaxy is compared to the seeing, the more we underestimate the intrinsic rotation velocity and overestimate the intrinsic velocity dispersion. Measurements of rotation velocity are much less sensitive to the mass, inclination or dark matter fraction of the galaxy, and corrections can therefore be universally applied as a function of R_d/R_{PSF}.

However, the intrinsic velocity dispersion is overestimated far more for high mass, high inclination galaxies. We therefore split corrections for these measurements into four different "tracks" of observed rotation velocity.

Through this work we have established a simple look-up table of beam smearing corrections which can be used to efficiently make robust estimates of intrinsic velocity dispersion and rotation velocity. This is a useful tool. Corrections can be applied not only to our KROSS observations (Chapter 4; §6.1.3), but also to other IFU samples across a range of redshifts and seeing conditions.

6.1.3 Turbulence in the ISM of High Redshift Galaxies

Observations of distant galaxies have revealed a population quite unlike that found in the local Universe. The average star formation rate at $z \sim 1-3$ is an order of magnitude higher than today, and galaxies have high molecular gas fractions and clumpy, irregular morphologies. Studying the ionised gas kinematics of these galaxies provides valuable insight as to why this may be so. In Chapter 4 we analysed the velocity dispersion properties of 472 star-forming galaxies observed as part of the KROSS survey. The majority of this sample are rotationally dominated ($83 \pm 5\%$ with $v_C/\sigma_0 > 1$) but also dynamically hot and highly turbulent. After correcting for beam smearing effects, the median intrinsic velocity dispersion for the final sample is $\sigma_0 = 43.2 \pm 0.8\,\mathrm{km\,s^{-1}}$ with a rotational velocity to dispersion ratio of $v_C/\sigma_0 = 2.6 \pm 0.1$.

To explore the relationship between velocity dispersion, stellar mass, star formation rate and redshift we combined KROSS with data from the SAMI survey ($z \sim 0.05$) and an intermediate redshift MUSE sample ($z \sim 0.5$). While we find a weak trend between velocity dispersion and stellar mass, at fixed mass there is a strong increase in velocity dispersion with redshift. At all redshifts, galaxies appear to follow the same weak trend of increasing velocity dispersion with star formation rate. Results for these three samples are consistent with an evolution of galaxy dynamics driven by disks that are more gas rich, and increasingly gravitationally unstable, as a function of increasing redshift.

We also used KROSS sample to test two analytic models, which predict turbulence in the ISM (as measured by the velocity dispersion) is driven either by gravitational instability in the disk, or stellar feedback. We found that both prescriptions provide an adequate

description of the data, and we were unable to rule out either model. Direct measurements of the gas fraction of the galaxies, or more precise dynamical measurements, would help to provide further constraints.

6.1.4 Galaxy Dynamics and Optical Morphology

Finally, in Chapter 5 we investigated how the galaxy dynamics derived for the KROSS sample in Chapter 4 may relate to optical morphology. To explore the idea that an increase in angular momentum and disk stability (Toomre Q) is what drives the morphological evolution from clumpy, irregular galaxies at high redshift, to thin disks at low redshift, we studied the *HST* images of 231 KROSS galaxies.

Our KROSS sample exhibit a wide range of morphologies, from bulge-dominated disks with spiral arms, to highly asymmetric and clumpy. We quantified these differences using the asymmetry parameter, A. This metric correlates very well with our visual interpretation of "clumpiness", however there are no strong trends as a function of galaxy kinematics. We also studied the properties of individual clumps, crossmatching their positions with the KMOS dynamical maps. On average, the velocity dispersion of these clumps is consistent with the underlying disk, with a median ratio of $\sigma_{\rm clump}/\sigma_{\rm ISM} = 1.02 \pm 0.02$. We found no evidence to suggest that these star-forming regions are preferentially located towards the outskirts of the galaxy.

To investigate this issue further, we propose that adaptive optics assisted IFU observations would be beneficial. High resolution observations would allow us to identify individual star-forming clumps in Hα emission, and measure their properties (e.g. sizes, luminosities, dynamics and metallicities). This would allow us to test whether the clumps are short-lived, or survive long enough to migrate inwards, eventually forming the bulge of the galaxy.

6.2 Ongoing and Future Work

6.2.1 Cluster Starbursts

Following the successful pilot study of cluster starbursts in Cl 0024+17 (Chapter 2; §6.1.1), we were awarded time (PI: Johnson) to observe an additional two clusters

($0.19 < z < 0.25$) with FLAMES and three ($0.58 < z < 0.84$) with KMOS. This extends our original sample of 28 to a total of ~ 100 galaxies. Observations were taken between April 2015 and August 2016, and are summarised in Table 6.1. We targeted spectroscopically confirmed 24 μm-bright galaxies, which are also detected in Hα or [OII] emission, to isolate a population of obscured cluster starbursts. Any "spare" IFUs were then placed on Hα-bright (24 μm faint) cluster members, in order to create a control sample of more typical star-forming galaxies in the same environment.

Table 6.1: Observations of additional clusters

Cluster	Semester	Redshift	Instrument	Time (hr)
Abell 68	P97	0.22	FLAMES	1.0
Abell 2485	P97	0.25	FLAMES	3.0
MS2053-04	P95	0.58	KMOS	2.0
MS1054-03	P95	0.82	KMOS	2.0
RXJ0152-13	P95	0.84	KMOS	2.0

Dividing this sample into bins of stellar mass, luminosity, redshift and environment, will help us to understand the physical processes which transform blue, star-forming spirals – through an obscured starburst – into passive S0 galaxies. We will use the Hα velocity fields to study the fraction of disks as a function of cluster-centric radius, and to identify asymmetries which may be associated with galaxy-galaxy interactions (e.g. Mihos & Bothun 1998; Colina et al. 2005). We will also derive the spin parameter, λ_R for each of the galaxies. The cluster starbursts in Cl 0024 have high specific angular momentum (comparable to field spirals of a similar mass; Fig. 2.12) – is this true of all galaxies in our sample, or are the galaxies in Cl 0024 atypical because of the apparently strong merger state of the cluster? Finally, we will use the spatially-resolved [NII]/Hα emission line ratios to measure abundance gradients. Positive gradients may suggest that metal-rich gas has been redistributed following an interaction-induced central starburst (e.g. Kewley et al. 2010; Rupke et al. 2010; Rich et al. 2012). These diagnostics can then be compared to field spirals at the same redshift. Differences between the two populations may highlight which physical mechanisms (e.g. ram pressure stripping, strangulation, tidal interactions) are most effective in transforming spirals to S0s.

6.2.2 The Peak of Cosmic Star Formation

The redshift range $1 < z < 3$ was a crucial period during which today's massive galaxies formed the bulk of their stars. An important observational challenge is to understand how and why the cosmic star formation rate was so much higher at this epoch. Our KMOS guaranteed-time programme, KROSS (Chapters 4 and 5), has been highly successful in establishing the star-formation properties and global kinematics of galaxies at $z \sim 1$. However there are still many questions which remain unanswered. In this section we identify a number of areas for future study.

6.2.2.1 Further KMOS Observations

One project already underway is the KMOS Galaxy Evolution Survey (KGES), a Guaranteed Time programme to study the ionised gas kinematics of typical star-forming galaxies at $z \sim 1.5$. Our aim is to build a statistically significant sample which can then be compared to KROSS. We will again target the Hα emission of galaxies in the COSMOS, UDS, ECDFS and SA22 fields. So far 171 galaxies have been observed, of which 162 are detected (Tiley et al. in prep). Observations are due to be completed at the end of 2017, when it is hoped that the combined KROSS + KGES sample will total ~ 1100 galaxies.

Applying the same analysis techniques to both samples will allow us to identify key differences between the two populations, and investigate what drives the emergence of the Hubble sequence. For example, we will test whether the more disordered morphologies at $z \sim 1.5$ correlate with lower specific angular momentum and lower Toomre Q. We will measure metallicity gradients to test competing theories of "outside-in" versus "inside-out" disk growth (e.g. Stott et al. 2014 and references within). We can also continue to study the evolution of turbulence in the ISM, and how this relates to global properties such as stellar mass and star formation rate. As with our $z \sim 1$ sample, the possibilities are many and varied.

6.2.2.2 AO-Assisted IFU Observations

As discussed in Chapters 3 and 5, a key limitation of the KROSS survey is that our observations are seeing-limited. We are able to resolve star formation and galaxy dynamics on

5-10 kpc scales, however to study regions smaller than this (e.g. individual star-forming clumps) requires adaptive optics. To address this, we are currently undertaking a study of ~ 30 star-forming galaxies between $0.8 < z < 3.5$, using SINFONI (Spectrograph for INtegral Field Observations in the Near Infrared) and NIFS (Near-Infrared Integral Field Spectrometer) on the VLT and Gemini-North, respectively. We hope to follow this with a SINFONI study of ~ 50 KGES galaxies (proposal submitted, PI: Swinbank).

These high resolution IFU observations will allow us to study the radial distribution of angular momentum and spatial variation of the Toomre Q parameter. We can then correlate these properties with galaxy morphology, local star formation density and the number and distribution of star-forming clumps. We will test clump evolution theories (see Chapter 5), and whether it is the redistribution of specific angular momentum that leads to bulge formation and the stabilisation of the disk.

6.2.2.3 ALMA Observations

To explain the ubiquity of gas-rich, turbulent disks at high redshift, numerical simulations suggest that galaxies are continuously fed by cold, clumpy streams of gas from the intergalactic medium. Understanding how this process shapes the formation and evolution of galaxies is essential. Using ALMA, we intend to study the interaction between star formation and gas dynamics in a small sample of $z \sim 1.5$ KGES galaxies (proposal submitted, PI: Gillman). We will combine our KMOS measurements of the Hα dynamics with spatially resolved CO(2-1) and CO(5-4) observations on the same scale.

Using this data, we will compare the spatial extent of the cold molecular gas to that of the star-forming gas (as traced by Hα emission), and study the fraction of gas in the cold versus warm phase (using the CO(2-1)/CO(5-4) emission line ratio). Observations of high redshift starbursts suggest that the cold molecular gas is far more extended than the star-forming disk (e.g. Ivison et al. 2011; Thomson et al. 2012). We will therefore search for this spatially extended emission, and measure how the angular momentum of the gas is lost as it is transported inwards towards the disk. Finally, we will test whether the relationship between gas surface density and star formation rate density established in the local Universe (i.e. the Kennicutt-Schmidt law) holds for galaxies at high redshift.

6.2.2.4 Stellar Kinematics using JWST

The *James Webb Space Telescope* (*JWST*; Gardner et al. 2006), due for launch in 2018, will revolutionise our understanding of the high redshift Universe. The telescope's Near-Infrared Spectrograph (NIRSpec) will be equipped with an IFU mode of 3×3 arcsec field-of-view and 0.1 arcsec spatial sampling, allowing us to obtain spatially-resolved stellar kinematics of $z \geq 1$ galaxies for the first time. Such measurements will provide information on the biases inherent in using gas phase emission lines to study galaxy kinematics, and crucial insight into the star formation and mass assembly history of high redshift (and hence present day) galaxies. These observations will also allow us to place further constraints on the mass distribution within early galaxies, and the ages and metallicities of different components.

6.3 The Bigger Picture

One of the greatest challenges in modern astronomy is to understand the formation of the Hubble Sequence. What drives the transition between clumpy, irregular galaxies at high redshift, and the bimodality of blue, star-forming spirals and "red and dead" early-types at low redshift? Through the work presented in this thesis, it is hoped that we have inched just a little bit closer to being able to answer this question.

Galaxy evolution is a complex interplay of different physical processes, but a number of recent studies have suggested that the formation of a stellar bulge is particularly important. In the local Universe, passive galaxies have larger bulge-to-total light ratios than star-forming galaxies (e.g. Baldry et al. 2004) This could be achieved if quenching occurs via gas-poor major mergers at intermediate redshift. However, a tight star-forming "main sequence" (e.g. Speagle et al. 2014), and the existence of blue bulges and red disks (e.g. Bamford et al. 2009; Masters et al. 2010), suggest this may not be the dominant mechanism. An alternative is the growth of a bulge via disk instabilities.

As shown by our results in Chapter 4 and 5, most star-forming galaxies at high redshift are turbulent, gas-rich disks. Within these galaxies, viscous dissipation is expected to drive efficient radial inflows that lead to the formation of a bulge (e.g. Dekel et al. 2009; Dekel & Burkert 2014). Genzel et al. (2014) suggest that, combined with a decrease in

the gas accretion rate (either gradually over cosmic time, or because the halo grows too large for efficient cold mode accretion), this will eventually cause the disk to become globally stable (see also Martig et al. 2009; 2013). This means that while star formation can still occur in local regions of high density, the disk will no longer fragment into large, star-forming clumps. The galaxy would begin to look more like a local spiral. Star formation would continue in this way until quenched by e.g. AGN feedback or environmental effects.

In other systems, morphological changes may happen more rapidly. A fraction of high redshift galaxies are thought to undergo a process of "fast compaction", where violent disk instabilities lead to the formation of massive, gas-rich bulges (e.g. Zolotov et al. 2015; Barro et al. 2016; Burkert et al. 2016; Tadaki et al. 2017). The result is a population of compact star-forming galaxies with spheroid-like morphologies – so-called "blue nuggets" (e.g. Barro et al. 2013; Wisnioski et al. 2017). In Chapter 5 we identified a number of very small, high velocity dispersion galaxies which may be of this type. These galaxies are expected to quench rapidly, forming compact quiescent galaxies with similar structural properties.

Barro et al. (2017) suggest that through these two modes of transformation – fast and slow compaction – the basis of the modern Hubble sequence can be formed. To understand whether this is the case, we must continue to carefully analyse the kinematics, morphology and star formation properties of galaxies at different epochs. We must understand the turbulence and clumps ubiquitous in high redshift galaxies, and how these properties relate to the re-distribution of gas and angular momentum. Finally, while the focus of this thesis has been star-forming galaxies, it is clear that we must also study quiescent galaxies for a complete picture of this evolution.

6.4 Final Remarks

A fundamental pursuit of astronomy is to understand how galaxies form and evolve, but this is no easy task. To even begin to unravel the complexities of these systems requires a multifaceted approach. Galaxy evolution is influenced by processes on a wide range of scales, from the cosmic web to individual star-forming regions. We must study galaxies in

the local population and those at high redshift, galaxies in the field and in dense clusters. We must combine detailed observations of the extraordinary with well-selected, statistical samples. Most importantly, we must exploit a range of techniques and data at different wavelengths.

Significant progress has been made in recent years. Detailed observations of obscured star formation have been possible with *Herschel*, and ALMA allows us to study the gas in galaxies – the "fuel for the fire" – with unprecedented resolution and sensitivity. With second-generation IFU instruments (e.g. KMOS, MUSE, SAMI) we can now spatially resolve the kinematics of many galaxies simultaneously, building large samples at both low and high redshift. Even how we study galaxy morphologies is changing, with innovative citizen-science projects such as Galaxy Zoo (Lintott et al. 2008).

However astronomy is now on the verge of a new revolution, thanks to *JWST* and the next generation of ground-based telescopes – the European Extremely Large Telescope (E-ELT), Thirty Meter Telescope (TMT) and Giant Magellan Telescope (GMT) – which will see first-light in the early 2020's. It is hoped that in the coming decade we can combine this wealth of observational data with results from state-of-the-art cosmological simulations (e.g. EAGLE; Crain et al. 2015; Schaye et al. 2015), to address some of the following questions ...

- What drives the morphological transition between clumpy, irregular disks at high redshift and thin, spiral disks at low redshift?
- How does star formation evolve from a global to a local process?
- Which processes are most important for regulating/quenching star formation?
- How does environment influence galaxy evolution?

... and, of course, uncover many more questions to be answered!

Bibliography

Abadi, M. G., Moore, B., & Bower, R. G. 1999, MNRAS, 308, 947

Alberts, S., Pope, A., Brodwin, M., et al. 2014, MNRAS, 437, 437

Alexander, D. M., & Hickox, R. C. 2012, NewAR, 56, 93

Allen, J. T., Croom, S. M., Konstantopoulos, I. S., et al. 2015, MNRAS, 446, 1567

Amanullah, R., Lidman, C., Rubin, D., et al. 2010, ApJ, 716, 712

Aumer, M., Burkert, A., Johansson, P. H., & Genzel, R. 2010, ApJ, 719, 1230

Bacon, R., Accardo, M., Adjali, L., et al. 2010, in Proc. SPIE, Vol. 7735, Ground-based and Airborne Instrumentation for Astronomy III, 773508

Baldry, I. K. 2008, Astronomy and Geophysics, 49, 5.25

Baldry, I. K., Balogh, M. L., Bower, R. G., et al. 2006, MNRAS, 373, 469

Baldry, I. K., Glazebrook, K., Brinkmann, J., et al. 2004, ApJ, 600, 681

Balogh, M. L., Navarro, J. F., & Morris, S. L. 2000, ApJ, 540, 113

Balogh, M. L., Pearce, F. R., Bower, R. G., & Kay, S. T. 2001, MNRAS, 326, 1228

Bamford, S. P., Nichol, R. C., Baldry, I. K., et al. 2009, MNRAS, 393, 1324

Barnes, J. E., & Hernquist, L. 1996, ApJ, 471, 115

Barro, G., Faber, S. M., Pérez-González, P. G., et al. 2013, ApJ, 765, 104

—. 2014a, ApJ, 791, 52

Barro, G., Trump, J. R., Koo, D. C., et al. 2014b, ApJ, 795, 145

Barro, G., Kriek, M., Pérez-González, P. G., et al. 2016, ApJL, 827, L32

Barro, G., Faber, S. M., Koo, D. C., et al. 2017, ApJ, 840, 47

Behroozi, P. S., Wechsler, R. H., & Conroy, C. 2013, ApJ, 770, 57

Bekki, K. 2009, MNRAS, 399, 2221

—. 2014, MNRAS, 438, 444

Bekki, K., & Couch, W. J. 2003, ApJL, 596, L13

—. 2011, MNRAS, 415, 1783

Bekki, K., Couch, W. J., & Shioya, Y. 2002, ApJ, 577, 651

Bell, E. F., McIntosh, D. H., Katz, N., & Weinberg, M. D. 2003, ApJL, 585, L117

Bellocchi, E., Arribas, S., Colina, L., & Miralles-Caballero, D. 2013, A&A, 557, A59

Bendo, G. J., Wilson, C. D., Pohlen, M., et al. 2010, A&A, 518, L65

Bertin, E., & Arnouts, S. 1996, AAPS, 117, 393

Bialas, D., Lisker, T., Olczak, C., Spurzem, R., & Kotulla, R. 2015, A&A, 576, A103

Bigiel, F., Leroy, A., Walter, F., et al. 2010, AJ, 140, 1194

—. 2008, AJ, 136, 2846

Bland-Hawthorn, J., Bryant, J., Robertson, G., et al. 2011, Optics Express, 19, 2649

Blumenthal, G. R., Faber, S. M., Primack, J. R., & Rees, M. J. 1984, Nature, 311, 517

Bolatto, A. D., Wolfire, M., & Leroy, A. K. 2013, ARAA, 51, 207

Bolatto, A. D., Leroy, A. K., Jameson, K., et al. 2011, ApJ, 741, 12

Bolzonella, M., Miralles, J.-M., & Pelló, R. 2000, A&A, 363, 476

Boselli, A., Cortese, L., Boquien, M., et al. 2014a, A&A, 564, A67

—. 2014b, A&A, 564, A66

Boselli, A., & Gavazzi, G. 2006, PASP, 118, 517

—. 2014, A&ARv, 22, 74

Boselli, A., Cuillandre, J. C., Fossati, M., et al. 2016, A&A, 587, A68

Bournaud, F., Elmegreen, B. G., Teyssier, R., Block, D. L., & Puerari, I. 2010, MNRAS, 409, 1088

Bournaud, F., Perret, V., Renaud, F., et al. 2014, ApJ, 780, 57

Bower, R. G., & Balogh, M. L. 2004, Clusters of Galaxies: Probes of Cosmological Structure and Galaxy Evolution, 325

Bower, R. G., Benson, A. J., & Crain, R. A. 2012, MNRAS, 422, 2816

Bower, R. G., Lucey, J. R., & Ellis, R. S. 1992, MNRAS, 254, 601

Bradshaw, E. J., Almaini, O., Hartley, W. G., et al. 2013, MNRAS, 433, 194

Bruce, V. A., Dunlop, J. S., McLure, R. J., et al. 2014, MNRAS, 444, 1001

Bruzual, G., & Charlot, S. 2003, MNRAS, 344, 1000

Bryant, J. J., Bland-Hawthorn, J., Fogarty, L. M. R., Lawrence, J. S., & Croom, S. M. 2014, MNRAS, 438, 869

Bryant, J. J., Owers, M. S., Robotham, A. S. G., et al. 2015, MNRAS, 447, 2857

Buitrago, F., Trujillo, I., Conselice, C. J., & Häußler, B. 2013, MNRAS, 428, 1460

Burgarella, D., Buat, V., & Iglesias-Páramo, J. 2005, MNRAS, 360, 1413

Burgarella, D., Buat, V., Gruppioni, C., et al. 2013, A&A, 554, A70

Burkert, A. 1995, ApJL, 447, L25

Burkert, A., Förster Schreiber, N. M., Genzel, R., et al. 2016, ApJ, 826, 214

Burstein, D., Ho, L. C., Huchra, J. P., & Macri, L. M. 2005, ApJ, 621, 246

Butcher, H., & Oemler, Jr., A. 1978, ApJ, 219, 18

Byrd, G., & Valtonen, M. 1990, ApJ, 350, 89

Cacciato, M., Dekel, A., & Genel, S. 2012, MNRAS, 421, 818

Calzetti, D., Armus, L., Bohlin, R. C., et al. 2000, ApJ, 533, 682

Cantale, N., Jablonka, P., Courbin, F., et al. 2016, A&A, 589, A82

Cappellari, M., Emsellem, E., Krajnović, D., et al. 2011, MNRAS, 416, 1680

Carilli, C. L., & Walter, F. 2013, ARAA, 51, 105

Catinella, B., Giovanelli, R., & Haynes, M. P. 2006, ApJ, 640, 751

Catinella, B., Schiminovich, D., Kauffmann, G., et al. 2010, MNRAS, 403, 683

Cattaneo, A., Faber, S. M., Binney, J., et al. 2009, Nature, 460, 213

Cava, A., Bettoni, D., Poggianti, B. M., et al. 2009, A&A, 495, 707

Ceverino, D., Dekel, A., & Bournaud, F. 2010, MNRAS, 404, 2151

Chabrier, G. 2003, PASP, 115, 763

Chapin, E. L., Hughes, D. H., & Aretxaga, I. 2009, MNRAS, 393, 653

Chapman, S. C., Helou, G., Lewis, G. F., & Dale, D. A. 2003, ApJ, 588, 186

Chary, R., & Elbaz, D. 2001, ApJ, 556, 562

Christlein, D., & Zabludoff, A. I. 2004, ApJ, 616, 192

Coia, D., McBreen, B., Metcalfe, L., et al. 2005, A&A, 431, 433

Colina, L., Arribas, S., & Monreal-Ibero, A. 2005, ApJ, 621, 725

Combes, F., García-Burillo, S., Braine, J., et al. 2013, A&A, 550, A41

Comerford, J. M., Meneghetti, M., Bartelmann, M., & Schirmer, M. 2006, ApJ, 642, 39

Conroy, C., & Wechsler, R. H. 2009, ApJ, 696, 620

Conselice, C. J. 2003, APJS, 147, 1

—. 2014, ARAA, 52, 291

Conselice, C. J., Bluck, A. F. L., Ravindranath, S., et al. 2011, MNRAS, 417, 2770

Cortese, L., Catinella, B., Boissier, S., Boselli, A., & Heinis, S. 2011, MNRAS, 415, 1797

Cortese, L., Davies, J. I., Pohlen, M., et al. 2010, A&A, 518, L49

Cortese, L., Fogarty, L. M. R., Ho, I.-T., et al. 2014, ApJL, 795, L37

Cortesi, A., Merrifield, M. R., Coccato, L., et al. 2013, MNRAS, 432, 1010

Couch, W. J., & Sharples, R. M. 1987, MNRAS, 229, 423

Courteau, S. 1997, AJ, 114, 2402

Cox, T. J., Dutta, S. N., Di Matteo, T., et al. 2006, ApJ, 650, 791

Crain, R. A., Schaye, J., Bower, R. G., et al. 2015, MNRAS, 450, 1937

Cresci, G., Hicks, E. K. S., Genzel, R., et al. 2009, ApJ, 697, 115

Croom, S. M., Lawrence, J. S., Bland-Hawthorn, J., et al. 2012, MNRAS, 421, 872

Czoske, O., Kneib, J.-P., Soucail, G., et al. 2001, A&A, 372, 391

Czoske, O., Moore, B., Kneib, J.-P., & Soucail, G. 2002, A&A, 386, 31

Daddi, E., Bournaud, F., Walter, F., et al. 2010, ApJ, 713, 686

Dale, J. E., Ngoumou, J., Ercolano, B., & Bonnell, I. A. 2014, MNRAS, 442, 694

Dalla Vecchia, C., & Schaye, J. 2012, MNRAS, 426, 140

Danovich, M., Dekel, A., Hahn, O., Ceverino, D., & Primack, J. 2015, MNRAS, 449, 2087

Davé, R., Finlator, K., & Oppenheimer, B. D. 2012, MNRAS, 421, 98

Davies, R., Förster Schreiber, N. M., Cresci, G., et al. 2011, ApJ, 741, 69

Davis, M., Efstathiou, G., Frenk, C. S., & White, S. D. M. 1985, ApJ, 292, 371

De Lucia, G., Poggianti, B. M., Halliday, C., et al. 2009, MNRAS, 400, 68

de Vaucouleurs, G. 1959, Handbuch der Physik, 53, 275

—. 1963, APJS, 8, 31

Dekel, A., & Birnboim, Y. 2006, MNRAS, 368, 2

Dekel, A., & Burkert, A. 2014, MNRAS, 438, 1870

Dekel, A., & Krumholz, M. R. 2013, MNRAS, 432, 455

Dekel, A., Sari, R., & Ceverino, D. 2009, ApJ, 703, 785

Dekel, A., & Silk, J. 1986, ApJ, 303, 39

Di Matteo, T., Springel, V., & Hernquist, L. 2005, Nature, 433, 604

Diaferio, A., Geller, M. J., & Rines, K. J. 2005, ApJL, 628, L97

Djorgovski, S., & Davis, M. 1987, ApJ, 313, 59

Draine, B. T., Dale, D. A., Bendo, G., et al. 2007, ApJ, 663, 866

Dressler, A. 1980, ApJ, 236, 351

Dressler, A., Oemler, Jr., A., Couch, W. J., et al. 1997, ApJ, 490, 577

Dubois, Y., & Teyssier, R. 2008, A&A, 477, 79

Elbaz, D., Daddi, E., Le Borgne, D., et al. 2007, A&A, 468, 33

Elbaz, D., Dickinson, M., Hwang, H. S., et al. 2011, A&A, 533, A119

Eliche-Moral, M. C., González-García, A. C., Aguerri, J. A. L., et al. 2012, A&A, 547, A48

Elmegreen, B. G. 1989, ApJ, 338, 178

Elmegreen, B. G., & Burkert, A. 2010, ApJ, 712, 294

Elmegreen, B. G., & Elmegreen, D. M. 2005, ApJ, 627, 632

Elmegreen, B. G., Elmegreen, D. M., Fernandez, M. X., & Lemonias, J. J. 2009, ApJ, 692, 12

Elmegreen, B. G., & Scalo, J. 2004, ARAA, 42, 211

Elmegreen, D. M., Elmegreen, B. G., Ravindranath, S., & Coe, D. A. 2007, ApJ, 658, 763

Emsellem, E., Cappellari, M., Krajnović, D., et al. 2007, MNRAS, 379, 401

—. 2011, MNRAS, 414, 888

Epinat, B., Amram, P., Balkowski, C., & Marcelin, M. 2010, MNRAS, 401, 2113

Epinat, B., Amram, P., Marcelin, M., et al. 2008, MNRAS, 388, 500

Epinat, B., Tasca, L., Amram, P., et al. 2012, A&A, 539, A92

Fabello, S., Kauffmann, G., Catinella, B., et al. 2012, MNRAS, 427, 2841

Faber, S. M., & Jackson, R. E. 1976, ApJ, 204, 668

Fabian, A. C. 2012, ARAA, 50, 455

Farouki, R. T., & Shapiro, S. L. 1982, ApJ, 259, 103

Faucher-Giguère, C.-A., Quataert, E., & Hopkins, P. F. 2013, MNRAS, 433, 1970

Federrath, C. 2013, MNRAS, 436, 3167

—. 2015, MNRAS, 450, 4035

Ferrarese, L., & Merritt, D. 2000, ApJL, 539, L9

Fogarty, L. M. R., Scott, N., Owers, M. S., et al. 2015, MNRAS, 454, 2050

Förster Schreiber, N. M., Genzel, R., Lehnert, M. D., et al. 2006, ApJ, 645, 1062

Förster Schreiber, N. M., Genzel, R., Bouché, N., et al. 2009, ApJ, 706, 1364

Förster Schreiber, N. M., Shapley, A. E., Genzel, R., et al. 2011, ApJ, 739, 45

Freeman, K. C. 1970, ApJ, 160, 811

Fujita, Y. 1998, ApJ, 509, 587

Fukugita, M., & Peebles, P. J. E. 2004, ApJ, 616, 643

Fumagalli, M., Fossati, M., Hau, G. K. T., et al. 2014, MNRAS, 445, 4335

Galametz, M., Kennicutt, R. C., Albrecht, M., et al. 2012, MNRAS, 425, 763

Galilei, G. 1610, Sidereus Nuncius

Gao, Y., & Solomon, P. M. 2004, ApJ, 606, 271

Gardner, J. P., Mather, J. C., Clampin, M., et al. 2006, Space Science Reviews, 123, 485

Gavazzi, G., Fumagalli, M., Fossati, M., et al. 2013, A&A, 553, A89

Geach, J. E., Smail, I., Moran, S. M., et al. 2011, ApJL, 730, L19

Geach, J. E., Smail, I., Moran, S. M., Treu, T., & Ellis, R. S. 2009, ApJ, 691, 783

Geach, J. E., Smail, I., Ellis, R. S., et al. 2006, ApJ, 649, 661

Gebhardt, K., Kormendy, J., Ho, L. C., et al. 2000, ApJL, 543, L5

Genzel, R., Tacconi, L. J., Eisenhauer, F., et al. 2006, Nature, 442, 786

Genzel, R., Burkert, A., Bouché, N., et al. 2008, ApJ, 687, 59

Genzel, R., Tacconi, L. J., Gracia-Carpio, J., et al. 2010, MNRAS, 407, 2091

Genzel, R., Newman, S., Jones, T., et al. 2011, ApJ, 733, 101

Genzel, R., Tacconi, L. J., Kurk, J., et al. 2013, ApJ, 773, 68

Genzel, R., Förster Schreiber, N. M., Lang, P., et al. 2014, ApJ, 785, 75

Genzel, R., Tacconi, L. J., Lutz, D., et al. 2015, ApJ, 800, 20

Glazebrook, K. 2013, PASA, 30, 56

Gnerucci, A., Marconi, A., Cresci, G., et al. 2011, A&A, 528, A88

Goldbaum, N. J., Krumholz, M. R., & Forbes, J. C. 2015, ApJ, 814, 131

—. 2016, ApJ, 827, 28

Gómez, P. L., Nichol, R. C., Miller, C. J., et al. 2003, ApJ, 584, 210

Green, A. W., Glazebrook, K., McGregor, P. J., et al. 2010, Nature, 467, 684

—. 2014, MNRAS, 437, 1070

Grogin, N. A., Kocevski, D. D., Faber, S. M., et al. 2011, APJS, 197, 35

Guilloteau, S., & Lucas, R. 2000, in Astronomical Society of the Pacific Conference Series, Vol. 217, Imaging at Radio through Submillimeter Wavelengths, ed. J. G. Mangum & S. J. E. Radford, 299

Gunn, J. E., & Gott, III, J. R. 1972, ApJ, 176, 1

Guo, Y., Giavalisco, M., Ferguson, H. C., Cassata, P., & Koekemoer, A. M. 2012, ApJ, 757, 120

Guo, Y., Ferguson, H. C., Bell, E. F., et al. 2015, ApJ, 800, 39

Haines, C. P., Smith, G. P., Egami, E., et al. 2009, MNRAS, 396, 1297

Hao, C.-N., Kennicutt, R. C., Johnson, B. D., et al. 2011, ApJ, 741, 124

Harrison, C. 2014, PhD thesis, Durham University

Harrison, C. M. 2017, Nature Astronomy, 1, 0165

Harrison, C. M., Alexander, D. M., Mullaney, J. R., et al. 2016, MNRAS, 456, 1195

Harrison, C. M., Johnson, H. L., Swinbank, A. M., et al. 2017, MNRAS, 467, 1965

Hayward, C. C., Torrey, P., Springel, V., Hernquist, L., & Vogelsberger, M. 2014, MNRAS, 442, 1992

Heckman, T. M., & Best, P. N. 2014, ARAA, 52, 589

Henriksen, M., & Byrd, G. 1996, ApJ, 459, 82

Hernquist, L. 1992, ApJ, 400, 460

Herschel, W. 1786, Philosophical Transactions of the Royal Society of London Series I, 76, 457

Hinz, J. L., Engelbracht, C. W., Skibba, R., et al. 2012, ApJ, 756, 75

Hoekstra, H. 2007, MNRAS, 379, 317

Hogg, D. W., Masjedi, M., Berlind, A. A., et al. 2006, ApJ, 650, 763

Hopkins, P. F., Hernquist, L., Cox, T. J., et al. 2006, APJS, 163, 1

Hopkins, P. F., Kereš, D., & Murray, N. 2013, MNRAS, 432, 2639

Hopkins, P. F., Kereš, D., Murray, N., Quataert, E., & Hernquist, L. 2012, MNRAS, 427, 968

Hopkins, P. F., Kereš, D., Oñorbe, J., et al. 2014, MNRAS, 445, 581

Hopkins, P. F., Quataert, E., & Murray, N. 2011, MNRAS, 417, 950

Hubble, E. 1929, Proceedings of the National Academy of Science, 15, 168

Hubble, E., & Humason, M. L. 1931, ApJ, 74, 43

—. 1934, Proceedings of the National Academy of Science, 20, 264

Hubble, E., & Rosseland, S. 1936, Science, 84, 509

Hubble, E. P. 1925, Popular Astronomy, 33

—. 1926, ApJ, 64

Hudson, M. J., Stevenson, J. B., Smith, R. J., et al. 2010, MNRAS, 409, 405

Hung, C.-L., Hayward, C. C., Smith, H. A., et al. 2016, ApJ, 816, 99

Immeli, A., Samland, M., Westera, P., & Gerhard, O. 2004, ApJ, 611, 20

Ivison, R. J., Papadopoulos, P. P., Smail, I., et al. 2011, MNRAS, 412, 1913

Ivison, R. J., Swinbank, A. M., Smail, I., et al. 2013, ApJ, 772, 137

Jaffé, Y. L., Smith, R., Candlish, G. N., et al. 2015, MNRAS, 448, 1715

Jeans, J. H. 1902, Philosophical Transactions of the Royal Society of London Series A, 199, 1

Johnson, H. L., Harrison, C. M., Swinbank, A. M., et al. 2016, MNRAS, 460, 1059

—. 2017, ArXiv e-prints

Johnston, E. J., Aragón-Salamanca, A., & Merrifield, M. R. 2014, MNRAS, 441, 333

Jones, T. A., Swinbank, A. M., Ellis, R. S., Richard, J., & Stark, D. P. 2010, MNRAS, 404, 1247

Joung, M. R., Mac Low, M.-M., & Bryan, G. L. 2009, ApJ, 704, 137

Kant, I. 1755, Allgemeine Naturgeschichte und Theorie des Himmels

Karim, A., Schinnerer, E., Martínez-Sansigre, A., et al. 2011, ApJ, 730, 61

Kassin, S. A., Weiner, B. J., Faber, S. M., et al. 2007, ApJL, 660, L35

—. 2012, ApJ, 758, 106

Katz, N., Weinberg, D. H., & Hernquist, L. 1996, APJS, 105, 19

Kenney, J. D. P., van Gorkom, J. H., & Vollmer, B. 2004, AJ, 127, 3361

Kennicutt, R. C., & Evans, N. J. 2012, ARAA, 50, 531

Kennicutt, Jr., R. C. 1989, ApJ, 344, 685

—. 1998a, ARAA, 36, 189

—. 1998b, ApJ, 498, 541

Kennicutt, Jr., R. C., Hao, C.-N., Calzetti, D., et al. 2009, ApJ, 703, 1672

Kereš, D., Katz, N., Davé, R., Fardal, M., & Weinberg, D. H. 2009a, MNRAS, 396, 2332

Kereš, D., Katz, N., Fardal, M., Davé, R., & Weinberg, D. H. 2009b, MNRAS, 395, 160

Kereš, D., Katz, N., Weinberg, D. H., & Davé, R. 2005, MNRAS, 363, 2

Kerr, R. P. 1963, Physical Review Letters, 11, 237

Kewley, L. J., Dopita, M. A., Leitherer, C., et al. 2013, ApJ, 774, 100

Kewley, L. J., Rupke, D., Zahid, H. J., Geller, M. J., & Barton, E. J. 2010, ApJL, 721, L48

Kim, C.-G., Ostriker, E. C., & Kim, W.-T. 2013, ApJ, 776, 1

—. 2014, ApJ, 786, 64

Kim, W.-T., & Ostriker, E. C. 2007, ApJ, 660, 1232

King, A., & Pounds, K. 2015, ARAA, 53, 115

Klessen, R. S., & Hennebelle, P. 2010, A&A, 520, A17

Kneib, J.-P., Hudelot, P., Ellis, R. S., et al. 2003, ApJ, 598, 804

Kocevski, D. D., Lemaux, B. C., Lubin, L. M., et al. 2011, ApJ, 736, 38

Kodama, T., Balogh, M. L., Smail, I., Bower, R. G., & Nakata, F. 2004, MNRAS, 354, 1103

Kodama, T., & Smail, I. 2001, MNRAS, 326, 637

Koekemoer, A. M., Faber, S. M., Ferguson, H. C., et al. 2011, APJS, 197, 36

Kormendy, J., & Ho, L. C. 2013, ARAA, 51, 511

Kormendy, J., & Richstone, D. 1995, ARAA, 33, 581

Koyama, Y., Kodama, T., Shimasaku, K., et al. 2008, MNRAS, 391, 1758

Krumholz, M. R. 2015, ArXiv e-prints

Krumholz, M. R., & Burkhart, B. 2016, MNRAS, 458, 1671

Krumholz, M. R., Burkhart, B., Forbes, J. C., & Crocker, R. M. 2017, ArXiv e-prints

Krumholz, M. R., & Dekel, A. 2010, MNRAS, 406, 112

Krumholz, M. R., Dekel, A., & McKee, C. F. 2012, ApJ, 745, 69

Lagos, C. d. P., Theuns, T., Stevens, A. R. H., et al. 2017, MNRAS, 464, 3850

Larson, R. B. 1974, MNRAS, 169, 229

—. 1981, MNRAS, 194, 809

Larson, R. B., Tinsley, B. M., & Caldwell, C. N. 1980, ApJ, 237, 692

Law, D. R., Steidel, C. C., Erb, D. K., et al. 2009, ApJ, 697, 2057

Law, D. R., Steidel, C. C., Shapley, A. E., et al. 2012, ApJ, 759, 29

Lawrence, A., Warren, S. J., Almaini, O., et al. 2007, MNRAS, 379, 1599

Le Tiran, L., Lehnert, M. D., van Driel, W., Nesvadba, N. P. H., & Di Matteo, P. 2011, A&A, 534, L4

Leauthaud, A., Massey, R., Kneib, J.-P., et al. 2007, APJS, 172, 219

Leethochawalit, N., Jones, T. A., Ellis, R. S., et al. 2016, ApJ, 820, 84

Lehnert, M. D., Le Tiran, L., Nesvadba, N. P. H., et al. 2013, A&A, 555, A72

Lehnert, M. D., Nesvadba, N. P. H., Le Tiran, L., et al. 2009, ApJ, 699, 1660

Leitherer, C., Schaerer, D., Goldader, J., et al. 2011, Starburst99: Synthesis Models for Galaxies with Active Star Formation, Astrophysics Source Code Library

Lemoine-Busserolle, M., Bunker, A., Lamareille, F., & Kissler-Patig, M. 2010, MNRAS, 401, 1657

Leroy, A. K., Walter, F., Sandstrom, K., et al. 2013, AJ, 146, 19

Lewis, I., Balogh, M., De Propris, R., et al. 2002, MNRAS, 334, 673

Lilly, S. J., Le Fevre, O., Hammer, F., & Crampton, D. 1996, ApJL, 460, L1

Lintott, C. J., Schawinski, K., Slosar, A., et al. 2008, MNRAS, 389, 1179

Livermore, R. C., Jones, T., Richard, J., et al. 2012, MNRAS, 427, 688

Livermore, R. C., Jones, T. A., Richard, J., et al. 2015, MNRAS, 450, 1812

Lutz, D., Poglitsch, A., Altieri, B., et al. 2011, A&A, 532, A90

Ma, C.-J., Smail, I., Swinbank, A. M., et al. 2015, ApJ, 806, 257

Mac Low, M.-M. 1999, ApJ, 524, 169

Mac Low, M.-M., & Klessen, R. S. 2004, Reviews of Modern Physics, 76, 125

Mac Low, M.-M., Klessen, R. S., Burkert, A., & Smith, M. D. 1998, Physical Review Letters, 80, 2754

Madau, P., & Dickinson, M. 2014, ARAA, 52, 415

Madau, P., Ferguson, H. C., Dickinson, M. E., et al. 1996, MNRAS, 283, 1388

Magorrian, J., Tremaine, S., Richstone, D., et al. 1998, AJ, 115, 2285

Mandelker, N., Dekel, A., Ceverino, D., et al. 2017, MNRAS, 464, 635

—. 2014, MNRAS, 443, 3675

Marchesini, D., van Dokkum, P. G., Förster Schreiber, N. M., et al. 2009, ApJ, 701, 1765

Marcillac, D., Rigby, J. R., Rieke, G. H., & Kelly, D. M. 2007, ApJ, 654, 825

Martig, M., Bournaud, F., Teyssier, R., & Dekel, A. 2009, ApJ, 707, 250

Martig, M., Crocker, A. F., Bournaud, F., et al. 2013, MNRAS, 432, 1914

Martin, C. L., & Kennicutt, Jr., R. C. 2001, ApJ, 555, 301

Masters, K. L., Mosleh, M., Romer, A. K., et al. 2010, MNRAS, 405, 783

Mastropietro, C., Moore, B., Mayer, L., et al. 2005, MNRAS, 364, 607

McCarthy, I. G., Frenk, C. S., Font, A. S., et al. 2008, MNRAS, 383, 593

McGaugh, S. S., Schombert, J. M., de Blok, W. J. G., & Zagursky, M. J. 2010, ApJL, 708, L14

McKee, C. F., & Ostriker, E. C. 2007, ARAA, 45, 565

McLure, R. J., Pearce, H. J., Dunlop, J. S., et al. 2013, MNRAS, 428, 1088

McNamara, B. R., & Nulsen, P. E. J. 2012, New Journal of Physics, 14, 055023

Merloni, A., Rudnick, G., & Di Matteo, T. 2004, MNRAS, 354, L37

Merluzzi, P., Busarello, G., Dopita, M. A., et al. 2013, MNRAS, 429, 1747

Messier, C. 1781, Catalogue des Nébuleuses et des Amas d'Étoiles (Catalog of Nebulae and Star Clusters), Tech. rep.

Mihos, J. C., & Bothun, G. D. 1998, ApJ, 500, 619

Mihos, J. C., & Hernquist, L. 1996, ApJ, 464, 641

Moiseev, A. V., Tikhonov, A. V., & Klypin, A. 2015, MNRAS, 449, 3568

Molina, J., Ibar, E., Swinbank, A. M., et al. 2017, MNRAS, 466, 892

Momcheva, I. G., Brammer, G. B., van Dokkum, P. G., et al. 2016, APJS, 225, 27

Moore, B., Katz, N., Lake, G., Dressler, A., & Oemler, A. 1996, Nature, 379, 613

Moore, B., Lake, G., & Katz, N. 1998, ApJ, 495, 139

Moran, S. M., Ellis, R. S., Treu, T., et al. 2005, ApJ, 634, 977

Moran, S. M., Miller, N., Treu, T., Ellis, R. S., & Smith, G. P. 2007, ApJ, 659, 1138

Morrissey, P., Schiminovich, D., Barlow, T. A., et al. 2005, ApJL, 619, L7

Mortlock, A., Conselice, C. J., Hartley, W. G., et al. 2013, MNRAS, 433, 1185

Moster, B. P., Naab, T., & White, S. D. M. 2013, MNRAS, 428, 3121

Muzzin, A., Marchesini, D., Stefanon, M., et al. 2013, ApJ, 777, 18

Naab, T., & Burkert, A. 2003, ApJ, 597, 893

Nelson, E., van Dokkum, P., Franx, M., et al. 2014, Nature, 513, 394

Nelson, E. J., van Dokkum, P. G., Förster Schreiber, N. M., et al. 2016, ApJ, 828, 27

Newman, S. F., Genzel, R., Förster-Schreiber, N. M., et al. 2012, ApJ, 761, 43

Newman, S. F., Genzel, R., Förster Schreiber, N. M., et al. 2013, ApJ, 767, 104

Noeske, K. G., Weiner, B. J., Faber, S. M., et al. 2007, ApJL, 660, L43

Obreschkow, D., Glazebrook, K., Bassett, R., et al. 2015, ApJ, 815, 97

Ocvirk, P., Pichon, C., & Teyssier, R. 2008, MNRAS, 390, 1326

Oemler, Jr., A., Dressler, A., Kelson, D., et al. 2009, ApJ, 693, 152

Oklopčić, A., Hopkins, P. F., Feldmann, R., et al. 2017, MNRAS, 465, 952

Oliver, S. J., Bock, J., Altieri, B., et al. 2012, MNRAS, 424, 1614

Oppenheimer, B. D., & Davé, R. 2006, MNRAS, 373, 1265

Osterbrock, D. E., & Ferland, G. J. 2006, Astrophysics of gaseous nebulae and active galactic nuclei

Ota, N., Pointecouteau, E., Hattori, M., & Mitsuda, K. 2004, ApJ, 601, 120

Owers, M. S., Allen, J. T., Baldry, I., et al. 2017, MNRAS, 468, 1824

Peebles, P. J. E. 1982, ApJL, 263, L1

Peng, Y., Maiolino, R., & Cochrane, R. 2015, Nature, 521, 192

Peng, Y.-j., Lilly, S. J., Kovač, K., et al. 2010, ApJ, 721, 193

Persic, M., & Salucci, P. 1988, MNRAS, 234, 131

Planck Collaboration, Ade, P. A. R., Aghanim, N., et al. 2014, A&A, 571, A16

—. 2016, A&A, 594, A13

Poggianti, B. M., Smail, I., Dressler, A., et al. 1999, ApJ, 518, 576

Poggianti, B. M., & Wu, H. 2000, ApJ, 529, 157

Poggianti, B. M., Aragón-Salamanca, A., Zaritsky, D., et al. 2009, ApJ, 693, 112

Postman, M., Coe, D., Benítez, N., et al. 2012, APJS, 199, 25

Pracy, M. B., Couch, W. J., Blake, C., et al. 2005, MNRAS, 359, 1421

Puech, M., Hammer, F., Lehnert, M. D., & Flores, H. 2007, A&A, 466, 83

Putman, M. E., Peek, J. E. G., & Joung, M. R. 2012, ARAA, 50, 491

Querejeta, M., Eliche-Moral, M. C., Tapia, T., et al. 2015, A&A, 579, L2

Quilis, V., Moore, B., & Bower, R. 2000, Science, 288, 1617

Rawle, T. D., Rex, M., Egami, E., et al. 2012, ApJ, 756, 106

Rees, M. J., & Ostriker, J. P. 1977, MNRAS, 179, 541

Rich, J. A., Torrey, P., Kewley, L. J., Dopita, M. A., & Rupke, D. S. N. 2012, ApJ, 753, 5

Rieke, G. H., Alonso-Herrero, A., Weiner, B. J., et al. 2009, ApJ, 692, 556

Rix, H.-W., Barden, M., Beckwith, S. V. W., et al. 2004, APJS, 152, 163

Rodighiero, G., Daddi, E., Baronchelli, I., et al. 2011, ApJL, 739, L40

Rodríguez Del Pino, B., Bamford, S. P., Aragón-Salamanca, A., et al. 2014, MNRAS, 438, 1038

Rousselot, P., Lidman, C., Cuby, J.-G., Moreels, G., & Monnet, G. 2000, A&A, 354, 1134

Rupke, D. S. N., Kewley, L. J., & Chien, L.-H. 2010, ApJ, 723, 1255

Saintonge, A., Kauffmann, G., Kramer, C., et al. 2011, MNRAS, 415, 32

Saintonge, A., Lutz, D., Genzel, R., et al. 2013, ApJ, 778, 2

Sales, L. V., Vogelsberger, M., Genel, S., et al. 2015, MNRAS, 447, L6

Salucci, P., & Burkert, A. 2000, ApJL, 537, L9

Sánchez, S. F., Kennicutt, R. C., Gil de Paz, A., et al. 2012, A&A, 538, A8

Sandage, A. 2005, ARAA, 43, 581

Schäfer, B. M. 2009, International Journal of Modern Physics D, 18, 173

Schaller, M., Frenk, C. S., Bower, R. G., et al. 2015, MNRAS, 451, 1247

Schawinski, K., Urry, C. M., Simmons, B. D., et al. 2014, MNRAS, 440, 889

Schaye, J., Dalla Vecchia, C., Booth, C. M., et al. 2010, MNRAS, 402, 1536

Schaye, J., Crain, R. A., Bower, R. G., et al. 2015, MNRAS, 446, 521

Schmidt, M. 1959, ApJ, 129, 243

Schreiber, C., Pannella, M., Elbaz, D., et al. 2015, A&A, 575, A74

Shapiro, S. L., & Teukolsky, S. A. 1983, Black holes, white dwarfs, and neutron stars: The physics of compact objects

Shapley, A. E., Steidel, C. C., Pettini, M., & Adelberger, K. L. 2003, ApJ, 588, 65

Shapley, H., & Curtis, H. D. 1921, Bulletin of the National Research Council, Vol. 2, Part 3, No. 11, p. 171-217, 2, 171

Sharp, R., Saunders, W., Smith, G., et al. 2006, in Proc. SPIE, Vol. 6269, Society of Photo-Optical Instrumentation Engineers (SPIE) Conference Series, 62690G

Sharp, R., Allen, J. T., Fogarty, L. M. R., et al. 2015, MNRAS, 446, 1551

Sharples, R., Bender, R., Agudo Berbel, A., et al. 2013, The Messenger, 151, 21

Sharples, R. M., Bender, R., Lehnert, M. D., et al. 2004, in Proc. SPIE, Vol. 5492, Ground-based Instrumentation for Astronomy, ed. A. F. M. Moorwood & M. Iye, 1179–1186

Shetty, R., & Ostriker, E. C. 2012, ApJ, 754, 2

Shibuya, T., Ouchi, M., Kubo, M., & Harikane, Y. 2016, ApJ, 821, 72

Simien, F., & de Vaucouleurs, G. 1986, ApJ, 302, 564

Simons, R. C., Kassin, S. A., Trump, J. R., et al. 2016, ApJ, 830, 14

Simons, R. C., Kassin, S. A., Weiner, B. J., et al. 2017, ApJ, 843, 46

Simpson, C., Westoby, P., Arumugam, V., et al. 2013, MNRAS, 433, 2647

Sivanandam, S., Rieke, M. J., & Rieke, G. H. 2014, ApJ, 796, 89

Slipher, V. M. 1914, Lowell Observatory Bulletin, 2, 66

Smail, I., Geach, J. E., Swinbank, A. M., et al. 2014, ApJ, 782, 19

Smith, G. P., Treu, T., Ellis, R. S., Moran, S. M., & Dressler, A. 2005, ApJ, 620, 78

Smith, R., Davies, J. I., & Nelson, A. H. 2010, MNRAS, 405, 1723

Smith, R., Sánchez-Janssen, R., Beasley, M. A., et al. 2015, MNRAS, 454, 2502

Sobral, D., Smail, I., Best, P. N., et al. 2013a, MNRAS, 428, 1128

Sobral, D., Swinbank, A. M., Stott, J. P., et al. 2013b, ApJ, 779, 139

Sobral, D., Matthee, J., Best, P. N., et al. 2015, MNRAS, 451, 2303

Solomon, P. M., & Vanden Bout, P. A. 2005, ARAA, 43, 677

Somerville, R. S., Hopkins, P. F., Cox, T. J., Robertson, B. E., & Hernquist, L. 2008, MNRAS, 391, 481

Soucail, G., Ota, N., Böhringer, H., et al. 2000, A&A, 355, 433

Sparre, M., & Springel, V. 2016, MNRAS, 462, 2418

Speagle, J. S., Steinhardt, C. L., Capak, P. L., & Silverman, J. D. 2014, APJS, 214, 15

Spergel, D. N., Bean, R., Doré, O., et al. 2007, APJS, 170, 377

Springel, V., & Hernquist, L. 2003, MNRAS, 339, 289

Stark, D. P., Swinbank, A. M., Ellis, R. S., et al. 2008, Nature, 455, 775

Stone, J. M., Ostriker, E. C., & Gammie, C. F. 1998, ApJL, 508, L99

Stott, J. P., Sobral, D., Swinbank, A. M., et al. 2014, MNRAS, 443, 2695

Stott, J. P., Swinbank, A. M., Johnson, H. L., et al. 2016, MNRAS, 457, 1888

Strateva, I., Ivezić, Ž., Knapp, G. R., et al. 2001, AJ, 122, 1861

Swinbank, A. M., Smail, I., Sobral, D., et al. 2012a, ApJ, 760, 130

Swinbank, A. M., Sobral, D., Smail, I., et al. 2012b, MNRAS, 426, 935

Swinbank, A. M., Edge, A. C., Smail, I., et al. 2007, MNRAS, 379, 1343

Swinbank, A. M., Webb, T. M., Richard, J., et al. 2009, MNRAS, 400, 1121

Swinbank, A. M., Papadopoulos, P. P., Cox, P., et al. 2011, ApJ, 742, 11

Swinbank, A. M., Simpson, J. M., Smail, I., et al. 2014, MNRAS, 438, 1267

Swinbank, A. M., Harrison, C. M., Trayford, J., et al. 2017, MNRAS, 467, 3140

Symeonidis, M., Vaccari, M., Berta, S., et al. 2013, MNRAS, 431, 2317

Tacconi, L. J., Genzel, R., Neri, R., et al. 2010, Nature, 463, 781

Tacconi, L. J., Neri, R., Genzel, R., et al. 2013, ApJ, 768, 74

Tadaki, K.-i., Genzel, R., Kodama, T., et al. 2017, ApJ, 834, 135

Taylor, E. N., Hopkins, A. M., Baldry, I. K., et al. 2011, MNRAS, 418, 1587

Thomson, A. P., Ivison, R. J., Smail, I., et al. 2012, MNRAS, 425, 2203

Tiley, A. L., Stott, J. P., Swinbank, A. M., et al. 2016, MNRAS, 460, 103

Toomre, A. 1964, ApJ, 139, 1217

Tran, K.-V. H., Franx, M., Illingworth, G. D., et al. 2007, ApJ, 661, 750

Tran, K.-V. H., Papovich, C., Saintonge, A., et al. 2010, ApJL, 719, L126

Treu, T., Ellis, R. S., Kneib, J.-P., et al. 2003, ApJ, 591, 53

Treyer, M., Schiminovich, D., Johnson, B. D., et al. 2010, ApJ, 719, 1191

Tully, R. B., & Fisher, J. R. 1977, A&A, 54, 661

Turner, O. J., Cirasuolo, M., Harrison, C. M., et al. 2017, MNRAS, 471, 1280

Umetsu, K., Medezinski, E., Broadhurst, T., et al. 2010, ApJ, 714, 1470

Valluri, M. 1993, ApJ, 408, 57

van de Voort, F., & Schaye, J. 2012, MNRAS, 423, 2991

van de Voort, F., Schaye, J., Booth, C. M., Haas, M. R., & Dalla Vecchia, C. 2011, MNRAS, 414, 2458

van der Hulst, J. M., Skillman, E. D., Smith, T. R., et al. 1993, AJ, 106, 548

van der Kruit, P. C., & Allen, R. J. 1978, ARAA, 16, 103

van der Wel, A., Bell, E. F., Holden, B. P., Skibba, R. A., & Rix, H.-W. 2010, ApJ, 714, 1779

van der Wel, A., Chang, Y.-Y., Bell, E. F., et al. 2014, ApJL, 792, L6

Veilleux, S., Cecil, G., & Bland-Hawthorn, J. 2005, ARAA, 43, 769

Vergani, D., Epinat, B., Contini, T., et al. 2012, A&A, 546, A118

Vogelsberger, M., Genel, S., Springel, V., et al. 2014, MNRAS, 444, 1518

Vulcani, B., Poggianti, B. M., Aragón-Salamanca, A., et al. 2011, MNRAS, 412, 246

Wang, B., & Silk, J. 1994, ApJ, 427, 759

Westfall, K. B., Andersen, D. R., Bershady, M. A., et al. 2014, ApJ, 785, 43

Westmoquette, M. S. 2007, PhD thesis, University of London, University College London

Whitaker, K. E., van Dokkum, P. G., Brammer, G., & Franx, M. 2012, ApJL, 754, L29

Whitaker, K. E., Franx, M., Leja, J., et al. 2014, ApJ, 795, 104

White, S. D. M., & Frenk, C. S. 1991, ApJ, 379, 52

White, S. D. M., & Rees, M. J. 1978, MNRAS, 183, 341

White, S. D. M., Clowe, D. I., Simard, L., et al. 2005, A&A, 444, 365

Wisnioski, E., Glazebrook, K., Blake, C., et al. 2012, MNRAS, 422, 3339

—. 2011, MNRAS, 417, 2601

Wisnioski, E., Förster Schreiber, N. M., Wuyts, S., et al. 2015, ApJ, 799, 209

Wisnioski, E., Mendel, J. T., Förster Schreiber, N. M., et al. 2017, ArXiv e-prints

Wolf, C., Aragón-Salamanca, A., Balogh, M., et al. 2009, MNRAS, 393, 1302

Wright, T. 1750, An Original Theory or New Hypothesis of the Universe

Wuyts, S., Förster Schreiber, N. M., Genzel, R., et al. 2012, ApJ, 753, 114

Wuyts, S., Förster Schreiber, N. M., Nelson, E. J., et al. 2013, ApJ, 779, 135

Young, J. S., & Scoville, N. Z. 1991, ARAA, 29, 581

Zhang, Y.-Y., Böhringer, H., Mellier, Y., Soucail, G., & Forman, W. 2005, A&A, 429, 85

Zhou, L., Federrath, C., Yuan, T., et al. 2017, ArXiv e-prints

Zitrin, A., Broadhurst, T., Umetsu, K., et al. 2009, MNRAS, 396, 1985

Zolotov, A., Dekel, A., Mandelker, N., et al. 2015, MNRAS, 450, 2327

Appendix A

HST Thumbnails of KROSS Galaxies

In this section we provide broad-band *HST* images for all 231 KROSS galaxies studied in Chapter 5. Thumbnails are ranked by the intrinsic velocity dispersion of the galaxy (σ_0). Full details of our dynamical analysis can be found in Chapter 4.

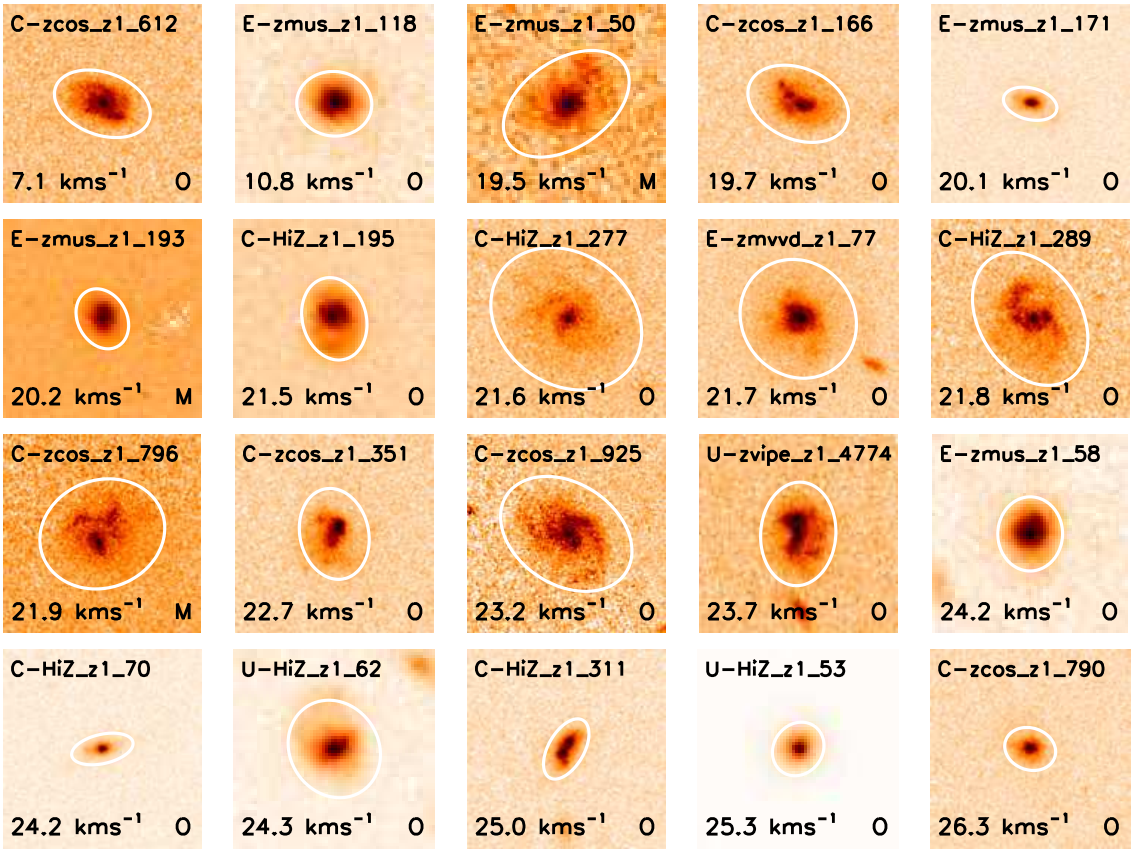

Figure A.1: All *HST* images available for KROSS, ranked by increasing velocity dispersion (σ_0, inset values). Each thumbnail covers an area of 4×4 arcsec and we overlay an ellipse at three times the half-light radius. We differentiate between dispersions measured in the outskirts of the disk ('O') and those calculated from the median of all pixels ('M').

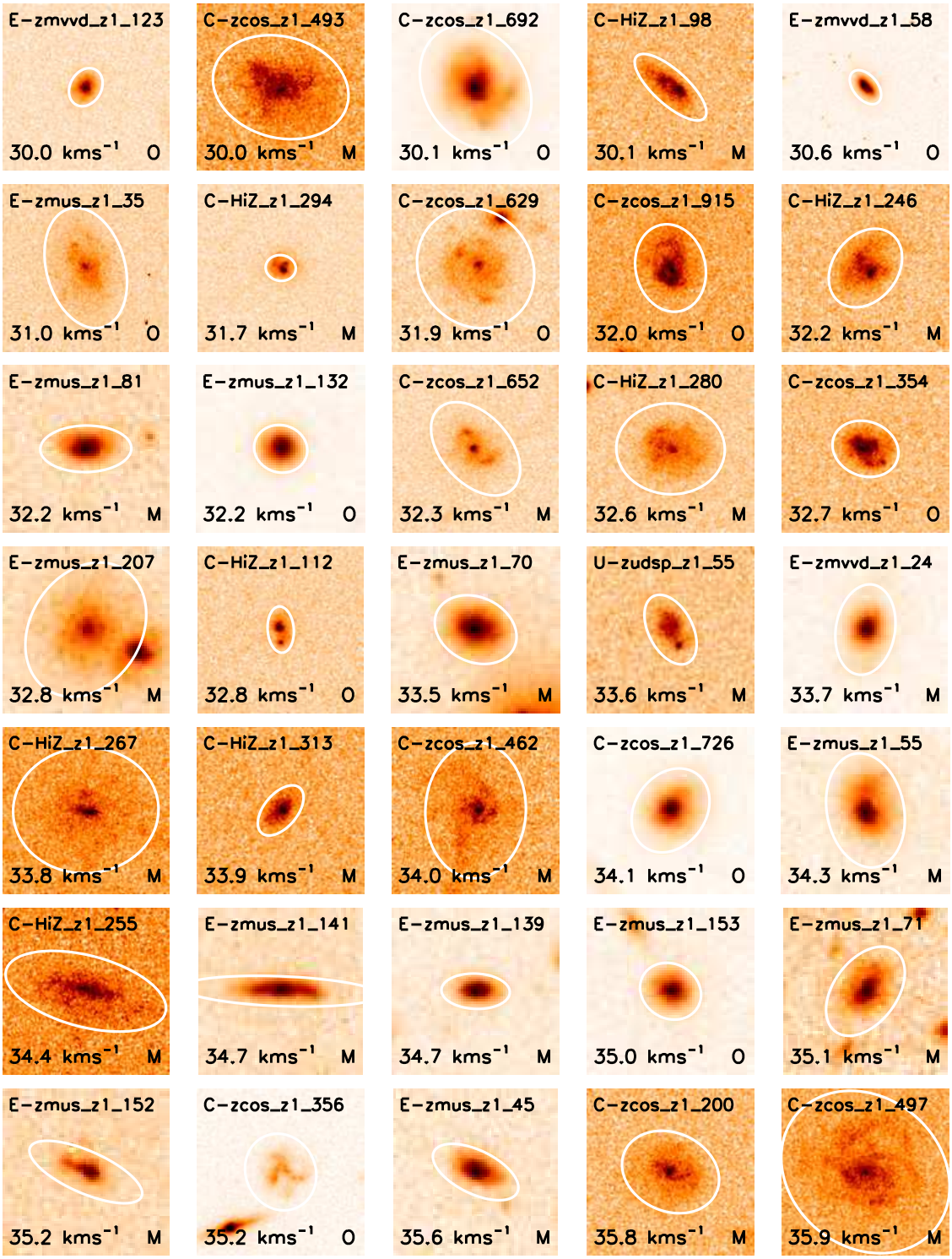

Figure A.1: *continued*

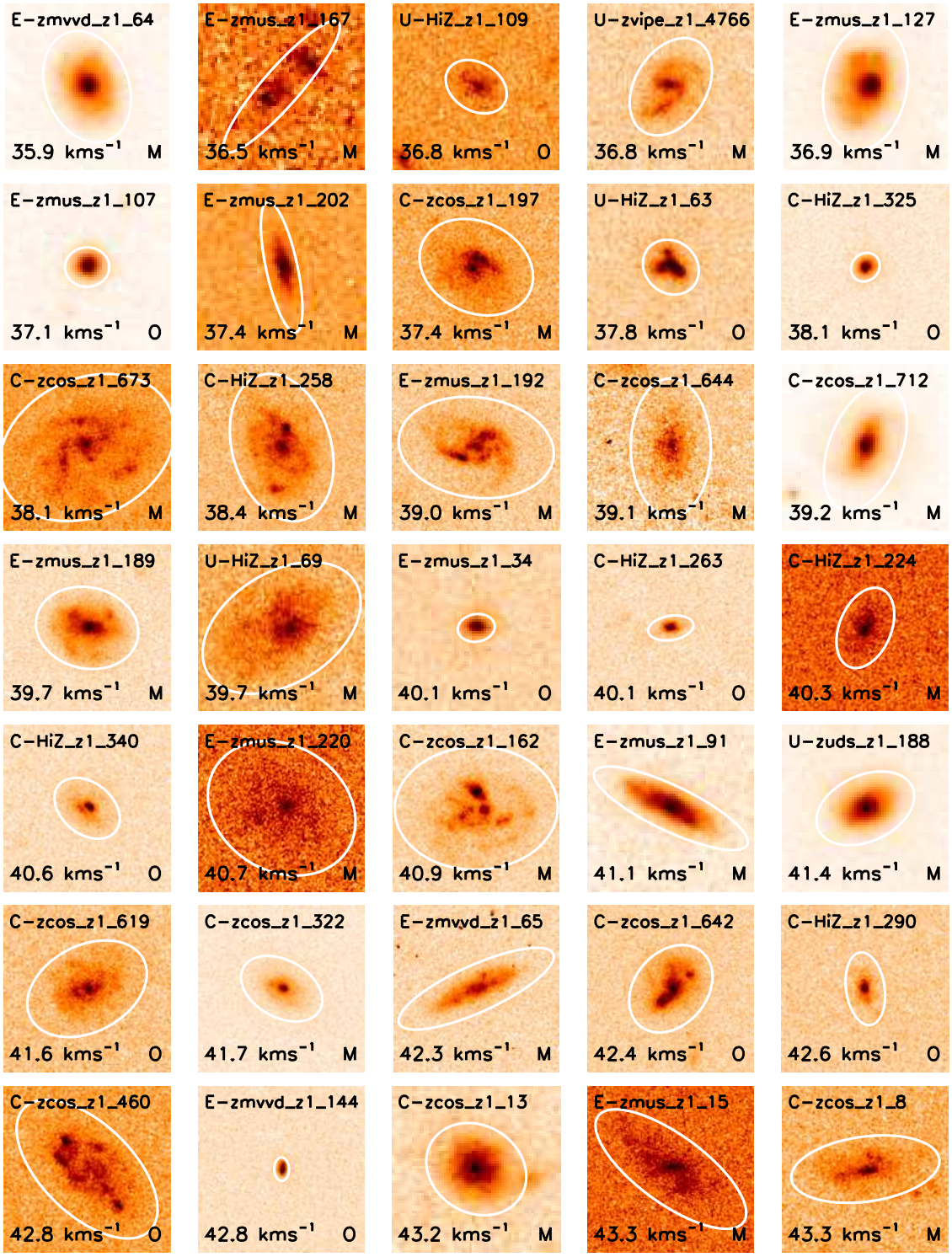

Figure A.1: *continued*

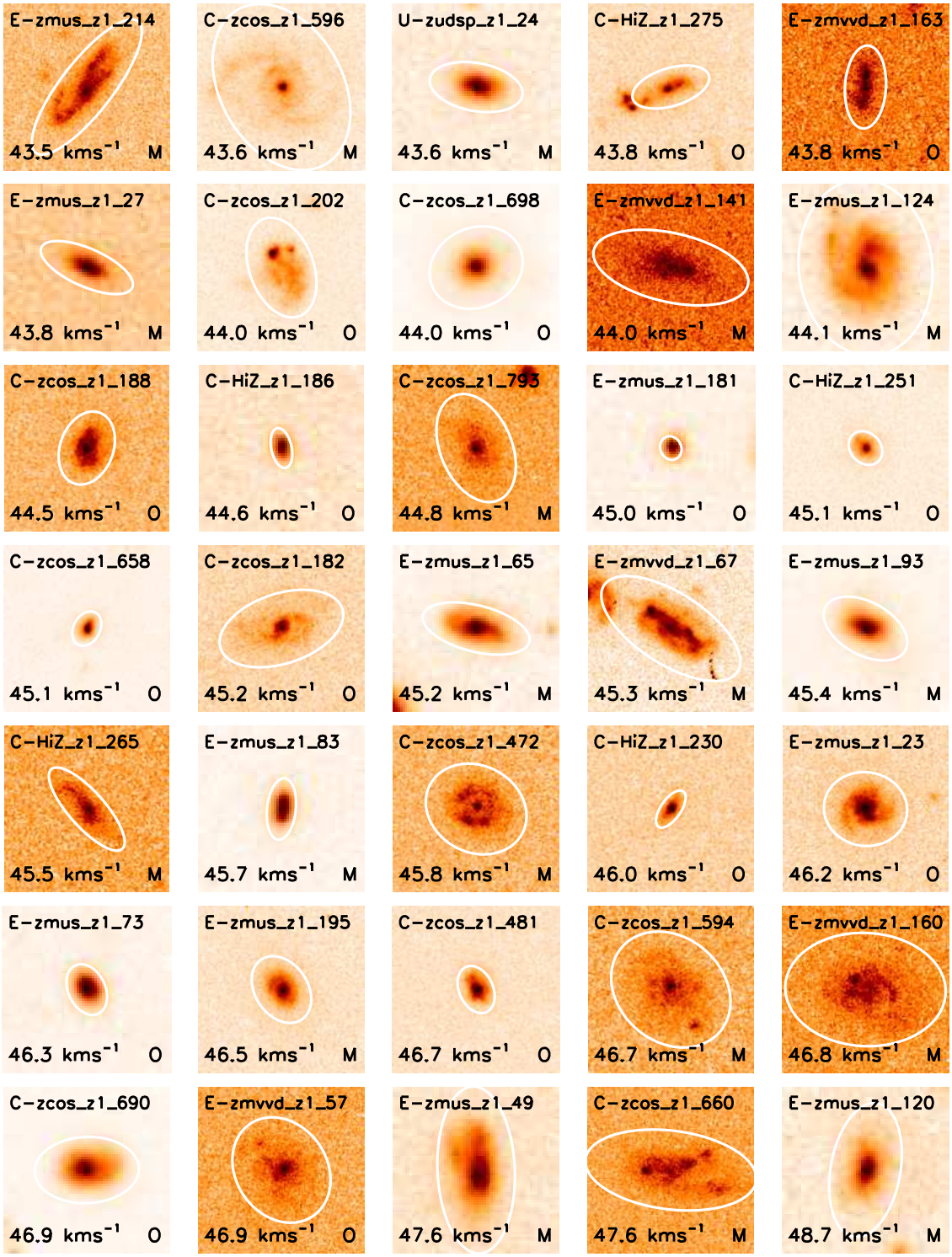

Figure A.1: *continued*

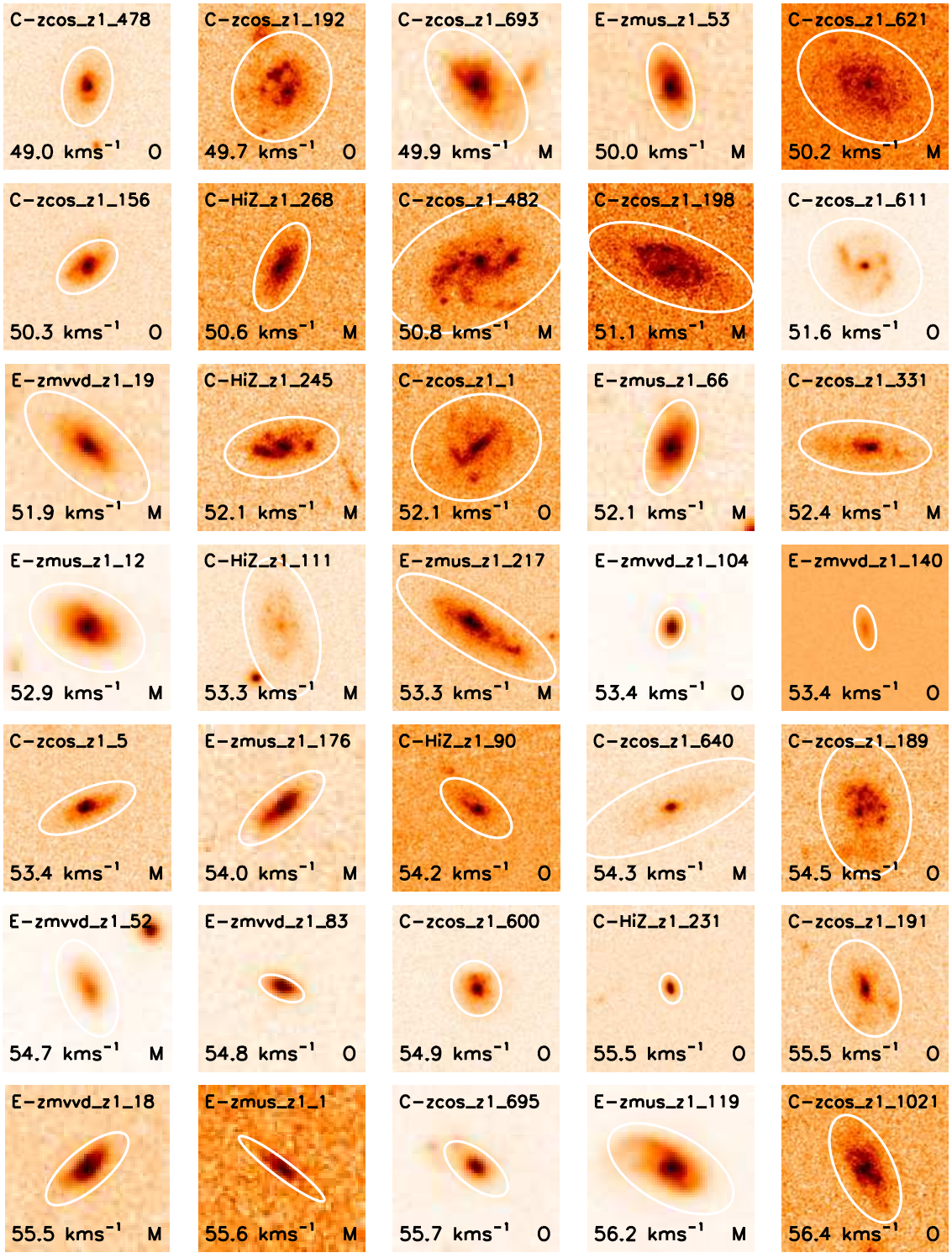

Figure A.1: *continued*

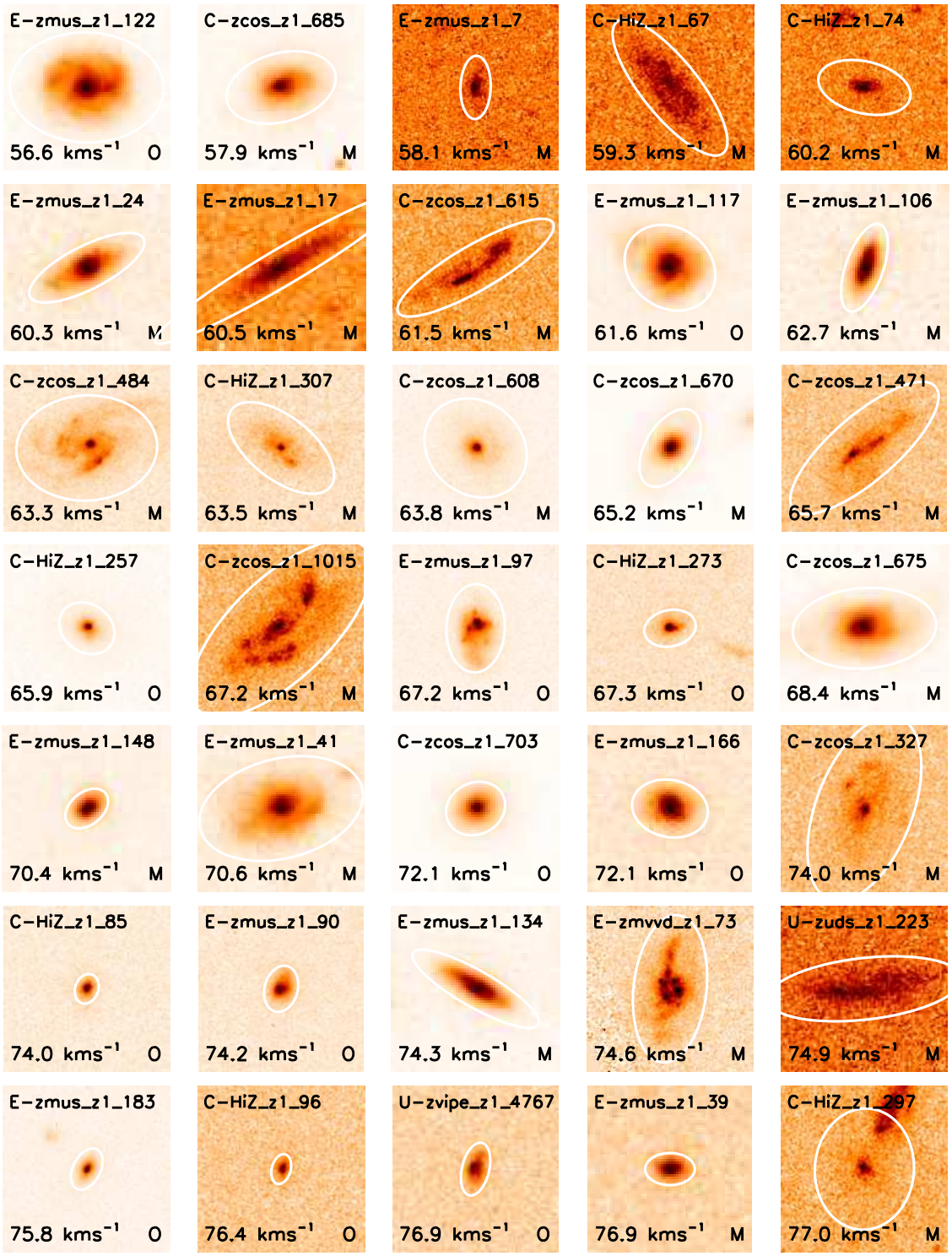

Figure A.1: *continued*

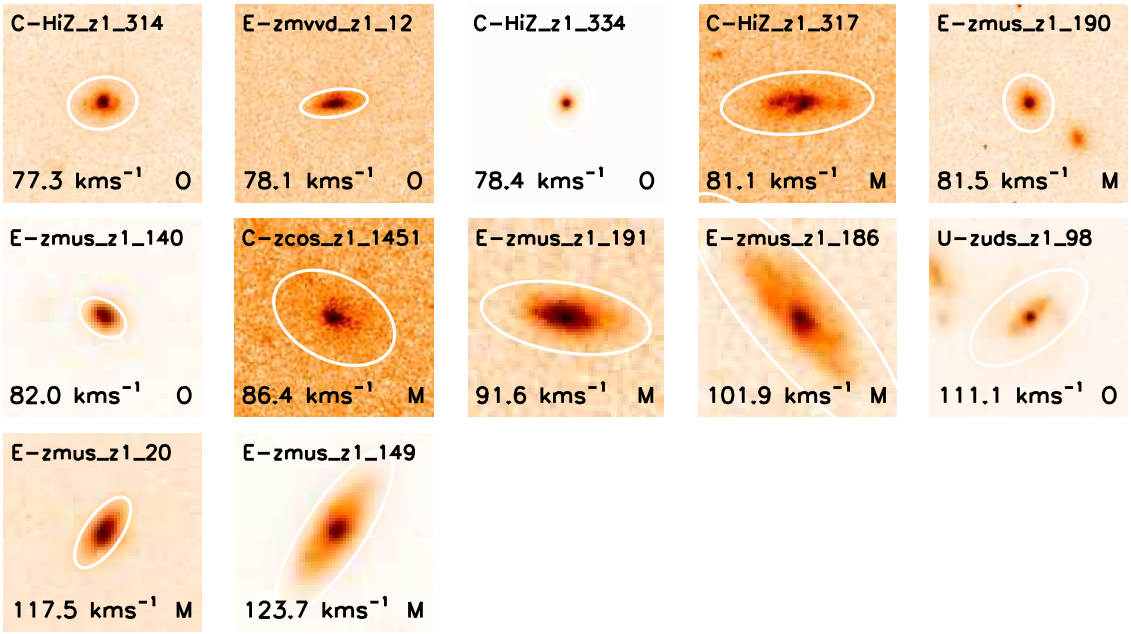

Figure A.1: *continued*